technische universität
dortmund

Biological systems: semiflexible polymer networks and active rods

Dissertation
to obtain the academic degree
Doctor rerum naturalium (Dr. rer. nat.)

submitted to the
Faculty of Physics, TU Dortmund

Pascal Müller
from Dortmund

Dortmund, December 2016

Abstract

In this thesis, the investigation of two different biological systems is described. Both are studied numerically and analytically.
In the first part, wrinkling of semiflexible polymer networks under shear strain is investigated. Due to their importantance in many biological systems and their unique mechanical properties, such networks are relevant in the fields of biology as well as materials science. Linear elasticity theory was used to analyse fundamental properties of wrinkling in sheared membranes such as the critical shear angle for the onset of wrinkling, the wrinkles' amplitude, and their wavelength. The obtained predictions were applied to discrete networks and compared to simulation results for such networks. The aim was to test under which conditions wrinkling in semiflexible polymer networks is accurately described by linear elasticity theory for thin membranes. Simulations were performed using networks with either regular or random microstructure that were generated in two dimensions but could access three-dimensional configurations during simulations. The comparison of analytical and numerical results showed good agreement regarding the critical shear angle and the wrinkles' wavelength. This indicates that these quantities can be used to identify the elastic properties of semiflexible polymer networks in experimental setups. At large strains, nonlinear effects were identified based on the wrinkles' amplitude and the networks' elastic energy. Furthermore, an analysis of the dominant deformation mode indicated that wrinkling would cause an immediate transition into a stretching dominated regime.
In the second part, two-dimensional systems of active rodlike particles are studied. Active systems are a key issue for understanding living matter and also a relevant topic in nanotechnology. They exhibit a wide variety of collective phenomena that can be understood as different manifestations of phase separation with an ordered high-density phase and an unordered low-density phase. The primary aim was to derive an analytical model capable of predicting the coexisting densities in such phase-separated systems. The secondary aim was to reproduce rotating structures in simulations that have been observed mainly in experiments. Numerical results were obtained using agent-based Brownian dynamics simulations. These would exhibit a variety of collective phenomena similar to those reported in the literature. Rotating structures were not observed though. A phase diagram was generated indicating the coexisting densities in the phase-separated configurations as a function of particle motility. For the analytical investigation, two different models originally developed for spherical particles were adapted to the systems at hand. A force equilibrium approach yielded good agreement with the simulation results at large particle motilities and average densities. This model could not describe the phase separation at small particle motilities though. In a second approach, the coexisting densities were derived from the systems' free energy density. The two different variants of this model would reproduce one of the densities but not both of them simultaneously. Therefore, in the form presented here, both approaches are only partially successful in describing the phase separation.

Zusammenfassung

In dieser Arbeit werden zwei verschiedene biologische Systeme numerisch und analytisch untersucht.
Der erste Teil behandelt Faltenbildung in semiflexiblen Polymernetzwerken aufgrund von Scherdeformation. Als wesentlicher Bestandteil in vielen biologischen Systemen und durch ihre einzigartigen mechanischen Eigenschaften sind diese Netzwerke ein interessanter Forschungsgegenstand in der Biologie und den Materialwissenschaften. Mithilfe linearer Elastizitätstheorie wurden grundlegende Eigenschaften der Faltenbildung in gescherten Membranen analysiert, z.B. der kritische Scherwinkel sowie Amplitude und Wellenlänge der Falten. Die so erzielten Vorhersagen wurden auf diskrete Netzwerke übertragen. In Simulationen von Netzwerken mit regelmäßiger und ungeordneter Mikrostruktur wurde getestet, unter welchen Bedingungen diese sich korrekt durch lineare Elastizitätstheorie für dünne Membranen beschreiben lassen. Die Netzwerke wurden in zwei Dimensionen erzeugt, konnten aber während der Simulation dreidimensionale Konfigurationen annehmen. Der Vergleich von analytischen und numerischen Ergebnissen zeigt, dass diese in Bezug auf kritischen Scherwinkel und Wellenlänge der Falten gut übereinstimmen. Dies deutet darauf hin, dass beide Größen genutzt werden können um die elastischen Eigenschaften von semiflexiblen Polymernetzwerken in Experimenten zu bestimmen. Bei großen Verformungen wurden nichtlineare Effekte anhand der Amplitude der Falten und der elastischen Energie der Netzwerke beobachtet. Außerdem wurde festgestellt, dass Faltenbildung einen sofortigen Übergang in ein streckdominiertes Regime verursacht.
Im zweiten Teil werden zweidimensionale Systeme von aktiven stäbchenförmigen Teilchen untersucht. Aktive Systeme spielen eine zentrales Rolle in lebender Materie und sind außerdem für Nanotechnologien von Interesse. In diesen Systemen kann eine Vielzahl kollektiver Phänomene beobachtet werden, die als Phasenseparation in eine geordnete Phase hoher Dichte und eine ungeordnete Phase niedriger Dichte verstanden werden können. Vorrangiges Ziel war die Entwicklung eines analytischen Modells, das diese koexistierenden Dichten korrekt vorhersagt. Ein zweites Ziel war, experimentell beobachtete rotierende Strukturen in Simulationen zu reproduzieren. Numerische Ergebnisse wurden anhand teilchenbasierter Brownsche-Dynamik-Simulationen erzeugt. Diese zeigten eine Vielzahl kollektiver Phänomene ähnlich den in der Literatur beschriebenen, jedoch keine rotierenden Strukturen. Anhand der Ergebnisse wurde ein Phasendiagramm erstellt, das die koexistierenden Dichten in phasenseparierten Systemen als Funktion der Motilität der Teilchen beschreibt. Für die analytische Untersuchung wurden zwei Modelle für phasenseparierte Systeme von kugelförmigen Teilchen abgewandelt. Der erste Ansatz über ein Kräftegleichgewicht ergab gute Übereinstimmung mit den Simulationsergebnissen für ausreichend große Motilitäten und mittlere Dichten, lieferte jedoch keine korrekte Beschreibung bei geringen Motilitäten. Im zweiten Ansatz wurden die koexistierenden Dichten aus der freien Energiedichte des Systems hergeleitet. Die zwei Varianten dieses Modells konnten eine der beiden Dichten korrekt wiedergeben, jedoch nicht beide gleichzeitig. Folglich können beide Ansätze in der hier vorgestellten Form die Phasenseparation nur teilweise beschreiben.

Contents

List of symbols

Sheared semiflexible polymer networks

α	exponent describing the dependence of the critical shear angle γ_c on the rods' bending rigidity, p. 39
α_{LET}	α as predicted by linear elasticity theory, p. 39
γ	shear angle, p. 22
$\tilde{\gamma}$	rescaled shear angle, p. 45
$\delta\gamma$	shear increment, p. 32
γ_c	critical shear angle, p. 23
γ_{max}	shear angle up to which the wrinkles' amplitude increases with γ, p. 44
$\tilde{\gamma}_{\mathrm{max}}$	universal shear angle up to which the wrinkles' amplitude increases with γ, p. 45
$\boldsymbol{\epsilon}$	three-dimensional strain tensor, p. 19
$\boldsymbol{\epsilon}_{\mathrm{2D}}$	strain tensor in a two-dimensional membrane, p. 21
$\boldsymbol{\epsilon}'_{\mathrm{2D}}$	strain tensor in a two-dimensional membrane in a rotated coordinate system, p. 22
$\boldsymbol{\epsilon}_{\mathrm{m}}$	strain tensor in a two-dimensional membrane including stretching contributions due to bending, p. 21
$\boldsymbol{\epsilon}'_{\mathrm{m}}$	strain tensor in a two-dimensional membrane in a rotated coordinate system including stretching contributions due to bending, p. 23
ζ	empirical rescaling factor yielding data collapse for the wrinkles' amplitude, p. 45
η	a random network's crosslinking density, p. 32
$\eta^{\triangle}$	a triangular network's crosslinking density, p. 31
κ	a rod's bending modulus, p. 20
$\kappa_{\alpha\beta}$	a membrane's second fundamental form in Monge parametrisation, p. 21
λ	the wrinkles' wavelength, p. 23
λ_1	largest discrete wavelength under periodic boundary conditions, p. 29
λ_c	the wrinkles' wavelength at the critical shear angle γ_c, p. 23
λ_n	discrete wavelength under periodic boundary conditions with n indicating the number of wrinkles, p. 28
μ	a rod's stretching modulus, p. 20
ν	Poisson ratio, p. 19
$\nu^{\triangle}$	Poisson ratio of a triangular network, p. 27
ν^{r}	Poisson ratio of a random network, p. 28
$\boldsymbol{\sigma}$	three-dimensional stress tensor, p. 19
$\boldsymbol{\sigma}_{\mathrm{2D}}$	stress tensor in a two-dimensional membrane, p. 21

t a membrane's thickness, p. 20
u' local strain, p. 20
Y Young's modulus, p. 19
Y_2 two-dimensional Young's modulus, p. 20
$Y_2^{\triangle}$ two-dimensional Young's modulus of a triangular network, p. 27
Y_2^{r} two-dimensional Young's modulus of a random network, p. 28
z out-of-plane displacement field, p. 21
z_{CET} wrinkling pattern as expected from continuum elasticity theory, p. 33

Collective behaviour of active rods

α degree of ordering, p. 117
α_{min} degree of ordering that minimises the free energy density, p. 119
$\gamma_{\parallel}$ translational friction coefficient parallel to a particle's main axis, p. 63
$\gamma_{\perp}$ translational friction coefficient perpendicular to a particle's main axis, p. 63
γ_{rot} rotational friction coefficient, p. 64
ϵ strength of the Lennard-Jones potential, p. 53
η the medium's viscosity, p. 63
$\eta\mathrm{r}$ fraction of rejected moves, p. 94
λ_1 greater eigenvalue of the mass distribution tensor, p. 92
Λ thermal de Broglie wavelength, p. 58
$\boldsymbol{\xi}_{\parallel}$ stochastic force parallel to a rod's main axis, p. 63
$\boldsymbol{\xi}_{\perp}$ stochastic force perpendicular to a rod's main axis, p. 64
$\boldsymbol{\xi}_{\mathrm{rot}}$ stochastic torque, p. 64
ρ particle density, p. 58
$\Delta\rho$ resolution of a measured density distribution, p. 94
$\tilde{\rho}$ reduced particle density, p. 89
$\tilde{\rho}^*$ parameter determining the rapidity of linear/exponential decrease in velocity as a function of density, p. 118
$\tilde{\rho}_{\mathrm{iso}}$ density of the isotropic phase in a phase-separated system, p. 112
$\tilde{\rho}_p$ dimensionless density in the model taking into account the particles' effective elongation due to propulsion, p. 126
$\tilde{\rho}_{\mathrm{pol}}$ density of the polar phase in a phase-separated system, p. 121
$\tilde{\rho}_{\mathrm{sp}}$ splitting density for calculating the phase separation from a density distribution, p. 95
σ length scale of the Lennard-Jones potential, p. 53
τ_{rot} rotational relaxation time, p. 66
φ a particle's orientation relative to the x-axis, p. 63
ψ_α orientational distribution function, p. 117
Ω spatial angle, p. 58
a a particle's aspect ratio, p. 52

Chapter 1

Introduction

1.1 Relevance of biological research

In 1818, Mary Shelley's novel "Frankenstein" was first published – a story about a scientist bringing to life a humanoid creature made from non-living matter. Almost 200 years later, the novel is still present in our cultural memory and has inspired numerous films and other works of art [1] which is not surprising since the creation of life and its enhancement have fascinated mankind for centuries. People's attitude towards the subject is ambivalent: on the one hand, the nonbiological creation of life is portrayed as the cause for horror and misery as in "Frankenstein" or as an integral part of a dystopian society as in Aldous Huxley's "Brave New World" [2]. On the other hand, the promise of longevity is seen as a blessing that used to inspire alchemists centuries ago in their search for an elixir of life [3] and still drives modern research ranging from the medical challenges of curing diseases to the transhumanist movement aiming to use technological advancements to not only overcome the aging process but also improve our intellectual and physical abilities [4].
These recent endeavours require a detailed knowledge of human biology from macroscopic anatomy to the subcellular scale. Our physical abilities such as muscular strength or endurance are mainly determined by our musculoskeletal system including bones, muscles, and tendons [5]. Hence, understanding their functionality and interplay is key to enhancing physical capacities. On the cellular and subcellular scale, understanding the biological processes associated with certain diseases or aging could enable the application of nanotechnology in medicine. In the best-case scenario, this would ultimately lead to personalised medicine preventing or reversing severe diseases such as cancer and delaying the aging process [6–8].
The musculoskeletal system and the interior of a single cell are two examples for biological systems – systems that are composed of living organisms or parts of them. Their properties are greatly dependent on their components' biological functions but not exclusively. Physical laws also apply in these systems, and many aspects of biological systems can be understood from the physics within them. This approach is the origin of biophysics – a scientific discipline bridging the gap between biology and physics that has grown enormously in the 20th century [9]. It can be understood either as "the field where one extracts interesting physics from biological systems" [9] or as a field of research applying physical tools and methods to complex biological systems in order to study them quantitatively and provide a solid theoretical foundation [10, 11]. Examples for the contribution of physics to studying biological systems include the development

of experimental methods such as modern optical and electron microscopes, fluorescent probes enabling visualisation of living cells, and also computational methods such as molecular dynamics simulations [11].
This thesis falls into the category of biophysics as it investigates biological systems from a physical point of view. The topics in question are networks of biopolymers and systems of active rods both of which are relevant for several reasons. Networks of biopolymers are an integral part of the cytoskeleton of eukaryotic cells and many other biological systems, so studying these networks provides an opportunity to get a better understanding of those systems [12]. Additionally, networks of biopolymers exhibit fundamentally different mechanical properties than synthetic materials [12]. Due to this, they are of great interest in materials science as they could inspire the creation of novel materials and allow the utilisation of biomimetic materials [13]. The main reason for studying active rods is the fact that they are a typical representative of active matter. In biology, active matter is prevalent on all length scales from the subcellular to the macroscopic scale, so the study of active systems is a promising approach to understanding living matter in general [14, 15]. Active matter is also a relevant topic in nanotechnology: the imitation of biological swimmers and engines could lead to the development of artificial counterparts that are strongly desired for a variety of tasks on the nanoscale such as transport, organisation processes, and control of material properties [16, 17]. These applications would entail significant advances in medicine, materials science, and environmental science [18]. From a purely physical point of view, active matter is an interesting subject because it is a type of nonequilibrium system. This field has been subject to an increased interest in the last years [19]. The unique feature of active matter is that the energy input driving these systems out of equilibrium occurs at the level of individual particles instead of the macroscopic level as is the case in other nonequilibrium systems [14]. Also, the direction of motion in active matter is determined by its components' orientation and not by an external field [15].
In order to give an introduction into the studied systems, the following section presents the fundamentals of cells. The main focuses are the cytoskeleton in which biopolymer networks are a key element and bacteria as an example of active matter. In Section 1.3, an outline of the thesis is given.

1.2 Cells

Cells are the basic units forming all living organisms as they are the smallest units that can replicate independently. In order to do so, they duplicate the genetic information they carry within themselves in the form of DNA. In the process of cell division, a cell splits itself into two passing on one copy of the DNA to each of the new cells. When not indicated otherwise, the information presented here on cells, biofilaments, and bacteria was taken from the book "Molecular Biology of the Cell" by Bruce Alberts et al. [20]. Additional information on biofilaments stems from articles by Jülicher et al. [21], Pollard and Cooper [22], and Wen and Janmey [23]. Information on actin networks was adapted from articles by Lieleg et al. [24] and Fletcher and Mullins [25].

There are two types of cells – eukaryotic and prokaryotic cells, both of which are illustrated in Fig. 1.1. Both types contain a large number of components within a fluid called cytoplasm, and their outer shell is a membrane which separates the cells' insides from their environment. It acts as a selective barrier which controls the exchange of

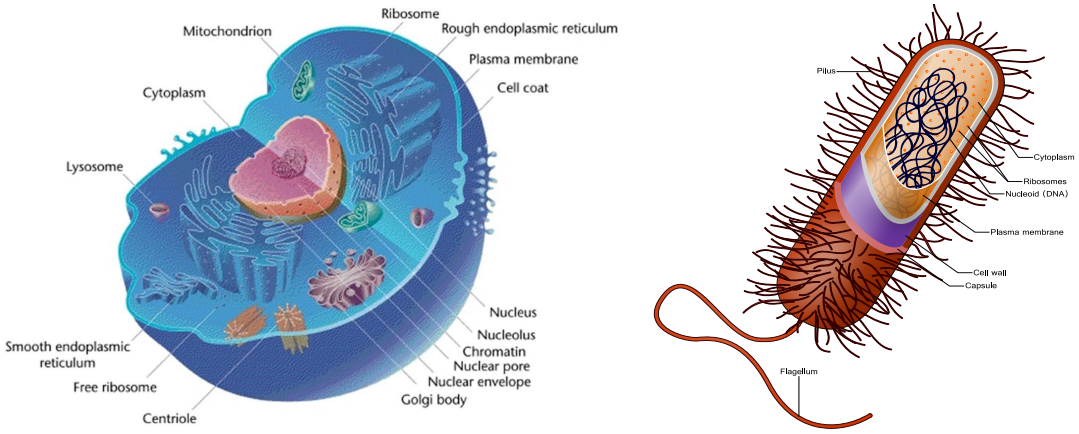

Figure 1.1: Left: Sketch of a typical eukaryotic cell showing many of its components such as the nucleus, cytoplasm, cell membrane, and a number of organelles. Image by Mediran (own work) (CC BY-SA 3.0), via Wikimedia Commons. Right: Sketch of a typical prokaryotic bacteria cell. In contrast to the eukaryotic cell, its constituents such as the chromosome are unorganised within the cytoplasm. Image by Ali Zifan (own work) (CC BY-SA 4.0).

molecules with the environment and hence allows the cell to take in nutrients and excreting waste products.
The main distinction between the two types is that in eukaryotic cells, the cell components are organised in subunits called organelles. One particularly important one is the nucleus which contains the cell's chromosomes and therefore genetic information. Some other organelles are the mitochondria which generate energy in the form of adenosine triphosphate (ATP) to fuel cell processes, the Golgi apparatus which – among other tasks – packages proteins before their transport to other destinations within the cell, and the centrosome which organises the cytoskeleton.
Prokaryotic cells do not contain organelles, so their constituents are unorganised within the cytoplasm. The genetic information of these cells is stored in a single chromosome. Two of the three domains of life – bacteria and archaea – are organisms that consist of single prokaryotic cells. In contrast to this, the third domain – eukaryotes – consists of organisms that can consist of a single eukaryotic cell but also of a large number of these.
Next, we will give a brief introduction into the main components of the cytoskeleton, and rodlike bacteria as these are relevant to this work.

1.2.1 Cytoskeleton

As mentioned before, cells have a membrane separating their insides from the environment. However, this membrane itself does not account for the cells' mechanical properties that are crucial for cellular processes such as deformation, migration, and division. These properties are mainly determined by the cytoskeleton – a dynamic network of biopolymers that spans the space between cell nucleus and membrane, see Fig. 1.2. In addition to the features mentioned above, the cytoskeleton is also responsible for providing mechanical stability and enabling transport within the cell. It is composed mainly of three polymers – actin filaments, intermediate filaments, and

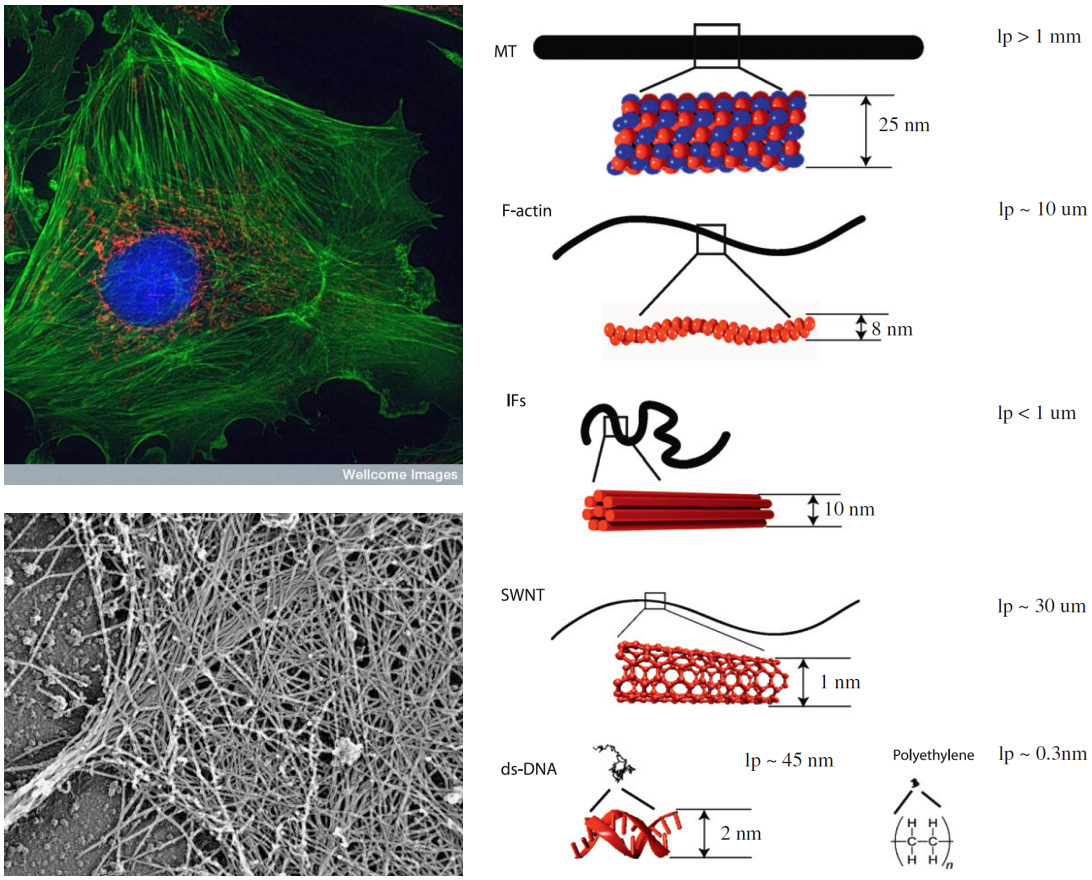

Figure 1.2: Top left: Micrograph of an artery cell with fluorescent labelled nucleus (blue) and actin filaments (green). The cytoskeleton of which actin is one of the main components spans the whole cell connecting the nucleus to the cell membrane. Image by Kevin MacKenzie, University of Aberdeen/ Wellcome Images (CC BY-NC-ND 2.0). Bottom left: Electron microscopy image of a PC12 cell providing a more detailed view of a network of actin filaments in the cytoskeleton. Source: National Heart, Lung, and Blood Institute, National Institutes of Health. Right: Comparison of the cytoskeleton's main components microtubules (MT), actin filaments (F-actin), and intermediate filaments (IFs) to other polymers such as single wall carbon nanotubes (SWNT), double strand DNA (ds-DNA), and polyethylene (PET). The polymers are drawn with a contour length of 10 µm as black lines demonstrating the effects of their significantly differing bending rigidities which are also indicated by their persistence lengths (lp). Reprinted with permission from Ref. [23]. Copyright 2011 Elsevier.

microtubules. Due to their elongated shape, these are also referred to as biofilaments. Their bending stiffness is enormous compared to synthetic polymers, see Fig. 1.2. A polymer's bending rigidity can be quantified by its persistence length l_p – the length scale on which it is straight, for details see Section 2.1.1. The larger persistence length of biofilaments leads to greater end-to-end lengths compared to synthetic polymers with the same contour length. Due to this, biofilaments can form extended networks already at low volume fractions.
Since experiments on actin filaments and microtubules served as a model for the simulations implemented in this work, these filaments will be introduced here in a bit more detail.

Actin filaments

Actin is a globular protein that can itself act as a monomer to form actin filaments – also referred to as microfilaments or F-actin. These filaments consist of two interlaced chains of actin and have a diameter of 8 nm [23]. Due to the structure of actin, microfilaments are polar with their two ends having fundamentally different properties. Under usual physiological conditions, a process called treadmilling occurs during which globular actin attaches to one end while dissociating from the other one. In eukaryotic cells, a large number of accessory proteins regulates actin polymerization and the treadmilling process as well as the formation of actin networks as shown in Fig. 1.2. A variety of crosslinking proteins such as filamin and myosin II is responsible for forming these. Actin networks are understood to be the primary component in the cytoskeleton for determining its mechanical properties. Myosin II belongs to the family of myosin proteins which contains a large number of proteins acting as molecular motors. These have the special ability to hydrolyse ATP and transform the released chemical energy into mechanical energy. Different myosins and their compounds perform different tasks in the cytoskeleton such as generating forces between actin filaments or moving along them. The former effect turns the networks into an active material and is crucial for cell migration, division, and deformation. This mechanism is also responsible for muscle contraction. The latter effect enables intracellular transport: by attaching to subcellular organelles or proteins, myosins can transport these along the microfilaments. The filaments' polarity determines the myosins' direction of movement. A similar mechanism which is in fact more important for intracellular transport is facilitated by the interplay of microtubules and the motor protein kinesin, see below.

Microtubules

Similarly to F-actin, the subunits forming microtubules are globular proteins: α- and β-tubulin. Dimers of these two proteins polymerise into protofilaments, and a number of those – usually 13 – arranged in a tube-like structure with a diameter of 25 nm form a microtubule. Since they are composed of dimers, microtubules are polar with a plus-end and a minus-end. They are typically oriented so that the plus-end points towards the cell's periphery while the minus-end is attached to a microtubule organizing center near the cell nucleus. This arrangement enables directed transport over long distances compared to the transport in actin networks. There are two motor proteins associated with microtubules: kinesin which moves towards the plus-end, and dynein which moves towards the minus-end. In combination, these two motor proteins enable bi-directional

transport between the cell's inside and its periphery.
With a persistence length of more than 1 mm, microtubules are the stiffest of the biofilaments in the cytoskeleton. However, its mechanical properties do not seem to be dominated by them – probably due to their lack of stable crosslinking. Also, microtubules do not have a stable structure. Instead, they constantly switch between a growing and a rapidly shrinking state. Due to this dynamic behaviour, they can only exert small forces on their surroundings and are not able to provide significant mechanical stability to the cytoskeleton.

Actin networks

Actin networks are the component of the cytoskeleton that mainly provides it with mechanical stability. At the same time, these networks are crucial for dynamic processes such as cell migration and division. Therefore, actin networks need to have structural integrity which is necessary for mechanical stability while also being able to restructure and reorganise. This versatility originates from a large number of crosslinking proteins that are present in the cell and interact with actin filaments. These are also referred to as actin binding proteins and play a major part in determining the structure, viscoelastic properties, and dynamic behaviour of F-actin assemblies.
One example for the variety resulting from the interaction of different crosslinking proteins with F-actin is the polymorphism observed in F-actin assemblies. There are two main types of occurring structures – bundles and networks. In bundles, the filaments are tightly packed and parallel while in networks, single filaments are crosslinked at greater angles creating a less dense and more wide-spread structure. Composite structures of networks and bundles are also possible.
Different actin binding proteins interact with F-actin in a variety of ways creating a number of different networks. One of the most prominent examples is a protein complex called Arp2/3 complex that creates branched networks in which the filaments are connected at a fixed angle of 70°. These networks are dense and can usually be found at the cell's leading edge. Other proteins such as filamin, α-actinin, or heavy meromyosin do not impose a fixed angle and therefore result in a more disordered network structure. Usually, the concentration of crosslinking proteins also affects the networks's structure. At low concentrations, networks are necessarily weakly crosslinked. High concentrations of heavy meromyosin lead to the formation of isotropically crosslinked networks while high concentrations of filamin or α-actinin yield composite structures or even networks of actin bundles.

1.2.2 Bacteria

Bacteria are unicellular organisms that belong to the oldest lifeforms on earth. With a typical size of a few micrometres, they are about one tenth the size of eukaryotic cells. Other major differences between these two types of cells result from the fact that bacteria are prokaryotes. As such, they are composed of a cell membrane enclosing the cytoplasm which contains the cell's components like proteins and the DNA. Even though bacteria exhibit subcellular structure and also have a cytoskeleton, their degree of internal organisation is not as high as in eukaryotic cells.
On the outside, bacteria have a cell wall that is in most cases made of a polymer called peptidoglycan. This cell wall is essential for protection – a fact that is exploited by the antibiotic penicillin which inhibits the renewal of the cell wall and thereby causes the

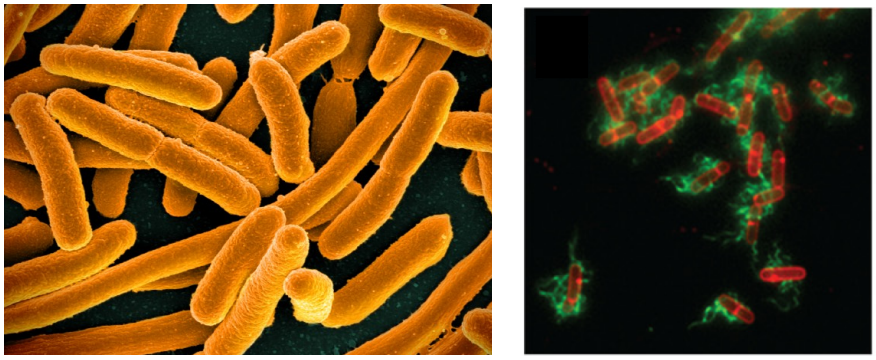

Figure 1.3: Left: A colourized scanning electron micrograph of E. coli. Courtesy: National Institute of Allergy and Infectious Diseases. Right: A fluorescence micrograph of B. subtilis with their membrane false coloured red and their flagella false coloured green. Reprinted with permission from Ref. [26].

cells to die.
Many bacteria also have the ability to self-propel, e.g., due to flagella. These are semi-rigid filamentous structures that grow from the bacteria's surface. They are connected to a tiny motor within the cell membrane that causes them to rotate and thereby generate propulsion.
Bacteria can be found in a large variety of shapes such as spheres, rods, and spirals. Two species that are commonly used in experiments similar to the simulations implemented for this work are Escherichia coli and Bacillus subtilis, see Fig. 1.3. Both of these are cylindrically shaped and of similar size. E. coli has a diameter of about 0.5 µm and a length of about 2 µm [20] while B. subtilis is a little larger with a diameter of 0.7 µm and a length varying from 4 to 7.4 µm [27, 28]. They belong to different classes of bacteria with E. coli being a Gram-negative bacterium while B. subtilis is a Gram-positive bacterium. The two classes represent different compositions of the bacteria's cell wall.
Both bacteria are naturally part of humans' and other animals' gut flora and have a long history as objects of research. E. coli is known to be the most studied bacteria of all and is still frequently used as a model organism due to a number of advantages such as its simplicity, wide availability, and short replication time of as low as 20 minutes under favourable conditions. For example, most of what we know about the replication of DNA and how information is decoded within it is a direct result of studying E. coli. B. subtilis is probably the most studied Gram-positive bacterium and known for its ability to survive in hostile environments by forming resistant endospores – structures that can be understood as the dormant form of the bacterium.
E. coli and B. subtilis are both capable of self-propulsion due to a number of helical flagella growing from their surface. Each of these is driven by a motor that can rotate in both directions – clockwise and counter-clockwise. Simultaneous counter-clockwise rotation causes the flagella to form a bundle yielding straight propulsion along the bacterium's main axis. On the other hand, clockwise rotation of just one flagellum is sufficient to cause the bacterium to rotate randomly while maintaining its position. These dynamics are a prime example for run-and-tumble motion, see Section 3.2.2. For E. coli, the swim speed is known to be about $20\,\mu\mathrm{ms}^{-1}$ [29] with the straight 'runs' lasting for approximately 1 s while 'tumbling' events only take about 0.1 s [30].

Besides swimming in a fluid, E. coli and B. subtilis can also use their flagella for moving on surfaces such as agar plates. This kind of movement is called swarming motility. Even though a number of bacteria are capable of swarming motility, this process is not as well understood as swimming. For example, B. subtilis is known to secrete a slime layer on which they can then glide, but this does not seem to be required by E. coli [31]. Swarming motility is a useful feature for performing two-dimensional experiments with motile bacteria.

1.3 Outline of this thesis

This thesis presents results from numerical investigations of two different systems that are modelled after biological systems. Since the problems are not directly related, they will be discussed separately.
In Chapter 2, the elastic response of semiflexible polymer networks is studied. A prime example for these are actin networks in the cytoskeleton of eukaryotic cells – see Section 1.2.1. The main focus lies on wrinkling of planar networks due to in-plane shear deformation. This effect has been studied numerously in continuous sheet-like materials but not in materials in which their discrete microstructure is critically important. Elasticity theory is used to derive predictions for fundamental properties such as the critical strain for the onset of wrinkling, wrinkle wavelength, and amplitude. These predictions are tested in numerical simulations. For more details on the focus of that chapter, see Section 2.1.5.
In Chapter 3, the collective behaviour of active rodlike particles in two dimensions is investigated. These represent cylindrically shaped bacteria like E. coli or B. subtilis swarming on a surface – see Section 1.2.2. Active systems like these exhibit a variety of collective phenomena ranging from static asters over collectively moving clusters to swirling motion. Many of these phenomena can be classified as phase-separated configurations with an ordered high-density phase and an unordered low-density phase. The main focus of this work is the attempt to find an analytical model predicting the densities in the coexisting phases. For more details, see Section 3.1.6.

Chapter 2

Sheared semiflexible polymer networks

2.1 Semiflexible polymer networks

Semiflexible polymers have become a topic of large interest over the last years since they are essential components of living organisms. Assemblies of semiflexible biopolymers constitute various fundamental structural components in biological systems – one prominent example being the polymer networks forming the cytoskeleton, see Section 1.2.1. The following section gives a brief introduction into the subject of semiflexible polymer networks following mainly review articles by Picu [13] and Broedersz and MacKintosh [12]. Subsequently, the focus and outline of this chapter are presented in Section 2.1.5.

2.1.1 Semiflexible polymers

Polymers are divided into three categories according to their bending rigidity: flexible, semiflexible, and stiff polymers. The bending rigidity is quantified by their persistence length l_p – the length scale over which they appear straight in the presence of thermal fluctuations. By comparing l_p to the contour length l of a specific polymer, we can assign it to one of three categories: when l_p is small compared to l, the polymer is called flexible. Polymers with $l_p \approx l$ are referred to as semiflexible, and $l_p \gg l$ defines stiff polymers.
The fact that $l_p \approx l$ for a semiflexible polymer can be understood as its bending rigidity being large enough to partially compensate for its tendency to crumple in order to maximise entropy. As a result of this competition, the polymer's conformation is essentially straight with small thermal fluctuations.

Since it is very difficult to study biopolymers in vivo, i.e., in their native environment [25], experiments are usually performed on in vitro systems – these are reconstituted systems that are artificially generated from the same but fewer components in a well-controlled environment. In the context of biopolymer networks, this means limiting the number of crosslinking proteins that interact with the polymers.
Despite the similarity of in vitro systems to in vivo systems, one has to be careful when applying results from one to the other. The systems may still have very different prop-

erties, e.g., Gardel et al. measured a mechanical stiffness in their generated networks that was "significantly weaker" than in the cellular cytoskeleton [32].

2.1.2 Models for semiflexible polymer networks

Since experiments on biopolymer networks are difficult and a comprehensive theory describing their behaviour in the full range of relevant parameters does not exist yet, a common approach to these networks are simplified models that can be implemented in computer simulations or studied analytically. These models can be distinguished by the networks' dimensionality, their internal geometry, and the polymers' mechanical response. Before discussing the differences between these models, we introduce the concept of affine and nonaffine deformations which plays a major role in the elasticity of semiflexible polymer networks.

Affine and nonaffine deformations

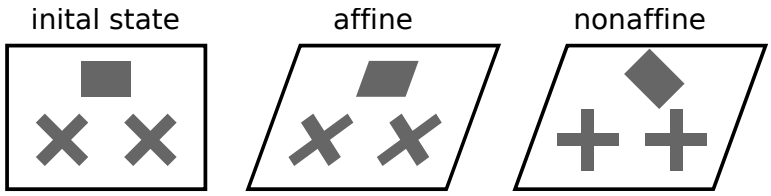

Figure 2.1: Illustration of affine and nonaffine deformations. A rectangular object with a substructure represented by geometrical shapes is sheared from its initial state (left). In case of an affine deformation, strain is universal, so the object's microstructure is deformed according to the macroscopic deformation (centre). For nonaffine deformations, microscopic and macroscopic deformation are different (right).

The deformation of an object is called affine when the strain within the object is universal. This automatically implies that the deformation of each microscopic part of the object is equivalent to its macroscopic deformation. In case of a deformed network, this means that the strain in each fibre is the same as the externally applied strain. Deformations for which this is not the case are called nonaffine, see Fig. 2.1 for an illustration. One of the most basic examples for this is Euler buckling of a straight elastic rod. When such a rod is under axial compressive stress, it is compressed up to a certain force threshold. At this threshold, the rod undergoes a buckling instability and gets bent. Since this deformation is perpendicular to its axis which is also the direction of the external strain, buckling is a nonaffine deformation.

2D and 3D networks

One major distinction between different models is whether they represent two-dimensional or three-dimensional networks. Since networks in biological systems are usually three-dimensional, it is obvious that three-dimensional models should be more realistic. However, they are also computationally more expensive since a larger number of fibres is required to achieve the same crosslinking density as in a two-dimensional

network. For this reason, two-dimensional networks are better studied than their three-dimensional counterparts. However, it is not entirely clear whether two-dimensional and three-dimensional networks behave similarly. In particular, it can be argued that the mechanical response of three-dimensional networks is more likely to be dominated by nonaffine deformations. Due to this, it still needs to be determined to what extent the results from two-dimensional models can be applied to realistic three-dimensional networks.

Thermal and athermal networks

The next distinction one can make is between thermal and athermal networks, i.e., whether or not thermal fluctuations are taken into account. These two approaches differ significantly in the polymers' response to stretching. In the thermal model, they are treated as entropic chains. These resist stretching since it decreases their entropy which is equivalent to an increase in free energy. In the athermal model, the polymers are modelled as elastic thin rods – see Section 2.2.2. Stretching increases their contour length, so their response is purely mechanical. In a real semiflexible polymer, the elastic response is a combination of the two contributions. However, the thermal response can be estimated to be dominant as long as $l^3 \gtrsim \frac{1}{4} d^2 l_p$ with d being the polymer's diameter [12]. So, the elastic response only becomes important for very small l.
For thermal networks, the shear modulus G can be derived assuming exclusively affine deformation. In the affine model, all crosslinks strictly follow the macroscopic shear strain γ. This implies that only stretching deformations are considered. In the limit of small γ, the polymers' entropic force-extension relation is approximately linear which makes it possible to calculate the occurring stress σ. This ultimately leads to the shear modulus

$$G_0 = 6\rho \frac{\kappa^2}{k_B T l_c^3} \ , \tag{2.1}$$

where ρ is the network's line density, κ is the polymers' bending modulus, k_B is the Boltzmann constant, T is the temperature, and l_c is the mean distance between crosslinks. Since $G_0 \propto l_c^{-3}$, the network's crosslinking density has a big impact on its elastic properties. Considering larger strains, the affine model also predicts a characteristic shear strain $\gamma_{\mathrm{nl}} = \frac{1}{6} \frac{l_c}{l_p}$ for the onset of nonlinearity in the network due to the nonlinear force-extension relation of the individual rods at large strains. The differential shear modulus which is defined as $K' = \frac{d\sigma}{d\gamma}$ becomes proportional to $\sigma^{3/2}$ in this strain regime while at small strains, $K' = \text{const.}$
This transition from $K' = \text{const.}$ to $K' \propto \sigma^{3/2}$ has been confirmed in experiments with actin networks [33–35], networks of intermediate filaments [36, 37] and even in synthetic polymer networks [38], see Fig. 2.2 for an illustration.

It should be noted though that the prediction from the affine model requires a purely entropic response to stretching which is not the case in real polymers. Evidence for this can be found – for example – in experiments with networks of intermediate filaments at large stresses [36, 37]. Also, some experiments with actin networks indicate that the scaling exponent α in $K \propto \sigma^\alpha$ depends on the concentration of crosslinkers [39].
One of the main approximations of the affine model is that the network's fibers are only deformed by stretching. Hence, when bending deformations become important, the affine model breaks down. Since bending of semiflexible polymers is typically much

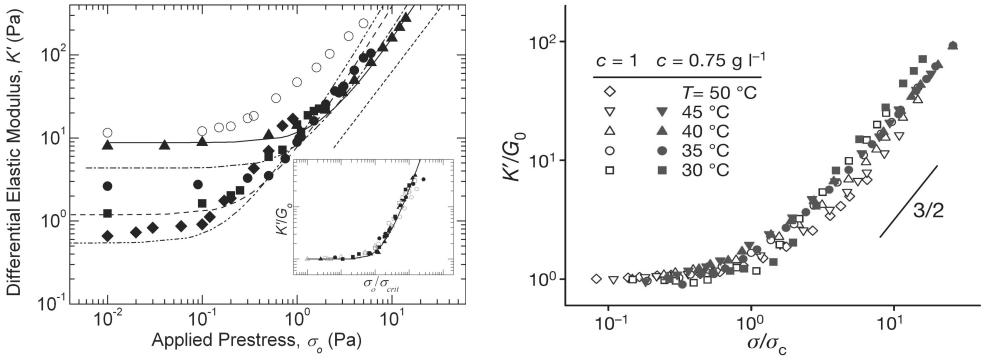

Figure 2.2: Experimental results showing nonlinear elasticity in thermal networks. The differential shear modulus K', which is constant at small strains, becomes proportional to the shear stress σ (σ_0 in the left plot) at large strains resulting in $K' \propto \sigma^{3/2}$. Left: experimental data from actin networks with the crosslinker scruin at different actin concentrations. The dashed line indicates the asymptotic dependence $K' \propto \sigma^{3/2}$. The inset shows data collapse due to rescaling. From Ref. [34]. Reprinted with permission from AAAS. Right: Similar rescaled data for synthetic polymer networks at different polymer concentrations c and temperatures. Adapted with permission from Ref. [38]. Copyright 2013 Nature Publishing Group.

easier than stretching, this is a crucial factor for their networks. This aspect is taken into account by athermal models. These approximate the polymers' elastic properties by treating them as thin rods with a purely mechanical response to deformations – see Section 2.2.2. The most prominent example for such a model is the Mikado model [40–42]. In the Mikado model, networks are constructed by depositing filaments at random positions with random orientations in a two-dimensional area. Filaments are crosslinked where they intersect and these crosslinks are treated as permanent and freely rotating. Analogously to the thermal model, the affine model can be applied to athermal networks which yields the affine shear modulus

$$G_{\text{aff}} = \frac{\pi}{16} \frac{\mu}{l_c} \,, \tag{2.2}$$

with the filaments' stretching modulus μ. This shear modulus can be expected to be valid as long as stretching is the dominant mode of deformation in the networks. In general, this affine regime is associated with large strains [43], but other factors are also relevant: large densities and bending rigidities favour affine behaviour [40–42]. Accordingly, the networks' elasticity tends to be dominated by bending deformations at small strains, low densities, and low bending rigidities [40–43].

In this nonaffine regime, the shear modulus is predicted to be $G \propto \kappa$. This has been confirmed using simulations of the Mikado model [40–42, 44], see Fig. 2.3. These works also find a universal form for the dependence of G on the network density ρ in the nonaffine regime. This can be expressed as $G \propto (\rho - \rho_c)^{\alpha_1}$ with a critical density ρ_c. The exponent α_1 can be predicted via different approaches [40–42, 45, 46] yielding similar results that show good agreement with simulation data.

The above results for the affine model in athermal networks assume linear elasticity, so they are not valid for large deformations that cause nonlinear behaviour such as strain stiffening and negative normal stress. It is worth pointing out that nonlinear

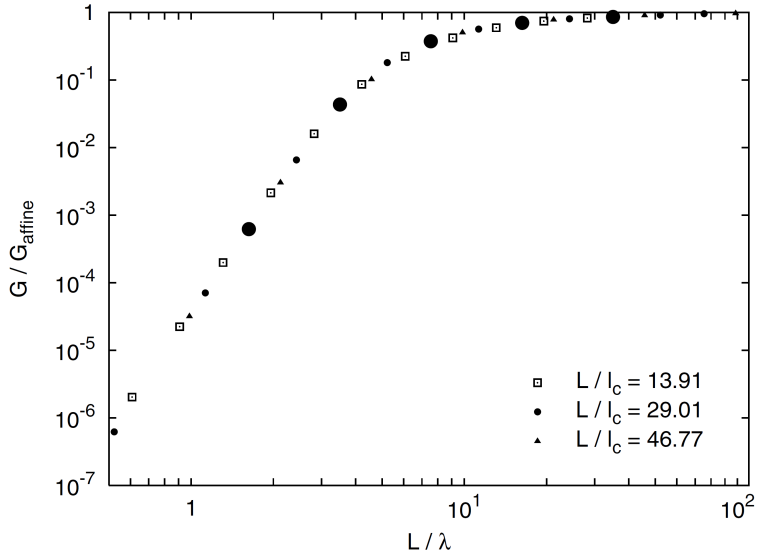

Figure 2.3: Rescaled shear modulus G/G_{affine} (with G_{affine} being the shear modulus in the affine limit) as a function of bending rigidity in simulations of athermal networks generated using the Mikado model. The ratio L/λ is proportional to the filaments bending modulus: $L/\lambda \propto \kappa^{1/3}$. In the nonaffine regime associated with small bending rigidities, $G \propto \kappa$ in contrast to the affine regime at large bending rigidities where G does not depend on κ. Reprinted with permission from Ref. [40]. Copyright 2003 American Physical Society.

elasticity even occurs when the individual fibers' elasticity is strictly linear – which is counterintuitive. Nonlinear effects are discussed in more detail in Section 2.1.3.

Internal geometry

Depending on how they are constructed, networks can have different microstructure. It is possible to generate networks from a repeated pattern yielding a perfectly regular geometry. These kinds of networks have proven very useful for understanding linear elasticity. However, real polymer networks are not perfectly ordered, so the models used to study them usually include some kind of randomness. One can distinguish two approaches to this – lattice-based and off-lattice models. Examples for both kinds of models are shown in Fig. 2.4. Lattice-based networks are constructed similarly to the regular networks mentioned before, but randomness is introduced into their microstructure by randomly displacing the nodes or randomly eliminating individual fibers. The other option are off-lattice networks which are generated from randomly placed fibers. One example for this was already mentioned in the previous section: the Mikado model. Another example would be letting the fibers grow from seeds at random positions.
The networks' properties are also influenced by the type of crosslinks that is used. Some examples would be crosslinks with fixed positions in space, crosslinks that are free to move but have a fixed position relative to the adjoined fibers, and crosslinks that can glide along polymers. Also, crosslinks can differ in the way they restrict rotation of the adjoining fibers relative to each other. Freely rotating crosslinks – or "rotating joints" – do not impede rotation at all whereas "welded joints" enforce a fixed angle between

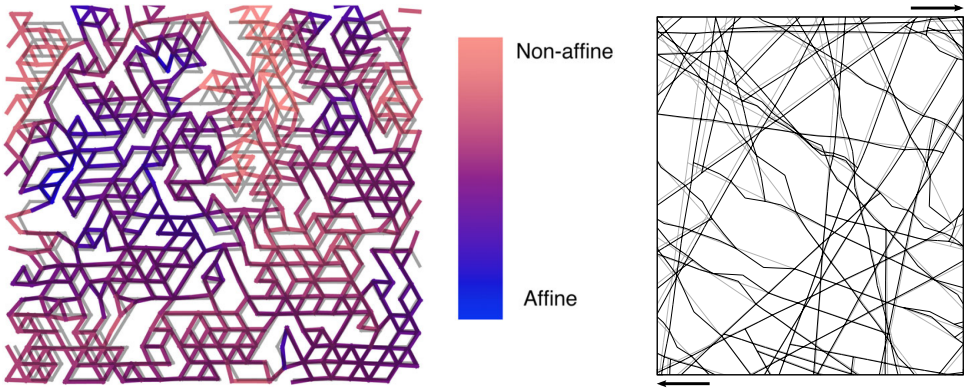

Figure 2.4: Two examples for network geometries used in simulations. Left: a deformed fiber network generated from a triangular lattice by eliminating individual fibers. Colour coding indicates the degree of nonaffinity, and the gray lines indicate the configuration resulting from a perfectly affine deformation. Reprinted with permission from Ref. [12]. Copyright 2014 American Physical Society. Right: cutout from a sheared fiber network generated using the Mikado model. Arrows indicate the shearing direction, and gray lines indicate the affine configuration.

the fibers. It is also be possible to have joints that allow rotation but deviations from a preferred angle are associated with an energy cost.

2.1.3 Nonlinear behaviour of semiflexible polymer networks

Networks of semiflexible polymers have been reported to have a nonlinear elastic response to external stresses or strains. Some of the most common observed effects are negative normal stress [47, 48] as well as stiffening [32–34, 36, 37, 39, 49–54] and softening [50, 52, 53, 55] at large strains.

Strain stiffening

Many applications of deformed networks involve large strains which is why the networks' elastic response to large strains is relevant. One effect that is especially pronounced in semiflexible polymer networks is strain stiffening [13]. Strain stiffening refers to an increase of the material's elastic moduli with increasing strain. This is a nonlinear effect since the elastic properties of an object are independent of the applied strain in the limit of linear elasticity.
Strain stiffening has been observed experimentally in actin networks [32–34, 39, 49–54] and networks of intermediate filaments [36, 37]. For an example plot, see Fig. 2.5. The universal finding is that networks stiffen at strains above a critical value. However, the degree of stiffening has been reported to be influenced by a number of factors such as the crosslinker concentration, filament length, or the type of crosslinker in the networks. Low crosslinker concentrations can reduce the degree of stiffening or even lead to softening of the networks [34, 39, 53]. Kasza et al. found that rigid crosslinkers yield weaker stiffening than flexible crosslinkers [50]. They also reported that networks of shorter filaments can exhibit softening at medium strains before stiffening at large strains. Tseng et al. observed that actin networks crosslinked with filamin or α-actinin exhibit strain stiffening while networks with fascin crosslinkers do not stiffen [53].

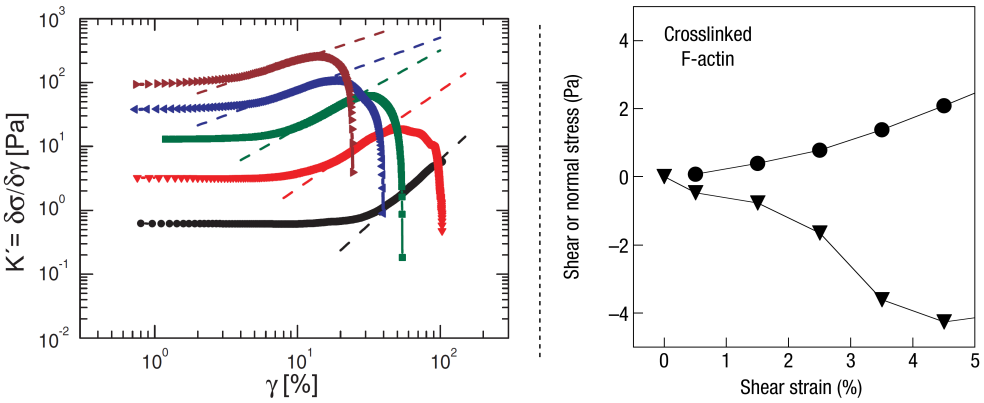

Figure 2.5: Examples for nonlinear behaviour in actin networks. Left: differential shear modulus K' as a function of shear strain γ in actin networks with different densities. Increasing K' indicates stiffening of the networks, and rapid decrease indicates softening caused by rupturing. Reprinted with permission from Ref. [39]. Copyright 2007 American Physical Society. Right: shear (circles) and normal stress (triangles) as a function of shear strain γ in actin networks. Decreasing normal stress indicates negative normal stress. Reprinted with permission from Ref. [47]. Copyright 2007 Nature Publishing Group.

These findings demonstrate that all network components – filaments as well as crosslinkers – determine the networks' elasticity. A comprehensive explanation for strain stiffening has not been found at this point. Different models have been suggested that seem to contradict each other: While Gardel et al. conclude from their findings that the networks' elasticity is mainly entropic and stiffening is caused by the nonlinear force-extension behaviour of the individual filaments [33, 34], Kasza et al. find evidence that the networks' elasticity is dominated by the crosslinkers [50].
Strain stiffening can be observed not only in experimental setups but also in simulations of semiflexible polymer networks in two [43, 46, 56] and three dimensions [57–59]. These findings are especially interesting because the filaments in the simulated networks were modelled as linearly elastic at all strains. Due to this, one would not necessarily expect the networks to exhibit nonlinear elasticity. Since strain stiffening still occurs, Onck et al. concluded that this nonlinear behaviour is a structural effect of the networks resulting from the re-orientation of filaments [43]. At small strains, the networks' elasticity would be dominated by bending deformations. With increasing strain, filaments would align with the principal stress direction causing stretching to become the dominant deformation mode. Since stretching of semiflexible polymers is generally harder than bending, this results in an overall stiffening of the networks. This explanation was confirmed by Heussinger et al. [46]. An alternative model was suggested by Storm et al. [60] identifying the nonlinear force-extension relation of individual filamets as the main cause for strain stiffening. Both models were compared by van Dillen et al. [61] finding both explanations valid but the re-orientation to be the dominant mechanism at large strains. Another explanation assigning stiffening to the crosslinks' mechanical properties was put forward by Broedersz et al. [62].

Strain softening and negative normal stress

Semiflexible polymer networks have also been reported to exhibit an opposite effect to strain stiffening. Networks were found to become easier to deform with increased strain in experiments [39, 50, 52, 53, 55, 63] as well as in simulations [56, 59]. The softening mechanism is not understood very well yet. While Tseng et al. reported softening at low crosslinker concentrations and stiffening at high crosslinker concentrations [53], Lieleg et al. observed just the opposite behaviour [52]. On the one hand, softening was observed to preceed stiffening [50] but also to occur at larger strains than stiffening [39, 50, 52]. One example for the latter effect can be seen in Fig. 2.5.
Also, there is still some dispute about the cause for stress softening. The simulations by Åström et al. suggest that the unbinding of crosslinkers is responsible for softening [59]. The same is true for the experimental results presented by Lee et al. showing irreversible strain softening [63]. However, the unbinding of crosslinkers cannot be the cause for reversible softening as reported in dendritic actin networks by Chaudhuri et al. [55]. Instead, the authors suggested that buckling of compressed filaments decreasing the networks' stiffness.

Another example for nonlinear elasticity that can be observed in semiflexible polymer networks is negative normal stress. When subject to shear, most materials expand along an axis that is perpendicular to the direction of shear. This phenomenon is known as positive normal stress [47]. Sheared networks of semiflexible polymers were reported to exhibit the opposite behaviour. When sheared between two plates networks of such biofilaments were reported to exert a tensile force on these plates [47, 48], see Fig. 2.5 for an example. This effect was also found in two-dimensonal simulations using the Mikado model [44, 46, 56]. Negative normal stress is an intrinsically nonlinear effect that is not to be confused with lateral contraction determined by the material's Poisson ratio ν, see Section 2.2.1. It has been explained in a thermal model as the result of an asymmetric force-extension relation of the individual fibers, i.e., the fact that compression requires less force than stretching [47]. However, this does not explain the occurence of negative normal stress in simulations of athermal networks without an asymmetric force-extension relation. An alternative explanation which is also valid for these networks attributes the negative normal stress to buckling of compressed filaments [46, 56]. This model was also found to be in better agreement with experimental results than the thermal model [48].

2.1.4 Measuring nonaffinity

As outlined in the previous sections, the elastic response of deformed networks often depends on whether the deformations within the network are affine or nonaffine. For example, the affine model which only considers stretching deformations yields good predictions in thermal networks under shear. In athermal networks though, nonaffine bending deformations are important – see Section 2.1.2. Also, as described in Section 2.1.3, the transition from a bending dominated – or nonaffine – regime to a stretching dominated – or affine - regime has been linked to the onset of strain stiffening. Moreover, buckling of compressed filamets which is a nonaffine deformation has been suggested as a mechanism explaining strain softening and negative normal stress – see Section 2.1.3.
Hence, there is interest in measuring the degree of (non-)affinity in deformed networks,

and there are several methods for doing this. The most general one was presented by DiDonna and Lubensky [64]. They defined a correlation function Γ at position vector $\boldsymbol{r}$ as follows:

$$\Gamma(\boldsymbol{r}) = \langle(\delta\boldsymbol{u}(\boldsymbol{r}) - \delta\boldsymbol{u}(0))^2\rangle \ . \tag{2.3}$$

Here, $\delta\boldsymbol{u}(\boldsymbol{r}) = \boldsymbol{u}(\boldsymbol{r}) - \boldsymbol{u}_{\text{aff}}(\boldsymbol{r})$ denotes the difference between the actual displacement $\boldsymbol{u}(\boldsymbol{r})$ caused by a deformation and the corresponding affine displacement $\boldsymbol{u}_{\text{aff}}(\boldsymbol{r})$. The authors showed that many other parameters used for measuring nonaffinity can be expressed in terms of this correlation function. In some cases, there are good reasons for using other parameters though, e.g., they may be easier to measure.
One other example for a nonaffinity parameter was introduced by Head et al. [40, 41]. In their simulations of sheared networks, they considered difference vectors between crosslinks at a distance r and measured the angular change $\theta(r)$ for these vectors. Compared with the angular change expected for an affine deformation $\theta_{\text{aff}}(r)$, this gave the parameter

$$\langle\Delta\theta^2(r)\rangle = \langle(\theta(r) - \theta_{\text{aff}}(r))^2\rangle \ . \tag{2.4}$$

Using this parameter, the authors found the degree of nonaffinity decreasing with increasing r and a general increase in nonaffinity at low bending stiffness.
Another method of measuring nonaffinity was presented by Onck et al. for simulations of sheared networks [43]. They used a parameter ΔA measuring the the amount of deviation between a network's deformation and a purely affine deformation. This parameter is calculated as an average over the n points of the network:

$$\Delta A = \frac{1}{n}\sum_{k=1}^{n}\frac{|\Delta\boldsymbol{r}_k - \Delta\boldsymbol{a}_k|}{|\Delta\boldsymbol{a}_k|} \ . \tag{2.5}$$

Here, $\Delta\boldsymbol{r}_k$ is the displacement vector of point k due to the shear deformation, and $\Delta\boldsymbol{a}_k$ is the displacement of the same point that would occur in a purely affine deformation. The close relation between ΔA and Γ introduced in Eq. 2.3 is quite obvious from the equivalence of the numerator in Eq. 2.5 and $\delta\boldsymbol{u}(\boldsymbol{r})$. The authors found that a peak in ΔA marks the the transition from a bending dominated regime to a stretching dominated one as it coincides with the onset of strain stiffening – see Section 2.1.3.
An entirely different approach for measuring nonaffinity was suggested by Åström et al. [59]. Instead of deriving the degree of nonaffinity from the actual displacements in the network, they used the fraction f_s of the total elastic energy resulting from stretching. Lower values of f_s indicate an increase in bending deformations and hence nonaffinity. Since the energy contributions resulting from stretching and bending are not accessible in experiments, this method is only applicable to simulations.
In conclusion, we see that there is a wide range of different methods available for measuring nonaffinity. Even though the resulting parameters are very useful, they should be interpreted cautiously as a high value in the nonaffinity parameter could still coincide with a mechanical response that is dominated by affine deformations [12].

2.1.5 Focus and outline of this chapter

As outlined in the preceding sections, semiflexible polymer networks in two and three dimensions have been studied extensively in the last years. Despite this amount of

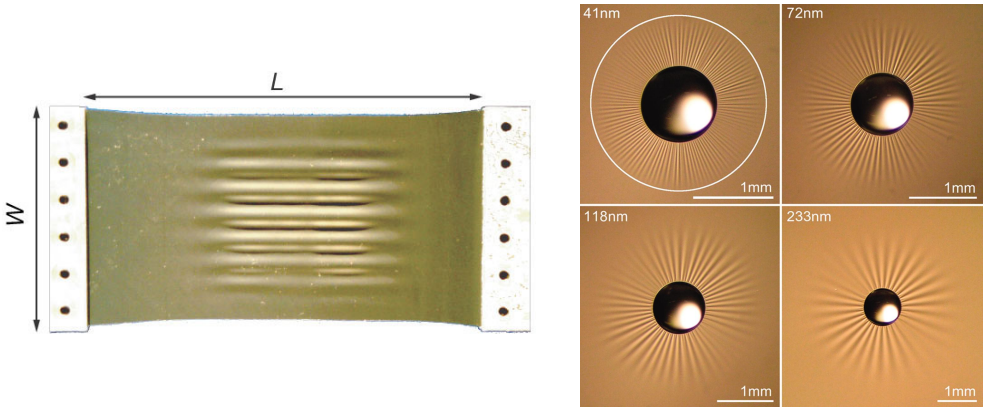

Figure 2.6: Examples for wrinkling in sheet-like materials. Left: in a uniaxially stretched polyethylene sheet, wrinkles form parallel to the stretching direction. Reprinted with permission from Ref. [65]. Copyright 2002 Nature Publishing Group. Right: droplets of water cause wrinkling of polystyrene films of different thicknesses. Numbers in the upper left corners indicate the wrinkles' length. From Ref. [72]. Reprinted with permission from AAAS.

experimental, numerical, and analytical work on the subject, one aspect has not gotten much attention so far: three-dimensional deformations of sheet-like networks. Such deformations are a common phenomenon in a wide range of sheet-like materials though. A prime example for this is wrinkling in response to compressive stresses which has been reported in a large number of experimental works [65–80]. Wrinkling in deformed sheet-like materials has also been studied analytically [65–67, 74, 81–85] and in many cases, the analytical predictions have been confirmed by the aforementioned experiments.

One frequently used material for experiments on wrinkling in sheet-like materials are polymer films constituted of flexible polymers, e.g., polyethylene, polystyrene, or polyimide. Due to their increased bending stiffness, semiflexible polymers are fundamentally different from flexible polymers, so it would be interesting to study whether semiflexible polymer films are similar to flexible polymer films with regards to wrinkling. It is fair to assume that a network's mechanical response can be greatly dependent on the elastic properties of its components – especially on length scales comparable to the mesh size.

In this chapter, wrinkling as a result of shearing is studied numerically in two-dimensional networks of semiflexible polymers. The results were already published in an article [86]. As the author is not aware of any prior publications regarding wrinkling in sheet-like materials composed of semiflexible polymers, that article might be the first work investigating this topic. Here, the material is presented in more detail. Networks are generated using the Mikado model [40–42] which is an athermal model hence neglecting the polymers' entropic elasticity but considering bending deformations – an aspect that is missing in thermal models. This work's focus is on fundamental properties of wrinkles such as the onset of wrinkling and wrinkle wavelength and amplitude. The numerical results are compared to predictions from elasticity theory in order to find out to what extent wrinkling in semiflexible polymer networks can be described by linear elasticity theory for thin membranes. Also, the influence of wrinkling on the dominant

deformation regime is examined.
The outline of this chapter is as follows: In Section 2.2, linear elasticity theory is introduced with a special emphasis on thin membranes and their wrinkling due to shear deformations. After obtaining predictions for fundamental wrinkle properties, these are applied to discrete networks. In Section 2.3, the numerical model is presented as well as the simulation routine and the measurements evaluated during simulation. In Section 2.4, the numerical results are presented and analysed. Finally, a conclusion of the chapter and a discussion of the results is given in Section 2.5.

2.2 Elasticity theory

Elasticity theory is a mathematical framework for the elastic deformation of solid bodies and makes predictions about the strain resulting from applied stresses. An elastic deformation is characterised by the fact that the deformed body relaxes to its initial shape when stresses are relieved. When the deformed body can not recover its initial shape, we call this an inelastic or plastic deformation. In the limit of small strains, deformations are usually elastic.
Most of the fundamentals of elasticity theory relevant to this work have been presented in detail in the author's diploma thesis [87] and will not be repeated here. Instead, a brief summary of the main aspects is given below. The derivation of the elastic energy and wrinkling properties of thin elastic membranes presented in Section 2.2.3 was not part of the diploma thesis and is therefore discussed in more detail. The information presented here was adapted from the books "Einführung in die Technische Mechanik: Festigkeitslehre" by Herbert Balke [88] and "Theory of Elasticity" by Lew Landau et al. [89].

2.2.1 Stress-strain relation and elastic moduli

Elasticity theory is used to calculate the strain that occurs in a solid body that is subject to external stresses. It is convenient to express these stresses and strains in three-dimensional tensors $\boldsymbol{\sigma}$ and $\boldsymbol{\epsilon}$. In the limit of linear-elastic deformations, the tensors are linearly related:

$$\epsilon_{\alpha\beta} = Y^{-1}\left[(1+\nu)\sigma_{\alpha\beta} - \delta_{\alpha\beta}\nu \operatorname{Tr}\boldsymbol{\sigma}\right] \ . \tag{2.6}$$

The factors Y and ν are material constants called elastic moduli. These moduli determine the material's elastic response to various deformations. The Young's modulus Y is associated with stretching deformation while the Poisson ratio ν quantifies transverse deformation. One simple example for transverse deformation is the contraction of a rubber band due to stretching. A number of other elastic moduli can be defined – two of which are the shear modulus G and the compression modulus K. All these moduli are dependent on each other by a number of relations. As a result, any two moduli of a perfectly isotropic material are sufficient to determine all other moduli.
Stress and strain tensor can also be used to calculate the elastic energy density e of a deformation:

$$e = \frac{1}{2}\sigma_{\alpha\beta}\epsilon_{\alpha\beta} \ . \tag{2.7}$$

2.2.2 Elasticity of thin rods

Since we consider networks of actin filaments in this work, we need to know the elastic properties of these filaments. Due to their elongated shape, they can be approximated as thin rods. In the limit of thin rods, radial deformations are neglected which makes it very easy to calculate the stress-strain relations for the deformation of thin rods. For example, stretching of a thin rod by a force $\boldsymbol{F}_x$ acting along its main axis elongating it from L to $L + \delta L$ can be described by a one-dimensional equation:

$$F_x = \mu \frac{\delta L}{L} \ , \tag{2.8}$$

Here, $\mu = YA$ is the rod's stretching modulus with A being its cross-sectional area. The resulting stretching energy $E^{(s)}$ can be written as an integral along the rod's arc length s:

$$E^{(s)} = \int_0^L \frac{\mu}{2} \left(u'(s)\right)^2 \, ds \ , \tag{2.9}$$

with $u'(s)$ denoting the local strain.
The energy resulting from a bending deformation $E^{(b)}$ can be expressed in a similar way:

$$E^{(b)} = \int_0^L \frac{\kappa}{2} \left(\phi'(s)\right)^2 \, ds \ , \tag{2.10}$$

where $\phi'(s)$ is the local curvature, and κ is the rod's bending modulus. Similar to the stretching modulus, the bending modulus is proportional to Young's modulus. This is because bending causes stretching of some parts of the rod and compression of others and the energy cost of bending results from these deformations. The second factor determining κ is the rod's moment of inertia I: $\kappa = YI$. For a cylindrical rod of diameter d, we have $I = \frac{\pi}{64} d^4$.
Comparing the rod's stretching and bending moduli, we see that $\mu \propto d^2$ while $\kappa \propto d^4$ which means that κ decreases more rapidly with decreasing diameter than μ. This implies that bending of thin rods is much easier than stretching them.

2.2.3 Thin membranes

For continuous isotropic materials like elastic membranes, we can calculate the response to shear strains analytically. Here, we focus on thin membranes in particular as the networks we study are composed of thin rods. An elastic membrane is considered to be thin if its thickness t is very small compared to its other dimensions. In this case, compressive and stretching stresses perpendicular to the surface can be neglected and the membrane can be treated as quasi two-dimensional. The elastic properties of such a material are characterised by the 2D Young's modulus Y_2, the compression modulus K, the shear modulus G, and the Poisson ratio ν. These are connected via the following relations:

$$G = \frac{Y_2}{2(1+\nu)} \ , \qquad K = \frac{Y_2}{2(1-\nu)} \ . \tag{2.11}$$

Bending of a membrane perpendicular to its surface is characterised by a bending modulus

$$B = \frac{Y_2 t^2}{12(1-\nu^2)} \ . \tag{2.12}$$

We now consider an in-plane deformation of a two-dimensional membrane in the xy-plane. Assuming a strain tensor

$$\boldsymbol{\epsilon}_{\mathrm{2D}} = \begin{bmatrix} \epsilon_{11} & \epsilon_{12} \\ \epsilon_{12} & \epsilon_{22} \end{bmatrix} \ , \tag{2.13}$$

we can derive the associated stress tensor using Hooke's Law:

$$\boldsymbol{\sigma}_{\mathrm{2D}} = \begin{bmatrix} \frac{Y_2}{1-\nu^2}(\epsilon_{11}+\nu\epsilon_{22}) & 2G\epsilon_{12} \\ 2G\epsilon_{12} & \frac{Y_2}{1-\nu^2}(\epsilon_{22}+\nu\epsilon_{11}) \end{bmatrix} \ . \tag{2.14}$$

With the two tensors, we can calculate the elastic energy density:

$$\begin{aligned} e_{\mathrm{2D}} &= \frac{Y_2}{2(1-\nu^2)}\left(\epsilon_{11}^2+\epsilon_{22}^2\right) + \frac{Y_2\nu}{1-\nu^2}\epsilon_{11}\epsilon_{22} + 2G\epsilon_{12}^2 \\ &= \frac{1}{2}G\left(\epsilon_{11}-\epsilon_{22}\right)^2 + \frac{1}{2}K\left(\epsilon_{11}+\epsilon_{22}\right)^2 + 2G\epsilon_{12}^2 \ . \end{aligned} \tag{2.15}$$

An out-of-plane displacement field $z(x,y)$ will give additional contributions to the elastic energy density due to the occurring bending energy and additional stretching strains within the membrane. When the displacements are small, we can use a Monge parameterisation of the displacement field and approximate the membrane's second fundamental form as

$$\kappa_{\alpha\beta} \approx \partial_\alpha \partial_\beta z + \mathcal{O}(z^2) \ , \tag{2.16}$$

with ∂_α denoting the partial derivative with respect to spatial coordinate α. With this, the bending energy density associated with bending can be written as

$$e_{\mathrm{B}} = \frac{1}{2}B\left(\kappa_{11}^2+\kappa_{22}^2+2\nu\kappa_{11}\kappa_{22}+2(1-\nu)\kappa_{12}^2\right) \ . \tag{2.17}$$

Out-of-plane deformation does not only introduce a bending energy but also causes stretching within the membrane. Taking into account the additional stretching strains yields a stretching tensor

$$\boldsymbol{\epsilon}_{\mathrm{m}} = \begin{bmatrix} \epsilon_{11}+\frac{1}{2}\left(\partial_x z\right)^2 & \epsilon_{12}+\partial_x z\partial_y z \\ \epsilon_{12}+\partial_x z\partial_y z & \epsilon_{22}+\frac{1}{2}\left(\partial_y z\right)^2 \end{bmatrix} \ . \tag{2.18}$$

This modified stretching tensor has to be used when calculating the elastic energy e_{m} associated with deformations within the membrane. The total energy density is then

$$e = e_{\mathrm{m}} + e_{\mathrm{B}} \ . \tag{2.19}$$

To find the equilibrium configuration, we have to find the configuration of lowest total elastic energy. This configuration is characterised by vanishing of the in-plane forces as well as vanishing of the forces perpendicular to the plane. This force equilibrium is expressed by the following equations:

$$\sum_\alpha \partial_\alpha \sigma_{\alpha\beta} = 0 \ , \qquad B\sum_{\alpha\beta}\partial_\alpha^2\partial_\beta^2 z = \sum_{\alpha\beta}\sigma_{\alpha\beta}\kappa_{\alpha\beta} \ . \tag{2.20}$$

Solving these equations for given stresses and boundary conditions yields the according equilibrium out-of-plane displacement field z and in-plane deformations defined by ϵ_{m}.

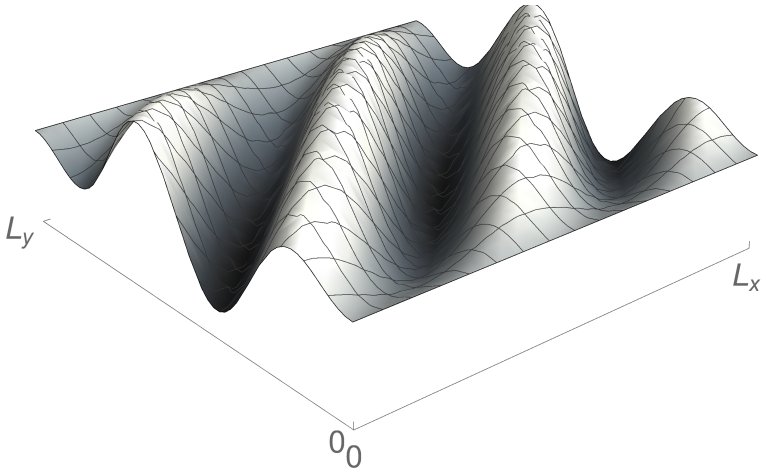

Figure 2.7: Example of a wrinkling pattern in a sheared membrane according to Eq. (2.25) with $L_x = L_y$ and $\lambda = \frac{1}{2}\frac{L_x}{\sqrt{2}}$.

Shearing of thin membranes

We now consider a pure shear deformation along the x-axis of a two-dimensional membrane in the xy-plane. Its lengths in x- and y-direction are L_x and L_y respectively. According to the equations derived above, a shear angle γ yields the strain tensor

$$\boldsymbol{\epsilon}_{\mathrm{2D}} = \begin{bmatrix} 0 & \gamma/2 \\ \gamma/2 & 0 \end{bmatrix} , \tag{2.21}$$

and the stress tensor

$$\boldsymbol{\sigma}_{\mathrm{2D}} = \begin{bmatrix} 0 & G\gamma \\ G\gamma & 0 \end{bmatrix} . \tag{2.22}$$

In a coordinate system rotated by $\pi/4$, these tensors become diagonal:

$$\boldsymbol{\epsilon}'_{\mathrm{2D}} = \begin{bmatrix} \gamma/2 & 0 \\ 0 & -\gamma/2 \end{bmatrix} , \qquad \boldsymbol{\sigma}'_{\mathrm{2D}} = \begin{bmatrix} G\gamma & 0 \\ 0 & -G\gamma \end{bmatrix} . \tag{2.23}$$

We see that pure shear in the initial coordinate system is equivalent to pure stretching in x'-direction and pure compression in y'-direction in the rotated coordinate system. As mentioned in Section 2.1.5, wrinkles tend to form perpendicular to compressive stresses. Hence, we can conclude that in a sheared membrane, wrinkles will form at an angle of $\pi/4$ to the x-axis in the initial coordinate system.
The calculation of the elastic energy density in case of in-plane deformation is straightforward and yields

$$e_{\mathrm{sh,2D}} = \frac{1}{2} G\gamma^2 . \tag{2.24}$$

Next, we also want to consider out-of-plane deformation. When we want to find the membrane's equilibrium configuration under shear, we could solve the force equilibrium equations given above. However, we can also make an ansatz for the resulting displacement field and then minimise the total elastic energy. The orientation of wrinkles derived above in combination with the boundary conditions $z(y = 0) = z(y = L_y) = 0$ motivate the following ansatz:

$$z(x, y) = A \sin\left(\pi \frac{y}{L_y}\right) \sin\left(\sqrt{2}\pi \frac{y - x}{\lambda}\right) , \tag{2.25}$$

with λ being the wrinkles' wavelength and A their amplitude. An example of this wrinkling pattern is plotted in Fig. 2.7.

Critical shear angle

We now want to derive the smallest shear angle that is sufficient to induce wrinkling in a sheared membrane – the critical shear angle γ_c. At the onset of wrinkling, the amplitude A can be expected to be small, so we will neglect all terms of higher order than $\mathcal{O}(A^2)$ in the following calculation. According to Eq. (2.15), we can write the in-plane elastic energy density as

$$e_\mathrm{m} = \frac{1}{2}G\left(\epsilon'_{\mathrm{m},11} - \epsilon'_{\mathrm{m},22}\right)^2 + \frac{1}{2}K\left(\epsilon'_{\mathrm{m},11} + \epsilon'_{\mathrm{m},22}\right)^2 + 2G\,{\epsilon'_{\mathrm{m},12}}^2 \ . \tag{2.26}$$

with the strain tensor

$$\boldsymbol{\epsilon}'_\mathrm{m} = \begin{bmatrix} \frac{1}{2}\gamma + \frac{1}{2}(\partial_{x'}z)^2 & \partial_{x'}z\,\partial_{y'}z \\ \partial_{x'}z\,\partial_{y'}z & -\frac{1}{2}\gamma + \frac{1}{2}(\partial_{y'}z)^2 \end{bmatrix} \ , \tag{2.27}$$

in a coordinate system rotated by $\pi/4$. In order to proceed, we can calculate the derivatives of z and average the resulting terms over the membrane's surface area which yields the following expressions:

$$\langle(\partial_{x'}z)^2\rangle = \frac{A^2\pi^2}{8L_y^2} \ , \quad \langle(\partial_{y'}z)^2\rangle = \frac{A^2\pi^2}{8L_y^2} + \frac{A^2\pi^2}{\lambda^2} \ , \quad \langle(\partial_{x'}z)(\partial_{y'}z)\rangle = \frac{A^2\pi^2}{8L_y^2} \ . \tag{2.28}$$

This allows us to derive the spatial average of the in-plane elastic energy density:

$$\langle e_\mathrm{m}\rangle = \frac{1}{2}G\gamma^2 - \frac{1}{2}G\gamma\frac{A^2\pi^2}{\lambda^2} + \mathcal{O}(A^4) \ . \tag{2.29}$$

Analogously, we can calculate the spatial average of the bending energy density:

$$\langle e_\mathrm{B}\rangle = 2BA^2\pi^4\left(\frac{1}{16L_y^4} + \frac{1}{L_y^2\lambda^2} + \frac{1}{\lambda^4}\right) \ . \tag{2.30}$$

Wrinkling will occur when total energy density $e = e_\mathrm{m} + e_\mathrm{B}$ is lower than the elastic energy density $e_\mathrm{sh,2D}$ resulting from exclusively in-plane deformation. Using the spatial averages in the wrinkled configuration yields the inequality

$$e_\mathrm{sh,2D} > \langle e_\mathrm{m}\rangle + \langle e_\mathrm{B}\rangle \tag{2.31}$$

$$0 > -\frac{1}{2}G\gamma\frac{\pi^2}{\lambda^2} + 2B\pi^4\left(\frac{1}{16L_y^4} + \frac{1}{L_y^2\lambda^2} + \frac{1}{\lambda^4}\right) \ . \tag{2.32}$$

From this, we get the critical shear angle $\gamma_c(\lambda)$ at which a wrinkling pattern with wavelength λ is energetically favourable over a planar configuration:

$$\gamma_c(\lambda) = 4\pi^2\frac{B}{G}\left(\frac{\lambda^2}{16L_y^4} + \frac{1}{L_y^2} + \frac{1}{\lambda^2}\right) \ . \tag{2.33}$$

Minimising the term in brackets leads to the conclusion that a wavelength $\lambda_c = 2L_y$ yields the smallest possible value for γ_c.

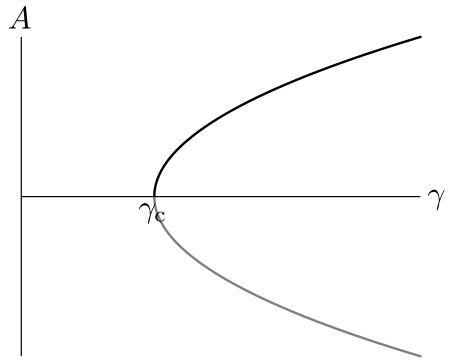

Figure 2.8: Amplitude as a function of shear angle near γ_c. The dependence $A^2 \propto (\gamma - \gamma_c)$ resembles a supercritical pitchfork bifurcation and can be utilised to extrapolate the critical shear angle in simulations, see Section 2.3.7 for details.

Taking a second look at the energy density difference Δe between wrinkled and planar configuration, we see that it can be written as

$$\begin{aligned} \Delta e &= e_{\mathrm{sh,2D}} - \langle e_{\mathrm{m}} \rangle + \langle e_{\mathrm{B}} \rangle \\ &= \alpha_1(\gamma - \gamma_c)A^2 - \alpha_2 A^4 \ , \end{aligned} \tag{2.34}$$

where α_1 and α_2 are positive coefficients. Maximising Δe with respect to A yields

$$A^2 \propto (\gamma - \gamma_c) \ , \tag{2.35}$$

which allows us to identify the onset of wrinkling as a supercritical pitchfork bifurcation, see Fig. 2.8 for an illustration.

Wavelength and amplitude for large shear angles

For shear angles $\gamma \gg \gamma_c$, we can find expressions for the wrinkle wavelength λ and amplitude A as functions of γ.

First, we will derive the amplitude as a function of λ and γ starting from the assumption that a wrinkled membrane can only support small compressive stress σ'_{22} perpendicular to the wrinkles [85]. Setting $\sigma'_{22} \approx 0$ allows us to approximate the in-plane strains and the stretching stress parallel to the wrinkles from the following two relations we get by applying Hooke's Law:

$$\sigma'_{22} = \frac{Y_2}{1-\nu^2}(\epsilon'_{11} + \nu\epsilon'_{22}) \approx 0 \quad \Rightarrow \quad \epsilon'_{22} = -\nu\epsilon'_{11} \ , \tag{2.36}$$

$$\epsilon'_{11} = \frac{1}{Y_2}(\sigma'_{11} - \nu\sigma'_{22}) \approx \frac{1}{Y_2}\sigma'_{11} \ . \tag{2.37}$$

Since we consider large shear angles $\gamma \gg \frac{A^2}{L_y^2}$, we can neglect the term $(\partial_{x'} z)^2$ in the strain parallel to the wrinkles:

$$\epsilon'_{11} = \frac{1}{2}\gamma + \frac{1}{2}(\partial_{x'} z)^2 = \frac{1}{2}\gamma + \mathcal{O}\left(\frac{A^2}{L_y^2}\right) \approx \frac{1}{2}\gamma \ . \tag{2.38}$$

Analogously, we can assume that the stress parallel to the wrinkles is unaffected by wrinkling:

$$\sigma'_{11} \approx Y_2 \frac{\gamma}{2} \ . \tag{2.39}$$

Since the approximation $\sigma'_{22} \approx 0$ is best in the membrane's centre in y-direction, we now consider the case $y = L_y/2$. We have the strain perpendicular to the wrinkles

$$\epsilon'_{22} = -\frac{1}{2}\gamma + \frac{1}{2}(\partial_{y'} z)^2 \ . \tag{2.40}$$

Averaging this over the distance corresponding to one wavelength in x-direction yields

$$\langle \epsilon'_{22} \rangle = -\frac{1}{2}\gamma + \frac{A^2\pi^2}{\lambda^2} \ . \tag{2.41}$$

Combining this with ϵ'_{11}, we get an expression for the amplitude as a function of the shear angle and wavelength:

$$-\frac{1}{2}\gamma + \frac{A^2\pi^2}{\lambda^2} = -\nu\frac{1}{2}\gamma \tag{2.42}$$

$$A = \frac{1}{\sqrt{2}\pi}\left(\gamma(1-\nu)\right)^{1/2}\lambda \ . \tag{2.43}$$

To derive the wavelength, we consider the force equilibrium given in Eq. (2.20):

$$B\left[\partial^4_{x'} z + \partial^4_{y'} z + \partial^2_{x'}\partial^2_{y'} z\right] = \sigma'_{11}\partial^2_{x'} z + \sigma'_{22}\partial^2_{y'} z + \sigma'_{12}\partial_{x'}\partial_{y'} z \ . \tag{2.44}$$

On the left-hand side of the equation, we can neglect the first and third term since

$$\partial^4_{x'} z \propto L_y^{-4} \ , \qquad \partial^4_{y'} z \propto \lambda^{-4} \ , \qquad \partial^2_{x'}\partial^2_{y'} z \propto L_y^{-2}\lambda^{-2} \ , \tag{2.45}$$

and $\lambda \ll L_y$. On the right-hand side, we use $\sigma'_{22} \approx 0$ as explained above. Also, $\sigma'_{12} = 0$ in the chosen coordinate system. This leaves us with

$$B\partial^4_{y'} z \approx \sigma'_{11}\partial^2_{x'} z \ . \tag{2.46}$$

Caclulating the derivatives and evaluating the equation at a wrinkle maximum $z = A$ yields

$$BA\left(\frac{2\pi}{\lambda}\right)^4 \approx Y_2\frac{\gamma}{2}A\frac{\pi^2}{2L_y^2} \tag{2.47}$$

$$\lambda^4 \approx 64\pi^2 L_y^2 \frac{B}{Y_2\gamma} \ , \tag{2.48}$$

Therefore, the wrinkles' wavelength λ at large shear angles can be written as

$$\lambda = \left(64\pi^2 L_y^2 \frac{B}{Y_2\gamma}\right)^{1/4} \ , \tag{2.49}$$

or – using $Y_2 = 2(1+\nu)G$ – as

$$\lambda = \left(\frac{32\pi^2 L_y^2}{1+\nu}\frac{B}{G\gamma}\right)^{1/4} \ . \tag{2.50}$$

Elastic energy at large shear angles

With the strains at large shear angles derived above

$$\epsilon'_{11} \approx \frac{1}{2}\gamma \ , \qquad \langle \epsilon'_{22} \rangle = -\frac{1}{2}\gamma + \frac{A^2\pi^2}{\lambda^2} \ , \tag{2.51}$$

we can calculate the in-plane elastic energy density

$$\langle e_\mathrm{m} \rangle = \frac{1}{2}\left(\epsilon'_{11}\sigma'_{11}\gamma^2 + \epsilon'_{22}\sigma'_2\right) \ . \tag{2.52}$$

With the strains

$$\sigma'_{11} \approx Y_2\frac{\gamma}{2} \ , \qquad \sigma'_2 \approx 0 \ , \tag{2.53}$$

this yields

$$\langle e_\mathrm{m} \rangle \approx \frac{1}{2}Y_2\gamma^2 \ . \tag{2.54}$$

The bending contribution e_B to the total elastic energy density $e = e_\mathrm{m} + e_\mathrm{B}$ can be neglected since it is of order $\mathcal{O}(\gamma^{3/2})$, so e_m is the dominant term in e. In Eq. (2.24), we have

$$e_\mathrm{sh,2D} = \frac{1}{2}G\gamma^2 \tag{2.55}$$

for the elastic energy density of a sheared membrane with only in-plane deformation. Hence, we can write the ratio of the two energy densities as

$$\frac{e}{e_\mathrm{sh,2D}} \approx \frac{Y}{4G} = \frac{1+\nu}{2} \ . \tag{2.56}$$

The ratio of the corresponding total energies equals the ratio of energy densities

$$\frac{E_\mathrm{3D}}{E_\mathrm{2D}} = \frac{e}{e_\mathrm{sh,2D}} \ , \tag{2.57}$$

with E_3D the total elastic energy for three-dimensional deformation and E_2D for two-dimensional deformation. Therefore, this energy ratio should equal the above value at large shear angles in membranes that follow linear elasticity theory.

2.2.4 Application to networks

We now want to apply the above results from continuum elasticity theory for elastic membranes to discrete networks consisting of thin elastic rods. On length scales at which the networks' microscopic structure can be ignored, we can treat discrete networks as effectively homogeneous membranes. The most important aspect for this is finding the networks' elastic moduli. With these, the predictions for critical shear angle, wrinkle wavelength and wrinkle amplitude can be applied to networks without further modifications.
In this work, we consider networks with a regular triangular geometry and disordered networks – also referred to as random networks. Details on these types of networks are given in Section 2.3.4.

The networks' elastic moduli can be calculated explicitly assuming affine deformation. For triangular networks, this is done by considering the effect of an applied force to the individual unit cells. This approach is outlined in Ref. [90] and yields

$$\begin{aligned} G^{\triangle} &= \frac{\sqrt{3}}{4}\frac{\mu}{l_c^{\triangle}} , & Y_2^{\triangle} &= \frac{8}{3}G^{\triangle} , \\ K^{\triangle} &= 2G^{\triangle} , & \nu^{\triangle} &= \frac{1}{3} . \end{aligned} \tag{2.58}$$

Here, μ is the rods' stretching modulus and $l_c^{\triangle}$ is the networks' lattice constant. The bending modulus $B^{\triangle}$ can be calculated as

$$B^{\triangle} = 3G^{\triangle}\frac{\kappa}{\mu} , \tag{2.59}$$

with κ being the rods' bending modulus.

Since random networks do not consist of uniform unit cells, we have to use a different approach for deriving their elastic moduli. One possible approach assuming purely affine deformation and utilising the fact that we have a large number of filaments N has been described by Head et al. [40, 41]. Since the rods' orientations φ are chosen randomly, we can assume a uniform distribution function $p(\varphi) = (2\pi)^{-1}$ for orientation angles when N is large. In this case, we can calculate the average energy per rod resulting from an applied strain by averaging over all possible orientation angles φ.
As an example, we will outline the derivation of the shear modulus G^{r} here. The network is defined by the total number of rods N, their length L, their stretching modulus μ and bending modulus κ, and the average distance between rod intersections l_c. The rods' effective length is $L' = L - 2l_c$ since free ends can relax freely and therefore do not give an energy contribution – see also Section 2.3.4.
A shear strain γ in x-direction will result in an average energy per rod

$$E_{\mathrm{rod}}(\gamma) = \frac{1}{2\pi}\int_0^{2\pi}\frac{\mu}{2}\gamma^2\sin^2(\varphi)\cos^2(\varphi)(L-2l_c)\,d\varphi = \frac{\mu}{16}(L-2l_c)\gamma^2 , \tag{2.60}$$

from which the total energy is obtained by multiplying N:

$$E_{\mathrm{tot}} = \frac{\mu}{16}\gamma^2 N(L-2l_c) . \tag{2.61}$$

Since we will characterise random networks by their crosslinking density

$$\eta = \frac{L'}{l_c} , \tag{2.62}$$

we want to express the total energy as a function of η. A geometrical analysis yields the following relation between η and N:

$$\frac{2NL^2}{\pi A_{\mathrm{tot}}} = \eta - 1 . \tag{2.63}$$

Here, A_{tot} is the network's surface area. We can now eliminate N from the the total energy. We also divide by A_{tot} to get the total energy density

$$e_{\mathrm{tot}} = \frac{\mu\pi}{32L}\gamma^2\left(\eta + \frac{2}{\eta} - 3\right) \tag{2.64}$$

Comparison with Eq. (2.24) gives us the shear modulus

$$G^{\mathrm{r}} = \frac{\mu\pi}{16L}\left(\eta + \frac{2}{\eta} - 3\right) \ . \tag{2.65}$$

Similar calculations for the remaining elastic moduli lead to the following results:

$$Y_2^{\mathrm{r}} = \frac{8}{3}G^{\mathrm{r}} \ , \quad K^{\mathrm{r}} = 2G^{\mathrm{r}} \ , \quad \nu^{\mathrm{r}} = \frac{1}{3} \ , \quad B^{\mathrm{r}} = 3G^{\mathrm{r}}\frac{\kappa}{\mu} \ . \tag{2.66}$$

We now have the elastic moduli for discrete networks which enables us to treat them as effectively homogeneous membranes and apply the predictions for critical shear angle, wrinkle wavelength and wrinkle amplitude derived for elastic membranes. With the relation of the networks' bending modulus B and their shear modulus G, we can express the critical shear angle as a function of the rods' elastic moduli μ and κ:

$$\gamma_c = \frac{12\pi^2}{L_y^2}\frac{\kappa}{\mu}\left(\frac{L_x^2}{32L_y^2} + 1 + \frac{2L_y^2}{L_x^2}\right) \ . \tag{2.67}$$

We see that γ_c does not depend on the absolute values of μ and κ but only on their ratio. The same is true for the wavelength:

$$\lambda = \left(72\pi^2 L_y^2 \frac{\kappa}{\mu\gamma}\right)^{1/4} \ . \tag{2.68}$$

The equivalent for the ratio of μ and κ in elastic membranes is the ratio of bending and shear modulus:

$$\frac{\kappa}{\mu} \equiv \frac{B}{3G} = \frac{t^2}{18(1-\nu)} \ . \tag{2.69}$$

Hence, the square root of κ/μ in a network is similar to the thickness in an elastic membrane and can therefore be interpreted as the network's thickness.
Since the relation of the B and G is equivalent in random and regular networks, the above expressions are valid for both network geometries.

Periodic boundary conditions

In our simulations, we enforced periodic boundary conditions in x-direction – see Section 2.3.1. This can be expressed as $z(0, y) = z(L_x, y)$ with L_x being the networks' length in x-direction. This periodicity only allows discrete wavelengths

$$\lambda_n = \frac{1}{n}\frac{L_x}{\sqrt{2}} \ , n = 1, 2, \dots \ , \tag{2.70}$$

which is why the wrinkles' wavelength cannot be predicted by the expression we derived for elastic membranes. Instead, wrinkles will have the wavelength λ_n that minimises the elastic energy. For a given shear angle γ, we can expect a wavelength close to the value $\lambda(\gamma)$ predicted by Eq. (2.49) though. Still, the discretisation of wavelengths has to be taken into consideration when calculating γ_c and A.

For elastic membranes, we found that a wavelength $\lambda_c = 2L_y$ yields the smallest possible value for γ_c. Since periodic boundary conditions only allow discrete wavelengths

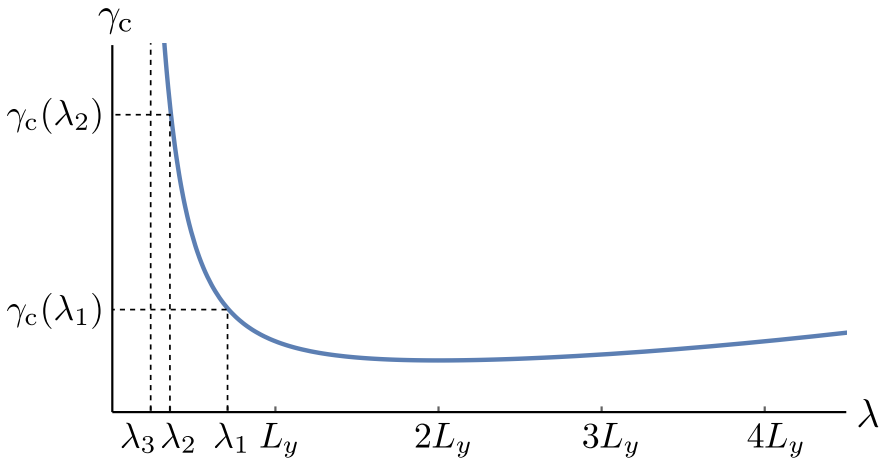

Figure 2.9: Illustration for determining the smallest possible value for γ_c. The plot represents γ_c as a function of the wavelength λ according to Eq. (2.33). This function has a minimum at $\lambda_c = 2L_y$. However, periodic boundary conditions only allow discrete wavelengths λ_n. For $L_x = L_y$, the three largest wavelengths are marked in the plot showing that $\gamma_c(\lambda_1)$ is the smallest shear angle for which wrinkling can occur.

λ_n, they may cause the onset of wrinkling to occur at a different wavelength than λ_c and therefore at a different critical shear angle than the minimal γ_c.

The largest discrete wavelength is $\lambda_1 = L_x/\sqrt{2}$ which is smaller than λ_c as long as $L_x < \sqrt{8}L_y$. In our simulations, we used $L_x = L_y$, so we can only find wrinkling patterns with wavelengths smaller than λ_c. From Eq. (2.33), we can conclude that γ_c increases with decreasing $\lambda < \lambda_c$. Hence, the onset of wrinkling will occur at the largest possible wavelength λ_1 as this yields the smallest critical shear angle. For an illustration, see Fig. 2.9. Entering λ_1 into Eq. (2.33), we get

$$\gamma_c = \frac{4\pi^2}{L_y^2}\frac{B}{G}\left(\frac{L_x^2}{32L_y^2} + 1 + \frac{2L_y^2}{L_x^2}\right) \overset{L_x=L_y}{=} \frac{291\pi^2}{8L_y^2}\frac{\kappa}{\mu} \,. \tag{2.71}$$

For the wrinkles' amplitude in a sheared elastic membrane at large shear angles, we derived the expression in Eq. (2.43). In networks, we have $\nu = 1/3$ which yields for the amplitude

$$A = \frac{1}{\sqrt{3}\pi}\gamma^{1/2}\lambda \,. \tag{2.72}$$

Since we treated γ and λ as constants during derivation, this result is still valid with periodic boundary conditions. However, if λ was a continuous function of γ as expressed in Eq. (2.49), we could replace λ and write A as a function of the shear angle alone. Due to the discretisation of wavelengths, this is not possible for periodic boundary conditions.

2.3 Modelling of the sheared networks

This section presents the implementation of actin networks and how their shearing is simulated.

2.3.1 Environment

We are studying intrinsic properties of the networks, so we simulate them without any surrounding medium or other external components. We use a rectangular simulation cell in the xy-plane with side length L_x in x-direction and L_y in y-direction. The boundaries in y-direction are fixed, i.e., rods intersecting with these boundaries are crosslinked to them analogously to crosslinking between rods – see Section 2.3.3. In x-direction periodic boundary conditions are implemented.

2.3.2 Rods

Semiflexible polymers are approximated as straight rods of length L. Their elastic properties are determined by a stretching modulus μ and a bending modulus κ according to linear elasticity theory of thin cylindrical rods. As outlined in Section 2.2.2, these quantities can be derived from the rods' geometrical properties – such as its cross-sectional area – and material constants like its Young's modulus. The elastic energy necessary to cause stretching and bending of a thin rod is determined by μ and κ respectively.
It is useful to define a length scale

$$l_b = \sqrt{\frac{\kappa}{\mu}} \,, \tag{2.73}$$

quantifying the rod's resistance to bending compared to stretching. In networks composed of thin rods that are subject to shear stress, the ratio of μ and κ determines the critical shear angle for wrinkling as well as the wrinkles' wavelength – see Section 2.2.4. Also, we see that l_b can be interpreted as the thickness of the simulated networks. This is not surprising as calculating l_b for thin cylindrical rods yields the proportionality $l_b \propto r$ with the rods' radius r.
Of course, we must look at l_b in relation to other length scales in the system, so we will usually use the ratio l_b/L as a measurement and refer to it as the rods' bending rigidity.

2.3.3 Crosslinks

All intersections of rods are identified as crosslinks. During simulation, these are treated as permanent, i.e., their position relative to the attached rods is fixed. The crosslinks allow free rotation of the attached rods though which is a common property of many actin binding proteins, e.g., α-actinin has been reported to allow actin filaments crosslinked by it to rotate easily [91].
Equivalent crosslinks are used where rods intersect with the simulation cell's boundaries in y-direction. The important difference to usual crosslinks is that crosslinks with the boundary are fixed at their position during simulation. This prevents the simulated networks from relaxing to their initial state after deformation.
As mentioned before, the crosslinks' relative positions are fixed. Their positions in three-dimensional space are not though. In fact, these positions are the networks' degrees of freedom during simulation. However, the networks have additional degrees of freedom since we allow bending of individual segments. This is implemented by enabling displacements of the segments' midpoints during simulation. This approach neglects all but the first bending mode; however, this one is expected to be dominant in the absence of thermal fluctuations [40, 41].

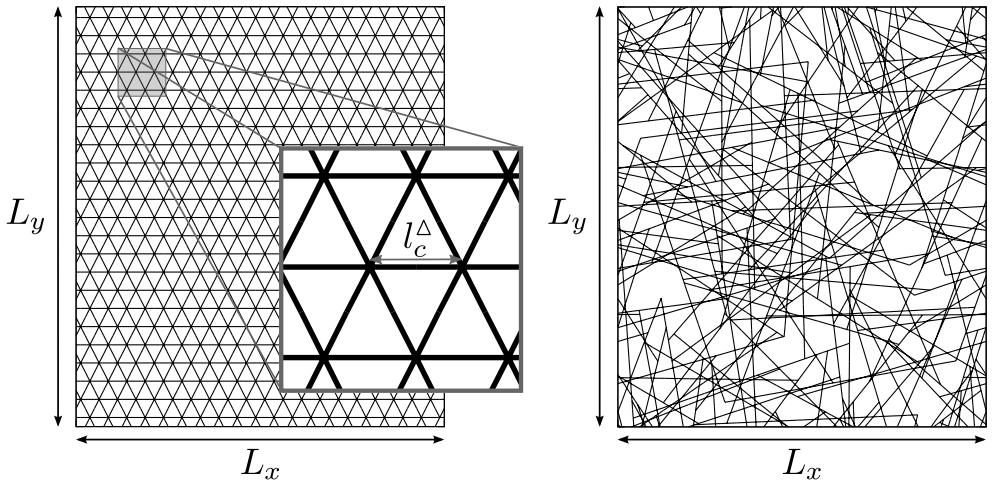

Figure 2.10: Illustration of the two types of networks studied in this chapter. Left: a triangular network with a lattice constant $l_c^{\triangle} = L_x/20$ and hence $\eta^{\triangle} = 20$. Right: a random network with a density $\eta = 32$ which is equivalent to an average distance between neighbouring crosslinks $l_c = L/34$.

2.3.4 Generation of networks

The networks are generated by placing a predetermined number of rods in the simulation cell and then crosslinking them to each other according to the description given in the above subsection. The network's spatial extent is determined by the cell's side lengths L_x and L_y. Since the individual rods' elasticity is purely elastic, this constitutes an athermal model, see Section 2.1.2.
By altering the deposition routine, different types of networks can be generated.

i. A triangular geometry can be accomplished by placing filaments with fixed orientations equidistantly in the cell. We call these networks triangular networks or regular networks.

ii. Adding rods at random positions with random orientations results in a disordered network geometry. This procedure is known as the Mikado model [40–42]. Throughout this chapter, these networks will be referred to as random networks.

Examples for both types are shown in Fig. 2.10. There are a few important differences between these as will be pointed out in the following paragraphs.

Triangular networks consist of rods that extend the whole simulation cell. This ensures a uniform network geometry. The rods' orientation angles with respect to the x-axis can be one of three values: $\varphi \in \left[0; \frac{\pi}{3}; \frac{2\pi}{3}\right]$. By placing the rods equidistantly in the cell with these orientations, we end up with a network that is composed of equilateral triangles with an edge length $l_c^{\triangle}$. This length is the network's lattice constant and is specified before starting the generation routine. In combination with the simulation cell's size, it determines the network's density $\eta^{\triangle} = L_x/l_c^{\triangle}$.
Since three rods intersect in each cross-link, the coordination number of triangular network is 6.

Random networks are generated using filaments of a fixed length L. Analogously to regular networks, the average distance between neighbouring crosslinks l_c can be used to classify these networks. We use the average number of crosslinks per rod η as the dimensionless network density and as a control parameter when generating random networks. Rods are added into the cell until η reaches a specified value. Then, dangling ends of the rods – segments that are only connected to one crosslink – are removed as they would be able to relax freely during simulation and hence not contribute to the elastic energy. Since each rod will have two dengling ends, and their average length will be equal to l_c, the rods' average length after removal is $L' = L - 2l_c$. This is taken into account by calculating the density as

$$\eta = \frac{L'}{l_c} \ . \tag{2.74}$$

Based on experimental data [92], we can estimate a typical range for the network density $\eta \in [5, 100]$.
In random networks, the coordination number is usually 4 since cross-links only occur between pairs of rods. Some crosslinks will have fewer neighbouring points though as they are located at the end of one or two rods.

Network configuration

After a network is generated, its configuration is defined by the positions of crosslinks and midpoints in three-dimensional space. In order to calculate the elastic energy in a deformed network, we need more information though. The details on how this energy is calculated are described in Section 2.3.7. For the stretching energy, we need to know which points are connected by a segment and how long this segment was when the network was generated. Hence, we have each point store the information which points it is connected to and additionally have each midpoint store the initial length of the segment it is located on. To calculate the bending energy, triples of points on the same rod have to be known, so we have the points also store the information which other points they form such a triple with.

2.3.5 Simulation

Simulations are performed in iterations each of which consists of the same three steps. First, the shear angle γ is increased by an increment $\delta\gamma$. The second step is only executed if we are running the simulation in three dimensions. In this case, we perturb the network in z-direction in order to enable deformation in three dimensions. In the final step, a conjugate gradient method is used to minimise the elastic energy and thereby find the ideal network configuration.
The incremental increasing of the shear deformation is achieved by displacing each point i in the network in x-direction – including points on the boundaries in y-direction. The latter will be fixed at their their new positions during the minimisation routine though. The displacements δx_i are calculated as

$$\delta x_i = y_i \cdot \delta\gamma \ , \tag{2.75}$$

with y_i being a point's y-coordinate. To be more precise, we would have to use the tangent of $\delta\gamma$, but for small shear increments, the above approximation is valid. These

displacements result in an affine deformation of the network, i.e., the deformation in each microscopic region is equal to the global deformation. We use this approach because we can expect the ideal configuration to be near the affinely deformed one, so we save simulation time by starting from there. A different approach would be to just move the boundaries to a new position and use that configuration as a starting point for the minimisation.
Perturbation is necessary for enabling three-dimensional configurations because - as pointed out in Section 2.3.7 – the gradient calculation does not give us forces perpendicular to the initial plane as long as all z-components are 0. The great advantage of this is that networks the are generated and deformed in the xy-plane will remain in the plane. Due to this, we can easily perform simulations in two dimensions. However, if we want to extend the simulation to the third dimension, we have to compensate for this by manually perturbing the network in z-direction.
We use two different methods of perturbation – random and predictive perturbation. For random perturbation, we define a maximum displacement $\delta z_{\max}$ and each point in the network – except for those on the boundaries – is displaced in z-direction by a value δz_i that is generated by a random number generator. The δz_i are uniformly drawn from the interval $[-\delta z_{\max}; \delta z_{\max}]$. Each point is displaced several times until the total elastic energy has increased by a predefined amount relative to the total elastic energy before perturbation. For the results presented here, this value was in the range between 1% and 10%.
Predictive perturbation is used when trying to find the wrinkling threshold. From continuum elasticity theory, we know the wrinkling pattern $z_{\mathrm{CET}}(x, y)$ that we can expect to find at the onset of wrinkling – see Eq. (2.25). Instead of applying random displacements to the points in the network, we set $z_i = \alpha_{\mathrm{pred}} z_{\mathrm{CET}}(x_i, y_i)$. As a result, we get the displacements we would expect at the onset of wrinkling according to continuum elasticity theory. The factor $\alpha_{\mathrm{pred}} < 1$ ensures that we only impose the general form of the resulting configuration but not its amplitude. Also, if the shear angle is still below the wrinkling threshold, the network will return to a plane configuration during the minimisation routine. We can assume that the simulation time required for this will be shorter when perturbations are small.
The last simulation step is finding the configuration of lowest elastic energy with a minimisation routine. We use a conjugate gradient method based on the algorithm described in [93] to vary the points' coordinates – effectively letting the network relax into its new equilibrium configuration.

2.3.6 Dimensionless parameters

Simulations were performed using dimensionless parameters. As calibrating values, we used the following relations:

$$50\,\mu\mathrm{m} \equiv 1\ , \qquad 1\,\mathrm{nN} \equiv 1\ . \tag{2.76}$$

A typical length for actin filaments in vitro is $20\,\mu$m [94, 95] which is equivalent to $L = 0.4$ in dimensionless units. The Young's modulus of single actin filaments has been measured in the range $1.3 - 2.9\,\mathrm{Nm}^{-2}$ [95–97], so we assume $Y = 2 \cdot 10^9\,\mathrm{Nm}^{-2}$ here. With a diameter of $d = 8\,$nm [23], we can calculate the filaments' stretching modulus $\mu = 100\,$nN which is equivalent to $\mu = 100$ in dimensionless units. The bending modulus

can be calculated analogously which yields $\kappa = 4 \cdot 10^{-25}\,\mathrm{Nm}^2$. In dimensionless units this corresponds to $\kappa = 1.6 \cdot 10^{-7}$. In combination with the stretching modulus, this gives us $l_b = 4 \cdot 10^{-5}$ and $l_b/L = 10^{-4}$.

2.3.7 Measurements

Elastic energy

In Section 2.2.2, the calculation of the the elastic energy contributions was introduced in a continuous model. The stretching energy contribution $E^{(s)}$ and the bending energy contribution $E^{(b)}$ for a filament of length l are

$$E^{(s)} = \int_0^l \frac{\mu}{2} \left(u'(s)\right)^2 \, ds \ , \tag{2.77}$$

$$E^{(b)} = \int_0^l \frac{\kappa}{2} \left(\phi'(s)\right)^2 \, ds \ , \tag{2.78}$$

where $u'(s)$ is the local strain and $\phi'(s)$ is the local curvature along the contour length s.

As outlined in Section 2.3.4, a network's configuration in our simulations is defined by a set of position vectors representing the crosslinks between rods and midpoints of the individual segments as well as the connections between these points and the segments' initial lengths. This is a discrete model, so we have to adjust the calculation of the elastic energy contributions accordingly.

For deriving the stretching energy contribution $E_{ij}^{(s)}$, we consider a segment between two points i and j that is stretched or compressed from an initial length $l_{ij}^{(0)}$ to a length l_{ij}. Assuming small deformations and a uniform local strain, we get

$$E_{ij}^{(s)} = \frac{\mu}{2} \frac{(l_{ij} - l_{ij}^{(0)})^2}{l_{ij}^{(0)}} \ . \tag{2.79}$$

For the bending energy contribution $E_{ijk}^{(b)}$, we have to look at triples of neighbouring points i, j, and k along the same rod. The two segments connecting these points form an angle φ_{ijk}, and if this angle is small, the square of the curvature of the part of the rod between the points i and k can be approximated as

$$\left(\phi'\right)^2 \approx \frac{2(1 - \cos\varphi_{ijk})}{(l_{ij} + l_{jk})^2} \ . \tag{2.80}$$

Consequently, the bending energy associated with the triple $\{i, j, k\}$ is

$$E_{ijk}^{(b)} = \kappa \, \frac{(1 - \cos\varphi_{ijk})}{l_{ij} + l_{jk}} \ . \tag{2.81}$$

Since we consider freely rotating crosslinks, varying the angles between crosslinked rods does not give a bending energy contribution.

The network's total stretching energy $E_{\mathrm{tot}}^{(\mathrm{s})}$ is calculated by summing over the stretching energy contributions of all segments, and the bending energy $E_{\mathrm{tot}}^{(\mathrm{b})}$ is the sum of the bending energy contributions of all triples of neighbouring points. The total elastic energy is then

$$E_{\mathrm{tot}} = E_{\mathrm{tot}}^{(\mathrm{s})} + E_{\mathrm{tot}}^{(\mathrm{b})} \ . \tag{2.82}$$

Forces

For the conjugate gradient method used to find a network's ideal configuration given a specific deformation, we have to calculate the forces acting on each point within the network. These forces can be derived directly from the energy contributions presented in the previous section. Details on this can be found in the author's diploma thesis [87]. Here, we just restate the results of this calculation.
Stretching deformation of a segment between two points i and j exerts a force $\boldsymbol{F}_{i,ij}^{(s)}$ onto point i. With the position vectors $\boldsymbol{r}_i$ and $\boldsymbol{r}_j$, this force is

$$\boldsymbol{F}_{i,ij}^{(s)} = -\mu \frac{l_{ij} - l_{ij}^{(0)}}{l_{ij}^{(0)}} \frac{\boldsymbol{l}_{ij}}{l_{ij}} \ . \tag{2.83}$$

Here, $\boldsymbol{l}_{ij} = \boldsymbol{r}_i - \boldsymbol{r}_j$ is a vector connecting i and j. As in the previous section, $l_{ij} = |\boldsymbol{l}_{ij}|$ is the segment's length and $l_{ij}^{(0)}$ its initial length.
For the force on a point i resulting from bending, the calculation is different depending on whether i is the midpoint of a triple jik or an endpoint of a triple ijk.
From the bending energy contribution, we derive the following force acting on an endpoint:

$$\boldsymbol{F}_{i,ijk}^{(b)} = \kappa \left[\frac{1 - \cos\varphi_{ijk}}{(l_{ij} + l_{jk})^2} - \frac{1}{l_{ij} + l_{jk}} \left(\frac{\cos\varphi_{ijk}}{l_{ij}} + \frac{1}{l_{jk}} \right) \right] \frac{\boldsymbol{l}_{ij}}{l_{ij}} \ . \tag{2.84}$$

For a midpoint, we get

$$\begin{aligned} \boldsymbol{F}_{i,jik}^{(b)} = & \kappa \frac{1 - \cos\varphi_{ijk}}{(l_{ij} + l_{ik})^2} \left(\frac{\boldsymbol{l}_{ij}}{l_{ij}} + \frac{\boldsymbol{l}_{ik}}{l_{ik}} \right) \\ & - \kappa \frac{1}{l_{ij} + l_{ik}} \left[\cos\varphi_{ijk} \left(\frac{\boldsymbol{l}_{ij}}{l_{ij}^2} + \frac{\boldsymbol{l}_{ik}}{l_{ik}^2} \right) + \frac{\boldsymbol{l}_{ij} + \boldsymbol{l}_{ik}}{l_{ij} l_{ik}} \right] \ . \end{aligned} \tag{2.85}$$

We get the total force $\boldsymbol{F}_i$ acting on a point i by adding up all the forces resulting from stretching and bending of its adjoining segments.
From the above calculations, we can see that $\boldsymbol{F}_i$ is proportional to a linear combination of the vectors connecting i to its neighbouring points. Here we see why perturbations are required when performing three-dimensional simulations. Consider a planar network in the xy-plane that is deformed in the same plane. All points in the network will have a z-coordinate 0, so the resulting forces can never have a non-zero z-component, and the network will remain planar.

Wavelength

From elasticity theory, we know the wrinkling pattern of a sheared thin membrane:

$$z_{\mathrm{CET}}(x, y) = A \sin\left(\pi \frac{y}{L_y} \right) \sin\left(\sqrt{2}\pi \frac{y - x}{\lambda} \right) \ , \tag{2.86}$$

compare Eq. (2.25). The zeros of $z_{\mathrm{CET}}(x, y)$ form parallel lines in the xy-plane at an angle of $\pi/4$ to the x-axis. The distance between these lines is $\lambda/2$. We can utilise this fact to determine the wavelength of a wrinkled network.
First, we find all segments that intersect with the xy-plane and calculate the intersection

points. Next, we use least-square fits to interpolate the points. Finally, we identify the average distance between the resulting lines and multiply it by 2 to get the wrinkles' wavelength λ.
This method can not only be used to determine λ but also to help identify wrinkling patterns. If the intersection points exhibit a disordered distribution instead of forming a pattern of parallel lines, the configuration is not wrinkled.

Amplitude

For measuring the amplitude of a wrinkled network, we also make use of the wrinkling pattern $z_{\mathrm{CET}}(x, y)$ expected in elasticity theory for a sheared elastic membrane. Integrating $z^2_{\mathrm{CET}}(x, y)$ over the membrane's surface area $L_x L_y$ yields

$$\int_0^{L_x} \int_0^{L_y} A^2 \sin^2\left(\pi \frac{y}{L_y}\right) \sin^2\left(\sqrt{2}\pi \frac{y-x}{\lambda}\right) dx\, dy = A^2 \frac{L_x L_y}{4} \ . \tag{2.87}$$

We can calculate an analogous quantity for networks by summing the squares of the z-components z_i of all points in the network. With the total number of points N, each point gets weighted with the factor $L_x L_y / N$:

$$\frac{L_x L_y}{N} \sum_{i=1}^{N} z_i^2 \ . \tag{2.88}$$

Now, we assume that the two expressions are equal for a wrinkled network and a wrinkled membrane when λ and A are equal. Solving for A, we get a formula for the amplitude of the wrinkling pattern in a sheared network:

$$A = \sqrt{\frac{4}{N} \sum_{i=1}^{N} z_i^2} \ . \tag{2.89}$$

Critical shear angle

When measuring a network's critical shear angle γ_c, we increase γ in discrete increments $\delta\gamma$, apply predictive perturbation, and then let the minimisation routine find the equilibrium configuration. Predictive perturbation was already described in Section 2.3.5. From elasticity theory, we expect the wavelength $\lambda_1 = L_x/\sqrt{2}$ – see Section 2.2.4 – and a wrinkling pattern $z_{\mathrm{CET}}(x, y)$ according to Eq. (2.25) at the onset of wrinkling. Hence, we perturb the network accordingly to minimise computation time.
The most basic method of determining γ_c is identifying the smallest value γ as γ_c for which the equilibrium configuration is wrinkled. However, since we have discrete increments $\delta\gamma$, the resulting error will be approximately $\delta\gamma$.
A more precise method can be derived from the form of the wrinkle amplitude near γ_c. When deriving the critical shear angle γ_c for wrinkling in elastic membranes, we found

$$A^2 \propto (\gamma - \gamma_c) \ , \tag{2.90}$$

see Section 2.2.3. We can utilise this expression to determine γ_c in regular networks by extrapolating A^2 as a function of γ. The zero of this extrapolation gives us γ_c. With this method, we do not limit γ_c to values dictated by the incremental increase of γ due to the simulation routine.

Nonaffinity

In Section 2.1.4, several methods for measuring nonaffinity were introduced. One of these was the calculation of a parameter ΔA measuring the the amount of deviation between a network's deformation and a purely affine deformation [43]. Since wrinkling causes out-of-plane deformations which are necessarily non-affine, it is unclear if such a parameter yields useful information in wrinkled networks. Instead, we choose an energy approach similar to the one suggested by Åström et al. [59]. We use the ratio $E_{\text{tot}}^{(\text{b})}/E_{\text{tot}}^{(\text{s})}$ of the total bending and stretching energy contributions $E_{\text{tot}}^{(\text{b})}$ and $E_{\text{tot}}^{(\text{s})}$ as an indicator for nonaffinity. As explained in Section 2.3.7, we are able to measure these contributions separately.
In control simulations of random networks in two dimensions, we found that the ratio $E_{\text{tot}}^{(\text{b})}/E_{\text{tot}}^{(\text{s})}$ has a maximum that coincides with a maximum in ΔA. Since such a maximum in ΔA was found to indicate the transition from a bending dominated regime to a stretching dominated one in sheared networks [43], we can use the energy ratio for identifying this transition. The major advantage of the ratio of the energy contributions is that its definition does not automatically entail peaking at the onset of wrinkling which could distort our measurements.

2.4 Results for sheared networks

The following section presents the results from simulations of regular and random networks under shear. The results are evaluated and discussed with regard to the linear elasticity theory introduced in Sections 2.2.3 and 2.2.4. As mentioned in Section 2.1.5, most of this material was already published in an article [86].
Unless otherwise specified, simulations were performed with simulation cells of size $L_x = L_y = 1.5L$.

2.4.1 Wrinkle formation

As predicted by elasticity theory for thin membranes, we find that sheared networks exhibit a buckling instability. Shear angles γ larger than a critical value γ_c result in wrinkled configurations. An example is shown in Fig. 2.11. Wrinkles form at an angle of $\pi/4$ to the shearing direction which is the x-axis. The occurring wrinkling patterns are in most cases in good agreement with the displacement field

$$z_{\text{CET}}(x,y) = A \sin\left(\pi \frac{y}{L_y}\right) \sin\left(\sqrt{2}\pi \frac{y-x}{\lambda}\right) \ , \tag{2.91}$$

expected from continuum elasticity theory, compare Eq. (2.25). Here, $z_{\text{CET}}(x,y)$ denotes the displacement perpendicular to the xy-plane of a network point with coordinates (x,y). Only discrete values

$$\lambda_n = \frac{1}{n}\frac{L_x}{\sqrt{2}} \ , n = 1, 2, \dots \ , \tag{2.92}$$

are allowed for the wavelength due to periodic boundary conditions, see Section 2.2.4. The above points are true for both regular and random networks. However, the disordered nature of random networks can make it difficult to identify wrinkling patterns

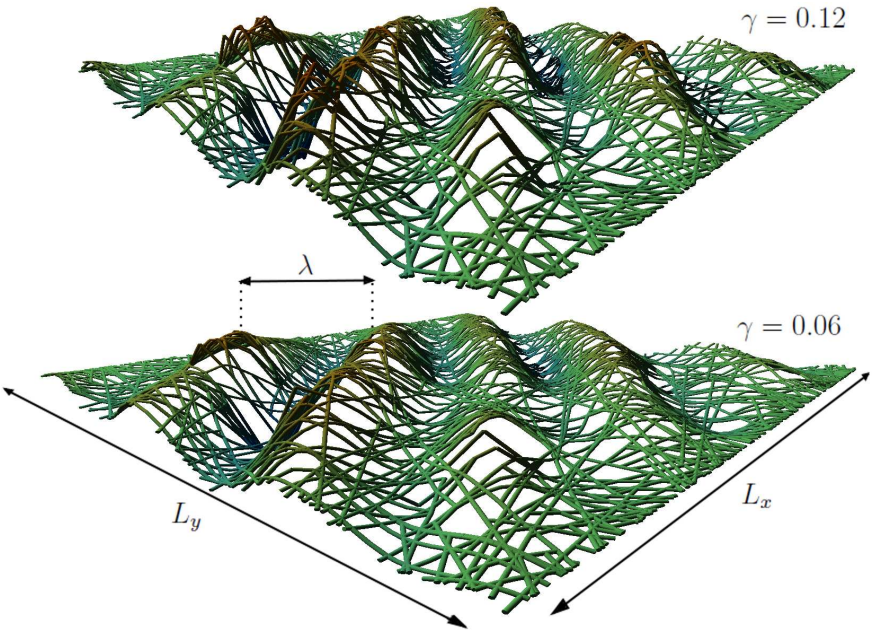

Figure 2.11: Example snapshots of a wrinkled random network at shear angles $\gamma = 0.06$ (bottom) and $\gamma = 0.12$ (top). The network has the spatial dimensions L_x and L_y, a density $\eta = 54$, and a bending rigidity $l_b/L = 2.5 \cdot 10^{-3}$. Wrinkles of wavelength λ form at an angle of $\pi/4$ to the shearing direction, which is parallel to the x-axis. The wrinkling pattern closely resembles the prediction from elasticity theory illustrated in Fig. 2.7. Colour coding indicates the dimensionless out-of-plane displacement z/λ demonstrating that the wrinkles' amplitude increases with the shear angle. Reprinted from [86].

at low densities $\eta \lesssim 30$. In this range of η, random networks tend to have regions of low local density in which the wrinkling pattern is not well defined due to the lack of network points. Therefore, we limit our simulations to densities $\eta > 30$ in random networks.

Critical shear angle

For the critical shear angle γ_c, we expect

$$\gamma_c = \frac{291\pi^2}{8L_y^2}\frac{\kappa}{\mu} = \frac{291\pi^2}{8L_y^2} l_b^2 \ , \tag{2.93}$$

as derived in Section 2.2.4 for networks with $L_x = L_y$. In order to test this, we performed simulations according to the protocol presented in Section 2.3.7 – using predictive perturbations with the wrinkling pattern we expect at the onset of wrinkling. We used regular networks with densities $\eta^{\triangle} = \{20, 30, 50\}$ and random networks with $\eta = 47$. For the bending rigidity, we used values in the range $l_b/L_x \in [1.18 \cdot 10^{-4}, 1.18 \cdot 10^{-2}]$ in regular networks and $l_b/L_x \in [5.27 \cdot 10^{-4}, 5.27 \cdot 10^{-3}]$ in random networks. We deviate from the definition l_b/L for the bending rigidity introduced in Section 2.3.2 here because we want to compare random and regular networks. However, L is

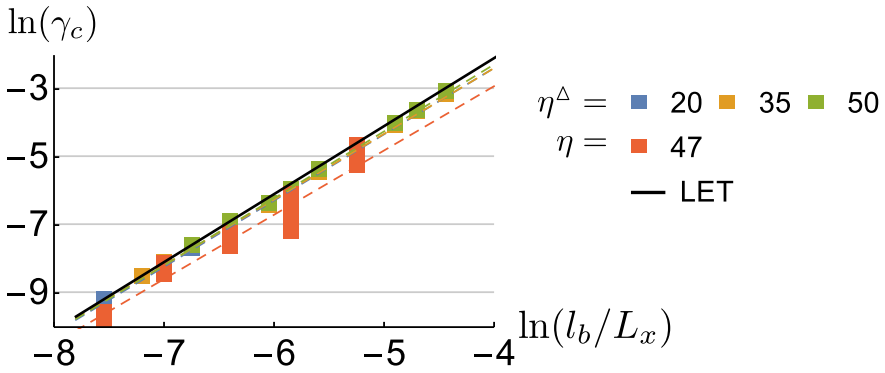

Figure 2.12: Double logarithmic plot of the critical shear angle γ_c as a function of bending rigidity. Simulation data of regular and random networks (squares) and corresponding least square fits $\gamma_c \propto l_b^\alpha$ (dashed lines) are compared to the prediction from linear elasticity theory (solid black line) as given in Eq. (2.93). The simulation results yield exponents α that are close to the predicted value.

not properly defined in regular networks since the rods extend the whole simulation cell, so we replace L with L_x. For random networks, we simulated 10 different network realisations for each bending rigidity to average out effects that may result from specific configurations.
For identifying γ_c, two different methods were used. In regular networks with large enough bending rigidities, we find a proportionality

$$A^2 \propto (\gamma - \gamma_c) \ , \tag{2.94}$$

allowing us to extrapolate A^2 to 0 as explained in Section 2.3.7. This proportionality does not remain valid when bending rigidities become too small, so we only consider values l_b/L_x for the evaluation that are large enough to allow the described extrapolation. In networks with $\eta^\triangle = 20$, the smallest bending rigidity considered is $l_b/L_x = 5.27{\cdot}10^{-4}$, for $\eta^\triangle = 35$, it is $l_b/L_x = 7.45 \cdot 10^{-4}$, and for $\eta^\triangle = 50$, it is $l_b/L_x = 1.18 \cdot 10^{-3}$.
In random networks, we do not find a similar proportionality. Instead, the amplitude jumps from 0 to a finite value. Therefore, we have to fall back on the less precise method of identifying the smallest shear angle yielding a wrinkled configuration during simulation as γ_c.

The results for γ_c are plotted in Fig. 2.12 with the predicted result from Eq. (2.93) for comparison. For regular networks, we find good agreement with the prediction. Fitting the simulation results with a function

$$\gamma_c \propto l_b^\alpha \ , \tag{2.95}$$

we find

$$\alpha(\eta^\triangle = 20) = 1.95 \pm 0.02 \ , \tag{2.96}$$
$$\alpha(\eta^\triangle = 35) = 1.93 \pm 0.02 \ , \tag{2.97}$$
$$\alpha(\eta^\triangle = 50) = 1.97 \pm 0.03 \ . \tag{2.98}$$

These exponents are close to the predicted value $\alpha_{\mathrm{LET}} = 2$ – compare Eq.(2.71).
For random networks with $\eta = 47$, a similar fit of the average γ_c yields an exponent

$\alpha = 1.90 \pm 0.07$ which is a bit lower than in regular networks but still close to the predicted value.
We can conclude that wrinkling is a universal feature of sheared semiflexible polymer networks because the critical shear angle in random and regular networks is well predicted by continuum elasticity theory. This is true for all evaluated bending rigidities. Varying the density in regular networks does not appear to have a significant effect. Since the critical shear angles are small, shear-induced wrinkling is a phenomenon that is relevant in all applications in which such networks are subject to shear stresses.
It should be noted that we cannot be certain if these findings are valid in realistic actin networks though. First of all, we only simulated random networks of one specific density. More importantly, the evaluated bending rigidities in random networks are larger than the estimate we gave for realistic F-actin in Section 2.3.6. Even though the simulation data does not indicate this, it is possible that networks deviate from linear elasticity theory when the bending rigidity becomes too small.

Hysteresis effects

When applying random perturbations instead of predictive perturbations to the sheared networks in our simulations, larger shear angles are required to induce wrinkling. In some cases, the difference between the two values is as large as two orders of magnitude. A direct comparison of the total elastic energies E_{wr} in wrinkled networks and E_{pl} in planar networks at shear angles $\gamma > \gamma_c$ reveals that the wrinkled configurations are energetically favourable. From this, we can draw two conclusions. First, it validates the application of predictive perturbations in order to find the critical shear angle. Secondly, it suggests that the planar and the wrinkled configuration are two minima in a high-dimensional energy landscape that are separated by an energy barrier. The latter point is supported by the observation that increasing the amplitude of random perturbations decreases the shear angle necessary to induce wrinkling. Larger perturbations correspond to a larger elastic energy in the network which would make it easier for the system to cross the energy barrier.

Another finding that advocates the existence of such an energy barrier can be made when reversing the simulations. Instead of starting from a planar network and increasing γ until we get a wrinkled configuration, we can start with a sheared network that is already wrinkled and let it relax by setting $\delta\gamma < 0$. Doing this, we find that the networks remain wrinkled at shear angles below γ_c even though the planar state is energetically favourable over the wrinkled state as a comparison of E_{wr} and E_{pl} shows. This effect in combination with the delayed wrinkling during simulations with increasing γ can be understood as a kind of hysteresis. An energy barrier between the planar and the wrinkled configuration would explain this behaviour. An example plot of illustrating the hysteresis by comparing E_{wr} and E_{pl} in a specific network can be found in Fig. 2.13.

Energy reduction

In the previous section, we introduced the total elastic energies E_{wr} and E_{pl} in the wrinkled and planar configuration of a network. For shear angles below γ_c, we have $E_{\mathrm{wr}} > E_{\mathrm{pl}}$ while for $\gamma > \gamma_c$, the wrinkled configuration becomes energetically favourable. In order to measure the energy reduction due to wrinkling as a function of γ, we

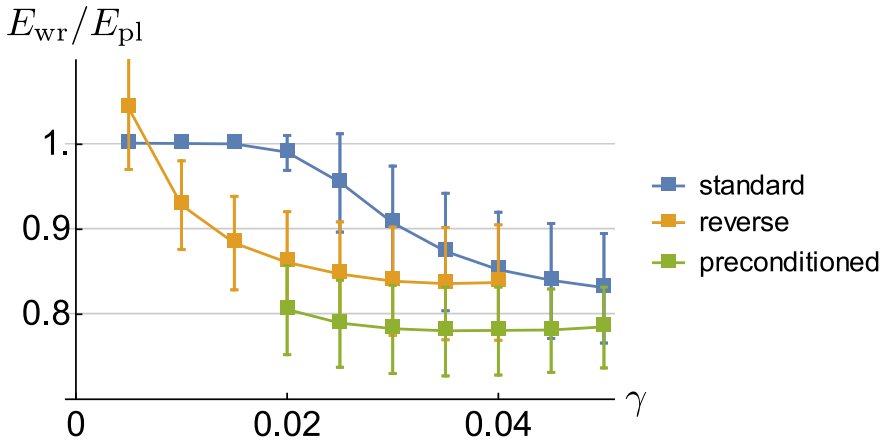

Figure 2.13: Ratio of the total elastic energies E_{wr} in wrinkled networks and E_{pl} in planar networks as a function of the shear angle γ in random networks with $\eta = 47$ and $l_b/L = 2.50 \cdot 10^{-3}$. Error bars indicate standard deviations due to averaging over 10 network realisations. The fact that networks remain in a planar configuration even though the wrinkled state is energetically favourable suggest the existence of metastable configurations. More evidence for this is found in networks that are preconditioned with the wrinkled configuration found in a regular network (here at $\gamma = 0.02$) This lowers the elastic energy that is even further demonstrating that the wrinkled state found in standard simulations is not the equilibrium configuration.

performed simulations of random networks – once allowing three-dimensional configurations and once enforcing two-dimensional configurations by omitting perturbation as described in Section 2.3.5. Random perturbations were used for three-dimensional simulations. We simulated networks with densities $\eta = \{32, 39, 47, 54\}$ and a bending rigidity $l_b/L = 2.50 \cdot 10^{-3}$. For each density, 10 network realisations were simulated. The obtained results were confirmed in sample checks for regular networks in analogous simulations.

The resulting ratios $E_{\mathrm{wr}}/E_{\mathrm{pl}}$ as a function of γ are plotted in Fig. 2.14. We find that wrinkling reduces the networks' total elastic energy up to 20% at shear angles just above the onset of wrinkling. The energy difference is larger in networks with larger density. The energy difference can be explained as a result of the different mechanisms by which the networks avoid compressive stress in two and three dimensions. For small bending rigidities $l_b/L \ll 1$ as we have in our simulations, a rod that is contracted due to compressive stress can bend in order to reduce its elastic energy. In two-dimensional simulations, only in-plane bending is allowed which limits the length scale of bending to the length of individual segments which is in the range of l_c – the average distance between neighbouring crosslinks. In three-dimensional simulations, out-of-plane displacements are allowed which result in wrinkling. The length scale of bending in this case is the wrinkles' wavelength which is in the order of the system size. Hence, bending in wrinkled networks occurs on larger length scales than in planar networks which means that the rods' curvature due to bending is smaller in wrinkled networks than in planar networks. Since a rod's bending energy is inversely proportional to the square of the curvature, less bending energy is required in wrinkled networks to avoid stretching energy resulting from compressive stress.

At larger shear angles, the ratio $E_{\mathrm{wr}}/E_{\mathrm{pl}}$ seems to approach 1 with increasing γ. This

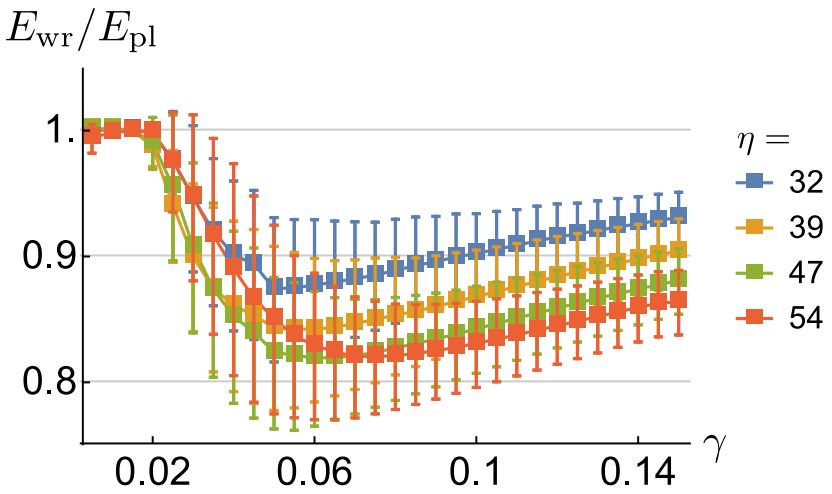

Figure 2.14: Ratio of total elastic energies $E_{\mathrm{wr}}/E_{\mathrm{pl}}$ as a function of γ in wrinkled and planar networks with $\eta = \{32, 39, 47, 54\}$ and $l_b/L = 2.50 \cdot 10^{-3}$. Error bars indicate standard deviations due to averaging over 10 network realisations. Wrinkling yields an energy reduction of up to 20% near the onset of wrinkling, and this energy gain increases with density. At large shear angles, the energy ratio approaches 1 which indicates nonlinear elasticity.

is an example of non-linear elasticity in semiflexible polymer networks. In a thin membrane following linear elasticity theory, the ratio would approach

$$\lim_{\gamma\to\infty} \frac{E_{\mathrm{wr}}}{E_{\mathrm{pl}}} \approx \frac{1+\nu}{2} \,. \tag{2.99}$$

For a derivation, see Section 2.2.3. A possible explanation for the different behaviour of networks is strain stiffening as described in Section 2.1.3. This effect occurs at large shear angles and leads to an effective increase in the shear modulus G. Strain stiffening has been explained to result from the networks' transition from a bending dominated regime to a stretching dominated one. We find that wrinkling induces this transition in our networks, see Section 2.4.3. As explained above, the energy difference in planar and wrinkled networks results from their different bending energies. Therefore, as stretching becomes increasingly dominant, the bending energies become less relevant, and the networks' total elastic energies approach each other.
Despite this deviation, the energy reduction is still relevant since the networks' elastic properties are derived from their elastic energy as a function of the applied stresses. Therefore, constraining networks to in-plane deformations in simulations will modify the elastic properties and may yield results that differ from real sheet-like materials that can deform in three dimensions.

Metastability in random networks

The hysteresis effects described in Section 2.4.1 suggest that sheared networks can have metastable configurations besides their equilibrium configuration. Additional evidence for this can be found in random networks simulated with random perturbations.
The wrinkling patterns occurring in these simulations are not always in good agreement with the wrinkling pattern $z_{\mathrm{CET}}(x, y)$ expected from continuum elasticity theory

as given in Eq. (2.25). When this is the case, we find that we can significantly lower the elastic energy by a method we call 'preconditioning'. For this, we take a regular network with the same density, elastic properties, and shear deformation as the random network in question and transfer the regular network's equilibrium configuration to the random network before running the minimisation routine. In a sense, this can be understood as a special case of predictive perturbation where we use a regular network's wrinkling pattern as the perturbation pattern. Even when the shear angle is further increased, the preconditioned network remains at a lower elastic energy compared to the network that is perturbed randomly. Since the configuration in the latter is still stable, this indicates the existence of several local minima in the energy landscape corresponding to different metastable configurations. Even though these configurations may only differ slightly, a transition from one to the other appears to be difficult for the network – possibly again due to an energy barrier.
There is a second important conclusion we can draw from the simulations of preconditioned networks. Since preconditioning always lowers the elastic energy, we can conclude that the equilibrium configuration in sheared networks is the same for regular and random networks. This is noteworthy because it means that the networks' microstructure does not influence the resulting wrinkling patterns.

2.4.2 Wrinkle properties

Wavelength

In Section 2.2.4, we used linear elasticity theory to derive the wavelength λ in sheared networks at large shear angles γ. According to Eq. (2.68), we have λ as a function of γ:

$$\lambda(\gamma) = \left(72\pi^2 L_y^2 \frac{\kappa}{\mu\gamma}\right)^{1/4} . \tag{2.100}$$

As pointed out though, this expression cannot remain valid in systems with periodic boundary conditions as λ is restricted to discrete values

$$\lambda_n = \frac{1}{n}\frac{L_x}{\sqrt{2}} \, , n = 1, 2, \dots \, . \tag{2.101}$$

Instead of a decreasing continuously with γ, the wrinkles' wavelength will be the value λ_n that minimises the network's elastic energy for a given shear angle. If the network's deformation is correctly described by linear elasticity theory, we can expect λ_n to be close to the predicted continuous value $\lambda(\gamma)$.
This kind of agreement can be observed in simulations of regular networks with random perturbations. For the simulations, densities in the range $\eta^{\triangle} \in [20, 50]$ and bending rigidities $l_b/L_x \in [3.33 \cdot 10^{-4}, 1.67 \cdot 10^{-3}]$ were used. Within the limits of discretisation, λ follows the prediction from Eq. (2.100). This indicates that regular networks are well described by continuum elasticity theory.
For random networks, this is not the case as they occasionally exhibit wrinkling patterns $z(x, y)$ deviating from the expected pattern according to continuum elasticity theory $z_{\mathrm{CET}}(x, y)$, see Eq. (2.25). However, as pointed out in Section 2.4.1, we find that the occurring wrinkling patterns do not actually represent the energetically ideal configurations. Preconditioning the random networks with the wrinkling patterns found in

comparable regular networks would yield an energetically more favourable configuration. Since this configuration is in agreement with elasticity theory within the limits of discretisation, we can conclude that the same is true for random networks.
The above findings imply that the networks' microstructure does not affect the validity of elasticity theory regarding wrinkling wavelength. This is useful for measuring elastic properties of sheet-like materials in experimental setups. According to Eq. (2.49), measuring the wavelength in such a material yields the ratio of bending to Young's modulus B/Y_2. A similar method has been used in experiments with polystyrene films for measuring their elasticity [72]. In case of networks, measuring λ would yield the ratio of the constituting rods' bending and stretching modulus κ/μ according to Eq. (2.100).

Amplitude

We measured the wrinkles' amplitude A in regular networks with densities in the range $\eta^{\triangle} \in [20, 50]$ and bending rigidities $l_b/L_x \in [3.33 \cdot 10^{-4}, 1.67 \cdot 10^{-3}]$. To enable out-of-plane deformations, random perturbations were applied.
As outlined in Section 2.2.4, the wrinkles' amplitude in a network at large shear angles should follow

$$A = \frac{1}{\sqrt{3}\pi}\gamma^{1/2}\lambda \ , \tag{2.102}$$

according to linear elasticity theory, compare Eq. (2.72).
In our simulations, we find a similar dependence – see Fig. 2.15. Up to a maximum shear angle $\gamma_{\max}$, the wrinkles' amplitude is slightly larger than the predicted value but still proportional to $\gamma^{1/2}$. The cause of the larger amplitudes is not entirely clear – they could result from nonlinear effects, be caused by boundary effects that are relevant due to the small system size, or simply be attributed to the approximations made when deriving the prediction for A such as the vanishing compressive stress – see Section 2.2.3.
Assuming the amplitude follows a linear function

$$A/\lambda = \frac{1}{\sqrt{2}\pi}\left(\gamma(1-\nu)\right)^{1/2} \tag{2.103}$$

according to Eq. (2.43), we can fit the simulation data treating the Poisson ratio ν as a fit parameter. Doing this, we get the best agreement for $\nu = -0.127$. However, there is no obvious reason why networks should deviate from linear elasticity theory in this aspect. This is especially true since negative Poisson ratios are extremely rare in natural materials [98].
For $\gamma > \gamma_{\max}$, the amplitude decreases with increasing shear angles and therefore exhibits a behaviour that completely contradicts linear elasticity theory. Hence, $\gamma_{\max}$ gives us an estimate for the shear angles up to which we can neglect the microstructure in regular networks and treat them as continuous materials approximately following linear elasticity theory. A similar amplitude-strain dependence was observed in stretched polyethylene sheets [76] and simulations of stretched hyperelastic sheets [75]. A possible explanation for this effect was given by Healey et al. [99] identifying a "geometrically nonlinear coupling between the large in-plane strain and out-of-plane deflection" [76] as the cause.

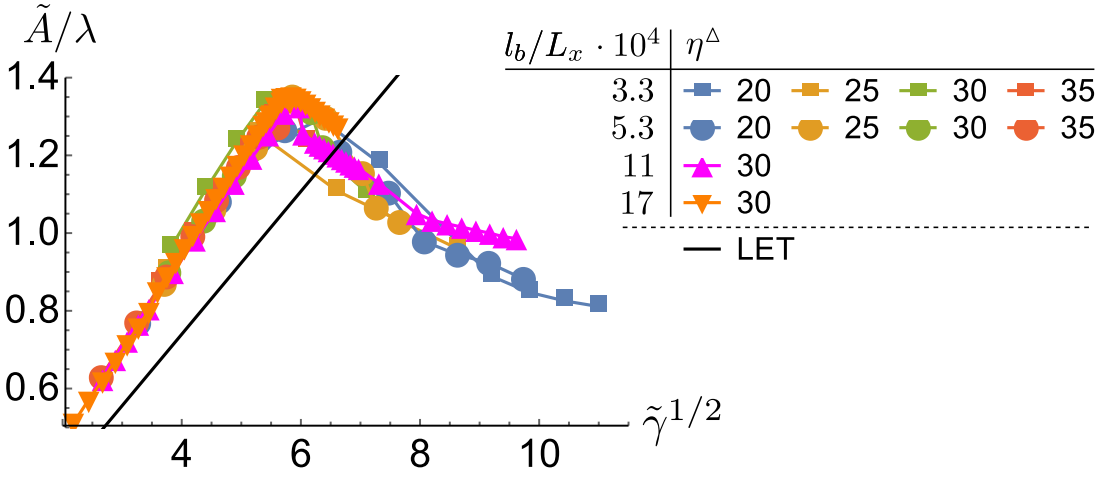

Figure 2.15: Rescaled amplitude $\tilde{A}/\lambda$ as a function of the rescaled shear angle $\tilde{\gamma}$ in regular networks with $\eta^\Delta \in [20, 50]$ and $l_b/L_x \in [3.33 \cdot 10^{-4}, 1.67 \cdot 10^{-3}]$. Up to a maximum shear angle, the amplitude approximately follows the prediction from linear elasticity theory (black line) as given in Eq. 2.102. Beyond the maximum shear angle, the amplitude decreases with increasing γ which is evidence for nonlinear elasticity.

Evaluating our simulation results, we find an empirical relation

$$\gamma_{\max} \propto \left(\frac{l_b}{l_c^\Delta}\right)^2 \sqrt{\frac{L_y}{\lambda}} =: \zeta \ . \tag{2.104}$$

Rescaling shear angles according to $\tilde{\gamma} = \gamma\zeta^{-1}$ and amplitudes according to $\tilde{A} = A\zeta^{-1/2}$ results in data collapse onto a master curve for the rescaled amplitude $\tilde{A}$ as a function of the rescaled shear angle $\tilde{\gamma}$ as shown in Fig. 2.15. In rescaled units, we find a numerical value of $\tilde{\gamma}_{\max}^{1/2} \approx 5.9$ for the maximum shear angle[1].
Entering $\gamma_{\max} \propto \zeta$ into the expression we have for the wrinkles' wavelength and solving for λ, we get

$$\lambda(\gamma_{\max}) \propto L_y^{3/7}\, {l_c^\Delta}^{4/7} \ . \tag{2.105}$$

Since λ decreases with increased shear angle, this gives us the minimum wavelength up to which linear elasticity theory describes the wrinkles' amplitude. Since this minimum wavelength only depends on the networks' lattice constant l_c^Δ and not on the elastic properties, the break-down of linear elasticity theory suggests that the networks' microstructure becomes relevant at shear angles $\gamma > \gamma_{\max}$.

In similar simulations with random networks, the resulting wrinkling patterns exhibit amplitudes that are not in agreement with Eq. (2.102) – not even at small shear angles as was the case for regular networks. We might assume that the wrinkling patterns deviating from linear elasticity theory in random networks are the cause for this effect. However, preconditioning does not improve the agreement between simulations and prediction either. Instead, we notice that the wrinkles' amplitude in preconditioned

[1]Due to a more accurate evaluation of the simulation data, the value given here is slightly larger than in the previous publication [86]

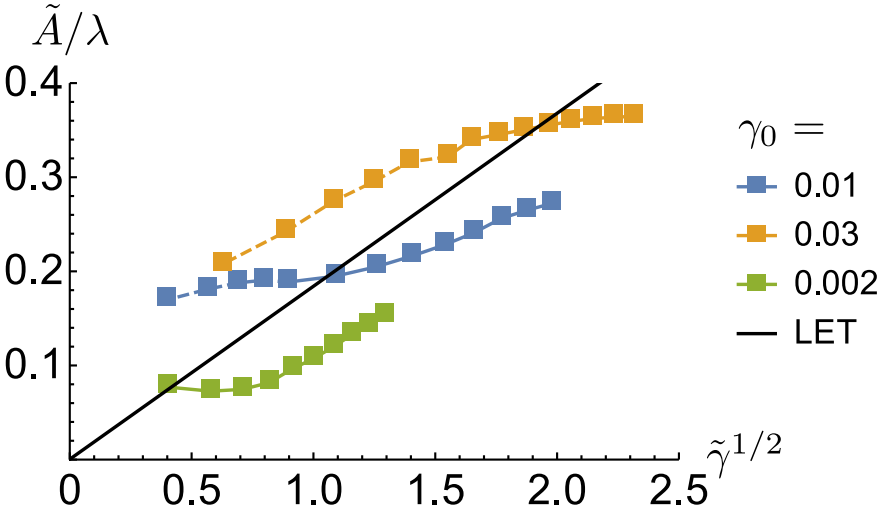

Figure 2.16: Rescaled amplitude $\tilde{A}/\lambda$ as a function of the rescaled shear angle $\tilde{\gamma}$ in random networks with $\eta = 39$ and $l_b/L = 2.5 \cdot 10^{-3}$. The networks were preconditioned at different shear angles γ_0 indicated by different colours; dashed lines indicate reverse simulations. The amplitudes in these networks do not agree with the prediction from linear elasticity theory (black line) as given in Eq. 2.102. Instead, the wrinkles' amplitude appears to be dependent on γ_0 which indicates the existence of multiple metastable configurations

networks is highly dependent on the initial state at which the preconditioning was performed, see Fig. 2.16 for an illustration. The networks corresponding to the plotted data were all preconditioned with a wrinkling pattern of the same wavelength – only at different shear angles γ_0. This indicates that several metastable configurations with different amplitudes at the same wavelength exist in random networks. Recalling the evidence for the existence of multiple metastable configurations in Section 2.4.1, this explanation seems plausible.

2.4.3 Deformation mode

We simulated the same random networks once allowing out-of-plane deformation and once restricting them to two dimensions in order to identify the influence of wrinkling on the dominant mode of deformation. As outlined in Section 2.1.3, networks can either be bending dominated or stretching dominated, and a transition between the two regimes is associated with the onset of nonlinear behaviour such as strain stiffening. As described in Section 2.3.7, we use the ratio of bending and stretching energy contributions $E_{\text{tot}}^{(\text{b})}/E_{\text{tot}}^{(\text{s})}$ in the networks to identify the dominant deformation mode.
We used networks with densities $\eta = \{32, 39, 47, 54\}$ bending rigidities $l_b/L = \{5.27 \cdot 10^{-4}, 1.67 \cdot 10^{-3}\}$. Out-of-plane deformations were enabled using random perturbations.
We find that wrinkled networks enter the stretching dominated regime at smaller strains than their two-dimensional counterparts. This is illustrated in Fig. 2.17. In fact, reverse simulations suggest that wrinkled networks are always stretching dominated. As explained in Section 2.4.1, reverse simulations start from a sheared network that is already wrinkled and incrementally reduce γ. During this procedure, networks remain

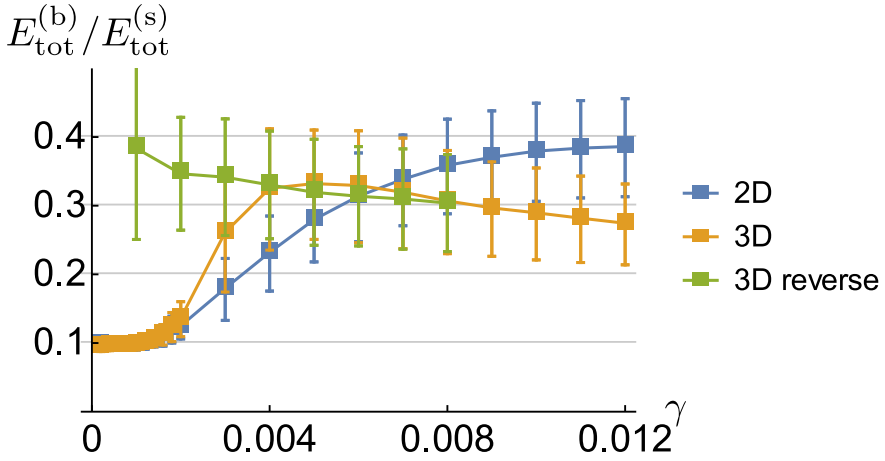

Figure 2.17: Ratio of bending and stretching energy contributions $E_{\mathrm{tot}}^{(\mathrm{b})}/E_{\mathrm{tot}}^{(\mathrm{s})}$ in random networks with $\eta = 39$ and $l_b/L = 7.91 \cdot 10^{-4}$ for different simulation modes. Error bars indicate standard deviations due to averaging over 10 network realisations.Negative slope indicates that the network is stretching dominated which occurs at smaller shear angles in three-dimensional simulations due to wrinkling. Reverse simulations show that wrinkled networks are always stretching dominated.

wrinkled even for $\gamma < \gamma_c$. The negative slope of $E_{\mathrm{tot}}^{(\mathrm{b})}/E_{\mathrm{tot}}^{(\mathrm{s})}$ in the entire range of simulated shear angles indicates that wrinkled networks are always stretching dominated, see Fig. 2.17 for an example.
We can conclude that wrinkling significantly influences a network's mode of deformation. Not only does it induce the transition to the stretching dominated regime at lower shear angles compared to networks that are restricted to two dimensions, but our results also indicate that wrinkled networks are always stretching dominated.

2.5 Conclusion and discussion

This chapter presented the author's work on the elastic response of semiflexible polymer networks with the main focus of wrinkling due to shear strain. In Section 2.2.3, elasticity theory was used to describe wrinkling in sheared membranes. Assuming linear elasticity, it was possible to derive predictions for the critical shear angle γ_c at which membranes start wrinkling, the wrinkles' wavelength and amplitude at large strains, and the membranes' elastic energy at large strains. These expressions were applied to networks of thin elastic rods in Section 2.2.4 yielding the following predictions: the critical shear angle is proportional to the square of the bending rigidity parameter l_b: $\gamma_c \propto l_b^2$. For the wrinkles' wavelength λ, the theory predicts $\lambda \propto l_b^{1/2}\gamma^{-1/2}$ with the shear angle γ. The wrinkles' amplitude is a function of λ and γ: $A \propto \gamma^{1/2}\lambda$.
The above predictions were tested using numerical simulations as described in Section 2.3. Implementing a two-dimensional athermal model, semiflexible polymers were modelled as thin elastic rods. Intersections of these were identified as permanent, and freely rotating crosslinks and the segments' midpoints were treated as additional degrees of freedom to enable bending deformations. Different generation routines were used to generate two types of network geometries: regular triangular networks and random networks. During simulation, three-dimensional configurations were enabled by

positional perturbations of the crosslinks and midpoints. Simulations were performed at various network densities in the typical range of densities found in actin networks. The individual rods' bending rigidity was also varied ranging from values comparable to actin filaments to larger values which would be expected in bundled networks.
In Section 2.4, the simulation results were presented and compared to the theoretical predictions. Sheared networks exhibited a wrinkling instability at a critical shear angle γ_c. Greater shear angles would result in the formation of wrinkles at an angle of $\pi/4$ to the shearing direction. Both aspects are in agreement with elasticity theory for thin membranes. Wrinkled networks had a significantly lower elastic energy than networks that remained planar. We found that the amount of energy reduction could be as large as 20% depending on the networks' density. The energy reduction would be maximal for shear angles slightly larger than γ_c and decrease at large shear angles. The energy reduction is relevant since a material's elastic moduli can be expressed as derivatives of its elastic energy, so wrinkling should have a significant effect on the networks' elastic properties.
For the critical shear angle, the simulations yielded a dependence on the rods' bending rigidity $\gamma_c \propto l_b^\alpha$ with $\alpha = 1.90 \pm 0.07$ for the studied random networks and $\alpha \in [1.93 \pm 0.02, 1.97 \pm 0.03]$ for the studied regular networks. These values are close to the predicted value $\alpha_{\mathrm{LET}} = 2$. Since the prediction was derived from a theory for thin membranes with a linear elastic response, this indicates that the networks' elastic response can be described by this theory at small strains. In particular, this means that their discrete microstructure and nonlinear elastic effects can be neglected.
Another point in which theory and simulation results are in agreement is the wrinkles' wavelength λ. Within the limits of discretisation outlined in Section 2.2.4, λ follows the prediction. However, there are multiple aspects in which the simulation results are not in agreement with the theory.
For the wrinkles' amplitude A, the simulation results deviated from the theoretical predictions qualitatively or quantitatively depending on a number of factors. In regular networks at small strains, the measured amplitudes agreed qualitatively with the theory but were slightly larger. Above a maximum strain, A started decreasing with increasing strain in contrast to the steady increase predicted by the theory. Since a similar behaviour has been reported in stretched sheet-like materials in experiments [76] and simulations [75], this phenomenon cannot be attributed to the networks' discrete microstructure. Instead, it is more likely that this is a nonlinear effect. In networks with a random microstructure, A did not even agree qualitatively with the theoretical predictions. For specific values γ and λ, the networks exhibited different wrinkle amplitudes depending on their initial state.
Another example for the breakdown of linear elasticity theory is the networks' elastic energy at large shear angles. According to the theory, the ratio of the total elastic energies in wrinkled and planar networks should approach a constant value with increasing γ. In the simulations, the energies appeared to become equal at large shear angles instead. The most likely explanation for this is strain stiffening – a nonlinear effect that causes the networks to become increasingly resistant to deformation with increasing strain, see Section 2.1.3.
Since the critical shear angle γ_c and the wrinkles' wavelength λ exhibited better agreement with the theoretical predictions, we concluded that these are more suitable for measuring the elastic properties of semiflexible polymer networks in experimental setups. In experiments with other sheet-like materials, a similar approach for determ-

ining the material's elasticity by measuring λ has been applied successfully [72].
Another aspect that is of interest with regard to nonlinear elasticity is the dominant mode of deformation in networks. As described in Section 2.1.3, nonlinear effects such as strain stiffening are associated with a transition from a bending dominated regime at small strains to a stretching dominated regime at large strains. This was explained as a structural effect of the networks rather than resulting from their components' elasticity [43, 46, 61]. In the simulations presented here, a separate analysis of the bending and stretching energy contributions indicated that wrinkling causes an immediate transition into the stretching dominated regime, see Section 2.4.3. This is also a structural effect and independent of the network components' properties.
Finally, the simulation results indicated the existence of metastable configurations in random networks but not in regular networks. Near γ_c, we found that the networks could remain in a planar configuration even though wrinkling was energetically favourable and vice versa. Also, measurements of the amplitude in preconditioned random networks indicated the existence of multiple metastable configurations with the same wavelength but different amplitudes. In combination with the observations regarding the wrinkles' amplitude, this leads to the conclusion that the networks' microstructure can have an influence on their elastic properties.

Chapter 3

Collective behaviour of active rods

3.1 Fundamentals of active matter

In physics, the term 'active matter' refers to materials or systems consisting of individual units that are able to turn available energy into propulsion [14–16, 18, 19]. Systems like this can be found in a large variety of realisations and on a wide range of length scales. In nature, the active units are usually alive – forming macroscopic active systems such as flocks of insects, fish, birds, sheep [102–105], or microscopic ones like swarms of bacteria, cell layers, and the cytoskeleton [14, 15, 18, 27, 105–107]. Two examples for active matter at different length-scales are shown in Fig. 3.1. The variety of different manifestations of active matter is one reason why this is an interesting subject of research within biological physics – understanding active matter in general should help to understand biological systems [15]. Another reason is that active matter is relevant for a number of problems in nanotechnology such as transport and organisation of nanoscale components [16]. Artificial swimmers and engines on the same length scale are required for those tasks, and a promising approach to designing these is imitating their biological counterparts [16, 17]. Finally, active matter is also interesting as an example for nonequilibrium systems which have been of growing interest in the field of statistical physics recently [19].

Active materials can also be man-made and consist of non-living components, e.g., colloidal particles on a vibrating plate [108–114], nanoscale artificial swimmers in a fluid [115–123], or motility assays of biofilaments [124–129]. Another class of active systems are agent-based simulations of pointlike and spherical [116, 120, 121, 124, 130–139] or rodlike particles [106, 110, 125, 126, 140–150].

Even though the above systems are fundamentally different on their components' level, they exhibit a wide range of uniform phenomena that can be observed regardless of these differences. Many of the observed effects include some kind of orientational order ranging from the formation of static structures such as asters [133, 140, 142, 146, 151] and vortices [140, 151] to collective movement of many particles in bands [125–127, 131–133, 152], lanes [133, 141, 143, 147, 148], clusters [28, 106, 108, 125, 127, 130, 132, 133, 138, 141–144, 147–150], and even circular structures [108–110, 124–126, 137, 153–155]. Another class of effects includes different types of density inhomogeneities such as giant number fluctuations [28, 108, 111, 116, 134, 141, 156] and phase separation [112, 114, 116, 121, 122, 133–136, 138, 147, 148, 157–160]. Of course, these categories are not necessarily exclusive.

The following section will introduce some fundamentals that are required for studying

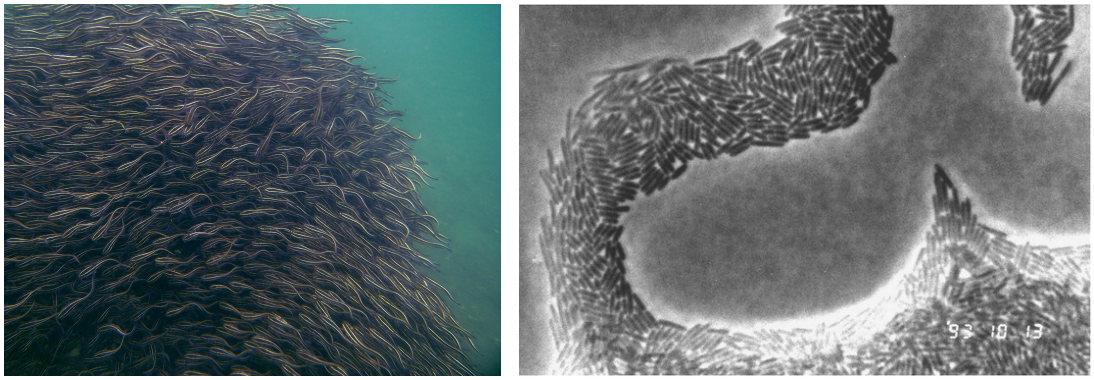

Figure 3.1: Two examples for naturally occurring active matter systems. Left: a school of striped eel catfish, photo by Sylke Rohrlach (CC BY-SA 2.0) [100], right: swarming in a colony of P. mirabilis bacteria, adapted from Ref. [101]. Despite the size difference, both systems exhibit similar collective behaviour in that their constituents align and form dense aggregates.

active matter in general and rodlike particles – which are the main focus of this work – in particular. The section will be concluded by a description of the focus and outline of this chapter in Section 3.1.6.

3.1.1 Rodlike particles

Many biological systems can be classified as active matter – materials in which free energy is consumed and converted into movement. One common property of biological active matter systems is that they consist of elongated particles [161]. The bacteria introduced in Section 1.2.2 were selected because they are candidates for constituting active systems and are examples of rodlike particles since their shape is approximately cylindrical. To account for their differing measurements, we introduce here a parameter that specifies the particles' geometry. This parameter is the aspect ratio a which is defined as the ratio of the particle's length L and its diameter d:

$$a = \frac{L}{d} \, . \tag{3.1}$$

The larger the aspect ratio the longer a particle is compared to its width. With the values given in Section 1.2.2, we can calculate the aspect ratios of the introduced bacteria. E. coli has an aspect ratio of about 4 while for B. subtilis, $a \approx 6 - 11$.

In order to constitute an active material, the particles have to be motile. The bacteria E. coli and B. subtilis are capable of self-propulsion due to their flagella. For this work, quasi-two-dimensional systems are especially relevant. These can be implemented using the aforementioned bacteria by confining them in a thin film of liquid [143, 162] or studying them on a two-dimensional surface [28, 106]. Another common experimental setup are motility assays of biofilaments [124–129]. Details on these experimental realisations can be found in Section 3.2.3.

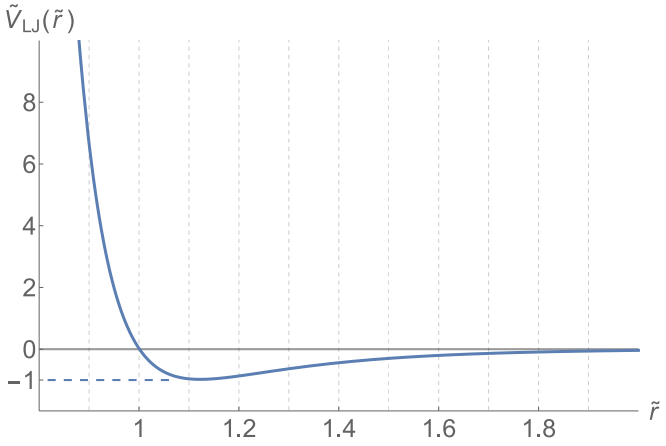

Figure 3.2: The dimensionless Lennard-Jones potential $\tilde{V}_{\mathrm{LJ}}(\tilde{r}) = 4\left[\tilde{r}^{-12} - \tilde{r}^{-6}\right]$ with $\tilde{r} = r\sigma^{-1}$ being the dimensionless distance. The potential has its zero at $\tilde{r} = 1$ and a minimum value -1 at $\tilde{r} = 2^{1/6}$. This corresponds to a minimum value of $-\epsilon$ at $r = 2^{1/6}\sigma$ in the nonscaled potential $V_{\mathrm{LJ}}(r)$ described in the text.

3.1.2 Van-der-Waals interaction

In biological systems, many interesting properties arise from the interplay between a large number of individual particles such as proteins, biofilaments, cells and bacteria. To understand this interplay, it is necessary to know the underlying interactions. Since the particles usually do not carry a charge, electrostatic interactions do not occur, and the van-der-Waals interaction is the dominant one. This section gives a brief summary of this type of interaction. Unless indicated otherwise, the information presented here was taken from the books "Festkörperphysik" by Rudolf Gross and Achim Marx [163] and "Festkörperphysik" by Siegfried Hunklinger [164].

In soft matter systems, the constituents are typically macromolecules or even bigger molecular compounds ranging from proteins over biofilaments to cells and bacteria. These objects are solid, so they cannot penetrate each other. The underlying cause for this is the Pauli exclusion principle which implies an energy cost for overlapping electron orbitals of two objects. This can be well approximated by a repulsive potential proportional to r^{-12} with r being the distance between the objects.

Besides this repulsive interaction, there is also an attractive interaction present in the form of van-der-Waals forces. Compared to other types of binding mechanisms in solid matter like ionic bonds or covalent bonds, the van-der-Waals interaction is weak on the level of single atoms or molecules with a typical bond energy of 0.1 eV per atom. On a macroscopic level, it can be very effective though as one can see from geckos' feet which are probably the most prominent example for the utilisation of van-der-Waals forces in nature [165].

The van-der-Waals force is generated by induced electric dipoles due to fluctuating charge distributions in the involved atoms. The resulting attraction can be described via a potential that is proportional to r^{-6}. Combining this with the repulsion caused by the Pauli exclusion principle gives the Lennard-Jones potential

$$V_{\mathrm{LJ}}(r) = 4\epsilon\left[\left(\frac{\sigma}{r}\right)^{12} - \left(\frac{\sigma}{r}\right)^{6}\right] . \tag{3.2}$$

This is an empiric potential describing the interaction between neutrally charged atoms or molecules. The Lennard-Jones potential includes two parameters: ϵ defining the depth of the potential and thereby its strength and σ providing the length scale. An example plot of the potential is shown in Fig. 3.2.

3.1.3 Classical density functional theory

A recurring theme in biological systems are fluids that are inhomogeneous due to a variety of reasons, e.g., confinement, interfaces, crystallisation, or phase separation – which is the main focus of this chapter. A powerful tool for studying the thermodynamic properties of these fluids is classical density functional theory [166, 167]. This method makes use of the fact that the equilibrium density distribution $\rho_0(\boldsymbol{r})$ is uniquely defined as the one that minimises the system's free energy. The following introduction is adapted from Robert Evans' original article in which classical density functional theory was first introduced [168].
The idea of classical density functional theory is to find equations describing statistical mechanics in terms of functionals. Consider a grand canonical ensemble with the Hamiltonian

$$H = H_0 + V = H_0 + \sum_{i=1}^{N} V_{\text{ext}}(\boldsymbol{r}_i) \ , \tag{3.3}$$

where N is the total number of particles, H_0 is the part of the Hamiltonian including kinetic energy and interparticle interactions, and $V_{\text{ext}}(\boldsymbol{r}_i)$ is an external potential with $\boldsymbol{r}_i$ denoting the position of particle i. We define the equilibrium probability density f_0 as

$$f_0 = Z_g^{-1} \exp\left(-\beta(H - \mu N)\right) \ , \tag{3.4}$$

with the chemical potential μ and the grand canonical partition function

$$Z_g = \operatorname{Tr}\left[\exp\left(-\beta(H - \mu N)\right)\right] \ . \tag{3.5}$$

In accordance with the grand canonical potential J_0, we can define the functional

$$J[f] = \operatorname{Tr}\left[f(H - \mu N + \beta^{-1} \ln f)\right] \ . \tag{3.6}$$

We see that $J[f = f_0] = J_0$, and it can be proven that for $f \neq f_0$, $J[f] > J_0$. Due to the specific form of H, we can write $J[f]$ as a functional of the particle density $\rho(\boldsymbol{r})$:

$$J[\rho] = \int d^3r \, \rho(\boldsymbol{r}) V_{\text{ext}}(\boldsymbol{r}_i) + F[\rho] - \mu \int d^3r \, \rho(\boldsymbol{r}) \ . \tag{3.7}$$

This equation can alternatively be derived by expressing J as a functional of the local chemical potential $\psi(\boldsymbol{r}) = \mu - V_{\text{ext}}(\boldsymbol{r})$ and then making the transition to $\rho(\boldsymbol{r})$ as the local variable by using a Legendre transformation [169].
The functional

$$F[\rho] = \operatorname{Tr} f_0(H_0 + \beta^{-1} \ln f_0) \tag{3.8}$$

can be identified as the intrinsic Helmholtz free energy. The fact that F is independent of V_{ext} and can therefore be studied independently will prove useful later.
Just as $J[f]$ is minimal for the equilibrium probability density f_0, it can be proven that $J[\rho]$ is minimal for the equilibrium density $\rho_0(\boldsymbol{r})$. This can be expressed as a functional derivative:

$$\left.\frac{\delta J[\rho]}{\delta \rho(\boldsymbol{r})}\right|_{\rho_0} = 0 \ . \tag{3.9}$$

From this, we derive the expression

$$\left.\frac{\delta F[\rho]}{\delta \rho(\boldsymbol{r})}\right|_{\rho_0} + V_{\text{ext}}(\boldsymbol{r}) - \mu = 0 \ , \tag{3.10}$$

which is the key equation for classical density functional theory. In principle, this equation enables us to calculate the equilibrium density $\rho_0(\boldsymbol{r})$ for any given external potential with the great advantage that F is independent of V_{ext}. In practice, this is rather difficult though since $F[\rho]$ is usually not known precisely for a system of many interacting particles. For an ideal gas, it is known exactly [169]:

$$F_{\text{id}}[\rho] = k_B T \int d^3r \, \rho(\boldsymbol{r}) \left[\ln\left(\rho(\boldsymbol{r})\Lambda^3\right) - 1\right] \ , \tag{3.11}$$

where Λ is the thermal de Broglie wavelength. In other systems, $F[\rho]$ has to be approximated in order to calculate the equilibrium density.

3.1.4 Nematic ordering of elongated particles

Systems of anisotropic particles can exhibit a number of phases that are neither liquid nor crystalline but share some properties of those phases. More specifically, these phases have orientational order – which is typical for crystals – and either no positional order – which is typical for liquids – or only partial positional order. For this reason, these phases are called liquid crystal phases, and materials in these phases are referred to as liquid crystals.
The most common phase in liquid crystals is the nematic phase in which the particles are aligned along a common axis without pointing in the same direction. If their directions were also aligned, this would be called polar ordering. Another liquid crystal phase is the smectic phase that is characterised by orientational order in combination with positional order in one direction. An illustration of these phases as well as the liquid – or isotropic – phase can be found in Fig. 3.3.
Following mainly the book "Introduction to the Theory of Soft Matter" by Jonathan V. Selinger [170], the following section gives a brief introduction into nematic ordering, how to quantify it, and how to calculate the isotropic-nematic phase transition. The summary of the Onsager theory for the isotropic-nematic phase transition also utilises material from the book "Basic concepts for Simple and Complex Liquids" by Jean-Louis Barrat and Jean-Pierre Hansen [169] and a review article by Vroege and Lekkerkerker [171].

Nematic order parameter in three dimensions

In order to quantify the degree of nematic ordering, we need an order parameter measuring how well the particles' orientations are aligned. For polar order, it is easy to find an orientational order parameter as we only need to average over all orientations in the systems. Denoting the orientation vectors of the particles as $\boldsymbol{u}_i$, the polarisation vector is given as

$$\boldsymbol{P} = \langle \boldsymbol{u}_i \rangle \ . \tag{3.12}$$

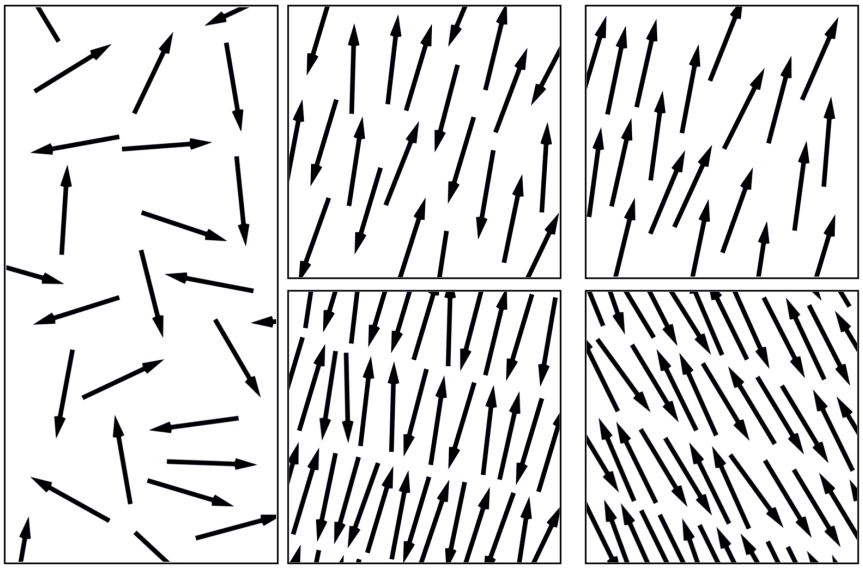

Figure 3.3: Two-dimensional illustration of different phases in a system of polar rodlike particles (arrows indicate orientation). Left: isotropic; top centre: nematic; top right: polar; bottom centre: smectic A; bottom right: smectic C

The degree of polar order is simply the absolute value of $\boldsymbol{P}$, and the direction of $\boldsymbol{P}$ indicates the axis of polar ordering. This parameter cannot be used to measure nematic order though since in that case, the $\boldsymbol{u}_i$ are aligned along a common axis but not along a common direction, so the average over all orientations would vanish. It turns out that the tensor

$$Q_{\alpha\beta} = \left\langle \frac{3}{2} u_{i,\alpha} u_{i,\beta} - \frac{1}{2}\delta_{\alpha\beta} \right\rangle \tag{3.13}$$

is suitable for quantifying nematic order. The letters α, β indicate components in three-dimensional space. The tensor is symmetric and traceless and constructed so that $Q_{\alpha\beta} = 0$ in an isotropic system and for perfect nematic ordering along one of the system's coordinate axes, the corresponding diagonal element is 1. A scalar order parameter can be derived from the eigenvalues $\boldsymbol{Q}$ which are S, $-S/2$, and $-S/2$. We can define S as the scalar order parameter quantifying the degree of nematic ordering equivalent to $|\boldsymbol{P}|$ for polar order. Typically, S is between 0 and 1 with $S = 0$ indicating a completely isotropic phase and $S = 1$ indicating perfect nematic ordering. The eigenvector associated with S is the director $\boldsymbol{n}$ – a unit vector indicating the orientation axis of the particles.

Nematic order parameter in two dimensions

In two dimensions, the nematic order parameter can be derived by following the approach for three dimensions. However, the prefactors in the definition of $\boldsymbol{Q}$ have to be adjusted yielding

$$Q_{\alpha\beta} = \langle 2u_{i,\alpha} u_{i,\beta} - \delta_{\alpha\beta} \rangle \ . \tag{3.14}$$

This makes sure that $Q_{\alpha\beta} = 0$ in the isotropic phase, and perfect nematic ordering along the x-axis or y-axis yields $Q_{xx} = 1$ or $Q_{yy} = 1$ respectively.

As mentioned before, we have to calculate the tensor's eigenvalues in order to get S. This is pretty straightforward in two dimensions. Introducing the orientation vectors

$$\hat{\boldsymbol{u}}_i = \begin{pmatrix} \cos\varphi_i \\ \sin\varphi_i \end{pmatrix} . \tag{3.15}$$

With φ_i being the particles' angles relative to the x-axis, we get

$$\boldsymbol{Q} = \begin{bmatrix} \left\langle 2\cos^2\varphi_i - 1 \right\rangle & \langle 2\cos\varphi_i \sin\varphi_i \rangle \\ \langle 2\cos\varphi_i \sin\varphi_i \rangle & \left\langle 2\sin^2\varphi_i - 1 \right\rangle \end{bmatrix} = \begin{bmatrix} q_1 & q_2 \\ q_2 & -q_1 \end{bmatrix} , \tag{3.16}$$

where we defined $q_1 = \left\langle 2\cos^2\varphi_i - 1 \right\rangle$ and $q_2 = \langle 2\cos\varphi_i \sin\varphi_i \rangle$. We can identify the positive eigenvalue of this tensor $S = \sqrt{q_1^2 + q_2^2}$ as the scalar order parameter. The associated eigenvector is the director

$$\boldsymbol{n} = \sqrt{\frac{q_2^2}{2q_1^2 + 2q_2^2 - 2q_1\sqrt{q_1^2+q_2^2}}} \begin{pmatrix} 1 \\ \frac{q_1 - \sqrt{q_1^2+q_2^2}}{q_2} \end{pmatrix} . \tag{3.17}$$

We see that we cannot calculate $\boldsymbol{n}$ like this for $q_2 = 0$ since we would divide by 0. However, $\boldsymbol{Q}$ would already be diagonal in this case with the eigenvalues q_1 and $-q_1$. Hence, the director would have to be parallel to one of the coordinate axes with the sign of q_1 indicating which one. For positive q_1, the greater of the two eigenvalues would be in the element Q_{xx}, so the director would be parallel to the x-axis. Analogously, the director would be parallel to the y-axis for $q_1 < 0$.

Isotropic-nematic phase transition

As explained earlier, liquid crystals are materials that can exhibit a variety of different phases – one of which is the nematic phase. It is obviously interesting to find out under which conditions the nematic phase occurs and what is required to induce a phase transition either into or out of the nematic phase. With the nematic order parameter introduced above, we can distinguish between the isotropic phase with $S = 0$ and the nematic phase with $S > 0$. When we want study the transition between these two phases, there are several approaches to choose from.

A general description of the transition is given by the Landau-de Gennes theory. This is a macroscopic theory assuming that the system's free energy density can be expressed as a power series in the nematic order parameter. It can be used to show that the transition is of first order.
A different approach can be taken by using a microscopic theory such as the Maier-Saupe theory. It derives the system's free energy F by assuming an aligning potential between interacting particles and using a mean-field approximation. It then determines the isotropic-nematic transition temperature by minimising F. This theory is useful when dealing with thermotropic liquid crystals, i.e., systems in which the isotropic-nematic transition is controlled by temperature. However, the main focus of this work are lyotropic systems in which the transition is controlled by particle concentration. In this case, the Onsager theory is more suitable to describe the transition.

The Onsager theory is also a microscopic theory and was first presented by Lars Onsager in 1949 [172]. It uses a virial expansion of the free energy to study the isotropic-nematic phase transition. It treats the particles as infinitely thin rods of length L and

diameter $d \to 0$. The particles interact via a hard-core potential u_{hc} which is infinite for overlapping particles and 0 otherwise. Due to this potential, only configurations without particle overlap are permitted. The volume excluded by this effect can be calculated explicitly. Assuming the particles are spherocylinders, the excluded volume between two particles is a function of their a relative angle γ. In order to avoid overlap, the second particle's centre of mass cannot penetrate a volume

$$V_{\mathrm{excl}} = 2L^2 d|\sin\gamma| + 2\pi d^2 L + \frac{4}{3}\pi d^3 \tag{3.18}$$

around the first one. In the limit of thin rods, the first term is dominant:

$$\lim_{d\to 0} V_{\mathrm{excl}} = 2L^2 d|\sin\gamma| \ . \tag{3.19}$$

The free energy in a system of particles interacting exclusively via excluded volume interactions is $F = -TS_E$ with the temperature T and the entropy S_E. Greater entropy is favourable as it reduces the free energy. In the system of thin rods considered here, there are two contributions to the entropy. The first one results from the particles' rotation and is maximal when they can rotate freely. The second one stems from the particles' positions. This contribution increases when V_{excl} is reduced as this yields more positional degrees of freedom. Therefore, the second contribution favours alignment. The competition between these two contributions is responsible for the existence of the isotropic and nematic phase.
In the limit of low particle concentration, we can approximate the free energy density $f = F/V$ – with V the system's volume – as follows:

$$\beta f = \rho\left(\ln\rho\Lambda^3 - 1\right) + B_2(T)\rho^2 + \mathcal{O}(\rho^3) \ , \tag{3.20}$$

where $\beta = k_B T$, ρ is the particle concentration, Λ is the thermal de Broglie wavelength, and $B_2(T)$ is the second virial coefficient – for a more detailed discussion of the virial expansion and the derivation of B_2, see App. A. In the limit of thin rods, higher virial coefficients can be neglected.
Since we are dealing with anisotropic particles, we have to consider their orientation in the calculation. We introduce a normalised orientational distribution function $\psi(\Omega)$:

$$\int d\Omega\, \psi(\Omega) = 1 \ , \tag{3.21}$$

with Ω being a spatial angle. The particles' orientational distribution gives a contribution f_{or} to the free energy density that results from the orientational entropy:

$$\beta f_{\mathrm{or}} = \rho \int d\Omega\, \psi(\Omega) \ln(4\pi\psi(\Omega)) \ . \tag{3.22}$$

Onsager derived this term by treating the system as a mixture of different species of particles – each associated with a specific orientation Ω. In this description, the above expression results from the mixing entropy.
The particles' orientations also have to be considered in the second virial coefficient. By averaging over the orientations, we arrive at

$$B_2(T) = -\frac{1}{2V}\int d^3r \int d^3r' \int d\Omega \int d\Omega'\, \Phi(\boldsymbol{r}, \boldsymbol{r}', \Omega, \Omega') \ , \tag{3.23}$$

where Φ is the Mayer function

$$\Phi(\boldsymbol{r}, \boldsymbol{r}', \Omega, \Omega') = \exp\left(-\beta u_{\mathrm{hc}}(\boldsymbol{r}, \boldsymbol{r}', \Omega, \Omega')\right) - 1 \ . \tag{3.24}$$

Since we consider a hard-core potential that is either infinite or 0, the Mayer function is in this case -1 for overlapping particles and 0 otherwise. Using Eq. (3.19), this allows us to evaluate the volume integrals reducing B_2 to

$$B_2 = L^2 d \int d\Omega \int d\Omega' \, \psi(\Omega)\psi(\Omega')|\sin\gamma| \ , \tag{3.25}$$

where γ is the angle between Ω and Ω'.
With the above expressions, the free energy density is now

$$\begin{aligned} \beta f[\psi(\Omega)] = \rho\left(\ln\rho\Lambda^3 - 1\right) + \rho \int \psi(\Omega)\ln(4\pi\psi(\Omega))\, d\Omega \\ + \rho^2 L^2 d \iint \psi(\Omega)\psi(\Omega')|\sin\gamma|\, d\Omega\, d\Omega' + \mathcal{O}(\rho^3) \ . \end{aligned} \tag{3.26}$$

We see that f is a functional of the orientational distribution function $\psi(\Omega)$. In order to study the system's phase behaviour, we have to minimise f with respect to $\psi(\Omega)$ for fixed density ρ. At this point, we recognise that this theory can be identified as an example for classical density functional theory for an inhomogeneous liquid. However, the inhomogeneity is not in the spatial density distribution $\rho(\boldsymbol{r})$ as presented in Section 3.1.3. Instead, the particles' orientations are distributed inhomogeneously.
Onsager's approach to the minimisation was choosing a trial function

$$\psi(\Omega) = \frac{\alpha\cosh(\alpha\cos\vartheta)}{4\pi\sinh\alpha} \ , \tag{3.27}$$

with the variational parameter α and then minimising f with respect to this parameter. The particles' orientation is expressed by the relative angle ϑ in relation to the director instead of the spatial angle Ω. This is possible since we have rotational symmetry around the director in a nematic system.
The available results for the phase transition are expressed in terms of the concentration $c = Ld^{-1}\phi$ with ϕ being the volume fraction occupied by the particles. The free energy density always has a minimum for $\alpha_I = 0$ which corresponds to the isotropic phase. A second minimum $\alpha_N > 0$ corresponding to the nematic phase can be found for $c > 4$. Since this bifurcation is discontinuous, phase coexistence of the isotropic and the nematic phase occurs. The concentrations of the coexisting phases are $c_I = 3.34$ and $c_N = 4.49$.

Isotropic-nematic phase transition in 2D

The Onsager theory can also be applied to a two-dimensional system of infinitely thin rods which was presented by Kayser and Raveché [173]. Using a bifurcation analysis, the authors found that the transition is continuous in two dimensions instead of first order as in three dimensions. The transition density can be derived as $\rho = \frac{3\pi}{2L^2}$. However, the authors pointed out that this result should be viewed as "merely suggestive rather than conclusive" because of the approximations made. The Onsager theory neglects terms of higher than second order in the virial expansion which is not justified in two

dimensions.
In fact, simulations of such infinitely thin hard rods have shown a continuous isotropic-nematic transition of the Kosterlitz-Thouless type[1] at a density $\rho = \frac{7}{L^2}$ [175].

3.1.5 Brownian Motion

Small particles such as dust particles or pollen have been observed to move in a fluid medium even though they are unable to propel themselves forward. This so-called Brownian motion results from interactions with the even smaller molecules within the medium. These move due to thermal fluctuations and as a result collide with the particle. Brownian motion can be described as a stochastic process using a macroscopic approach – meaning the derived equations are valid only on macroscopic length scales and time scales. The first option is to derive the macroscopic equation of motion from the diffusion equation which yields the Smoluchowski equation. The second option is using the Langevin equation, i.e., the microscopic equation of motion of a single particle. Following the book "The Theory of Polymer Dynamics" by Masao Doi and Sam Edwards [176] and a review article by Romanczuk et al. [19], both approaches will be outlined here.

The Smoluchowski equation can be derived from the thermodynamics of diffusion processes which we will first carry out in one dimension and then generalise to multiple degrees of freedom. In one dimension, the particle concentration $c(x,t)$ is a function of the position x and the time t. In the presence of an external potential $U(x)$, the particle current j is given by Fick's law:

$$j(x,t) = -D\frac{\partial c}{\partial x} + cv(x) \ , \tag{3.28}$$

with the diffusion constant D which is a measure for the speed of diffusion due to inhomogeneous concentration. In the second term, v denotes the speed resulting from the force U exerts on a single particle. This force is usually weak, so v can be written as a linear function of the force:

$$v(x) = -\frac{1}{\gamma}\frac{\partial U}{\partial x} \ . \tag{3.29}$$

The friction coefficient γ determines a single particle's speed in response to an external force. In combination with the continuity equation

$$\frac{\partial c}{\partial t} = -\frac{\partial j}{\partial x} \ , \tag{3.30}$$

we get the diffusion equation

$$\frac{\partial c}{\partial t} = \frac{\partial}{\partial x}\left(D\frac{\partial c}{\partial x} + \frac{1}{\gamma}c\frac{\partial U}{\partial x}\right) \ . \tag{3.31}$$

We can now make use of the Einstein relation

$$D = \frac{k_B T}{\gamma} \ , \tag{3.32}$$

[1] The Kosterlitz-Thouless transition is a phase transition in the two-dimensional XY-model which features a disclination unbinding mechanism [174].

which follows from the facts that in equilibrium, c is given by the Boltzmann distribution and the particle current must vanish. It allows us to replace the D in the diffusion equation which yields

$$\frac{\partial c}{\partial t} = \frac{\partial}{\partial x}\frac{1}{\gamma}\left(k_B T\frac{\partial c}{\partial x} + c\frac{\partial U}{\partial x}\right) \ . \tag{3.33}$$

This is the one-dimensional Smoluchowski equation describing the time evolution of the particle concentration c under the influence of thermal fluctuations and an external potential.
When dealing with multiple degrees of freedom x_α, we have to take into account that each of them may be associated with a different friction coefficient and diffusion constant. The components of the particles' velocity can be written as

$$v_\alpha = \sum_\beta \Gamma_{\alpha\beta}\frac{\partial U}{\partial x_\beta} \ , \tag{3.34}$$

where the matrix $\boldsymbol{\Gamma}$ contains the friction coefficients. The diffusive contribution to the particle current contains a similar matrix $\boldsymbol{D}$ and the Einstein relation becomes

$$D_{\alpha\beta} = \frac{k_B T}{\Gamma_{\alpha\beta}} \ . \tag{3.35}$$

Instead of the concentration, we now use the normalised probability distribution function $P(\{x_\alpha\}, t)$ for which the Smoluchowski equation reads:

$$\frac{\partial P}{\partial t} = \sum_{\alpha,\beta}\frac{\partial}{\partial x_\alpha}\Gamma_{\alpha\beta}\left(k_B T\frac{\partial P}{\partial x_\beta} + P\frac{\partial U}{\partial x_\beta}\right) \ . \tag{3.36}$$

The Smoluchowski equation does not tell us anything about single particles' trajectories. Instead, it gives a deterministic prediction of the particle concentration and therefore the probability of finding a particle at a position $\boldsymbol{r}$ at time t.

In the second approach, we start from Newton's equation of motion for a single particle in a medium. For a spherical particle of mass m at position $\boldsymbol{r}$ which is subject to an external potential U and a drag force according to Stokes' law, this is

$$m\frac{d^2\boldsymbol{r}}{dt^2} = -\gamma_{\text{sph}}\frac{d\boldsymbol{r}}{dt} - \boldsymbol{\nabla}U(\boldsymbol{r}) \ , \tag{3.37}$$

with γ_{sph} being the friction coefficient. Now, we also want to take into account the interaction between the solvent's molecules and a particle in solution. We do this by adding a stochastic random force $\boldsymbol{F}_{\text{th}}$. This gives the Langevin equation

$$m\frac{d^2\boldsymbol{r}}{dt^2} = -\gamma_{\text{sph}}\frac{d\boldsymbol{r}}{dt} - \boldsymbol{\nabla}U(\boldsymbol{r}) + \boldsymbol{F}_{\text{th}} \ , \tag{3.38}$$

which is named after Paul Langevin who originally suggested this approach [177].
It was shown that $\boldsymbol{F}_{\text{th}}$ can be modelled as Gaussian distributed with an average

$$\langle \boldsymbol{F}_{\text{th}} \rangle = 0 \ , \tag{3.39}$$

and the correlation between two of its components $F_{\mathrm{th},i}$ and $F_{\mathrm{th},j}$ at times t and t'

$$\langle F_{\mathrm{th},i}(t)F_{\mathrm{th},j}(t')\rangle = 2k_BT\gamma_{\mathrm{sph}}\delta_{ij}\delta(t-t') \ . \tag{3.40}$$

Since $\boldsymbol{F}_{\mathrm{th}}$ is a stochastic quantity, the particle it acts on does not follow a deterministic trajectory. The Langevin equation only allows us to calculate average properties of an ensemble of different trajectories. One example for such a quantity is the mean squared displacement $\langle r^2\rangle$ in the absence of an external potential. We can calculate it by first taking the scalar product of the Langevin equation with $\boldsymbol{r}$ and rewriting it as

$$\frac{m}{2}\frac{d^2}{dt^2}r^2 + \frac{\gamma_{\mathrm{sph}}}{2}\frac{d}{dt}r^2 - m\left(\frac{d\boldsymbol{r}}{dt}\right)^2 = \boldsymbol{r}\cdot\boldsymbol{F}_{\mathrm{th}} \ . \tag{3.41}$$

Calculating the ensemble average of this equation, we arrive at

$$\frac{m}{2}\frac{d^2}{dt^2}\langle r^2\rangle + \frac{\gamma_{\mathrm{sph}}}{2}\frac{d}{dt}\langle r^2\rangle - m\langle\dot{\boldsymbol{r}}^2\rangle = 0 \ . \tag{3.42}$$

The right hand side is 0 because the particle's position and the random force are uncorrelated, and the average of $\boldsymbol{F}_{\mathrm{th}}$ is zero. Since we assume the molecules in the medium to be in equilibrium, we can apply the equipartition theorem and rewrite the third term on the left hand side of the equation:

$$m\langle\dot{\boldsymbol{r}}^2\rangle = 3k_BT \ . \tag{3.43}$$

This turns the above equation into an inhomogeneous differential equation in $\langle r^2\rangle$:

$$m\frac{d^2}{dt^2}\langle r^2\rangle + \gamma_{\mathrm{sph}}\frac{d}{dt}\langle r^2\rangle = 6k_BT \ . \tag{3.44}$$

Assuming $\boldsymbol{r}(t=0)=0$, this is solved by

$$\langle r^2(t)\rangle = \frac{6k_BT}{\gamma_{\mathrm{sph}}}\left[t+\tau\left(\exp\left(-\frac{t}{\tau}\right)-1\right)\right] \tag{3.45}$$

with $\tau = \frac{m}{\gamma_{\mathrm{sph}}}$. We see that the particle's motion is ballistic on small time scales since

$$\langle r^2\rangle \approx \frac{3k_BT}{m}t^2 \ , \quad t \ll \tau \ , \tag{3.46}$$

and diffusive on long time scales:

$$\langle r^2\rangle \approx \frac{6k_BT}{\gamma_{\mathrm{sph}}}t \ , \quad t \gg \tau \ . \tag{3.47}$$

Here, we can identify the diffusion constant

$$D = \frac{k_BT}{\gamma_{\mathrm{sph}}} \ , \tag{3.48}$$

which is again the Einstein relation, see Eq. (3.32).
In the diffusive regime $t \gg \tau$, the inertial term can be neglected as it becomes very small compared to the drag term:

$$\left|m\frac{d^2\boldsymbol{r}}{dt^2}\right| \ll \left|\gamma_{\mathrm{sph}}\frac{d\boldsymbol{r}}{dt}\right| \ , \tag{3.49}$$

This is also called the overdamped limit since it is equivalent to γ_{sph} being very large. In this limit, the Langevin equation becomes

$$\gamma_{\text{sph}} \frac{d\boldsymbol{r}}{dt} = -\boldsymbol{\nabla} U(\boldsymbol{r}) + \boldsymbol{F}_{\text{th}}(t) \ . \tag{3.50}$$

This important special case of particle motion is referred to as Brownian dynamics. It is valid for bacteria and small micro-swimmers, and can therefore be implemented in computer simulations when these kinds of particles are studied.
Also, the probability distribution of the trajectories $P(\boldsymbol{r}(t))$ is the solution of the Smoluchowski equation which demonstrates the equivalence of both approaches.

Brownian dynamics for active rodlike particles

Above, the Langevin equation for a spherical particle in the limit of Brownian dynamics has been derived. For a rodlike particle, this equation has to be modified to account for its anisotropic shape. We will derive the relevant equations here following articles regarding systems similar to those studied in this work [14, 142, 145–147]. Since the subject of this chapter are two-dimensional systems, we will restrict the derivation to two dimensions.
The first thing to consider when deriving the Langevin equation for a rodlike particle is how to define its configuration. Due to the rod's anisotropic shape, we need to take into account its orientation in addition to its position in space. We denote the particle's orientation by a unit vector in the x-y-plane

$$\hat{\boldsymbol{u}} = \begin{pmatrix} \cos\varphi \\ \sin\varphi \end{pmatrix} \ , \tag{3.51}$$

with φ being the angle between the system's x-axis and the particle's main axis. It is also useful to express its velocity $\boldsymbol{v} = \dot{\boldsymbol{r}}$ as a sum of two velocities $\boldsymbol{v}_{\parallel}$ and $\boldsymbol{v}_{\perp}$ along and perpendicular to $\hat{\boldsymbol{u}}$ respectively:

$$\boldsymbol{v} = \boldsymbol{v}_{\parallel} + \boldsymbol{v}_{\perp} \ . \tag{3.52}$$

The particle's anisotropy causes it to respond to an external force $\boldsymbol{F}$ dependent on the direction of this force relative to the particle's orientation. Instead of one isotropic friction coefficient as for spherical particles, we need two friction coefficients: $\gamma_{\parallel}$ determines the particle's response to a force acting along $\hat{\boldsymbol{u}}$, and $\gamma_{\perp}$ is the equivalent for perpendicular forces. The relation between $\boldsymbol{F}$ and the particle's resulting velocity is then

$$\boldsymbol{F} = \gamma_{\parallel} \boldsymbol{v}_{\parallel} + \gamma_{\perp} \boldsymbol{v}_{\perp} \ . \tag{3.53}$$

The friction coefficients can be calculated as [176]

$$\gamma_{\parallel} = \frac{2\pi\eta L}{\ln(L/d)} \ , \qquad \gamma_{\perp} = \frac{4\pi\eta L}{\ln(L/d)} \ , \tag{3.54}$$

with η being the medium's viscosity, L the rod's length and d its diameter.
Due to this anisotropy, we also have to introduce two separate stochastic forces parallel

and perpendicular to the rod which we will denote as $\boldsymbol{\xi}_\parallel$ and $\boldsymbol{\xi}_\perp$. These are Gaussian distributed with

$$\langle \boldsymbol{\xi}_\alpha \rangle = 0 \ , \qquad \langle \boldsymbol{\xi}_\alpha(t) \boldsymbol{\xi}_\beta(t') \rangle = 2 k_B T \gamma_\alpha \delta_{\alpha\beta} \delta(t - t') \ , \tag{3.55}$$

where $\alpha, \beta = \{\parallel, \perp\}$. It should be noted that the above form of the noise terms assumes that the Einstein relation is valid which is not generally the case in active systems, so treating noise and friction as correlated is an approximation [14].
Next, we also have to take into account rotation. The particle is subject to torques resulting from the external potential U as well as thermal fluctuations. Since we consider a two-dimensional system, only in-plane rotations are possible which means all relevant torques can be expressed as vectors parallel to the z-axis. Hence, we will just write all torques as scalars.
Analogously to the stochastic forces $\boldsymbol{\xi}_\parallel$ and $\boldsymbol{\xi}_\perp$, we can introduce a stochastic torque ξ_{rot}. This is also Gaussian distributed:

$$\langle \xi_{\mathrm{rot}} \rangle = 0 \ , \qquad \langle \xi_{\mathrm{rot}}(t) \xi_{\mathrm{rot}}(t') \rangle = 2 k_B T \gamma_{\mathrm{rot}} \delta(t - t') \ . \tag{3.56}$$

Here, γ_{rot} is the rotational friction coefficient which determines the particle's angular velocity in response to an external torque τ:

$$\dot{\varphi} = \frac{1}{\gamma_{\mathrm{rot}}} \tau \ . \tag{3.57}$$

For a rodlike particle rotating around an axis perpendicular to its main axis, γ_{rot} can be shown to be approximately [176]

$$\gamma_{\mathrm{rot}} = \frac{\pi \eta L^3}{3 \ln(L/d)} \ . \tag{3.58}$$

Since we want to consider an active particle, we have to include another force in the Langevin equation. This is an internal force $\boldsymbol{f}_0$ acting along the particle's main axis causing self-propulsion with a velocity $\boldsymbol{v}_0$:

$$\boldsymbol{v}_0 = \gamma_\parallel^{-1} \boldsymbol{f}_0 \ . \tag{3.59}$$

Considering all of the above, we now have the Langevin equations for the particle's angular velocity $\dot{\varphi}$ and velocity $\boldsymbol{v}$:

$$\begin{aligned} \boldsymbol{v}_\parallel &= \gamma_\parallel^{-1} \left[- \left(\boldsymbol{\nabla} U(\boldsymbol{r}) \right)_\parallel + \boldsymbol{f}_0 + \boldsymbol{\xi}_\parallel \right] \ , \\ \boldsymbol{v}_\perp &= \gamma_\perp^{-1} \left[- \left(\boldsymbol{\nabla} U(\boldsymbol{r}) \right)_\perp + \boldsymbol{\xi}_\perp \right] \ , \\ \dot{\varphi} &= \gamma_{\mathrm{rot}}^{-1} \left[\tau_U + \xi_{\mathrm{rot}} \right] \ . \end{aligned} \tag{3.60}$$

Here, τ_U is the torque resulting from the external potential U. The above equations can be used in agent-based simulations to calculate the particles' trajectories.

3.1.6 Focus and outline of this chapter

The existence of the common phenomena mentioned in the introduction to this section gives rise to the question whether it is possible to universally describe some properties of active matter independently of the microscopic details. This would allow controlling

the formation of structures in active systems or utilising some of their specific functions. However, such a theory does not exist at this point in time [17]. As a result, there are few well-established approaches to describing active matter, and a lot of exploratory research is being done. In this context, this work studies two aspects regarding self-propelled rodlike particles: swirling and phase separation with the main focus being the latter. The two phenomena are studied in Brownian dynamics simulations of self-propelled rodlike particles in two dimensions as described in Section 3.1.5. One typical representative of active rodlike particles are swarming cylindrically shaped bacteria like E. coli or B. subtilis – see Section 1.2.2.
As will be described in more detail in Section 3.2.4, the occurrence of collectively moving circular patterns has been reported repeatedly in experiments [109, 110, 124–126] but rarely in simulations. Exceptions to this were simulations of particles that naturally moved along curved trajectories [124, 126], particles with hydrodynamic interactions [137, 155], and particles with an explicit aligning interaction [153]. This chapter aims to find out whether rotating structures can emerge when a simple model of straight-moving particles with steric interactions is used.
Phase separation has been studied extensively as will be outlined in Section 3.2.5, and for active spherical particles, a theoretical framework predicting the coexisting densities has been presented by Cates and Tailleur [178]. They successfully mapped the coarse-grained dynamics of these systems onto a passive fluid with attractive interactions. Phase separation also occurs in systems of active rodlike particles in several forms from the formation of asters [140, 142, 146, 151, 179] to collectively moving clusters [28, 125, 141–143, 147]. These configurations have in common that they consist of an ordered high-density phase and an unordered low-density phase. To the author's knowledge, a theory predicting the coexisting densities in systems of active rodlike particles is nonexistent at this point. Hence, this work will try to find an analytical model predicting the coexisting densities by adapting successful approaches for spherical particles.
The outline of this chapter is as follows: In Section 3.2, a brief overview of some of the progress made in this field of research is given – focussing mainly on aspects most relevant to this work. In this context, analytical models describing phase separation in systems of spherical particles are introduced which will later be applied to systems of rodlike particles. In Section 3.3, details on the numerical model, the simulation routine, and the evaluation during simulation are given. Section 3.4 presents the results obtained from simulations before different approaches for describing the occurring phase separation analytically are presented in Sections 3.5 and 3.6. Finally, a conclusion of this chapter is given in Section 3.7 with a special emphasis on a critical discussion of the derived analytical models.

3.2 Studying active matter

The following section presents some of the results regarding active matter that are most relevant for this work. It should be noted that this overview is by no means complete since active matter has become an important subject of research throughout the last years, and the number of publications regarding this topic is therefore large. From the many different approaches for studying different systems, only a fraction can be discussed here.
Experimental, numerical, and analytical approaches are presented for spherical particles in Section 3.2.2 and for rodlike particles in Section 3.2.3. Next, collective phenomena

are discussed in Section 3.2.4 with a special emphasis on collective motion and phase separation.

3.2.1 Parameters

In many active systems, particle dynamics are not exclusively determined by propulsion but also influenced by diffusive processes. One parameter indicating which of these contributions is predominant is the Péclet number Pe. It is defined as the ratio of the magnitudes of these two mechanisms. Small Péclet numbers are equivalent to particles moving mainly diffusively whereas high Péclet numbers indicate that the system's dynamics are dominated by propulsion. The Péclet number is generally of the form [18]

$$Pe = \frac{v_0 \lambda}{D} \ , \tag{3.61}$$

with v_0 being the particles' propulsion speed, λ a particle's typical length scale, e.g., its radius, and a diffusion constant D. The precise form depends on the system's properties such as the relevant length scale and diffusion constant.
Two other quantities that also yields information about the particles' dynamics - specifically about the relation of diffusion compared to propulsion – are the persistence length l_p and the rotational relaxation time τ_rot. The persistence length gives the distance over which a particle's orientation becomes uncorrelated and τ_rot defines the time scale of this process. Consider an active particle in two dimensions at a time $t = 0$ with a unit vector $\hat{\boldsymbol{u}}(0)$ denoting its initial orientation. Neglecting translational diffusion, the particle's dynamics can be described as follows: as time progresses, the particle is propelled forward along its orientation while rotating diffusively. The correlation between the orientation at time t with the orientation at $t = 0$ can be shown to decay exponentially [176]:

$$\langle \hat{\boldsymbol{u}}(t) \cdot \hat{\boldsymbol{u}}(0) \rangle = \exp\left(-\frac{t}{\tau_\mathrm{rot}} \right) \ . \tag{3.62}$$

The rotational relaxation time $\tau_\mathrm{rot} = \frac{1}{2D_\mathrm{rot}}$ – with the rotational diffusion constant $D_\mathrm{rot} = k_B T \gamma_\mathrm{rot}^{-1}$ according to Eq. (3.32) – determines how rapidly the correlation decays. Hence, it defines the time scale on which the particle's trajectory can be assumed to approximately follow the initial orientation $\hat{\boldsymbol{u}}(0)$. Since the particle moves with a constant speed v_0, we can calculate the distance travelled during a timespan τ_rot to get a corresponding length scale. We call this length scale the persistence length

$$l_\mathrm{p} = v_0 \tau_\mathrm{rot} \ . \tag{3.63}$$

It can be understood as the typical distance a particle travels along a straight trajectory.

3.2.2 Spherical particles

Recalling the aforementioned examples of active matter we can find in nature, we notice that most of them are constituted of anisotropic particles. Some of these - such as biofilaments, rod-shaped bacteria, or fish – can safely be approximated as elongated particles while others exhibit even more complex geometries, e.g., cells and birds. As illustrated in Fig. 3.1 though, these systems often have similar macroscopic properties

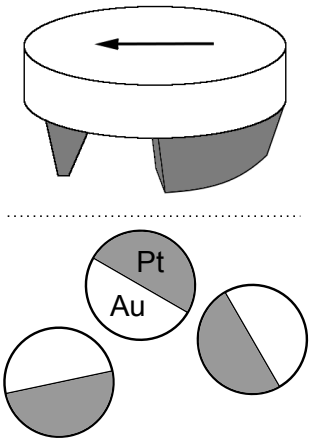

Figure 3.4: Schematic illustrations of man-made particles used in experiments of active spherical particles. Top: side view of a metallic disk with a diameter of a few millimetres that was used in experiments on a vibrating plate [108]. Since the dark grey 'leg' on the right is made of rubber and bigger than the left one, the discs are anisotropic as indicated by the arrow. This image was recreated from Ref. [132]. Bottom: top view of micrometre-sized spherical gold particles half covered in platinum. In a hydrogen peroxide solution, platinum acts as a catalyst generating propulsion [122, 123]. Similar experiments were performed with latex particles [115].

and display similar collective behaviour [14]. It is therefore fair to assume that there may be a few global principles applicable to any system of active particles regardless of the constituents' design. Hence, it makes sense to study active matter using basic systems in which the particles do not exhibit an anisotropic shape. Spherical particles are convenient for this as they have the advantage of being easy to model. Even though such systems may be hard to find in nature, valid general principles for active matter should still apply to them and therefore be possible to identify and analyse.
For simplicity, we will refer to all types of particles with rotational symmetry as spherical particles from now on – including actual spheres in three dimensional setups as well as disks or other circular shaped objects in two dimensions and point particles in simulations.

Experimental approaches

As mentioned before, systems of active spherical particles are not common in nature. Therefore, in order to generate such systems in a lab, particles have to be artificially provided with a propulsion mechanism. There are several ways of doing this, but most approaches use on of two methods – applying mechanical forces or preparing the particles in a way that they react chemically with the environment and thereby generate forces propelling themselves forward.

An example for mechanical propulsion can be found in vibrated millimetre-sized metallic disks with a built-in polar anisotropy in the form of two 'legs' of different size and materials at opposite sides [108], see also Fig. 3.4. The authors confined the particles to a quasi two-dimensional geometry in which they would move due to the vibration. The particles' anisotropic shape would determine their direction of propulsion. Besides enabling directed motion, vibration would also introduce noise into the system causing rotational diffusion.
Propulsion due to chemical reactions can be generated by using particles with an anisotropic surface. Two examples for this are spherical gold particles half covered with platinum [122, 123] and latex particles half covered with platinum [115] as shown in Fig. 3.4. These micrometre-sized particles were placed in a solution containing hydrogen peroxide. Since platinum acts as a catalyst favouring the splitting up of hydrogen peroxide into water and oxygen, this chemical reaction mostly occurs on a particle's coated side. The particle is then propelled into a specific direction likely due to dif-

fusiophoresis, i.e., motion along a gradient of pressures or chemicals [115, 122]. The same mechanism has been used with hematite cubes embedded in spheres of the polymer TPM [116]. In combination with blue light, hematite acts as a catalyst as well. The requirement of blue light makes it possible to turn particle propulsion on and off externally.
A different approach was used in experiments with micrometre-sized spherical SiO_2 particles in a near-critical mixture of water and lutidine [120, 121]. One hemisphere of these particles was coated with graphite. By illuminating the entire sample with a laser beam tuned to a wavelength absorbed by graphite, the particles' coated hemispheres were heated up. As a result, the solvent would locally cross the critical temperature causing demixing of water and lutidine which would result in a phoretic force propelling the particles forward.

Numerical and analytical descriptions

There are two related but different models that are widely used in simulations to describe the dynamics of active particles on small scales such as intracellular particles or bacteria: run-and-tumble particles (RTPs) and active Brownian particles (ABPs) [30, 180]. These models can be applied to differently shaped particles, but since they do not take into account the particles' geometry, they are most suitable for spherical ones. Both models describe the particles' dynamics as a diffusive random walk due to propulsion with a speed v_0 along an orientation axis and orientational relaxation of said axis. They assume different mechanisms causing the reorientation though. RTPs undergo so-called 'tumbles' – reorientation events of short duration compared to the straight 'runs' performed in between. The reorientation events randomly occur at a rate α and the particle's orientation before and after such an event are entirely uncorrelated. Consequently, the rotational relaxation time $\tau_{\mathrm{rot}}^{\mathrm{RTP}}$ – which is per definition the time after which the particle's orientational correlation is lost – is given as the inverse of the tumbling rate:

$$\tau_{\mathrm{rot}}^{\mathrm{RTP}} = \alpha^{-1} \ . \tag{3.64}$$

In contrast, ABPs do not reorientate via discrete events but gradually due to rotational diffusion. Hence, their orientational correlation also decays gradually, and the rotational relaxation time is proportional to the rotational diffusion constant as described in Section 3.2.1:

$$\tau_{\mathrm{rot}}^{\mathrm{ABP}} = \frac{1}{2D_{\mathrm{rot}}} \ . \tag{3.65}$$

The implementation of both models is quite similar with the main difference being the rotational diffusion. While the trajectories of ABPs can be calculated according to Brownian dynamics as outlined in Section 3.1.5, orientational relaxation of RTPs is implemented by deriving a probability for reorientation in a given timespan from their tumbling rate α [130, 181].
Simulations of spherical particles have been used to study their interactions with walls and other obstacles [120] as well as their aggregation in clusters or in a single bulk of high density within a gas-like phase – also referred to as phase separation [116, 121, 134–136]. This behaviour is noteworthy since interactions between the particles were

in most cases implemented as purely repulsive, so the aggregation does not result from attractive interactions. Instead, the particles' motility generates an effective attraction [135]. Phase separation seems to be independent of the precise form of repulsive interaction between particles as it occurs when these are implemented as a truncated Lennard-Jones potential [121, 135, 136], spring-like forces [134], as well as a hard-core potential [116].

In analytical works regarding active spherical particles, the systems' dynamics are often described via the particle density field $\rho(\boldsymbol{r})$. The time evolution of $\rho(\boldsymbol{r})$ can be derived either from the many-body Langevin equations [136] or by coarse-graining the microscopic equations of motion, i.e., the Langevin equations [134, 158, 178, 182, 183]. The resulting continuum models do not take into account that the systems they describe consist of individual particles. Still, they were successfully applied to identify an instability of the isotropic phase in such systems that would result in phase separation. Different factors have been found to be relevant for this phenomenon. For example, Bialké et al. found that a minimum particle speed was required for causing an instability of the isotropic phase [136]. Tailleur and Cates reported another condition for the particles' speed: for phase separation to occur in one dimension, the particles' speed would have to decay rapidly enough with the local density [157]. The authors also confirmed the validity of this condition in two dimensions [158]. In other works, a large enough average density has been identified as a cause for the instability of the isotropic phase resulting in phase separation [134, 178].
Besides identifying different causes for the occurrence of phase separation, continuum theories have also been used to describe the growth of the bulk domain in these systems [183] as well as predict densities of the coexisting phases [178, 183]. Analytical results regarding phase separation will be reviewed in more detail in Section 3.2.5 including a particle-based model by Redner et al. [135].
In addition to investigating phase separation, continuum models have been used to study other phenomena occurring in active matter consisting of spherical particles, e.g., sedimentation under gravity [157, 180–182] and confinement in external potentials [180, 181].

3.2.3 Rodlike particles

As mentioned before, most naturally occurring systems of active matter are constituted of elongated particles. It is therefore not surprising that a lot of research regarding active matter is done on such systems. The great advantages of experiments using naturally occurring active particles is that these are already available and the results are immediately relevant to actual systems. The latter point is also true for numerical and analytical work.

Experimental approaches

Even though active particles of all sizes ranging from micrometres (biofilaments, bacteria) to metres (sheep, fish) can be found in nature [14], most experiments focus on small particles.
On the subcellular scale, biofilaments such as actin filaments or microtubules are frequently used since their dynamics play a crucial role in a variety of cell functions. However, these particles have no propulsion mechanism themselves, so in experiments,

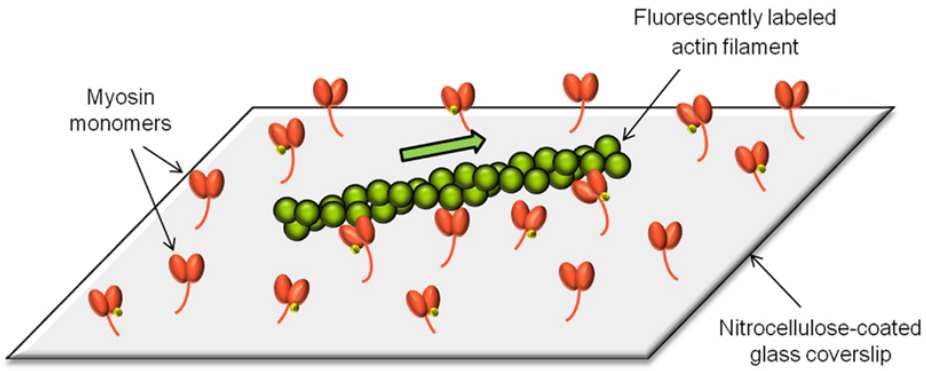

Figure 3.5: Sketch of a motility assay setup with actin filaments. The filaments are propelled forward by myosin motors attached to a glass surface. Image adapted from Ref. [186] (CC BY-NC 3.0).

motor proteins are used to drive them. In their natural environment, motor proteins move along the filaments consuming chemical energy in the form of ATP, see Section 1.2.1. This mechanism can be harnessed to propel the filaments: by fixing the motor proteins to a surface, they become immobile, so they would push the filaments forward resulting in them gliding over the surface. This class of experiments called motility assays was first described by Vale et al. for microtubules and kinesin [184] and by Kron and Spudich for F-actin and myosin motors [185]. The experimental setup is illustrated in Fig. 3.5 by the example of an F-actin motility assay. Motility assays of microtubules [124, 140, 151] and F-actin [125–128] are common examples for experimental active matter systems.

Another frequently studied type of active matter are bacteria colonies. Bacillus subtilis and Escherichia coli are two examples of bacteria frequently used in experiments studying active matter. As described in Section 1.2.2, their shape is almost cylindrical making them good representatives for rodlike active particles and also easy to model in computer simulations.

Independent from the type of bacteria used, experimental setups are quite similar. Frequently, bacteria are studied in quasi-two-dimensional geometries – either by creating a stretched droplet of fluid in which the bacteria would swim [162], growing bacteria colonies on agar substrates [28, 106], confining them in microfluidic chambers which are not high enough to allow bacteria to swim over each other [143], or by simply limiting analysis to bacteria moving close to a surface of the chamber containing the solution [118]. In addition to these examples, bacteria solutions have also been studied in three dimensions [27, 29, 143]. Since they are inherently able to move, bacteria dynamics can be studied without providing them with an external propulsion mechanism as is required for biofilaments in motility assays.

Active systems of rodlike particles have also been studied using experimental setups with man-made particles. These are mostly analogous to those for spherical particles described in Section 3.2.2. Systems of elongated particles on a vibrating plate have been realised using a wide variety of different particles including different types of rice or metallic pins [109, 112], cylindrical particles composed of nylon and steel with an anisotropic mass distribution [110], or polymer rods made of a composite of different plastics [113]. The length of these particles ranged from a few hundred micrometres

to centimetres. Setups in which chemical reactions were harnessed to propel rodlike particles have also been used – one recurring example being Au-Pt rods in a solution containing hydrogen peroxide [117–119]. These rods with a length in the micrometre range would move along their axis toward their platinum end due to the previously explained catalytic effect of platinum for the splitting of hydrogen peroxide.

Numerical and analytical descriptions

A variety of different models and algorithms have been used to simulate systems of active rodlike particles. Even though these various approaches have similarities, they differ, among other things, in how the particles are modelled, how they interact, and how they are propelled forward.
As described in Section 3.1.4, the excluded volume interaction between rodlike particles causes them to align – ultimately leading to nematic order at large densities. One of the most basic models capturing this intrinsic aligning mechanism are point particles with an explicit aligning interaction [131, 133]. The particles' dynamics were implemented via Brownian dynamics as outlined in Section 3.1.5 with self-propulsion resulting from a constant force acting on each particle along its orientation. Even though the particles in this model are points instead of rods, the alignment interaction causes them to behave very similarly to rodlike particles, e.g., exhibiting collective motion in bands, lanes, or clusters – see Section 3.2.4.
A more common method of simulating rodlike particles is not implementing explicit aligning interaction. Instead, particles are modelled as rods with a fixed length and width and steric interactions between them that would indirectly cause alignment. Usually, interactions betweeen the rods are calculated by discretising them into a number of spherical beads. Different methods have been used to implement steric interactions including contact forces between viscoelastic beads [110, 113], a repulsive Yukawa potential [141, 143, 146], and a Lennard-Jones potential [142, 147]. In most works, the particles' trajectories were calculated according to Brownian dynamics with self-propulsion resulting from a constant force along the particles' orientation. One exception to this has been presented by Kudrolli et al. who used random propulsion forces instead [110].
In some cases, the systems' components were modelled in even more detail, e.g., when simulating motility assays. For example, Kraikivski et al. performed such simulations not only taking into account the rods' shape and interactions but also explicitly modelling the motor proteins' dynamics and interactions with the rods [179]. Another example for simulations including the growing and shrinking dynamics of individual rods and crosslinking processes caused by crosslinking proteins was presented by Nédélec et al. [140].
All the works mentioned so far involved Brownian dynamics simulations in two spatial dimensions, but it should be noted that this is not the only conceivable approach to simulating active rodlike particles. One different method for simulating motility assays has been been employed by Schaller et al. [125]. They modelled the filaments as random walkers on a hexagonal lattice in two spatial dimensions with steric repulsion and aligning interactions.

The analytical approaches used to investigate systems of active rodlike particles are very similar to those for spherical particles outlined in Section 3.2.2. Systems are

mostly studied on a coarse-grained level using the continuous particle density field $\rho(\boldsymbol{r})$ instead of dealing with individual particles.
One powerful and widely used method in this regard is dynamical density functional theory (DDFT) which is an extension of classical density functional theory (cDFT) as introduced in Section 3.1.3. While cDFT yields equilibrium properties of inhomogeneous systems, DDFT describes nonequilibrium dynamics of these systems. Based on DDFT for spherical particles, Rex et al. derived this method for uniaxial anisotropic particles [187]. Starting from the Smoluchowski equation, they derived an equation of motion for density field $\rho(\boldsymbol{r}, \boldsymbol{u}, t)$ which is a function of the position in space $\boldsymbol{r}$ and the orientation $\boldsymbol{u}$. Approximating two unknown terms in the resulting equation by their averages in equilibrium yielded the time evolution of $\rho(\boldsymbol{r}, \boldsymbol{u}, t)$. As stated by the authors, this approximation has shown to be justified for spherical particles "even for strong inhomogeneities and strong time dependencies" which is an indication that it is valid also for anisotropic particles. This method has been applied in several works studying active systems of rodlike particles in confinement or external fields [146, 187]. Also, it has been generalised even further by Wittkowski and Löwen to describe biaxial particles as well [188].
A different formalism has been presented by Baskaran and Marchetti who derived equations for the collective dynamics of self-propelled rods with excluded volume interactions [189, 190]. Starting from the microscopic dynamics described by the Langevin equations, they derived the according Smoluchowski equation in an effective mean-field description. Using coarse-graining, they arrived at equations describing the time evolution of the system's "slow variables" which are density ρ, polarization vector $\boldsymbol{P}$, and nematic alignment tensor $\boldsymbol{Q}$. These equations give the system's dynamics on macroscopic time and length scales. Alternatively, they can also be derived phenomenologically from symmetry considerations [191, 192]. Baskaran and Marchetti used the equations to find the system's steady states – an isotropic state and a nematic liquid crystal [189]. A stability analysis with regards to fluctuations showed that density fluctuations can lead to propagating waves in the isotropic state and mass inhomogeneities in the nematic state. The authors also pointed out that a state of global polar order does not exist despite the polarity of the particles. The reason is that the considered excluded volume interaction is apolar and can therefore not generate polar order. In other works, the macroscopic equations were used to predict the formation of polar clusters [191] or lanes [192].
Of course, the above summary is not conclusive – a large number of other theories for describing active matter have been presented in the literature. The interested reader may find further information in recent review articles [14, 19].

3.2.4 Collective dynamics

The following section presents some collective phenomena that frequently occur in active systems consisting of all kinds of different components and that are relevant to this work. Collective phenomena include static particle aggregation with and without confinement as well as collectively moving structures. These phenomena have in common that they consist of an unordered low-density phase and a high-density phase that in most cases exhibits some kind of orientational order. The resulting non-uniform density distributions can be understood as different realisations of phase separation which is the main focus of this chapter.

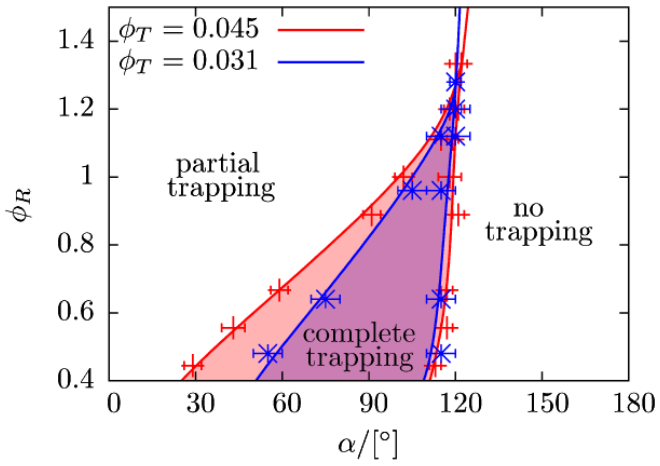

Figure 3.6: Phase diagram for capturing self-propelled rods in a static chevron-shaped trap. The phases representing no trapping, partial trapping, and complete trapping are plotted for two different area fraction covered by the trap ϕ_T. The axes indicate the trap's opening angle α and the quantity ϕ_R that is the ratio of particle density relative to ϕ_T. Up to an opening angle $\alpha > 120°$, larger opening angles favour trapping. Reprinted with permission from Ref. [145]. Copyright 2012 American Physical Society.

The outline of this section is as follows. First, particle aggregation in systems with and without confinement is discussed in Sections 3.2.4 and 3.2.4. Then, three examples of collective motion – lanes, clusters, swirls – are presented in Section 3.2.4. Finally, an introduction to works regarding phase separation in systems of active spherical particles is given in Section 3.2.5.

Confined geometries

One of the most basic ways of controlling active particles is capturing them in a specific location. Obviously, this requires an understanding of how they can be manipulated into aggregating in the desired location. Therefore, there has been some interest in investigating how obstacles and confinement can be used to achieve accumulation of active particles.

One example for capturing self-propelled rods in a static chevron-shaped trap has been reported by Kaiser et al. [145]. In simulations, the authors varied the trap's opening angle α and covering area as well as the particle density. Depending on these parameters, no trapping, partial trapping, or complete trapping would occur. The authors found that lower particle densities, larger traps, and larger opening angles would favour the trapping of particles. However, traps with an opening angle $\alpha > 120°$ would not capture any particles. The resulting phase diagram is shown in Fig. 3.6.

Similar simulations with moving traps display even more complex behaviour in that the number of captured particles becomes additionally dependent on the traps' velocity [193]. These results demonstrate that chevron-shaped edges can very effectively cause active particles to accumulate. This is especially relevant for self-propelled rods in confined geometries: since the confinement can be understood as a sequence of adjoining traps, we can expect the rods to accumulate near the edges given the right conditions. A related analytical study of self-propelled point-like particles in a two-dimensional

confined geometry has been presented by Fily et al. [194]. The authors considered non-interacting particles that were subject to rotational diffusion in a convex container. In containers that were small compared to the particles' persistence length, they derived an analytical expression for the particle density ρ at the container's boundary and found that particles would accumulate in regions of high local curvature. The authors also transferred their results to polygonal boxes in which the corners' opening angles would determine the density. Analogous to curved boundaries where high curvature would attract particles, corners with small opening angles would attract particles in polygonal boxes. These results were also confirmed in simulations. The authors' findings regarding polygonal boxes seem to contradict the results reported by Kaiser et al. indicating that larger angles should attract more particles. However, there is a fundamental difference in the two models: in systems with a single trap as considered by Kaiser et al., particles can avoid the trap which is likely when its opening angle is small. In a polygonal box as considered by Fily et al., particles avoiding one corner would run into a different one instead.
Particle accumulation was also observed at straight boundaries. In simulations of self-propelled rods in a two-dimensional channel, Wensink and Löwen found that particles would form semicircular hedgehog-like clusters at the channel walls [146]. The authors were able to correctly predict the formation and growth of these clusters using an analytical model derived from the Smoluchowski equation. In the context of the previously described findings, these results indicate that confinement aids the aggregation of active particles regardless of its exact form. However, the confinement's geometry still determines the extent of particle accumulation.

Asters

As described above, immobile clusters have been found to develop in systems of self-propelled rods in confinement. Walls and edges apparently support the formation of cluster nuclei. However, simulations and experiments with comparable systems have demonstrated that immobile clusters can also form without walls or edges aiding particle accumulation. Numerous publications have reported the formation of immobile clusters in systems of active spherical particles [116, 121, 133, 135, 136, 159], but we will mainly focus on rodlike particles here as these are more relevant for this work. The microscopic details vary among the systems presented here, so it is not easy to identify general mechanisms that cause particle accumulation.
In experiments using biofilaments and motor protein complexes acting as crosslinkers between filaments, microtubules were found to form asters under specific experimental conditions [140, 151]. Surrey et al. reported that for two different motor protein complexes, microtubules organized in asters when the motor concentration was sufficiently high [151]. In according simulations, the authors confirmed this observation and identified a second parameter affecting the formation of asters: a larger number of filaments would be incorporated in asters when motors were travelling a longer distance along the filaments before detaching. A similar finding has been reported by Kraikivski et al. [179] who simulated motility assays as described in Section 3.2.3. They found that large detachment forces for the motors – which imply long-lasting attachment – resulted in the formation of immobile clusters.

The formation of asters was also observed in very minimalistic simulations of self-propelled point particles by Farrell et al. [133] – see Fig. 3.7 for a snapshot. In order

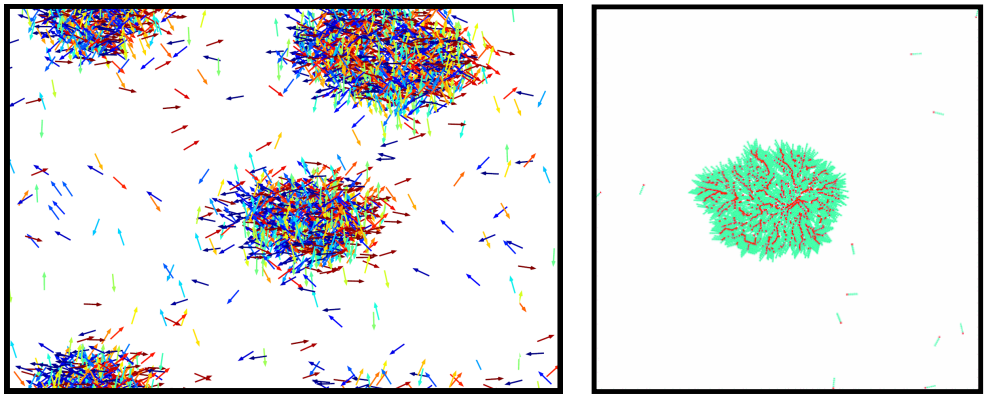

Figure 3.7: Simulation snapshots showing aster formation. Left: static asters in a simulation of self-propelled point particles with explicit aligning interaction. Arrows as well as colour-coding indicate the particles' orientations. Reprinted in part with permission from Ref. [133]. Copyright 2012 American Physical Society. Right: an immobile cluster in a simulation of self-propelled rods with repulsive interactions. Red dots indicate the particles' front ends. Reprinted with permission from Ref. [142]. Copyright 2010 American Physical Society.

to mimic rodlike particles, the authors implemented an explicit aligning interaction and a propulsion speed that decays exponentially with local particle density. They did not consider excluded volume interactions though. Depending on the simulation parameters, they found different patterns such as bands, lanes, mobile clusters, and asters. Asters would form at rapidly decaying speeds and strong thermal fluctuations. Using a continuum theory derived from the microscopic equations of motion, the authors could reproduce the formation of asters and other patterns found in simulations.
Asters have also been found in simulations of self-propelled rodlike particles. Yang et al. simulated rods with a constant propulsion force and purely repulsive interactions and observed the formation of giant immobile clusters [142] as shown in Fig. 3.7. These would form at high particle density and low thermal noise. Increased noise was found to result in the formation of smaller mobile clusters which seems to contradict the findings by Farrell et al. who reported that strong thermal fluctuations were required for the formation of asters [133]. The explanation for this could be an aspect that was addressed by Yang et al. when comparing their results to those of Peruani et al. [144] and Kraikivski et al. [179]. They concluded that the particles' aspect ratio and interactions are crucially important in that "longer rods and shorter-range interaction [favour] the giant-cluster formation". Considering this and recalling that Farrell et al. simulated point particles without excluded volume interactions, it is not surprising that the particles in the two models would form asters under different conditions. Also, the authors implemented a model in which the particles' speed only depended on local density but not on the particles' orientation which should significantly affect their collective behaviour.
In a more recent publication, Yang et al. reported another factor that would affect the formation of asters [153]. Using a continuum model with a density-dependent motility and an explicit aligning interaction, they found that pattern formation was controlled by the alignment strength with the formation of asters occurring when alignment was weak.

We can conclude that asters form in different active systems, but the constituents' properties determine the conditions required for aster formation. In motility assays, the concentration and dynamics of motors was found to be important. In simulations of self-propelled particles, the particles' properties such as aspect ratio and interactions were identified as the main factors controlling the formation of asters. Thermal noise was also found to be a relevant factor, but its influence seems to be different depending on the simulated model.

Collective motion

Reported findings of collective motion in active matter range from seemingly simple structures such as bands or waves [125, 131–133] over collectively moving clusters [28, 108, 125, 130, 132, 133, 141–143, 147] and rotating patterns [108–110, 124–126, 137, 153–155] to complex configurations such as lattices of vortices [124]. Illustrations of these structures are shown in Fig. 3.8.
In all of the above examples, the orientation of a single particle within a collectively moving structure varies only slightly compared to other particles in its immediate surrounding. If this was not the case, the observed structures would disassemble as the contained particles would move into different directions. It is therefore necessary that some kind of interaction exists that causes non-aligned particles to align and stabilises assemblies of aligned particles. This conclusion is confirmed by simulations using particles with a rotational symmetry such as point-like particles or disks with steric interactions. Due to their geometry, "these particles cannot interchange angular momentum and thus lack a mutual alignment mechanism" [135]. This can be easily understood by considering rotation of particles in regions of high particle density – see Fig. 3.9 for an illustration. First, we consider two parallel rodlike particles of length L at a distance $x < L/2$ that are not allowed to overlap due to steric interactions. If either of the particles rotates around its centre of mass, it will at some point be hindered by the other since their distance is smaller than half of their length. As described in Section 3.1.4, this excluded volume interaction ultimately leads to nematic order in dense systems of rodlike particles. The above is not true for particles with rotational symmetry. No matter how small the distance between them is, rotation will not lead to overlapping. Hence, steric interactions do not result in an indirect aligning interaction for particles with rotational symmetry.

As a result of this absence of an inherent alignment mechanism, none of the simulations and experiments of spherical particles exhibit collective motion[2] [116, 121, 135, 136]. However, when introducing explicit aligning interactions, collective motion can be observed in simulations of systems with such particles [124, 130–133, 138]. Therefore, we can conclude that aligning interactions are a necessary requirement for collective motion.
For rodlike particles, steric interactions are sufficient to yield alignment as is demonstrated by the nematic ordering of passive thin rods described in Section 3.1.4. It is therefore not surprising to discover that active rodlike particles exhibit collective motion without an explicit aligning interaction. Previous works have demonstrated a wide variety of collectively moving structures such as bands [125], clusters [28, 125, 141–143,

[2] An exception to this was presented by Weber et al. [132], but the authors modelled particle collisions explicitly which resulted in an effective alignment interaction.

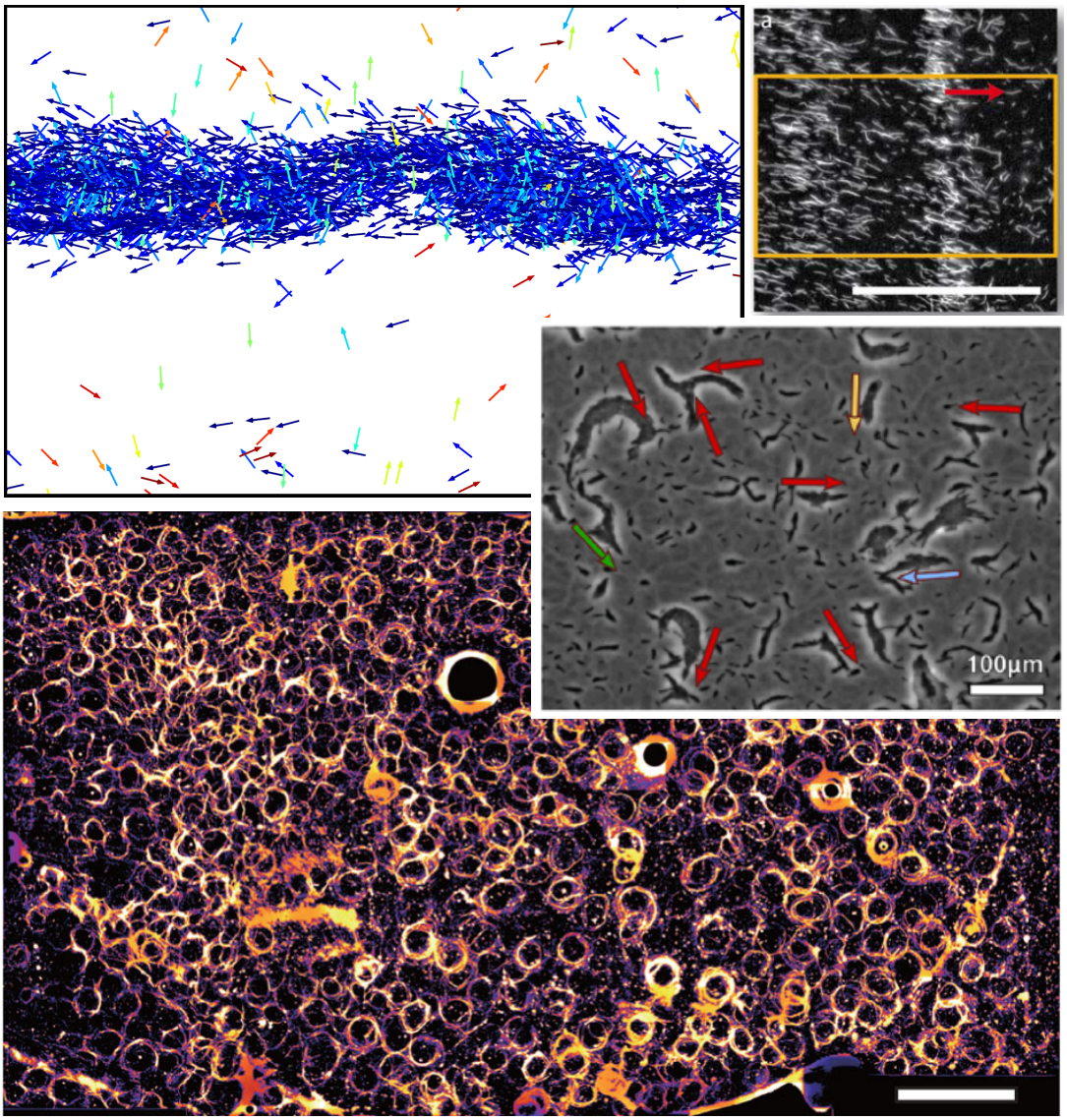

Figure 3.8: Examples of different types of collective motion in systems of active rodlike particles. Top left: lane pattern in a simulation of self-propelled point particles with explicit aligning interaction. Arrows as well as colour-coding indicate the particles' orientations. Reprinted in part with permission from Ref. [133]. Copyright 2012 American Physical Society. Top right: Density wave in a motility assay of fluorescently labelled actin filaments. The scale bar is 50 μm, and the red arrow indicates the wave's direction of motion. Reprinted with permission from Ref. [125]. Copyright 2010 Nature Publishing Group. Centre right: Collectively moving clusters of myxobacteria on an agar substrate. The scale bar is 100 μm, and the arrows indicate the clusters' directions of motion. Reprinted with permission from Ref. [106]. Copyright 2012 American Physical Society. Bottom: Lattice of vortices in a motility assay of fluorescently labelled microtubules. The scale bar is 2 mm. Reprinted with permission from Ref. [124]. Copyright 2012 Nature Publishing Group.

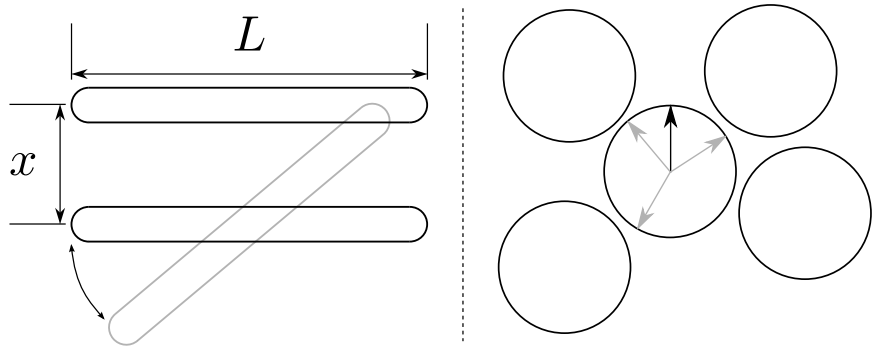

Figure 3.9: Illustration of steric hindrance occurring during rotation of differently shaped particles in two dimensions. Left: rodlike particles of length L at a distance x. The second particle cannot rotate as indicated since it would overlap with the first one. Right: spherical particles. The particle in the centre can rotate freely without overlapping with any of the surrounding particles as indicated by the arrows which denote different orientations.

147], and lanes [141, 143, 147] to occur in simulated systems of active rodlike particles. Rotating structures such as vortices or spirals have also been reported – mainly in experiments [109, 110, 124–126, 154], but in some cases, these were also found in simulations [110, 124, 137, 154, 155]. Some of these structures have not only been observed but have also been studied in more detail either by exploring the systems' parameter space in order to get an idea of its phase diagram or analytically deriving equations predicting the collective dynamics. Some of the work regarding lanes, clusters, and rotating patterns is briefly discussed in the following section.

Lanes Lanes can be understood as narrow assemblies of polarly aligned rods moving along the long axis of the structure – see Fig. 3.8 for an illustration.
In simulations of point particles, single lanes have been observed when the particles had an explicit aligning interaction [133]. However, most simulations in which the formation of lanes was observed consisted of rodlike particles that would form multiple lanes moving parallel to each other in opposite directions [141, 143, 147, 148]. Two requirements that were identified for the formation of lanes were aspect ratios $a \gtrsim 10$ [141, 143] and large particle densities [141, 143, 147]. Also, high particle motilities were found to facilitate the formation of lanes [147]. In analytical studies of similar systems, lanes have also been predicted [153, 192]. These predictions deviate from the simulations in that they only yielded single lanes instead of multiple lanes, but partly, they identified similar requirements for their formation. Using a continuum model for a nematic fluid, Putzig et al. found that lanes would occur in a range of densities above a critical value [192]. Larger motilities were found to increase this range. Yang et al. studied a different continuum model with a density-dependent motility and an explicit aligning interaction [153]. They found that lanes would form when the alignment was strong – an effect that was not reported in simulations.

Clusters Collectively moving clusters are another type of pattern that has been studied in numerous works. This kind of collective motion has been observed in experiments

as well as simulations of both spherical particles and rodlike particles.
The occurrence of collective motion in experiments with vibrated disks as reported by Deseigne et al. [108] is somewhat surprising since the particles do not have an explicit aligning interaction. However, the authors reported that a fraction of collisions between particles would actually result in alignment. In simulations replicating this experimental setup of vibrated disks, moving clusters were found as well [132]. Other simulations of point particles with an explicit aligning interaction also showed the formation of collectively moving clusters [133]. The authors were also able to reproduce this effect using a continuum theory derived from the microscopic equations of motion.
As described above, steric interactions of rodlike particles yield alignment, so the occurrence of collective motion in these systems is not surprising. Experimental setups in which collectively moving clusters were observed include motility assays with actin filaments [125] and colonies of B. subtilis in thin films [28]. In both cases, high densities were found to be required for cluster formation. In simulations of rodlike particles, a more complex – and sometimes contradictory – dependence on several parameters was identified. While the findings of Yang et al. confirmed the experimental results with a minimum density required for the formation of collectively moving clusters [142], other works demonstrated that such clusters would occur at low to medium densities, and large densities would cause the formation of lanes [141, 143, 147] or large immobile clusters [160]. Another parameter that was found to be important was the particles' aspect ratio. According to Wensink et al., motile clusters would only occur for aspect ratios $a \gtrsim 7$ [141, 143], but Weitz et al. also observed such clusters at smaller aspect ratios. Finally, simulations investigating the influence of the particles' motility reported that it has a significant effect. According to Yang et al., a minimum motility is required for the formation of collectively moving clusters [142]. In contrast to this, Abkenar et al. found that this was not the case for large enough densities [147]. The main influence of particle motility they reported was that large motilities would lead to the formation of smaller clusters.
The formation of motile clusters has been explained analytically by local symmetry-breaking [191, 195]. The particles' aligning interactions in combination with their self-propulsion were identified as the causes the symmetry-breaking. However, the analytical models did not specify the parameter ranges in which this effect would occur.
In conclusion, we have to note that the formation of collectively moving clusters seems to be very sensitive to several parameters such as particle density, aspect ratio, and motility. The precise dependence on these parameters is not clear at this point though.

Rotating patterns Vortices and other circular patterns of active particles have mainly been reported in experiments, but in a few instances, these have also been observed in simulations.
Experiments with spherical particles have been found to exhibit rotating structures when an aligning interaction between the particles existed [108, 154]. However, most examples of rotating structures have been observed in systems of rodlike particles including vibrated colloidal particles [109, 110] and motility assays [124–126]. In all cases, large densities were found to be necessary for the formation of these patterns. Apart from this, the experiments gave little indication what other factors were relevant for the formation of circular patterns.
In some cases, rotating structures were observed in simulations of rodlike particles – including swirls and vortices [110, 124, 137, 155] as well as rotating rings [126]. In some

works, the particles' motility was identified as a relevant parameter for the formation of rotating structures: swirling patterns were only observed for sufficiently large propulsion speeds [110, 137]. Other works were only able to reproduce rotating structures when the individual particles had a tendency to move along curved trajectories [124, 126]. Another important factor pointed out in many publications are the interactions between particles. For example, Schaller et al. found that rotating structures would remain stable for longer periods of time due to particle aggregation [126]. Sumino et al. concluded from their results that nematic ordering was a requirement for the formation of vortices [124]. Finally, Lushi et al. reported that vortices would only occur in their simulations when hydrodynamic interactions were considered [155].
Some of these aspects were also confirmed by analytical works. Using a continuum theory, Yang and Marchetti found that swirling patterns would form as a result of hydrodynamic interactions [196]. Also, another analytical investigation by Yang et al. showed that explicit aligning interactions between particles would cause the formation of rotating patterns when the alignment strength was in a specific range [153].
Even though these findings indicate that a variety of different factors is important for the formation of rotating structures, we can conclude that the interactions between the particles are crucially important – be it hydrodynamic interactions or aligning interactions.

3.2.5 Phase separation in active systems

As mentioned before, collective phenomena from particle aggregation to collectively moving patterns have in common that they exhibit non-uniform density distributions. Therefore, they can be understood as different types of phase separation. The previous sections have listed many examples for active systems in which phase separation was reported – in experiments as well as in simulations. Due to the complexity of many of these systems, a theoretical framework for the phase separation often does not exist or is incomplete. However, some progress has been made recently – mainly for spherical particles. Since these models will be the starting point for the analytical models derived for rodlike particles later in this chapter, they will be discussed here in more detail.

Particle currents

One approach for calculating the coexisting densities in a phase-separated system consisting of one dense cluster surrounded by a gas phase has been presented by Redner et al. [135]. They used a particle-based model to derive the density in the gas phase. The model was derived under the following assumptions: 1. the gas phase is homogeneous and perfectly isotropic, 2. particles are absorbed by the cluster when they collide with its surface, 3. this absorption does not affect the particles' rotational diffusion. The authors then calculated the rates for absorption and detachment from the cluster. In a steady state, these have to be equal, so the gas density in this dynamic equilibrium can be expressed as

$$\rho_{\mathrm{gas}} = \frac{\pi \kappa D_{\mathrm{rot}}}{dv} \ . \tag{3.66}$$

Here, D_{rot} is the rotational diffusion constant, d is the particles' diameter, and v their propulsion speed. The fitting parameter κ represents the average number of particles

simultaneously leaving the cluster during a detachment event. Due to several mechanisms, this number can be greater than 1.

The authors used the above expression to derive the fraction of particles in the cluster

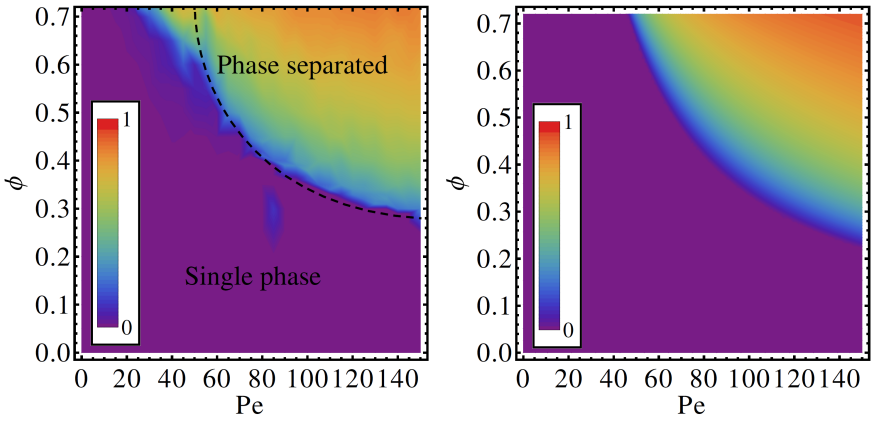

Figure 3.10: Fraction of particles in the cluster in phase-separated systems of self-propelled spherical particles as a function of Péclet number Pe and particle density ϕ [135]. The fraction of particles in the dense phase is indicated by colour. The left plot shows simulation results, and the right plot was generated using the authors' analytical model. Reprinted with permission from Ref. [135]. Copyright 2013 American Physical Society.

and compare this to their simulation results. They found good quantitative agreement with $\kappa = 4.5$ for packing fractions up to 0.7. The corresponding plot is shown in Fig. 3.10.

Density functional theory

A more thorough approach for studying the liquid-gas phase separation in systems of spherical particles with purely repulsive interactions has been presented by Cates and Tailleur [178]. As the cause for phase separation, they identified two basic mechanisms: first, particles tend to accumulate in regions where they move more slowly, and secondly, the particles' speed is dependent on local density and therefore leads to slowing down of particles as a result of local accumulation. Together, these two mechanisms can create a positive feedback loop enhancing density inhomogeneity. Since both mechanisms are related to the particles' motility, the authors refer to the resulting effect as motility-induced phase separation.

The presented model maps the coarse-grained dynamics of an active system onto the equilibrium dynamics of a passive fluid with attractive interactions. The densities of both coexisting phases are then obtained using classical density functional theory – see Section 3.1.3. This procedure is outlined in the following section.

As presented in Section 3.2.2, active spherical particles can be described either as run-and-tumble particles (RTPs) or as active Brownian particles (ABPs). These differ mainly in how they describe the particles' orientational relaxation. However, the authors considered time scales larger than the rotational relaxation time τ_{rot} at which

both models become equivalent. The diffusivity D can then be written as

$$D = \frac{v^2\tau}{d} + D_\mathrm{t} \ , \tag{3.67}$$

with v being the propulsion speed, d the dimensionality, $\tau = (\alpha + (d-1)D_\mathrm{rot})^{-1}$ the generalised reorientation time. The translational diffusivity D_t can often be neglected because the active term is dominant.
The authors started their derivation by considering the dynamics of a single particle. By coarse-graining its microscopic dynamics, they arrived at the time evolution of the probability density $\varphi(\boldsymbol{r})$ for finding a single particle at position $\boldsymbol{r}$:

$$\dot{\varphi} = -\boldsymbol{\nabla}\boldsymbol{j} = -\boldsymbol{\nabla}\left[-D\boldsymbol{\nabla}\varphi + \boldsymbol{V}\varphi\right] \ . \tag{3.68}$$

Here, D is the diffusivity as specified before with D_t set to 0, and $\boldsymbol{V} = -D\boldsymbol{\nabla}\ln v(\boldsymbol{r})$ is the drift velocity. Except for this drift velocity, the above description is the same as for a passive Brownian particle with a position-dependent diffusivity. By rewriting the drift velocity as a function of an external potential $U = k_B T \ln v(\boldsymbol{r})$, the authors made the transition to effectively treating the active particle as a passive Brownian particle in an external potential. The particles' motility enters the description only via the modified diffusivity and the potential.
Next, the dynamics of many particles were derived from those of a single particle resulting in the stochastic equation of motion for the coarse-grained particle density $\rho(\boldsymbol{r})$:

$$\dot{\rho} = -\boldsymbol{\nabla}\boldsymbol{J} = -\boldsymbol{\nabla}\left[-D\boldsymbol{\nabla}\rho + \boldsymbol{V}\rho + (2D\rho)^{1/2}\boldsymbol{\zeta}\right] \ , \tag{3.69}$$

where $\boldsymbol{\zeta}$ is a noise-term. However, in many-particle systems, interactions have to be considered which can be done by introducing a functional dependence of v and τ on density: $v\left([\rho], \boldsymbol{r}\right)$, $\tau\left([\rho], \boldsymbol{r}\right)$. The authors checked if such a many-particle system with interactions could still be represented by an equilibrium system of passive Brownian particles. They found that this was the case if the ratio of drift velocity over diffusivity could be expressed as the derivative of a functional $\mathcal{F}_\mathrm{ex}[\rho]$:

$$\frac{\boldsymbol{V}\left([\rho], \boldsymbol{r}\right)}{D\left([\rho], \boldsymbol{r}\right)} = -\beta\boldsymbol{\nabla}\frac{\delta\mathcal{F}_\mathrm{ex}}{\delta\rho} \ , \tag{3.70}$$

or equivalently

$$k_B T \ln v\left([\rho], \boldsymbol{r}\right) = \frac{\delta\mathcal{F}_\mathrm{ex}}{\delta\rho} \ . \tag{3.71}$$

Under this condition, the active system would be equivalent to a fluid of passive Brownian particles with the free energy functional

$$\mathcal{F}[\rho] = \mathcal{F}_\mathrm{ex}[\rho] + k_B T \int \rho(\ln\rho - 1)\, d^3 r \ . \tag{3.72}$$

The first term on the right-hand side is called excess free energy. If the particles were actually passive, this would result from the interaction between particles. In case of active particles, it results from the density-dependent propulsion speed $v\left([\rho], \boldsymbol{r}\right)$. The second term is the ideal gas contribution. From the above free energy functional, the

thermal equilibrium configuration $\rho(\boldsymbol{r})$ can be calculated which is exactly the idea of classical density functional theory – see Section 3.1.3. The equilibrium configuration would then give the coexisting densities in a phase-separated system.
During the above derivation, translational diffusion was neglected by setting $D_\mathrm{t} = 0$. Taking into account translational diffusion, the authors found that the integrability condition stated above would only have to be slightly modified to

$$\frac{\tau v \boldsymbol{\nabla} v}{v^2\tau + dD_\mathrm{t}} = \boldsymbol{\nabla}\frac{\delta \mathcal{F}_\mathrm{ex}}{\delta \rho} \ . \tag{3.73}$$

Local approximation The above many-particle description was derived without making any assumptions about how exactly v depends on the density. In this general case, mapping onto an equilibrium system would be possible if the integrability condition in Eq. (3.73) was met. Since this is not generally the case, the authors discussed a special case for which the condition could be shown to be met. They referred to this special case as the local approximation: the particles' propulsion speed is assumed to depend only on local density and not on any gradient terms: $v\left([\rho], \boldsymbol{r}\right) \to v(\rho)$. With this assumption, the excess free energy can be calculated from the integrability condition. For $D_\mathrm{t} \neq 0$, it is also required that τ and D_t are independent of ρ. In this case, the free energy functional can be written as

$$\begin{aligned} \mathcal{F}[\rho] = \int f(\rho)\, d^3r \ , \qquad & \beta f(\rho) = \rho(\ln\rho - 1) + \beta f_\mathrm{ex}(\rho) \ , \\ & \beta f_\mathrm{ex}(\rho) = \int_0^\rho \frac{1}{2} \ln\left(v^2(\rho')\tau + dD_\mathrm{t}\right)\, d\rho' \ , \end{aligned} \tag{3.74}$$

with the free energy density $f(\rho)$ and the excess free energy density $f_\mathrm{ex}(\rho)$. Given a specific $v(\rho)$, the free energy functional can be calculated for any density distribution ρ using the above equation.
To calculate the coexisting densities in a phase-separated systems from the free energy functional, the authors applied a mean-field theory in which spatial fluctuations were ignored. They treated the system as consisting of a number of homogeneous domains with densities ρ_i and volumes V_i. The system's free energy $\mathcal{F}_\mathrm{tot}$ would then be a sum of the domains' free energies: $\mathcal{F}_\mathrm{tot} = \sum_i V_i f(\rho_i)$.

In a homogeneous system with only a single domain of density ρ, the free energy could be calculated directly from Eq. 3.74. However, in a range where $f(\rho)$ would be concave, the system would be unstable with regards to phase separation into two domains of densities ρ_1 and ρ_2. The coexisting densities ρ_1 and ρ_2 can be determined via a common-tangent construction on $f(\rho)$. This automatically yields the density range $[\rho_1, \rho_2]$ in which phase coexistence lowers the total free energy compared to a single phase configuration. This range actually includes densities that are not in the instability range but for which the phase-separated configuration is still energetically favourable. For an illustration, see Fig. 3.11.

Application The authors tested the validity of their predictions by comparing them to a wide range of existing literature presenting numerical results from a number of different models.
As a first example, they compared their predictions to simulations of RTPs on a two-dimensional lattice [197]. These simulations qualitatively confirmed the occuring of

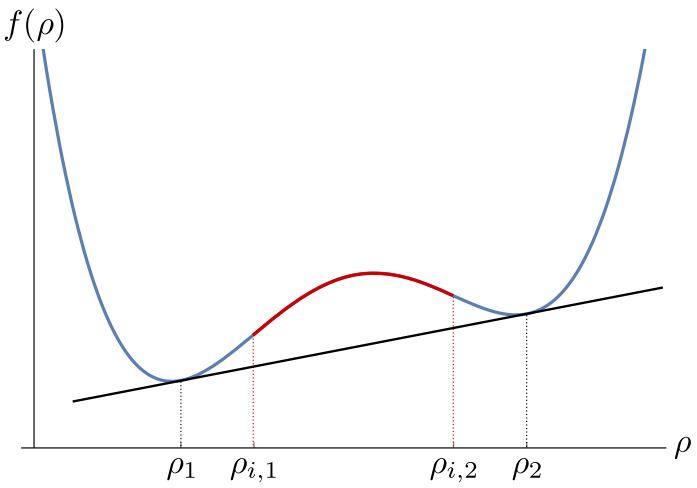

Figure 3.11: Exemplary plot of the free energy density as a function of density. The region $[\rho_{i,1}, \rho_{i,2}]$ in which the system is unstable with regards to phase separation since $f(\rho)$ is concave is indicated in red. However, phase separation lowers the system's total free energy in a wider density range $[\rho_1, \rho_2]$ given by the common-tangent construction on $f(\rho)$.

motility-induced phase separation. However, the authors' prediction for the coexisting densities did not agree with simulation data for systems with steric interactions.
When applying the authors' model to simulated ABPs, it should be noted that these do not include an explicit dependence of the particles' speed on density. Instead, these particles would slow down when colliding with each other due to steric interactions. This effect results in a particle velocity that linearly decreases with density [134, 135, 183] which is in agreement with theoretical predictions [134, 136, 183, 194]. Again, the authors found qualitative agreement when considering this dependence, but there were major deviations between the simulations and their theory. The numerical results showed a critical Péclet number below which phase separation would not occur [134, 135, 183] while the theory predicted phase separation to be independent of particle motility.
The authors pointed out that their model was incapable of accounting for various interactions such as colloidal, orientational, and hydrodynamic interactions which were commonly present in experiments. Hence, they concluded that further work would be required to apply the theory to systems in which these effects are important, e.g., for aspherical particles such as active Brownian rods.

3.3 Modelling of the active systems

The following section describes how the simulations of active rods were implemented. The applied models for particles and their environment are presented as well as the simulation routine and the measurement procedures during simulation.

3.3.1 Environment

The default simulation cell in which the simulations were performed is a rectangular box of length L_x in x-direction and L_y in y-direction. We use periodic boundary conditions meaning that whenever a particle would leave the cell, it is put back in at the opposing side. For certain tasks, we used a tube-like cell with fixed boundaries at $x = 0$ and $x = L_x$ and periodic boundary conditions in y-direction. Also, we did some simulations in cells with fixed boundaries. These were not necessarily rectangular but could have any polygonal shape. The interaction between fixed boundaries and particles was assumed to be the same as the the interaction between particles (see below).
We want the medium in which the particles are moving to emulate water at room temperate, so we set the temperature to $T = 300\,\mathrm{K}$. The medium's viscosity is set to $\eta = 10^{-3}\,\mathrm{Nsm}^{-2}$ resembling the viscosity of water $\eta_{\mathrm{H_2O}} = 1.002 \cdot 10^{-3}\,\mathrm{Nsm}^{-2}$ at $T = 20°\,\mathrm{C}$ [198].

3.3.2 Particles

Geometry

The active particles were modelled as spherocylinders, i.e., cylinders with a semi-sphere of the same diameter as the cylinder attached to each of their spherical surfaces. Projecting a spherocylinder into two dimensions gives a rectangle with two semi-circles attached to opposing edges. We call d the rectangle's short edge which is also the semi-circles' diameter and the total length L – the rectangle's long edge plus two times the radius of the semi-circles, see Fig. 3.12. The particles' aspect ratio was chosen as $a = \frac{L}{d} = 10$ with the length $L = 1\,\mu\mathrm{m}$ in order to represent rod-shaped bacteria like E. coli and B. subtilis, see Sections 1.2.2 and 3.1.1.
A rod's configuration is defined by the position $\boldsymbol{b}$ of its centre of mass and its orientation φ – defined as the angle between the rod's main axis and the system's x-axis. An equivalent description of a rod's orientation is the unit vector

$$\hat{\boldsymbol{u}} = \begin{pmatrix} \cos\varphi \\ \sin\varphi \end{pmatrix} . \tag{3.75}$$

Even though the rods' geometry is symmetrical, their ability to propel themselves forward along their main axis breaks the symmetry and assigns them polarity.

Interactions

Interactions between particles The simulated particles do not carry a charge, but as pointed out in Section 3.1.2, uncharged particles still interact with each other via a potential that can be approximated by the Lennard-Jones potential. For the sake of computational efficiency, an additional hard-core potential was implemented as well.

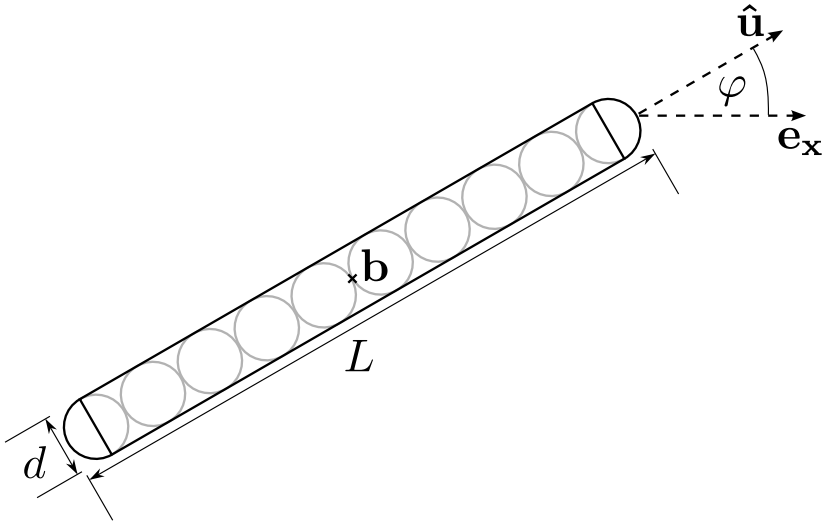

Figure 3.12: Sketch of a two-dimensional spherocylindrical particle with diameter d and total length L. The particle's centre of mass is $\boldsymbol{b}$, and $\hat{\boldsymbol{u}}$ indicates its orientation and hence defines the direction of self-propulsion. The angle between $\hat{\boldsymbol{u}}$ and the system's x-axis is φ which is an equivalent description of the orientation. Grey circles illustrate the shish-kebab model used to calculate interactions.

The interaction yields forces and torques when two rods come close to each other. For calculating these, the rods are split up into spherical segments of diameter d according to the shish-kebab model [176]. The Lennard-Jones potential between two of these segments at postitions $\boldsymbol{r}_i$ and $\boldsymbol{r}_j$ is only dependent on their distance $r = |\boldsymbol{r}_i - \boldsymbol{r}_j|$:

$$V_{\mathrm{LJ}}(r) = 4\epsilon \left[\left(\frac{\sigma}{r}\right)^{12} - \left(\frac{\sigma}{r}\right)^{6} \right] \tag{3.76}$$

As described in Section 3.1.2, the prefactor ϵ determines the strength of the potential, and σ is the relevant length scale. In our simulations, this length scale is the particles' diameter: $\sigma = d$. In order to limit the attraction resulting from the potential to a small contribution, we set $\epsilon = 0.0086\,\mathrm{eV}$ which is one order of magnitude smaller than the typical bond energy per atom for a van-der-Waals interaction.
At a distance $r_{\min} = d \cdot 2^{\frac{1}{6}}$, the potential has its minimum $V_{\mathrm{LJ}}(r_{\min}) = -\epsilon$. The limits of V_{LJ} are

$$\lim_{r\to 0} V_{\mathrm{LJ}} = \infty \ , \qquad \lim_{r\to\infty} V_{\mathrm{LJ}} = 0 \ . \tag{3.77}$$

At distances $r \gg d$, the potential is dominated by the term proportional to r^{-6} and quickly approaches 0. Therefore, we can safely neglect interactions with particles at great distances without considerably affecting the dynamics. We opt to cut off the potential at a distance $r_{\mathrm{co}} = 4r_{\min}$ where the potential's absolute value is already $|V_{\mathrm{LJ}}(4r_{\min})| < 5 \cdot 10^{-4}\epsilon$. For distances $r > r_{\mathrm{co}}$, we manually set the potential to 0.
At smaller distances, the force a segment at $\boldsymbol{r}_j$ exerts on a segment at $\boldsymbol{r}_i$ is

$$\boldsymbol{F}_{\mathrm{LJ}}(\boldsymbol{r}) = -\boldsymbol{\nabla} V_{\mathrm{LJ}}(r) = \left[48\frac{\epsilon}{r}\left(\frac{d}{r}\right)^{12} - 24\frac{\epsilon}{r}\left(\frac{d}{r}\right)^{6} \right] \frac{\boldsymbol{r}}{r} \tag{3.78}$$

with $\boldsymbol{r} = \boldsymbol{r}_i - \boldsymbol{r}_j$ being the difference vector between the two segments. For calculating the force $\boldsymbol{f}_{\alpha\beta}$ a rod at $\boldsymbol{b}_\beta$ exerts on a rod at $\boldsymbol{b}_\alpha$, we just sum over all segments:

$$\boldsymbol{f}_{\alpha\beta} = \frac{1}{n_\alpha} \sum_i^{n_\alpha} \boldsymbol{f}_i = \frac{1}{n_\alpha n_\beta} \sum_i^{n_\alpha} \sum_j^{n_\beta} \boldsymbol{F}_{\mathrm{LJ}}(\boldsymbol{r}_i - \boldsymbol{r}_j) \tag{3.79}$$

Here, the $\boldsymbol{r}_i$ and $\boldsymbol{r}_j$ are the positions of the segments belonging to the rods at $\boldsymbol{b}_\alpha$ and $\boldsymbol{b}_\beta$ respectively and n_α and n_β the number of segments for each rod.
The torque $\tau_{\alpha\beta}$ induced by the interaction is calculated by summing the torques m_α of the segments relative to the rod's centre of mass:

$$\tau_{\alpha\beta} = \sum_i^{n_\alpha} \tau_\alpha = \sum_i^{n_\alpha} P_\perp(\varphi_\alpha, \boldsymbol{f}_i - \boldsymbol{f}_{\alpha\beta}) s_i \tag{3.80}$$

Here, $P_\perp(\varphi_\alpha, \boldsymbol{f})$ is the projection of the force f onto an axis perpendicular to the rod's orientation φ_α and the s_i are the distances between the segments' positions $\boldsymbol{r}_i$ and the rod's centre of mass $\boldsymbol{b}_\alpha$. The sign of s_i takes into account on which side of the rod the segment is located.
Additional to the Lennard-Jones potential, a hard-core potential prevents rods to come closer to each other than the hard-core distance d_{hc}. We choose this parameter so that the force resulting from two parallel rods at a distance d_{hc} would cause them to move apart by a distance $2.5d$ in the next time-step of the simulation. If the movement of a rod would cause any part of it to come closer than d_{hc} to another rod, we would stop it at the point where the distance would be exactly the hard-core distance. Details on how d_{hc} is calculated can be found in App. B.

Thermal forces Particles do not only interact with each other but also with the molecules of the surrounding medium. As outlined in Section 3.1.5, these are small compared to the simulated particles and move on a shorter time scale. Hence, many collisions occur on the particles' time scale and their effect can be described as a statistical quantity. This is done by effectively integrating over all of these collisions which yields a random force $\boldsymbol{F}_{\mathrm{th}}$. This force is dependent on the medium's viscosity, temperature, and the particles' dimensions. It represents the thermal fluctuations caused by the medium. The $\boldsymbol{F}_{\mathrm{th}}$ are distributed according to a Gaussian distribution – the exact form of which will be given below. Hydrodynamic interactions were not considered.

Reversal at cell boundaries We can enable particles to reverse their orientation when hitting a cell boundary. Since this reversal is equivalent to rotating the particle by an angle π, we can simply execute this move as a rotation. The reversal mechanism is triggered when the particle's front end collides with a boundary, i.e., the distance between the two becomes smaller than the hard-core distance d_{hc}.
This mechanism imitates a naturally occurring phenomenon: a number of different types of bacteria have been reported to have the ability to reverse their direction of motion [199–203]. In particular, B. subtilis has been observed to reverse its orientation when encountering an obstacle [204].

Dynamics

The particles' dynamic behaviour is determined by their propulsion speed and their friction coefficients. We assume self-propelled particles which push themselves forward along their main axis with a propulsion speed v_0. The friction coefficients influence the interactions of the particles with the surrounding medium, i.e., rotational and translational diffusion. They were already introduced in Section 3.1.5.
The rotational friction coefficient γ_{rot} is a measure of how a particle in a medium reacts to an external torque $\boldsymbol{\tau}$. Assuming this torque is perpendicular to the simulation cell, this can be written as

$$\dot{\varphi} = \frac{1}{\gamma_{\mathrm{rot}}}\tau \ , \tag{3.81}$$

where $\tau = |\boldsymbol{\tau}|$. The rotational friction coefficient can be approximated as

$$\gamma_{\mathrm{rot}} = \frac{\pi\eta L^3}{3\ln(L/d)} \tag{3.82}$$

with η being the viscosity of the medium, L the rod's length and d its diameter.
The translational friction coefficients $\gamma_{\parallel}$ and $\gamma_{\perp}$ determine the speed $\boldsymbol{v}$ at which a particle moves when an external force $\boldsymbol{F}$ acts on it. With $\boldsymbol{v}_{\parallel}$ and $\boldsymbol{v}_{\perp}$ being the speed's components parallel and perpendicular to the rod's main axis, the relation between force, friction coefficients, and speed is as follows:

$$\boldsymbol{F} = \gamma_{\parallel}\boldsymbol{v}_{\parallel} + \gamma_{\perp}\boldsymbol{v}_{\perp} \tag{3.83}$$

The translational friction coefficients can be approximated as

$$\gamma_{\parallel} = \frac{2\pi\eta L}{\ln(L/d)} \ , \qquad \gamma_{\perp} = \frac{4\pi\eta L}{\ln(L/d)} \ . \tag{3.84}$$

As pointed out in Section 3.2.1, we use the Péclet number Pe to quantify if the particles' dynamics are dominated by propulsion or by diffusion. We will use the following definition for the Péclet number from here on:

$$Pe = \frac{v_0 L}{D_{\parallel}} = \frac{6v_0}{D_{\mathrm{rot}}L} \ , \tag{3.85}$$

where $D_{\parallel} = k_B T\,\gamma_{\parallel}^{-1}$ and $D_{\mathrm{rot}} = k_B T\,\gamma_{\mathrm{rot}}^{-1}$ according to Eq. (3.32). The two equivalent expressions represent a comparison of the particles' self-propulsion to translational diffusion parallel to their main axis or to rotational diffusion.

3.3.3 System initialisation

When generating a system, rods are deposited into the simulation cell at random positions $\boldsymbol{b}_i$ with random orientations φ_i. A rod is only deposited when it does not intersect with any of the rods already in the cell. Otherwise, a new position vector and orientation are generated. This process is repeated until either a configuration without intersections is generated or the rod has been attempted to be put into the cell 10^6 times. In the latter case, the simulation routine is performed for 10^2 time-steps which alters the positions and orientations of the already deposited rods. Afterwards,

the depositing routine for the next rod starts from the beginning. This procedure is completed when the desired particle density $\rho = N/(L_x L_y)$ is reached. Here, N is the total number of rods. An equivalent parameter in dimensionless units is the reduced density $\tilde{\rho} = \rho L^2$.
When generating a swirling configuration, the above routine is modified: the rods' orientations are chosen depending on their position in the cell in order to generate a swirling pattern. This is achieved by calculating the difference vector between a rod's position and the centre of the cell and then setting the orientation to be perpendicular to this vector.

3.3.4 Simulation

Starting from $t = 0$, the simulation time t is increased incrementally by time-steps Δt up to the maximum simulation time $t_{\max}$. At the beginning of each time-step, translational and angular velocities of the particles are set to 0. Next, forces and torques on each particle are calculated. There are two contributions to each of these – one from interaction with other particles and one from thermal forces. The interaction between particles has already been described above. The contribution from the medium is a noise term representing thermal interactions as described in Section 3.1.5. In the same section, we introduced the force's components $\boldsymbol{\xi}_\parallel$ and $\boldsymbol{\xi}_\perp$ as Gaussian distributed with the properties

$$\langle \boldsymbol{\xi}_\alpha \rangle = 0 \ , \qquad \langle \boldsymbol{\xi}_\alpha(t) \boldsymbol{\xi}_\beta(t') \rangle = 2 k_B T \gamma_\alpha \delta_{\alpha\beta} \delta(t - t') \ , \tag{3.86}$$

where $\alpha, \beta = \{\parallel, \perp\}$. For the random torques ξ_{rot}, we had

$$\langle \xi_{\mathrm{rot}} \rangle = 0 \ , \qquad \langle \xi_{\mathrm{rot}}(t) \xi_{\mathrm{rot}}(t') \rangle = 2 k_B T \gamma_{\mathrm{rot}} \delta(t - t') \ . \tag{3.87}$$

However, when dealing with discretised time, the correlations have to be adjusted as follows [205]:

$$\langle \boldsymbol{\xi}_{\alpha,n} \boldsymbol{\xi}_{\beta,m} \rangle = 2 \frac{k_B T \gamma_\alpha}{\Delta t} \delta_{\alpha\beta} \delta_{n,m} \ , \qquad \langle \xi_{\mathrm{rot},n} \xi_{\mathrm{rot},m} \rangle = 2 \frac{k_B T \gamma_{\mathrm{rot}}}{\Delta t} \delta_{n,m}, \tag{3.88}$$

where $t = n\Delta t$ and $t' = m\Delta t$.
The above properties result from the following Gaussian distributions:

$$p_\parallel(\boldsymbol{\xi}_\parallel) = \frac{1}{\sqrt{2\pi\sigma_\parallel}} \exp\left(-\frac{\xi_\parallel^2}{2\sigma_\parallel} \right) \ , \qquad \sigma_\parallel = \frac{2 k_B T \gamma_\parallel}{\Delta t} \ , \tag{3.89}$$

$$p_\perp(\boldsymbol{\xi}_\perp) = \frac{1}{\sqrt{2\pi\sigma_\perp}} \exp\left(-\frac{\xi_\perp^2}{2\sigma_\perp} \right) \ , \qquad \sigma_\perp = \frac{2 k_B T \gamma_\perp}{\Delta t} \ , \tag{3.90}$$

$$p_{\mathrm{rot}}(\xi_{\mathrm{rot}}) = \frac{1}{\sqrt{2\pi\sigma_{\mathrm{rot}}}} \exp\left(-\frac{\xi_{\mathrm{rot}}^2}{2\sigma_{\mathrm{rot}}} \right) \ , \qquad \sigma_{\mathrm{rot}} = \frac{2 k_B T \gamma_{\mathrm{rot}}}{\Delta t} \ . \tag{3.91}$$

Values for the random torques and forces are drawn using the ziggurat method implemented in the GNU Scientific Library.
After forces and torques are calculated, the particles' translational and angular velocities are calculated according to the Langevin equation (3.60):

$$\begin{aligned} \boldsymbol{v}_\parallel &= v_0 \hat{\boldsymbol{u}} + \gamma_\parallel^{-1} \left[- \left(\boldsymbol{\nabla} U(\boldsymbol{r}) \right)_\parallel + \boldsymbol{\xi}_\parallel \right] \\ \boldsymbol{v}_\perp &= \gamma_\perp^{-1} \left[- \left(\boldsymbol{\nabla} U(\boldsymbol{r}) \right)_\perp + \boldsymbol{\xi}_\perp \right] \ , \\ \dot{\varphi} &= \gamma_{\mathrm{rot}}^{-1} \left[\tau_U + \xi_{\mathrm{rot}} \right] \ . \end{aligned} \tag{3.92}$$

The terms resulting from the external potential are given by Eq. (3.79) and Eq. (3.80):

$$-\boldsymbol{\nabla} U(\boldsymbol{r} = \boldsymbol{b}_\alpha) = \sum_\beta \boldsymbol{f}_{\alpha\beta} \ , \qquad \tau_U = \sum_\beta \tau_{\alpha\beta} \ . \tag{3.93}$$

The particles are rotated and moved one by one. After each rotation and movement, it is checked whether the new configuration causes rods to intersect. Two rods intersect when any part of one of them is closer to the other one than the hard-core distance d_{hc}. If this is the case, the rotation or movement causing the intersection is rejected. If the simulation cell has fixed boundaries, intersections with these are prevented similarly. It is checked whether a particle's new configuration leads to an intersection with one of the boundaries. However, these rotations and movements are not rejected entirely. Instead, they are partly carried out up to the point that the minimum distance between particle and boundary is d_{hc}.

3.3.5 Discretised interactions

Since the interactions between particles have to be calculated in every time-step, a lot of computing time is spent on those calculations. However, we can save this time by discretising the interaction. The forces and torques generated by the interaction between two particles is only dependent on their position relative to each other. So, we can calculate forces and torques for all relevant positions, save these in an array, and read out the according values during simulation. Due to the large number of interactions that would have to be calculated during a simulation, this approach is significantly reducing computing time – especially since the array only has to be calculated once and can then be used for several simulations. The disadvantage of this method is that it is not as accurate as explicitly calculating the interactions.
For calculating the array, we consider a rod at position $(0, 0)$ parallel to the x-axis and a second rod exerting a force and a torque according to the Lennard-Jones interaction on the first one. For the second rod, we systematically change position and orientation in order to cover all configurations for which any part of the second rod is close enough to the first one to interact with it. These configurations can be interpreted as a volume C in configuration space (x, y, φ). We discretise this volume using the increments dx, dy, and $d\varphi$ dividing it into subvolumes $([x_i, x_i + dx], [y_j, y_j + dy], [\varphi_k, \varphi_k + d\varphi])$. For each of these small volumes, the resulting force and torque acting on the first rod are calculated and saved in an array. Additionally, it is checked whether a configuration leads to an intersection of the two rods. This information is also saved as it reduces the time spent on checking for intersections during simulation. The reason here is the same as for the interactions – reading a value from an array is much quicker than calculating whether two rods intersect.
During simulation, we can now obtain forces and torques resulting from the interaction between two rods by simply calculating their relative position (x, y) and relative orientation φ to each other. Next, we find the according subvolume in C, so that

$$x_i \leq x < x_i + dx \quad \wedge \quad y_i \leq y < y_i + dy \quad \wedge \quad \varphi_i \leq \varphi < \varphi_i + d\varphi \ . \tag{3.94}$$

Then, we can read the already calculated values from the array. The procedure for checking for intersections is analogous.

3.3.6 Dimensionless parameters

Simulations were performed using dimensionless parameters. As calibrating values, we used the following relations:

$$1\,\mu\mathrm{m} \equiv 1\ , \qquad 1\,\mu\mathrm{s} \equiv 1\ , \qquad k_B \cdot 1\,\mathrm{K} \equiv 1\ . \tag{3.95}$$

This results in a particle length $L = 1$ and diameter $d = 0.1$. In dimensionless energy units, the strength of the Lennard-Jones potential is $\epsilon = 100$.
The medium's viscosity of $10^{-3}\,\mathrm{Nsm}^{-2}$ becomes $\eta = 7.24297{\cdot}10^7$ in dimensionless units. Since we set the temperature to $T = 300\,\mathrm{K}$, we have $k_BT = 300$ in our simulations. With these values, we can calculate the friction coefficients

$$\gamma_\parallel = \frac{2\pi\eta L}{\ln(L/d)} = 1.97643 \cdot 10^8\ , \qquad D_\parallel = \frac{k_BT}{\gamma_\parallel} = 1.51789 \cdot 10^{-6}\ , \tag{3.96}$$

$$\gamma_\perp = \frac{4\pi\eta L}{\ln(L/d)} = 3.95286 \cdot 10^8\ , \qquad D_\perp = \frac{k_BT}{\gamma_\perp} = 7.58945 \cdot 10^{-7}\ , \tag{3.97}$$

$$\gamma_{\mathrm{rot}} = \frac{\pi\eta L^3}{3\ln(L/d)} = 3.29405 \cdot 10^7\ , \qquad D_{\mathrm{rot}} = \frac{k_BT}{\gamma_{\mathrm{rot}}} = 9.10734 \cdot 10^{-6}\ . \tag{3.98}$$

The rotational relaxation time is

$$\tau_{\mathrm{rot}} = \frac{1}{2D_{\mathrm{rot}}} = 5.49008 \cdot 10^4\ . \tag{3.99}$$

Unless indicated otherwise, simulations were performed using time-steps $\Delta t = 100$.

3.3.7 Measurements

During simulation, a variety of quantities is measured for later analysis.

Nematic ordering

Following Section 3.1.4, we use a tensor $\boldsymbol{Q}$ to get information about the nematic order in a system with N filaments at angles φ_i relative to the x-axis:

$$\begin{aligned} \boldsymbol{Q} &= \frac{1}{N}\sum_i \begin{bmatrix} 2\cos^2\varphi_i - 1 & 2\cos\varphi_i\sin\varphi_i \\ 2\cos\varphi_i\sin\varphi_i & 2\sin^2\varphi_i - 1 \end{bmatrix} = \begin{bmatrix} q_1 & q_2 \\ q_2 & -q_1 \end{bmatrix}\ , \\ q_1 &= \frac{1}{N}\sum_i 2\cos^2\varphi_i - 1\ , \qquad q_2 = \frac{1}{N}\sum_i 2\cos\varphi_i\sin\varphi_i \end{aligned} \tag{3.100}$$

The nematic order parameter S is the positive eigenvalue of $\boldsymbol{Q}$:

$$S = \sqrt{q_1^2 + q_2^2} \tag{3.101}$$

The director $\boldsymbol{n}$ is the associated eigenvector:

$$\boldsymbol{n} = \sqrt{\frac{q_2^2}{2q_1^2 + 2q_2^2 - 2q_1\sqrt{q_1^2+q_2^2}}} \begin{pmatrix} 1 \\ \frac{q_1 - \sqrt{q_1^2+q_2^2}}{q_2} \end{pmatrix}\ . \tag{3.102}$$

Centre of mass and mass distribution tensor

We call $\boldsymbol{c}$ the centre of mass of a system of N filaments. The centre of mass of a particle i is given by its position $\boldsymbol{b}_i$. The system's centre of mass is the average of all $\boldsymbol{b}_i$:

$$\boldsymbol{c} = \frac{1}{N}\sum_i \boldsymbol{b}_i \tag{3.103}$$

Since the centre of mass alone does not give us information about the mass distribution, we also calculate a mass distribution tensor which we write in analogy to a moment of inertia tensor as

$$\boldsymbol{C} = \begin{pmatrix} C_{xx} & C_{xy} \\ C_{xy} & C_{yy} \end{pmatrix} = \frac{1}{N}\sum_i \boldsymbol{\theta}_i \ , \tag{3.104}$$

where the $\boldsymbol{\theta}_i$ are the individual rods' contributions to the tensor. In a system with centre of mass $\boldsymbol{c}$, a rod with centre of mass $\boldsymbol{b}_i$ and orientation $\hat{\boldsymbol{u}}_i$ gives the contribution

$$\theta_{i,\alpha\beta} = \int_0^1 \left(c_\alpha - b_{i,\alpha} - \frac{L}{2}u_{i,\alpha} + sLu_{i,\alpha}\right)\left(c_\beta - b_{i,\beta} - \frac{L}{2}u_{i,\beta} + sLu_{i,\beta}\right) ds \ . \tag{3.105}$$

Introducing the expressions

$$d_{i,\alpha} = c_\alpha - b_{i,\alpha} \ , \qquad L_{i,\alpha} = Lu_{i,\alpha} \ , \tag{3.106}$$

we get

$$\begin{aligned} \theta_{i,\alpha\beta} &= \int_{-\frac{1}{2}}^{\frac{1}{2}} \left(d_{i,\alpha}d_{i,\beta} + d_{i,\alpha}L_{i,\beta}s' + d_{i,\beta}L_{i,\alpha}s' + L_{i,\alpha}L_{i,\beta}\ s'^2\right) ds' \\ &= d_{i,\alpha}d_{i,\beta} + \frac{1}{12}L_{i,\alpha}L_{i,\beta} \ . \end{aligned} \tag{3.107}$$

With this, we can write the mass distribution tensor as

$$C_{\alpha\beta} = \frac{1}{N}\sum_i d_{i,\alpha}d_{i,\beta} + \frac{1}{12}L_{i,\alpha}L_{i,\beta} \ . \tag{3.108}$$

This tensor can be understood as measuring the variance of the mass distribution in the system. By comparing it to the tensor resulting from a homogeneous mass distribution, we can determine whether the mass distribution of a system is inhomogeneous. In order to do this, we can illustrate the tensor as an ellipse by calculating its eigenvalues and eigenvectors. In two dimensions, the calculation of the eigenvalues λ_1 and λ_2 is straightforward yielding

$$\lambda_{1,2} = \frac{C_{xx}+C_{yy}}{2} \pm \sqrt{\left(\frac{C_{xx}+C_{yy}}{2}\right)^2 - \left(C_{xx}C_{yy} - C_{xy}^2\right)} \ . \tag{3.109}$$

The eigenvalues give us the lengths of the ellipse's main axes. The ellipse's orientation is indicated by the eigenvector $\boldsymbol{v}_{c,1}$ corresponding to the greater of the two eigenvalues λ_1. This eigenvector can be calculated as

$$\boldsymbol{v}_{c,1} = \begin{pmatrix} C_{xy} \\ \lambda_1 - C_{xx} \end{pmatrix} \ , \tag{3.110}$$

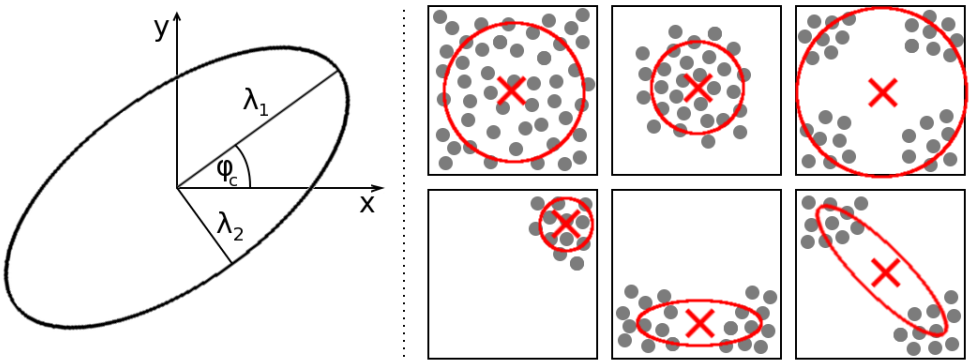

Figure 3.13: Left: Sketch of an ellipse constructed from a mass distribution tensor with eigenvalues λ_1 and λ_2 and an angle φ_c between the tensor's eigenvector $\boldsymbol{v}_{c,1}$ and the x-axis. Right: Examples of various mass distributions in a square cell. To simplify illustration, particles are represented by grey dots without indication of orientation. Red crosses mark the systems' centres of mass while red ellipses are drawn according to the systems' mass distribution tensors.

and the angle φ_c between the ellipse's greater main axis and the x-axis is then given as

$$\varphi_c = \tan^{-1} \frac{\lambda_1 - C_{xx}}{C_{xy}} \ . \tag{3.111}$$

An illustration of such an ellipse as well as a few examples for different mass distributions in a square cell can be found in Fig. 3.13.

Average speed

The average speed $\langle v(t, t_0) \rangle$ over a time period $[t_0, t]$ is calculated using the filament positions $\boldsymbol{b}_i(t_0)$ and $\boldsymbol{b}_i(t)$.

$$\langle v(t, t_0) \rangle = \frac{1}{N} \sum_i \frac{|\boldsymbol{b}_i(t) - \boldsymbol{b}_i(t_0)|}{t - t_0} \tag{3.112}$$

The average absolute speed $\langle |v(t, t_0)| \rangle$ over a time period $[t_0, t]$ is calculated using the sum of integrals

$$\langle |v(t, t_0)| \rangle = \frac{1}{N(t - t_0)} \sum_i \int_{t_0}^{t} \left| \frac{\partial \boldsymbol{c}_i(t')}{\partial t'} \right| dt' \ . \tag{3.113}$$

Since the simulation is discrete in time, the integral has to be transformed into a discrete sum with $n_t = \frac{t - t_0}{\Delta t}$ being the number of time-steps in the time interval $[t_0, t]$:

$$\langle |v(t, t_0)| \rangle = \frac{1}{N n_t} \sum_i \sum_{j=1}^{n_t} \left| \frac{\boldsymbol{b}_i(t_0 + j\Delta t) - \boldsymbol{b}_i(t_0 + (j-1)\Delta t)}{\Delta t} \right| \ . \tag{3.114}$$

Rejected moves

In a given time interval $[t_0, t]$ with $n_t = \frac{t - t_0}{\Delta t}$ being the number of time-steps in this interval, the total number of attempted moves is the product of the total number of

particles N and n_t. Here, a move is the combination of rotation and translational movement. Dividing the number of rejected moves by the total number of attempted moves gives us the fraction of rejected moves $\eta_{\mathrm{r}}(t, t_0)$.

Density distribution

For measuring the density distribution, we divide the simulation cell into a grid of smaller square-shaped cells with dimensions $l_\rho \times l_\rho$. The grid covers the whole simulation cell. In a single cell, the density is given by the number of rods in it divided by the cell's area. When a rod is only partly in the cell, it is only partly counted. A rod of length L of which the length l is in the cell contributes with the ratio l/L to the number of particles in the cell.
The density distribution at a certain time t is then calculated by using an array of discrete density intervals. The size of these intervals which we also call the resolution of the density distribution is $\Delta\rho$. So, the intervals are defined as $\{[i\Delta\rho, (i+1)\Delta\rho[\}$. For each of those intervals, we count the number of cells with a density in it. Also, the number of of cells with density 0 is counted separately. Since we want the distribution to be normalized, we divide all numbers by the total number of cells in the grid.
When mesuring the density distribution over a time interval $[t_0, t]$, we sum up the distributions at each time-step and normalize the resulting distribution by dividing by the number of time-steps in the interval.
The density distributions presented in the following sections were calculated using $l_\rho = 2.0\langle\tilde{\rho}\rangle^{-1}L$ since both isotropic and phase separated systems would be correctly identified for this cell size – see App. C.1.

Calculating phase separation from density distribution

We consider a system with two coexisting phases of low and high density. The density distribution will then exhibit two maxima – one at a low density and one at a high density. We want to determine the densities of the two phases from the density distribution. Ideally, the particles in the two phases would be evenly distributed so that the density would be homogeneous within each phase. Then, the density distribution would consist of only two peaks at the respective densities and we could determine the phases' densities by simply reading off the positions of the peaks.
However, this was not the case in the studied systems – the observed peaks were not as sharp for several reasons. First of all, we divide the simulation cell into a grid of small cells for measuring the local density. The grid's position is fixed, so it is unlikely that the phase boundary is equivalent to the cell boundaries. Instead, the phase boundary will usually cut through some of the cells which will cause the average density in these to be somewhere in between the densities of the two phases. Also, we do not analyse a system at a specific point in time but average over a time interval. We have to assume that the density in the two phases fluctuates over time yielding a smooth distribution after averaging instead of a sharply peaked one.
One option would be to use the positions of the two maxima, but this would not take into account the full information contained in the distribution. Instead, we split the distribution into two parts corresponding to low and high densities. Then, we average over these two partial distributions and get two densities representing the average densities in the two phases. This procedure guarantees that we use information about all densities present in the system instead of just the maximum values. However, by

splitting the distribution at a certain density $\tilde{\rho}_{\mathrm{sp}}$, we manually introduce a parameter that will affect the results we get for the densities. This parameter is obviously the value of $\tilde{\rho}_{\mathrm{sp}}$.
We opt to use the transition density for the isotropic-nematic phase transition in two-dimensional systems of infinitely thin rods without propulsion – see Section 3.1.4. According to Kayser and and Raveché, this is $\tilde{\rho}_{\mathrm{IN}} = 3\pi/2$ [173]. This value is the geometrical limit up to which an isotropic system of passive rod-like particles can exist without exhibiting ordering. Therefore, $\tilde{\rho}_{\mathrm{IN}}$ represents an upper bound for the density in the low-density phase, so we can definitely associate densities $\tilde{\rho} > \tilde{\rho}_{\mathrm{IN}}$ to belong to the high-density phase. Of course, this choice is somewhat arbitrary, and we could also use other values for $\tilde{\rho}_{\mathrm{sp}}$. The effect altering $\tilde{\rho}_{\mathrm{sp}}$ has on the results for the coexisting densities is discussed in App. C.2.

3.4 Simulation Results

The following section presents the results from simulations of active rodlike particles with and without confinement.

3.4.1 Inhomogeneity in confined geometries

Simulations were performed in confined geometries of various shapes – equilateral triangles, squares, and regular 12-sided polygons were used as simulation cells at average densities $\langle\tilde{\rho}\rangle = 1.0, 3.0, 5.0$. For self-propelled particles, we notice accumulation of particles near the cell's edges with time. This effect is not temporary but persists on large time scales. These inhomogeneities already occur at relatively low Péclet numbers like $Pe = 10$. For the same parameters, simulations with passive particles do not yield comparable effects. Instead, the particles in those simulations stay evenly distributed throughout the simulation cell. Snapshots of passive and active particles in a simulation cell shaped like a 12-sided regular polygon are shown in Fig. 3.14.
This observation is in qualitative agreement with the results presented by Fily et al. for spherical particles in a confined geometry [194] as well as the findings by Kaiser et al. for self-propelled rodlike particles trapped by a chevron-shaped obstacle [145]. These results are discussed in more detail in Section 3.2.4.
In most cases, the inhomogeneity in active systems can be identified by looking at the time-development of the system's centre of mass. In passive systems, this fluctuates around the position of the centre of mass in a homogeneous system $\boldsymbol{c}_{\text{hom}}$ within a radius dependent on the system's average density. In active systems, the distance between the centre of mass and $\boldsymbol{c}_{\text{hom}}$ is usually greater than in passive systems. Additionally, the centre of mass does not fluctuate around $\boldsymbol{c}_{\text{hom}}$ on the simulated time scales but tends to remain displaced towards one of the cell's edges. An example can be seen in Fig. 3.14. In case the centre of mass trajectories in comparable active and passive systems are very similar, we can still use the mass distribution tensor to identify inhomogeneity. This can happen when particles accumulate symmetrically in multiple edges which results in a centre of mass that is still near $\boldsymbol{c}_{\text{hom}}$. This kind of particle accumulation will yield greater eigenvalues compared to a homogeneous system though. An example for this is shown in Fig. 3.15.
The accumulation of particles near the edges creates an area of high density in which the particles consequently have a reduced free volume compared to an isotropic configuration. Due to the steric interactions between the particles, this should restrict their ability to move. By measuring the average speed, we can confirm this. It turns out that in the simulated active systems at $Pe = 10$, the average speed would be in the range $[0.15\, v_0, 0.30\, v_0]$ with v_0 being the propulsion speed. The exact value as well as the amount of fluctuations of the average speed depend on the cell shape and the systems' average density. Generally speaking, the average speed decreases with increased average density. The influence of the cell shape is not as clear. Cells with more edges and thereby wider angles in the edges tend to allow greater average speed.
The decrease of motility due to particle accumulation is so pronounced that the average speed in the active systems is lower than in the passive systems where particles move solely due to translational diffusion – at least this is what we find for $Pe = 10$. An example of this is shown in Fig. 3.14.
An explanation for the particles' reduced motility can be found by looking at the frac-

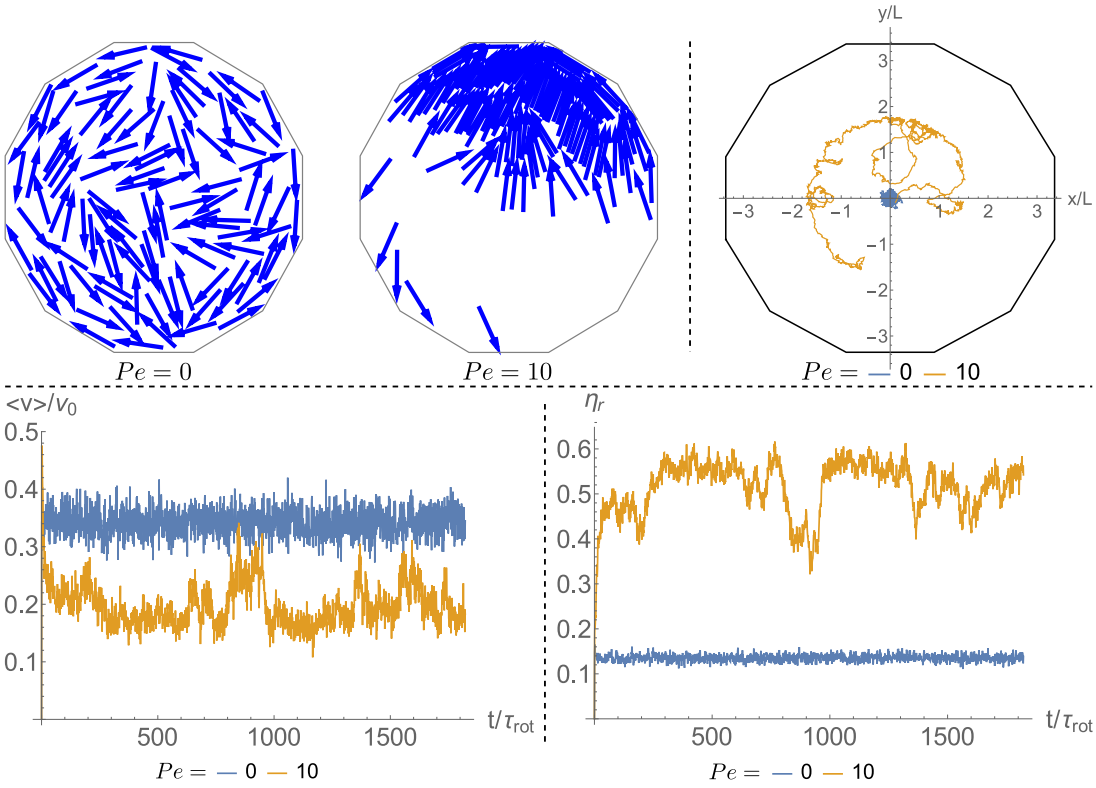

Figure 3.14: Top left: Typical snapshots of two systems of average density $\langle\tilde{\rho}\rangle = 3.0$ in a 12-sided regular polygon. The systems only differ in particle motility. Passive particles remain evenly distributed while self-propelled particles tend to accumulate near the cell's edges even at relatively small Péclet numbers. Arrows indicate the particles' orientations. Top right: Comparison of the time-development of the two systems' centres of mass over a time period $t_{\max} \approx 1800\tau_{\mathrm{rot}}$. In the passive system, the centre of mass fluctuates around the position expected for a homogeneous system. In the active system, the centre of mass is shifted towards the cell's edges which indicates particle accumulation. Its movement indicates that the accumulated structure is not static but changes position over time. Bottom left: Comparison of the time-development of the average speed $\langle v(t, t-\Delta t)\rangle$ in the two systems; v_0 denotes the propulsion speed of the particles in the active system. The timespan for averaging was chosen as $\Delta t = 0.91\,\tau_{\mathrm{rot}}$. We notice that the particles' average speed in the active system is lower than in the passive system despite self-propulsion. The reason for this is the significantly higher fraction of rejected moves. Bottom right: Comparison of the time-development of the fraction of rejected moves $\eta_{\mathrm{r}}(t, t-\Delta t)\rangle$ in the two systems with the same Δt as for the average speed. The fraction of rejected moves is significantly greater in the active system due to the reduced free volume per particle where they accumulate.

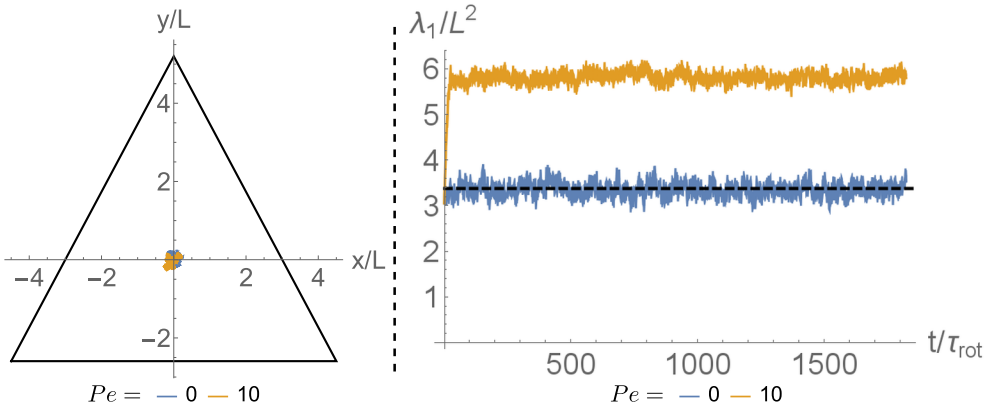

Figure 3.15: Left: Comparison of the centre of mass trajectories in a passive system and an active system with $Pe = 10$ in an equilateral triangle. Both systems have average density $\langle\tilde{\rho}\rangle = 3.0$. The trajectories are very similar making it impossible to decide whether the active system is inhomogeneous. Right: Comparison of the time-development of the mass distribution tensor's eigenvalue λ_1 in the two systems over a timespan $t \approx 1800\tau_{\mathrm{rot}}$. In the passive system, λ_1 remains similar to the value predicted for a homogeneous system (dashed line). In the active system, λ_1 is significantly greater – indicating inhomogeneity – at almost all times.

tion of rejected moves η_{r}. We notice that this value is significantly greater in active systems than in passive systems which indicates that particles collide more frequently as a result of their reduced free volume. This obviously leads to a decrease in average speed – when a large fraction of moves is rejected, particles need longer to travel a certain distance. Usually, η_{r} is in the range $[0.4, 0.6]$ in active systems. In passive systems, η_{r} strongly depends on the average density. For systems with $\langle\tilde{\rho}\rangle = 1.0$, it can be as low as 0.02 while for $\langle\tilde{\rho}\rangle = 5.0$, it can be in the range of 0.3. An example can be seen in Fig. 3.14.
Plotting the density distributions for the active and passive systems confirms what we can observe in the snapshots. Regardless of the cell shape, we find density distributions peaked around the system's average density indicating isotropy for passive particles. In active systems, we get distributions with one maximum at $\tilde{\rho} = 0$ and another one at a high density indicating phase separation. Density distributions for different cell shapes can be seen in Fig. 3.16.

Even though inhomogeneity is reflected in all of the measurements described above, it does not seem to have a clear effect on the degree of nematic order quantified by the nematic order parameter S. Comparisons of S in passive and active systems do not show any differences that are consistent for different cell geometries or average densities. Other works have reported enhanced ordering in active systems compared to passive systems [179]. However, those simulations were performed with periodic boundary conditions, so the confinement in our simulations could be the factor preventing this effect.

To conclude, we find inhomogeneity in active systems while similar systems with passive particles remain homogeneous on long time scales. This is not only observed in snapshots of the simulations but also reflected in the centres of mass, mass distribution tensors, and density distributions. Since the only difference in the systems is the

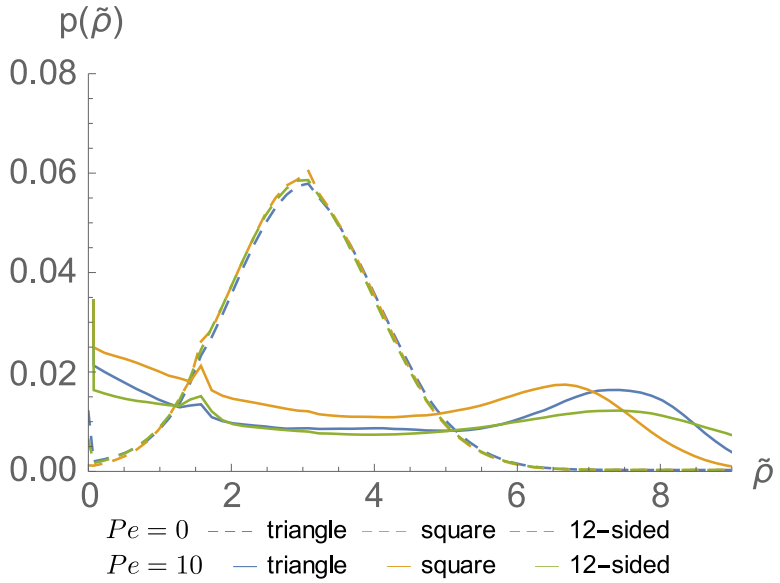

Figure 3.16: Density distributions for active and passive systems of average density $\langle\tilde{\rho}\rangle = 3.0$ in simulation cells of different shapes. The particles' motility in the active systems is $Pe = 10$. The simulated cell shapes were regular polygons with 3 (triangle), 4 (square), and 12 (12-sided) edges. Passive systems exhibit distributions that have a single peak at the average density which is characteristic for homogeneous systems. For active systems, we find two maxima – one at $\tilde{\rho} = 0$ and the second one at a density greater than the average density.

particles' motility, we can conclude that self-propulsion is the cause for the observed inhomogeneity. As we can see in snapshots, particles tend to accumulate near the edges of the simulation cell rather than within the cell. This is also confirmed by the centres of mass and mass distribution tensors in these systems. As a result of the accumulation, the particles are significantly slowed down as is reflected in the measured average speeds.
Active particles have also been observed to form immobile clusters without confinement though – see Section 3.2.4. The absence of this type of clustering in our simulations in combination with the occurrence of particle accumulation near the cell edges suggests that confinement is strongly beneficial for the observed inhomogeneity. The reasoning is that if particle accumulation is much more likely near the cell edges, immobile clusters within the cell will not be observed. Once the particles have accumulated near the edges, the density within the cell is too low to induce clustering.

Reversing orientation at cell boundaries

A first attempt to eliminate the influence of confinement was to provide the particles with the ability to reverse their orientation when hitting a cell boundary. As described in the previous section, we observe accumulation of particles near edges of the simulation cell. It is easy to see why a single self-propelled particle would get stuck in an edge of the simulation cell. The most likely case is that it arrived in the edge by actively moving there. It would also be possible for the particle to have been moved into the edge by translational diffusion, but this is less likely. Since $Pe \gg 1$ in our simulations,

particle motion is dominated by self-propulsion with translational diffusion being only a weak contribution.
Now, when assuming a particle was driven into an edge due to its self-propulsion, its front end will be pointing towards the edge. Since the cell boundaries are impenetrable, the particle can only escape from the edge by rotating until it is pointing away from the edge. However, the particles are not capable of actively rotating. The only mechanism causing rotation is rotational diffusion. Hence, the time scale for a single particle rotating away from an edge is the rotational diffusion time τ_{rot}.
When considering multiple particles, rotation could also be caused by angular momentum resulting from the interaction between particles. However, the main effect the presence of other particles has is that it significantly hinders rotation due to steric interactions. In order to rotate freely, a particle needs a free volume in the order of L^2 which is equivalent to a local density in the order of $\tilde{\rho} = 1$. As soon as the local density becomes greater than this, particles start blocking each other and preventing each other's rotation. Therefore, particle accumulation near edges is a self-perpetuating process – it increases the local density which in return slows down the breaking up of the accumulation. Since the rate of particles joining the accumulation does not change until the density in the rest of the system is significantly lowered, this leads to further growth, increasing the density even more.
Allowing the particles to reverse their orientation provides a possibility for them to rotate away from the edge on a time scale much shorter than the rotational diffusion time without being hindered by other particles. Hence, if this was enough to prevent particle accumulation, we would have a good indication that confinement is the main factor causing inhomogeneity.

Simulations were performed in the same simulation cells as the confined systems described above with the same simulation parameters. We find that the particles' ability to reverse their orientations does affect particle accumulation, but the extent of this depends on the system's average density. Evaluating the systems' centres of mass and their mass distribution tensors, we see that the degree of inhomogeneity is significantly reduced at the average densities $\langle\tilde{\rho}\rangle = 1.0$. Also, the particles' average speed is greater than in passive systems at this average density, and the fraction of rejected moves is almost as low as in passive systems. These observations are all indications that implementing a reversal mechanism greatly reduces the particles' tendency to accumulate. Their increased motility compared to the systems described above can be explained by the greater free volume they have when not accumulated.
At $\langle\tilde{\rho}\rangle = 5.0$, the picture completely changes. None of the measured quantities show a consistent deviation from the systems without reversal mechanism. Particle accumulation is as pronounced as in those simulations, the particles' average speed is mostly the same, and the fraction of rejected moves remains unchanged as well.
In systems of intermediate simulated density $\langle\tilde{\rho}\rangle = 3.0$, some of the effects observed at low densities can be found. The particles' average speeds in these systems is still significantly increased, and the fraction of rejected moves fluctuates between the values for regular active systems and passive systems. Hence, we still note an increased particle motility. The degree of inhomogeneity seems to be mainly unchanged though. Only the system in the 12-sided cell exhibits reduced inhomogeneity. In the other two cells, simulation snapshots indicate that particle accumulations tend to break up sooner than in regular systems, but these systems are still mostly inhomogeneous.

We can summarise that the particles' ability to reverse their orientation can eliminate or at least reduce the probability of particle accumulation in confined systems at low average densities. At medium densities, this ability does not notably suppress particle accumulation but still increases particle motility. At high densities, there is almost no difference between systems with and without a reversal mechanism though. Assuming that reversal of orientation reduces the influence of the confining walls on the system, we can confirm that confinement does promote particle accumulation, but at high densities, particle interactions may be the dominant mechanism driving accumulation.

3.4.2 Inhomogeneity in periodic systems

In order to study particle accumulation as a result of interactions, we performed simulations of self-propelled particles in periodic simulation cells at average densities from $\langle\tilde{\rho}\rangle = 2.0$ to $\langle\tilde{\rho}\rangle = 5.0$ at Péclet numbers $Pe = 10$ to $Pe = 100$. Several other works have presented the formation of immobile clusters as well as collectively moving patterns such as lanes, clusters, and swirls exclusively due to interactions among the particles – see Sections 3.2.4 and 3.2.4. All of these patterns involve inhomogeneous density distributions as the particle density is greater within the patterns than in the surrounding area. Hence, these patterns represent a kind of phase separation.
It turns out that we can observe such inhomogeneities at motilities as low as $Pe = 20$ even at average densities $\langle\tilde{\rho}\rangle = 2.0$. We find a variety of different types of configurations in inhomogeneous systems comparable to the patterns mentioned above. These include asters, polar clusters, and enclosed lanes.

Asters Asters are characterized by an approximately circular shape with the particles pointing towards the cluster's centre. Such a configuration causes the particles to block each other which is reflected in the particles' average speed $\langle v(t, t-\Delta t)\rangle$. Measuring this quantity over time intervals $\Delta t = 0.91\,\tau_{\mathrm{rot}}$ yields values as low as $\langle v(t, t-\Delta t)\rangle = 0.002 v_0$ – with v_0 being the particles' propulsion speed – when the system is in an aster configuration. Hence, particle motility is extremely suppressed. These immobile clusters appear at all simulated densities for $Pe \geq 30$ but are quite rare and break up quickly. The probability of their occurence as well as the time for which they are stable increases with particle motility. These observations agree well with the findings of Yang et al. presented in Section 3.2.4. The particles in our asters are also oriented towards the centre, and increased particle motility – which is equivalent to reduced noise in their simulations – increases the time it takes for asters to break up.

Polar clusters In a polar cluster, particles are aligned along a common axis with their orientations varying in a small range around the axis' orientation. Sometimes, these clusters are also referred to as swarms [125, 141, 143, 147]. Since the particles move roughly in the same direction instead of blocking each other, the average speed is significantly larger than in asters. For the simulated parameters, we find average speeds ranging from $0.3 v_0$ to $0.6 v_0$ in polar clusters. The lower values tend to occur in systems with larger average densities and higher Péclet numbers. Compared to asters, these clusters appear to be less dense which is probably another reason why particles are still motile.

Polar clusters are the dominant configuration for almost all simulated parameters. Only at high particle motilities, their occurence becomes less frequent. For average densities $\langle\tilde{\rho}\rangle = 2.0$, this is the case for $Pe \geq 80$ whereas for $\langle\tilde{\rho}\rangle = 5.0$, this can already be observed at $Pe \geq 40$. The observation of collectively moving clusters is in good agreement with previous works, see Section 3.2.4. Wensink et al. simulated self-propelled rods with steric interactions and found collectively moving clusters for volume fractions $\phi \approx 0.25$ and aspect ratios $a \gtrsim 7$ [141, 143]. The authors assumed a particle speed comparable to that of Bacillus subtilis which they specify as $30 - 100\,\mu\text{m/s}$. In our model, this corresponds to a Péclet number of $Pe = 20 - 66$. A volume fraction of $\phi = 0.25$ is equivalent to $\tilde{\rho} = 2.5$ for our particles of aspect ratio of $L/d = 10$. Since our simulation parameters are in a similar range, it is plausible that we find collectively moving clusters. Yang et al. performed similar simulations and found collectively moving clusters at all densities [142] which complies with our findings. However, they observed that the particles' motility needed to exceed a critical value in the range $Pe > 100$ to enable cluster formation which is not the case in our simulations. Abkenar et al. reported collectively moving clusters to be the predominant phase at small and medium densities in their simulations [147]. Our observations agree with this, but the simulations are not entirely comparable since Abkenar et al. implemented a soft potential that allowed overlapping of particles.

Enclosed lanes Enclosed lanes are similar to polar clusters in that they also exhibit a high degree of order. They consist of a central lane of mostly parallel particles that is enclosed by two layers of particles pointing towards the lane on either side. The particles in these layers are also mostly parallel. Due to the high degree of ordering, particles in enclosed lanes can be tightly packed – resulting in high densities. Judging from the snapshots, the density is clearly greater than in polar clusters. This high density significantly slows down the particles. However, the resulting average speed varies greatly with the particles' motility. Smaller Péclet numbers yield higher average speeds in enclosed lanes. For example, in systems with average density $\langle\tilde{\rho}\rangle = 5.0$, we get $\langle v(t, t - \Delta t)\rangle \approx 0.002 v_0$ for $Pe = 100$ and $\langle v(t, t - \Delta t)\rangle \approx 0.05 v_0$ for $Pe = 30$. Average speeds were again measured over a timespan $\Delta t = 0.91\,\tau_{\text{rot}}$. In fact, not only is $\langle v(t, t-\Delta t)\rangle/v_0$ greater in systems with smaller Péclet numbers but also the absolute average speed $\langle v(t, t-\Delta t)\rangle$. The reason for this is unclear. One possible explanation is that the pressure from the outer layers on the central lane decreases with the particles' propulsion speed. The lower pressure would lead to lower density in the central lane. This is equivalent to a greater free volume per particle which would allow them to move faster due to the reduced number of collisions. In fact, we find that the fraction of rejected moves η_{r} decreases with the Péclet number in enclosed lanes. In the example mentioned above of systems with average density $\langle\tilde{\rho}\rangle = 5.0$, we find $\eta_{\text{r}} \approx 0.98$ at $Pe = 100$ and $\eta_{\text{r}} \approx 0.84$ at $Pe = 30$.
The probability of finding enclosed lanes increases with particle motility and is also dependent on the system's average density. For $\langle\tilde{\rho}\rangle = 2.0$, they become increasingly prevalent at $Pe \geq 80$ whereas for $\langle\tilde{\rho}\rangle = 5.0$, this is already the case at $Pe \geq 40$. It should be pointed out that the enclosing layers we observe have not been reported in other works. Comparable simulations have shown either single lanes in which all particles move in the same direction or multiple lanes moving in opposite directions, see Section 3.2.4.

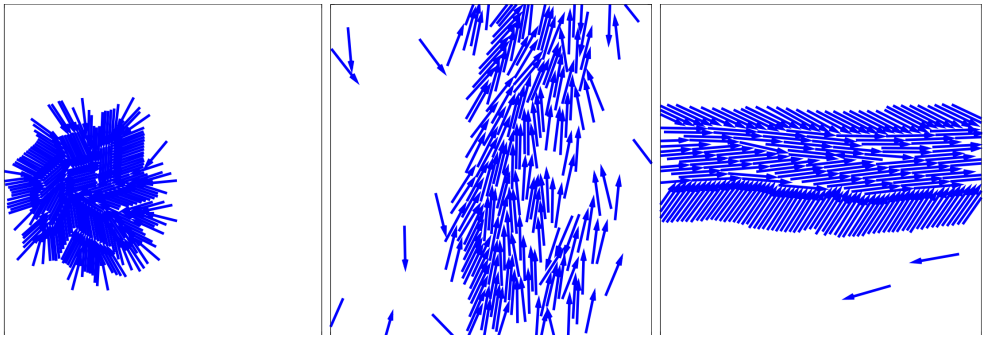

Figure 3.17: Examples for different types of phase-separated configurations. From left to right: 1. aster, snapshot from a system of average density $\langle\tilde{\rho}\rangle = 2.0$ with particle motility $Pe = 100$, 2. polar cluster, $\langle\tilde{\rho}\rangle = 3.0$, $Pe = 50$, 3. enclosed lane, $\langle\tilde{\rho}\rangle = 4.0$, $Pe = 80$.

Snapshots of the inhomogeneous patterns described above are shown in Fig. 3.17. They all have in common that they consist of two coexisting phases. One of these has a high density and exhibits some kind of order: in asters, particles point towards a common centre, and in collectively moving clusters as well as in enclosed lanes, particles are oriented along a common axis. The other phase is unordered and has a low density. We can therefore regard all the phenomena described above as a kind of phase separation.

In most cases, the patterns can be distinguished by their different nematic order parameters S. An example plot for a system in which all three patterns occur over time is shown in Fig. 3.18. In asters, S is low since the particles point towards the centre and therefore are not aligned. In polar clusters, we get the greatest values for S as the involved particles are aligned along a common axis with only small deviations. In enclosed lanes, S is lower than in polar clusters as the particles in the central lane are almost perfectly aligned, but the particles in the outer layers point towards the central lane at an angle. Depending on this angle as well as the ratio between the number of particles in the central lane and outer layers, S can vary significantly in enclosed lanes and can become as low as in asters. Hence, the nematic order parameter is not in all cases sufficient for identifying a system's configuration. However, we have never observed the formation of asters after the system had already been in one of the other two configurations. Hence, when observing a transition from a configuration with large S to another stable configuration with lower S, we can safely assume that this is a transition from a polar cluster configuration to an enclosed lane. This can of course easily be checked by looking at snapshots from the simulation.

The separation of the two coexisting phases seems to be more pronounced at higher propulsion speeds – increasing the density in the dense phase and further emptying the phase of low density. We want to quantify this observation and use the density distribution to measure the densities in the coexisting phases and how they depend on the particles' motility. The method we used is described in Section 3.3.7.
Using the values we obtain for the coexisting densities, we can plot a phase diagram illustrating the dependence of the resulting densities on the particles' motility – see Fig.

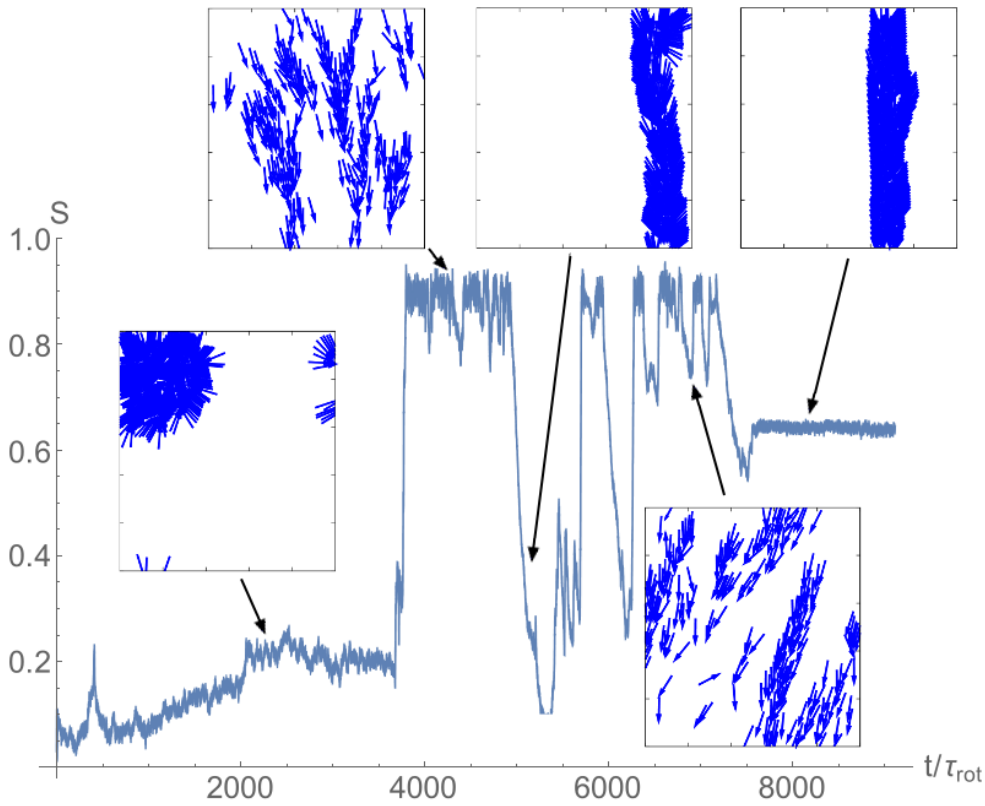

Figure 3.18: Time-development of the nematic order parameter in a system with average density $\langle\tilde{\rho}\rangle = 5.0$ and $Pe = 100$ and simulation snapshots. We see that the transition from an aster configuration at $t/\tau_{\text{rot}} < 3500$ to a polar cluster is accompanied by a drastic increase in S. For $t/\tau_{\text{rot}} > 7500$, the system exhibits an enclosed lane configuration with a nematic order parameter that is clearly lower than in the polar cluster configuration.

3.19. The data points in this plot are average values of simulations of 10 systems with about $N = 200$ particles each. The size of the simulation cell was adjusted to yield the desired average density for each system. We see that for all values $\langle\tilde{\rho}\rangle$, systems remain in a homogeneous single-phase state up to a Péclet number of $Pe = 10$. At $Pe \geq 20$, we find two coexisting phases of different densities. This phase separation becomes more pronounced at greater particle motilities meaning that the density of the high-density phase increases, and the density of the low-density phase decreases.

In conclusion, we can say that we can find a variety of collectively moving patterns as well as immobile clusters in systems without confinement. This is in agreement with a number of other works as outlined in Sections 3.2.4 and 3.2.4. All of these phenomena are associated with inhomogeneous density distributions as the patterns have greater particle densities than the surrounding area. These patterns also have a certain kind of order in contrast to the surrounding which is isotropic. Therefore, we have two coexisting phases, and we can therefore regard the phenomena described above as a kind of phase separation. By measuring the density distributions, we were able to get a phase diagram indicating the inhomogeneity. This diagram shows that phase

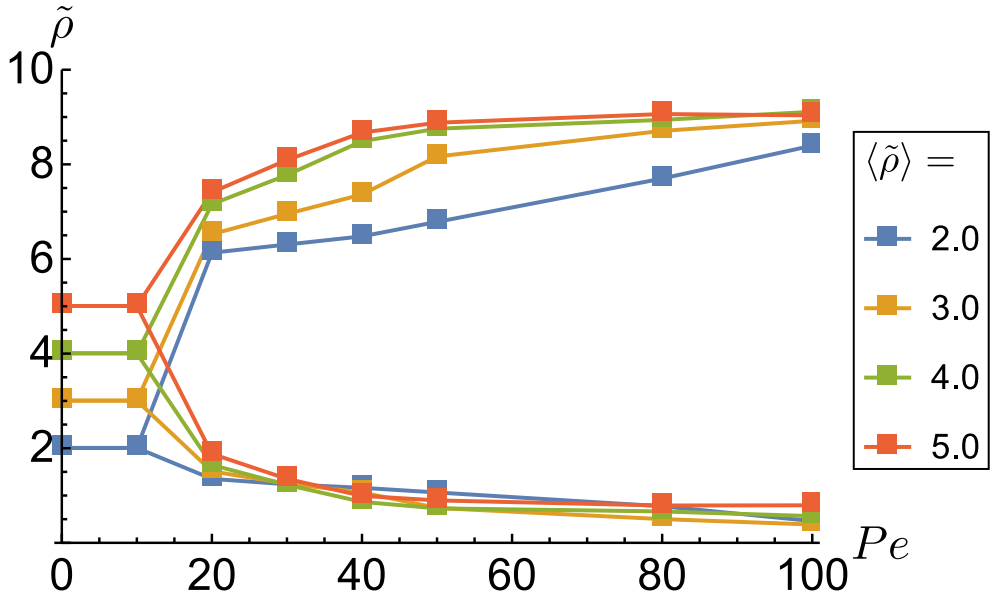

Figure 3.19: Coexisting densities as a function of particle motility in periodic systems of varying average densities. We see that for all average densities, phase separation occurs when $Pe \geq 20$. For smaller Péclet numbers, systems remain homogeneous. Phase separation becomes more pronounced with increased particle motility – the density of the high-density phase increases while the density of the low-density phase decreases.

separation occurs as soon as the particles' motility exceeds a certain Péclet number and becomes more pronounced with increasing Péclet numbers.

3.4.3 Swirling patterns

As described in Section 3.2.4, circular patterns have been observed in a number of different active particle systems. Swirls were reported to form in systems of vibrated rods with a non-symmetrical mass distribution [110] as well as in motility assays of biofilaments propelled by motor proteins [124–126]. In some cases, these findings could also be reproduced in simulations [110, 124, 126]. In all of these examples, a sufficiently large particle density was required to enable the formation of swirls. The swirls' typical diameters ranged from $5L$ [110] to $40L$ [125] with L denoting the particle size.

We did not observe any comparable patterns in our simulations even though our simulation parameters such as particle density and motility were in the same range as in the works mentioned above. One major difference was the particles' aspect ratio though. While the particles in our simulations had an aspect ratio of $a = 10$, the vibrated rods studied by Kudrolli et al. only had an aspect ratio of 2 [110] while the biofilaments in the motility assays by Schaller et al. and Sumino et al. had aspect ratios > 500 [124–126]. This could be a reason why swirls were not found in our simulations. Another possible explanation is the system size in our simulations which is significantly smaller than in the mentioned experiments. The maximum system size we used was in the range of $10L$ which is already smaller than the swirl sizes observed in the motility assays by Schaller et al. and Sumino et al. [124–126]. Even in comparison to the swirls observed by Kudrolli et al. for vibrated rods [110], this is not very large. A comparable swirl would have to span almost the entire simulation cell.

In order to check whether we might still be able to find swirling patterns, we generated systems that were already in a swirling configuration from the start of the simulation. This way, we could study if a swirling configuration would even be stable in our systems. It turned out that the swirling patterns would break up almost immediately regardless of cell shape and particle motility. Therefore, we have to conclude that our systems were not suitable for reproducing swirling patterns. These patterns were not even stable when they were manually generated, so they would not occur spontaneously during a regular simulation either.

3.5 Analytical approaches I: force equilibrium

3.5.1 Force equilibrium in enclosed lanes

In this section, we will try to find an approximation for the density of the high-density phase in a phase-separated system using a simplified model of the enclosed lanes commonly found in phase-separated systems. We derive this density from a force equilibrium ansatz.
In Fig. 3.17, snapshots of frequently observed configurations in phase-separated systems are shown. One recurring pattern are enclosed lanes. These can be described as being divided into three distinct areas. In the centre, we see a lane of particles with almost perfect alignment extending throughout the whole length of the simulation cell. This lane is enclosed by two layers of aligned particles pointing towards the centre. We will use an idealised version of this configuration to calculate the relevant forces and derive the lane's density.
We approximate the central lane to consist of N_{lane} parallel layers. Each layer consists of a column of particles in which each particle's front end is in direct contact with the rear end of the particle in front of it. The distance between two neighbouring layers is x. For the layers enclosing the central lane, we assume perfectly parallel particles at distance d_{out} to each other whose front end is in direct contact with the particles in the outmost layer of the central lane. The angle between these particles' orientation and an axis perpendicular to the central lane, we call α_{out}. A sketch of this approximation can be found in Fig. 3.20.
We know the particles' propulsion speed v_0 and their friction coefficient $\gamma_\parallel$, so we can calculate the force a single particle in the outer layer exerts on the central lane:

$$f_1(\alpha_{\text{out}}) = \gamma_\parallel v_0 \cos\alpha_{\text{out}} \ . \tag{3.115}$$

The distance l_{out} between the contact points on the central lane of two neighbouring particles in the outer layer is

$$l_{\text{out}} = \frac{d_{\text{out}}}{\cos\alpha_{\text{out}}} = \frac{L}{\tilde{\rho}_{\text{out}} \cos\alpha_{\text{out}}} \tag{3.116}$$

with $\tilde{\rho}_{\text{out}}$ being the dimensionless density of the outer layer. The number of particles exerting a force onto a single particle in the outmost layer of the central lane is then given by

$$n_{\text{out}} = \frac{L}{l_{\text{out}}} = \tilde{\rho}_{\text{out}} \cos\alpha_{\text{out}} \ , \tag{3.117}$$

so the total force exerted onto the same particle is

$$f_{\text{tot}}(\alpha_{\text{out}}) = n_{\text{out}} f_1(\alpha_{\text{out}}) = \tilde{\rho}_{\text{out}} \gamma_\parallel v_0 \cos^2\alpha_{\text{out}} \ . \tag{3.118}$$

Next, we calculate the forces within the central lane. As described in Section 3.3.2, we assume the interaction between particles to be given by a Lennard-Jones potential. The force $f_{\text{LJ}}(x)$ between two perfectly aligned filaments at a distance x can easily be calculated from the force between individual segments presented in (3.78):

$$f_{\text{LJ}}(x) = 48\frac{\epsilon}{x}\left(\frac{d}{x}\right)^{12} - 24\frac{\epsilon}{x}\left(\frac{d}{x}\right)^{6} \ . \tag{3.119}$$

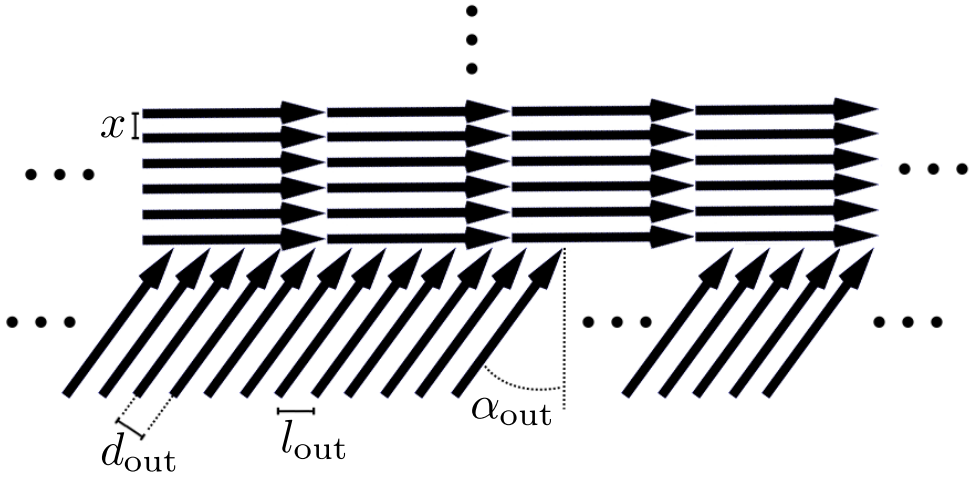

Figure 3.20: Sketch of the configuration used for calculating the density of the high-density phase in a phase-separated system via a force equilibrium. Particles in the central lane are perfectly aligned with their neighbours. Particles in the outer layer are also parallel to each other but hit the central lane at an angle α_{out}.

Since we assume the layers within the central lane to be equidistant, the forces acting between all of them are the same. Considering a section of length L of the central lane, the total force is then $f_{\text{LJ}}(x)$. On each side of this section, the outer layer exerts the force $f_{\text{tot}}(\alpha_{\text{out}})$. Hence, the force equilibrium is given by

$$f_{\text{tot}}(\alpha_{\text{out}}) - f_{\text{LJ}}(x) = 0 \tag{3.120}$$

$$\tilde{\rho}_{\text{out}}\gamma_{\parallel}v_0\cos^2\alpha_{\text{out}} - 48\frac{\epsilon}{x}\left(\frac{d}{x}\right)^{12} + 24\frac{\epsilon}{x}\left(\frac{d}{x}\right)^{6} = 0\ . \tag{3.121}$$

We solve this for x numerically using Mathematica[3] to get the distance of the particles in the central lane that leads to exact compensation of the forces exerted by the outer particles and the forces resulting from repulsive interaction within the central lane. With x, we can calculate the density of the central lane

$$\tilde{\rho}_{\text{in}} = \frac{L}{x}\ . \tag{3.122}$$

To get the total density of the whole area $\tilde{\rho}_{\text{fe}}$, we have to calculate the average of $\tilde{\rho}_{\text{in}}$ and $\tilde{\rho}_{\text{out}}$ weighted by the respective areas $A_{\text{in}} = N_{\text{lane}}Lx$ and $A_{\text{out}} = L^2\cos\alpha_{\text{out}}$:

$$\tilde{\rho}_{\text{fe}} = (\tilde{\rho}_{\text{in}}A_{\text{in}} + \tilde{\rho}_{\text{out}}A_{\text{out}})/(A_{\text{in}} + A_{\text{out}})\ . \tag{3.123}$$

The total density is affected by a number of parameters, namely: the density in the outer layer $\tilde{\rho}_{\text{out}}$, the outer filaments' angle relative to the central lane α_{out}, the particle motility Pe, and the number of layers in the central lane N_{lane}. We used the following parameter ranges for calculating the density: $\tilde{\rho}_{\text{out}} \in [5, 10]$, $\alpha_{\text{out}} \in [0, \frac{\pi}{4}]$, $Pe \in [10, 100]$, $N_{\text{lane}} \in [2, 20]$. Plotting $\tilde{\rho}_{\text{fe}}$ as a function of Pe for different parameters gives us curves that we can compare to the phase diagram we generated using our simulation results. Qualitatively, these look similar, i.e., the density increases with the Péclet

[3]Mathematica uses Newton's Method for finding roots

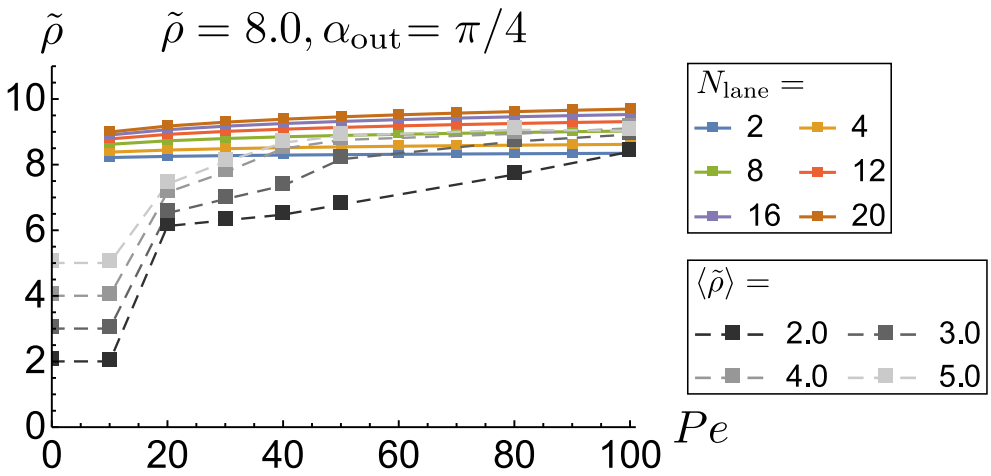

Figure 3.21: Total density $\tilde{\rho}_{\text{fe}}$ as a function of particle motility from force equilibrium calculation (coloured lines) compared with simulation results (dashed lines). Different shades of grey indicate different average densities in the simulated systems while different colours indicate different numbers of layers N_{lane} in the calculation. Parameter values for the density of the outer layer $\tilde{\rho}_{\text{out}} = 8.0$ and the angle $\alpha_{\text{out}} = \pi/4$ were chosen within the range that yields good agreement with the simulation data – especially at high particle motilities. At low Péclet numbers, the simulation results cannot be reproduced though. The different curves also demonstrate that larger N_{lane} yield larger total densities.

number. However, this dependence is very weak for the densities we derived using the above model – they are almost constant in contrast to the simulation results which exhibit a significant increase in density for particle motilities in the range $Pe < 50$. At higher particle motilities, the densities we obtain from simulations also become almost independent from the Péclet number – except for systems with average density $\langle\tilde{\rho}\rangle = 2.0$.
Quantitatively, we find that the analytical results vary a lot, and we only find good agreement for certain parameter values. The most significant parameter seems to be the density of the outer layer $\tilde{\rho}_{\text{out}}$ which is not surprising as it not only determines the density of the central lane but also directly affects the total density to a large extent – see Eq. (3.123). The number of layers in the central lane N_{lane} also has a significant effect on the calculated results while the angle α_{out} as well as the particle motility only have a minor influence. The calculated densities match best with simulation data for $\tilde{\rho}_{\text{out}} \in [6.5, 8.5]$. This is especially true at high particle motilities $Pe \geq 50$ and average densities $\langle\tilde{\rho}\rangle \geq 3.0$. As we can see in the simulation results, these values for $\tilde{\rho}_{\text{out}}$ are in the range we find for the high-density phase, so we can be assured that they are realistic. Higher values of $\tilde{\rho}_{\text{out}}$ result in significantly higher total densities while lower values result in lower total densities.
A direct comparison of simulation data and analytical results for $\tilde{\rho}_{\text{out}} = 8.0$ and $\alpha_{\text{out}} = \pi/4$ is shown in Fig. 3.21.

To conclude, this model can give a good estimate for the density of the high-density phase in a phase-separated system when the parameters are chosen accordingly. However, the model has a few weaknesses. First of all, it is based on a very specific config-

uration that occurs frequently in systems with high particle motility but is not the only configuration we find for phase-separated systems. Especially at lower Péclet numbers, polar clusters are more common than enclosed lanes. Since these clusters tend to have a lower density than enclosed lanes – judging from simulation snapshots – the average density in phase-separated systems will be decreased when the probability of finding enclosed lanes decreases. This is one likely reason why the model does not reproduce the total density's strong dependence on particle motility we find in simulation data at Péclet numbers $Pe < 50$.
Another weakness of the model is that it is not very sensitive to changes in the particle motility. This results from the Lennard-Jones potential between the particles – more precisely the repulsive contribution. This term is proportional to x^{-12}, so a small decrease in the layer distance would result in a greatly increased force between the layers. Vice versa, a great increase in force would be required to achieve even a small increase in density in the central lane as this density is inversely proportional to the layer distance. Since the force applied by the outer layers is directly proportional to the particle motility, such an increase in force is not achieved in the range of Péclet numbers we considered. This could be another explanation why the model does not simultaneously agree with the simulation data at low and high Péclet numbers.
Another major weak point is that this model does not take into account the low-density phase. Neither do we consider it for calculating $\tilde{\rho}_{\mathrm{fe}}$, nor do we get any prediction for the density of the low-density phase itself. Instead, the model includes the density of the outer layer $\tilde{\rho}_{\mathrm{out}}$ as a freely chosen parameter. To a large extent, the total density is immediately determined by this parameter as can be seen in Eq. (3.123). This aspect is another weakness of the model since we cannot gain a lot of new insight into the problem at hand when the results depend so strongly on a parameter that is not determined by prior experimental, analytical, or numerical results.

3.5.2 Particle currents

A method for approximating the density of the gas phase in a phase-separated system of active spherical particles has been presented by Redner et al. [135] – see Section 3.2.5. This has been adapted for rod-like particles by Abkenar et al. [147]. The general idea is to consider a dynamic equilibrium between a gas phase and a cluster of particles. Exchange of particles between the two phases is described by rate equations which have to give equal particle currents to maintain an equilibrium state. Assuming an isotropic distribution in the gas phase, the attachment rate can be derived as

$$J_{\mathrm{att}} = \frac{\rho_{\mathrm{gas}} D_{\parallel} Pe}{4L} \ . \tag{3.124}$$

For the cluster phase, it is expected that only particles at the outermost layer can leave the cluster by detaching. These particles are assumed to rotate freely until their orientation is perpendicular to the cluster surface and then detach. The time it takes a particle to rotate from an orientation parallel to the cluster surface by $\pi/2$ is determined by the rotational diffusion constant D_{rot}. The detachment rate is then given by

$$J_{\mathrm{det}} = \frac{8 D_{\mathrm{rot}}}{\pi^2 L} \ . \tag{3.125}$$

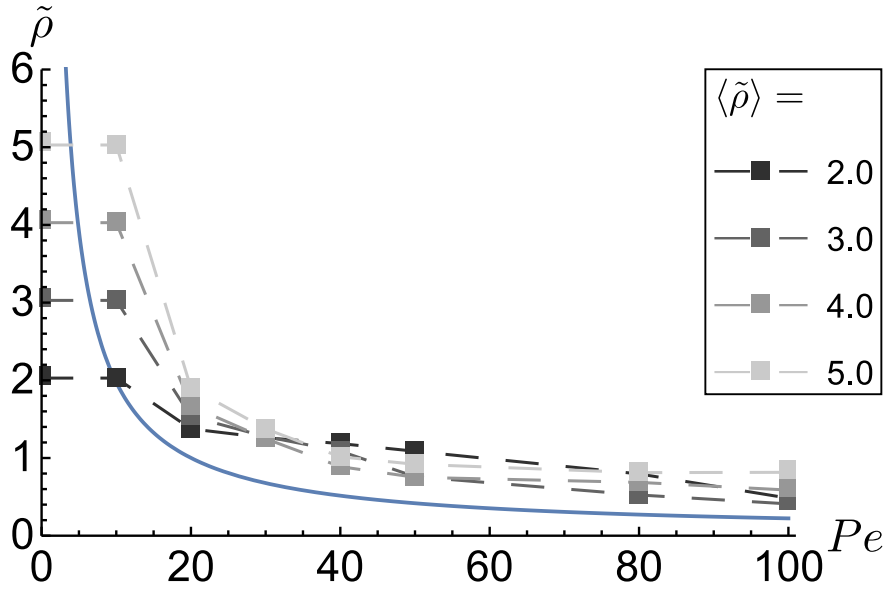

Figure 3.22: Density of the isotropic phase as a function of particle motility in a phase-separated system as derived from a model using attachment and detachment rates (blue line) compared to simulation results (dashed lines). At Péclet numbers that cause phase separation in simulated systems, the densities of the isotropic phase are greater than those predicted by the model but are generally in the same order of magnitude.

Equating the two and solving for ρ_{gas} gives us

$$\rho_{\text{gas}} = \frac{192}{\pi L^2}\frac{1}{Pe} \tag{3.126}$$

for the density of the gas phase. It is independent of the systems's average density. The calculation includes several approximations, e.g., particles are assumed to rotate freely even though they are part of the cluster. Also, they are assumed to stay attached to the cluster until they have rotated by an angle $\pi/2$. However, Abkenar et al. found good agreement between their analytical estimate and their simulation results for Péclet numbers $Pe \leq 25$. Also, their model allows particles to overlap for which an energy E is necessary. When increasing E, they found that their analytical result for the density of the gas phase held up for even higher values of Pe. Since our model does not allow particles to overlap – which could be expressed as the limit $E \to \infty$ – Eq. (3.126) should provide a good prediction for our simulation results.

The plot in Fig. 3.22 compares the theoretical prediction to our results. It shows qualitative agreement in that higher Péclet numbers result in lower densities for both. However, the model gives us the density of a gas phase for every Péclet number, while in simulations, we only find phase separation for $Pe \geq 20$. This discrepancy can be explained by the fact that the model already assumes the existence of phase separation without ensuring that this is a stable configuration at the given parameters. Quantitatively, the densities predicted by the above model agree fairy well with the simulation results for $Pe \geq 20$ even though they are generally lower. This deviation could have several causes. Considering the margins of error associated with the splitting density – see App. C.2 – it is possible that we just chose an incorrect value $\tilde{\rho}_{\text{sp}}$. Also, it is conceivable that the measured density distributions are smeared out due to the limited

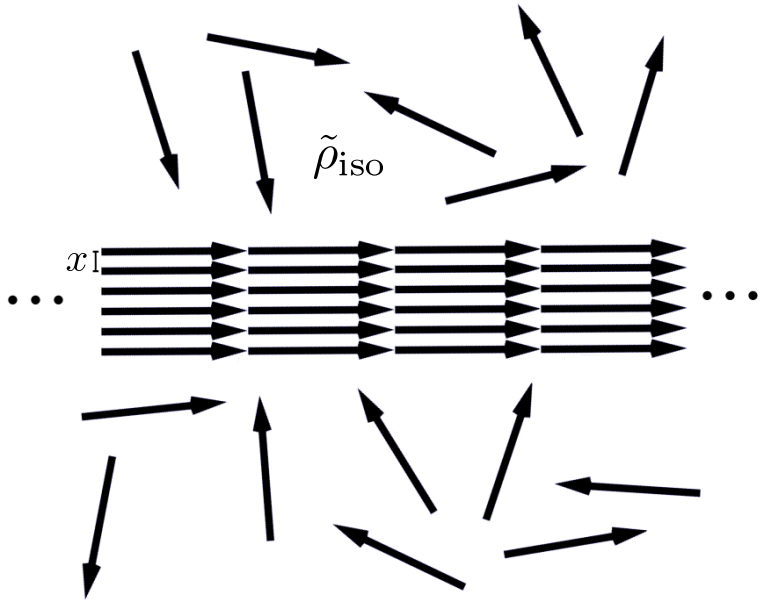

Figure 3.23: Sketch of the model used for deriving the density of the high-density phase from the forces applied by the two phases in a phase-separated system. Particles in the central lane are perfectly aligned with all their neighbours. The low-density phase is isotropic with a density $\tilde{\rho}_{\mathrm{iso}}$.

number of particles we used in the simulations. Density distributions of larger system would possibly have more pronounced peaks and densities between them would be less likely. This suppression of intermediate densities would yield an average density for the isotropic phase that was closer to the distribution's maximum at low densities. Additionally, there are still the approximations described above to derive Eq. (3.126). In contrast to the model implemented by Abkenar et al., the particles in our model are not allowed to overlap which makes them even more unlikely to rotate freely in the high-density phase. Particles hindering each other's rotation in the high-density phase would lower the detachment rate J_{det} and therefore result in lower values for ρ_{gas}.

3.5.3 Force equilibrium of coexisting phases

In Section 3.5.1, we found that we could derive a fairly good estimate for the density of the high-density phase in a phase-separated system – at least at high particle motility – from analysing the force equilibrium in a specific configuration. In Section 3.5.2, we saw that analysing the dynamic equilibrium of particle exchange between a coexisting gas phase and a dense cluster can yield a prediction for the density of the gas phase. We will now try to combine the two models in order to get a complete description of the densities in phase-separated systems. Similar to the approach in Section 3.5.1, we consider a lane of perfectly aligned particles as the high-density phase. Again, we assume this lane to consist of N_{lane} layers with a distance x between them. Instead of two high-density layers enclosing this lane, we now consider an isotropic phase of density $\tilde{\rho}_{\mathrm{iso}}$ exerting a force on the high-density phase; see Fig. 3.23.
This assumed configuration resembles characteristics of both polar clusters and enclosed lanes. The absence of enclosing lanes is a property we find in polar clusters. However,

the perfect alignment of particles is something we find in enclosed lanes rather than polar clusters.
We now consider a section S_{int} of length L from the interface between the two phases. For the force exerted on this section by the isotropic phase, we can calculate a statistical average. Let the normal vector of the interface be $\boldsymbol{n}_{\text{int}}$. To get the number of particles with orientation φ that will reach the section within a timespan Δt, we calculate the maximum distance parallel to $\boldsymbol{n}_{\text{int}}$ they will cover at a propulsion speed v_0. Multiplying this distance by the length of S_{int}, we get the area within which all particles of orientation φ will reach S_{int}. The number of particles $n_{\text{iso}}(\varphi)$ in this area is calculated by multiplying with the isotropic phase's density $\tilde{\rho}_{\text{iso}}$:

$$n_{\text{iso}}(\varphi) = \frac{\tilde{\rho}_{\text{iso}}}{L^2} L v_0 \Delta t (\boldsymbol{u}(\varphi) \cdot \boldsymbol{n}_{\text{int}}) \ . \tag{3.127}$$

Here, $\boldsymbol{u}(\varphi)$ is the orientation vector associated with a particle's orientation φ. The force a single particle exerts on the section is then given by

$$f_1(\varphi) = \gamma_{\parallel} v_0 (\boldsymbol{u}(\varphi) \cdot \boldsymbol{n}_{\text{int}}) \tag{3.128}$$

with the friction coefficient $\gamma_{\parallel}$. To get the total force f_{iso} of all particles reaching S_{int} within the timespan Δt, we have to multiply the number of particles $n_{\text{iso}}(\varphi)$ with the force per particle and integrate over all orientations. Only particles pointing towards the interface have to be considered since particles pointing away will obviously move away also. We assume the interface to be parallel to the axis defined by $\varphi = 0$, so we integrate over the interval $\varphi \in [0, \pi]$:

$$f_{\text{iso}} = \int_0^{\pi} \psi_{\text{iso}}(\varphi) n_{\text{iso}}(\varphi) f_1(\varphi) \, d\varphi \tag{3.129}$$

In an isotropic system, all angles are equally distributed, so we have $\psi_{\text{iso}}(\varphi) = \frac{1}{2\pi}$ in two dimensions. Using this, we get the total force

$$\begin{aligned} f_{\text{iso}} &= \int_0^{\pi} \frac{1}{2\pi} \frac{\tilde{\rho}_{\text{iso}}}{L^2} L v_0 \Delta t (\boldsymbol{u}(\varphi) \cdot \boldsymbol{n}_{\text{int}}) \gamma_{\parallel} v_0 (\boldsymbol{u}(\varphi) \cdot \boldsymbol{n}_{\text{int}}) \, d\varphi \\ &= \frac{\tilde{\rho}_{\text{iso}} v_0^2 \Delta t \gamma_{\parallel}}{2\pi L} \int_0^{\pi} \sin^2 \varphi \, d\varphi = \frac{\tilde{\rho}_{\text{iso}} v_0^2 \Delta t \gamma_{\parallel}}{4L} \ . \end{aligned} \tag{3.130}$$

The relevant time scale in this model is the rotational diffusion time τ_{rot} since this is the time we can assume particles in the isotropic phase to move straight. At longer times, the above derivation of the number of particles reaching S_{int} would be inaccurate since it assumes straight moving particles. The rotational diffusion time is $\tau_{\text{rot}} = \frac{1}{2D_r}$ with $D_{\text{rot}} = \frac{k_B T}{\gamma_{\text{rot}}} = \frac{6 k_B T}{L^2 \gamma_{\parallel}}$. Setting $\Delta t = \tau_{\text{rot}}$ and using $v_0 = \frac{Pe k_B T}{L \gamma_{\parallel}}$, we can rewrite (3.130) to

$$f_{\text{iso}} = \frac{\tilde{\rho}_{\text{iso}} Pe^2 k_B T}{48 L} \ . \tag{3.131}$$

Within the high-density lane, forces result from the Lennard-Jones interaction between the particles as outlined in Section 3.5.1:

$$f_{\text{LJ}}(x) = 48 \frac{\epsilon}{x} \left(\frac{d}{x} \right)^{12} - 24 \frac{\epsilon}{x} \left(\frac{d}{x} \right)^{6} \ . \tag{3.132}$$

Additionally, we also want to take into account diffusive effects within the lane. To include this, we first consider a single particle in a box of width w and length equal to the particle's length L. Due to its self-propulsion with speed v_0, the particle will exert a force on the box's walls when it hits them at an angle α_b:

$$f_\mathrm{box}(\alpha_\mathrm{b}) = \gamma_\parallel v_0 \sin\alpha_\mathrm{b} \ . \tag{3.133}$$

The maximum angle is defined by the dimensions of the box:

$$\alpha_\mathrm{b,max} = \arcsin\frac{w}{L} \ . \tag{3.134}$$

We limit the calculation to boxes with $w < L$. Assuming that α_b will take all possible values with equal probability, we can calculate the average force on one wall $\langle f_\mathrm{box}\rangle$ as a function of the box's dimensions. Even though $\alpha_\mathrm{b} \in [-\alpha_\mathrm{b,max}, \alpha_\mathrm{b,max}]$, only angles $\alpha_\mathrm{b} \geq 0$ give a contribution since $\alpha_\mathrm{b} < 0$ represents the particle pointing away from the wall and therefore not exerting a force:

$$\langle f_\mathrm{box}\rangle = \frac{1}{2\alpha_\mathrm{b,max}} \int_{-\alpha_\mathrm{b,max}}^{\alpha_\mathrm{b,max}} \gamma_\parallel v_0 \sin\alpha_\mathrm{b}\, d\alpha_\mathrm{b} = \frac{\gamma_\parallel v_0}{2\arcsin\frac{w}{L}} \left[1 - \sqrt{1 - \frac{w^2}{L^2}}\right] \ . \tag{3.135}$$

Now, we apply the above result to a particle within the lane. Its neighbouring particles constitute an effective box within which it can rotate. As stated earlier, x is the distance between the layers in the lane and therefore equal to the distance of neighbouring particles. In principle, we could use $2x$ as the box's width, but since the Lennard-Jones potential is strongly repulsive for distances smaller than r_min (see Section 3.3.2), we limit the width in which the particle can freely rotate to $w_\mathrm{lane} = 2(x - r_\mathrm{min})$. If x becomes smaller than r_min, there is no space for the particle to rotate and we set $w_\mathrm{lane} = 0$. With this, we get a force contribution of

$$f_\mathrm{box}(w_\mathrm{lane}) = \frac{\gamma_\parallel v_0}{2\arcsin\frac{w_\mathrm{lane}}{L}} \left[1 - \sqrt{1 - \frac{w_\mathrm{lane}^2}{L^2}}\right] \ . \tag{3.136}$$

This gives us the total force within the lane:

$$f_\mathrm{lane}(x) = f_\mathrm{LJ}(x) + f_\mathrm{box}\left(w_\mathrm{lane}(x)\right) \ . \tag{3.137}$$

As in Section 3.5.1, we now have a force equlibrium

$$f_\mathrm{iso} - f_\mathrm{lane}(x) = 0 \tag{3.138}$$

$$\begin{aligned} \frac{\tilde{\rho}_\mathrm{iso} Pe^2 k_B T}{48L} - 48\frac{\epsilon}{x}\left(\frac{d}{x}\right)^{12} + 24\frac{\epsilon}{x}\left(\frac{d}{x}\right)^{6} \\ - \frac{\gamma_\parallel v_0}{2\arcsin\frac{w_\mathrm{lane}(x)}{L}} \left[1 - \sqrt{1 - \frac{w_\mathrm{lane}^2(x)}{L^2}}\right] = 0 \ . \end{aligned} \tag{3.139}$$

Next, we eliminate $\tilde{\rho}_\mathrm{iso}$ using Eq. (3.126) which leaves us with the particle motility Pe as the only free parameter. Again, we solve the equation numerically using Mathematica for particle motilities $Pe \in [10, 100]$. Next, we calculate the lane's density

$$\tilde{\rho}_\mathrm{lane} = \frac{L}{x} \tag{3.140}$$

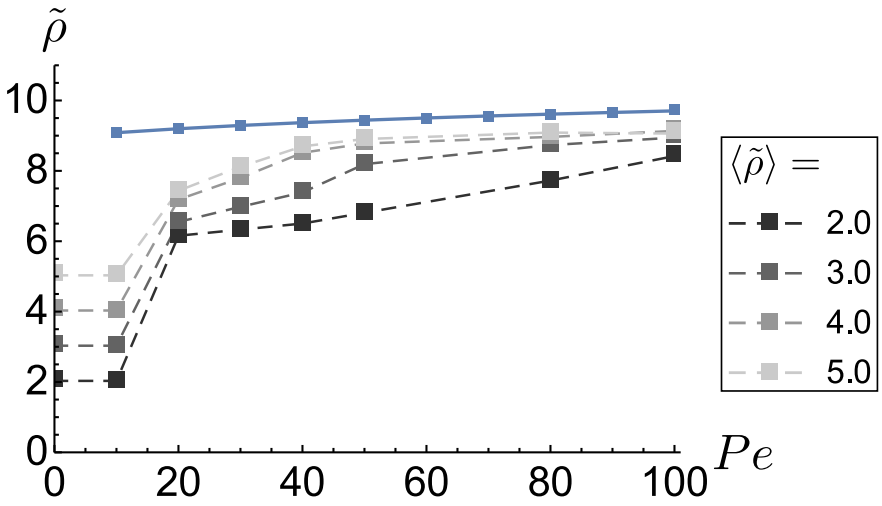

Figure 3.24: Lane density $\tilde{\rho}_{\text{lane}}$ as a function of particle motility calculated from force equilibrium of coexisting phases (blue line) in comparison with simulation results (dashed lines). Different shades of grey indicate different average densities in the simulated systems. We find fairly good agreement at Péclet numbers $Pe \geq 40$, but the calculated density is generally too high. At low particle motilities, this deviation is even more pronounced.

and plot the resulting values as a function of Pe. A comparison with simulation results can be seen in Fig. 3.24.

We find that $\tilde{\rho}_{\text{lane}}$ increases with the Péclet number but only to a small degree. This is in qualitative agreement with the simulation results at high particle motilities. At $Pe < 40$ though, $\tilde{\rho}_{\text{lane}}$ would have to depend strongly on Pe to match the simulation results.

When checking for quantitative agreement between our model and the simulation data, we also find differences between low and high Péclet numbers. At $Pe \geq 40$, our predicted densities are slightly larger than the densities we find in simulated systems at average densities $\langle\tilde{\rho}\rangle \geq 3.0$. Taking into account the degree of uncertainty regarding the simulation results (see below), we can still regard this as a fairly good agreement. At $Pe < 40$ however, we find significant deviations: since our model does not reproduce the strong dependence on particle motility we see in simulation results, the values we get for $\tilde{\rho}_{\text{lane}}$ are too high.

To conclude, this model for a phase-separated system gives good results for the density in the high-density phase at large particle motilities. We find fairly good agreement with simulation results for average densities $\langle\tilde{\rho}\rangle \geq 3.0$. This is plausible considering the fact that inhomogeneities with a very dense phase such as asters and enclosed lanes occur more frequently and are more stable at large particle motilities and average densities as described in Section 3.4.2. This stability is one of the assumptions of the model.

Unfortunately, the model cannot reproduce the density's strong dependence on particle motility we find in simulations at Péclet numbers $Pe < 40$. One possible explanation for this was already addressed in Section 3.5.1: the lane's density is not very sensitive to the particles' motility due to the repulsive term in the Lennard-Jones potential.

Another reason might be that that we assume a stable and perfectly ordered high-density phase even at low Péclet numbers. When looking at simulation snapshots though, we see a variety of different types of phase-separated configurations – especially in the relevant range of particle motilities. So, the densities measured in simulations are the result of averaging over several types of configurations and configurations that would occur as transitions between these. The configuration we presumed for our model may be too different from polar clusters to account for their frequent occurrence in systems with Péclet numbers $Pe < 40$. In polar clusters, the included particles are loosely packed and their orientations vary within a small range which is not resembled by our model in which the particles are perfectly ordered. Still, the model can be regarded as a rough approximation of polar clusters in contrast to configurations with even less order. Hence, the more frequent occurrence of those configurations – as is the case at low particle motilities – will only make the deviations from the model more pronounced.
Another factor that has to be considered regarding deviations between the analytical model and simulation results is that the measured densities depend on the splitting density $\tilde{\rho}_{\mathrm{sp}}$ as described in App. C.2. Therefore, the simulation results are not perfectly precise which could also be an explanation for the deviations.
One more weakness of this model is that it does not explicitly take into account thermal effects even though these are a significant factor in simulations. Within the high-density phase, thermal fluctuations would increase the distance between particles and thereby reduce its density. The rotational diffusion considered here is only a rough approximation of the relevant thermal effects.
The two major advantages of this model compared to the one presented in Section 3.5.1 are the occurrence of only one free parameter – the particle motility – and the integration of a model predicting the isotropic phase's density as a function of the Péclet number. Due to the second aspect, the model describes both phases simultaneously making it quite successful – particularly at large particle motilities.

3.6 Analytical approaches II: density functional theory

3.6.1 Basics

As described in Section 3.1.4, the coexisting densities of an isotropic and a nematic phase in a three-dimensional systems of hard rods without propulsion can be calculated by the Onsager theory – a density functional theory for a system with inhomogeneously distributed orientations. The theory uses the virial expansion – see App. A – to express the free energy density of infinitely thin rods as

$$\begin{aligned}\frac{\beta F}{V} =& \rho\left(\ln(\rho\Lambda^3)-1\right)+\rho\int\psi_\alpha(\Omega)\ln(4\pi\psi_\alpha(\Omega))\,d\Omega \\ &+\rho^2L^2d\iint\psi_\alpha(\Omega)\psi_\alpha(\Omega')\sin\gamma\,d\Omega\,d\Omega'+\mathcal{O}(\rho^3)\ .\end{aligned} \tag{3.141}$$

Here, $\beta=\frac{1}{k_BT}$ is the inverse temperature, V is the system's volume, and Λ is the thermal de Broglie wavelength. A rod's orientation is expressed using the spatial angle Ω, and the orientational distribution function is $\psi_\alpha(\Omega)$. In the third term, γ denotes the angle between two rods at spatial angles Ω and Ω'.
The first term in (3.141) is the ideal gas contribution, and the second term is an addition resulting from the rods' orientations not being distributed uniformly. The third term corresponds to the second virial coefficient and takes into account the excluded volume between two rods.
Onsager's approach was using a trial function $\psi_\alpha(\Omega)=\psi_\alpha(\vartheta)=\frac{\alpha\cosh(\alpha\cos\vartheta)}{4\pi\sinh(\alpha)}$ with ϑ being the angle between a rod's main axis and the nematic director and α being the degree of ordering – ranging from 0 for an isotropic system to ∞ for perfect ordering. In the isotropic phase, this yields $\psi_\alpha(\Omega)=\frac{1}{4\pi}$.
We see that for nematic ordering, the free energy is not only a function of ρ but also of α. At any given density, the particles will order themselves to a degree that minimises the free energy. This means that $F(\rho)$ for a specific ρ is given by the minimum of F with respect to α. For the isotropic phase, the calculation of $F(\rho)$ is straightforward. We then have two free energies describing the two phases. The coexisting densities are calculated by constructing a common tangent to the two curves.
Since we want to apply the above method to a two-dimensional system of active particles exhibiting polar ordering, we have to modify it. First of all, the rods' orientation is defined by a planar angle ϑ instead of a spatial angle Ω. We replace the orientation distribution function by a term that is similar to nematic ordering but takes into account polar ordering:

$$\psi_\alpha(\vartheta)=A\cosh(\alpha\cos\frac{1}{2}\vartheta) \tag{3.142}$$

The factor A can be calculated using the fact that the distribution function has to be normalized:

$$\int\psi_\alpha(\vartheta)\,d\vartheta=1\Rightarrow A=\frac{1}{2\pi I_0(\alpha)} \tag{3.143}$$

Here, I_0 is the modified Bessel function of the first kind. In the isotropic phase, $I_0(\alpha=0)=1$ and hence $\psi_\alpha(\vartheta)=\frac{1}{2\pi}$. Next, the excluded volume between two thin

rods is independent of their diameter in two dimensions which leads to a modified prefactor in the third term:

$$\rho^2 L^2 d \to \rho^2 L^2 \tag{3.144}$$

Also, we have to account for the rods' propulsion and therefore include an excess term

$$F_{ex} = \int_0^\rho \frac{1}{2} \ln(1 + \frac{v(s,\psi_\alpha)^2 \tau_{\text{rot}}}{2D_t})\, ds \tag{3.145}$$

as described by Cates and Tailleur [178] – see also Section 3.2.5. Since we are dealing with elongated particles, this term may depend on their orientations which is accounted for by considering a velocity that is a function of $\psi_\alpha(\vartheta)$.
Introducing the dimensionless density $\tilde{\rho} = \rho L^2$ and taking into account the above modifications, we arrive at the following expression for the rescaled free energy density:

$$\begin{aligned} \tilde{f} = \frac{\beta F L^2}{V} &= \tilde{\rho}\,(\ln(\tilde{\rho}) - 1) + \tilde{\rho} \int \psi_\alpha(\vartheta) \ln(2\pi\psi_\alpha(\vartheta))\, d\vartheta \\ &\quad + \tilde{\rho}^2 \iint \psi_\alpha(\vartheta)\psi_\alpha(\vartheta') \sin(\vartheta - \vartheta') d\vartheta d\vartheta' \\ &\quad + \int_0^{\tilde{\rho}} \frac{1}{2} \ln(1 + \frac{v(\tilde{s},\psi_\alpha)^2 \tau_{\text{rot}}}{2D_t})\, d\tilde{s} + \tilde{\rho} \ln \frac{\Lambda^2}{L^2} \end{aligned} \tag{3.146}$$

It can easily be shown that the addition of a linear term to both functions has no effect on the calculation of their common tangent, see App. D. Therefore, we can just ignore the last term when calculating the densities of the coexisting phases.

3.6.2 Basic Model

Now, we want to explicitly calculate the phase separation in a two-dimensional system of thin self-propelled rods. Since we do not know the exact dependence of a rod's velocity on the local density, we use two different forms that we derive by considering the main characteristics we can expect the velocity to exhibit. At densities approaching 0, we can expect the rods' velocity to be equal to their propulsion speed v_0 since no interactions are taking place. In an isotropic system, the rods will block each other's path and therefore be slower in areas of higher density. As a first ansatz for the velocity, we assume that there is a critical density $\tilde{\rho}^*$ at which rods become incapable of moving and their velocity decreases linearly up to this density:

$$v_{1,\text{iso}}(\tilde{\rho}) = \begin{cases} v_0 \left(1 - \frac{\tilde{\rho}}{\tilde{\rho}^*}\right) & , \tilde{\rho} \le \tilde{\rho}^* \\ 0 & , \tilde{\rho} > \tilde{\rho}^* \end{cases} . \tag{3.147}$$

This ansatz is motivated by the fact that a similar density-dependent velocity was predicted by kinetic theory and confirmed in simulations for spherical active Brownian particles [178].
For the second ansatz, we assume an exponentially decreasing velocity as this is a significantly different alternative to the first ansatz and was implemented in other works as well [133, 178]. In this case, an infinitely large density would be required to completely slow down the rods with $\tilde{\rho}^*$ defining the rapidity of the decrease:

$$v_{2,\text{iso}}(\tilde{\rho}) = v_0 \exp\left(-\frac{\tilde{\rho}}{\tilde{\rho}^*}\right) . \tag{3.148}$$

In the polar phase, we can expect the rods to still be motile at very high densities. Since this phase is highly ordered, collisions are happening at flat angles resulting in alignment of the rods rather than blocking. So, we modify the above ansatzes by making them dependent on an order parameter p ranging from 0 for no order to 1 for perfect ordering. These conditions are met when choosing $p(\alpha)$ to be the expected value of $\cos\vartheta$ with the orientation distribution given by $\psi_\alpha(\vartheta)$:

$$p(\alpha) = \int \psi_\alpha(\vartheta) \cos\vartheta \, d\vartheta = \frac{I_2(\alpha)}{I_0(\alpha)} \,, \tag{3.149}$$

where I_0 and I_2 are modified Bessel functions of the first kind. For the first ansatz, we assume that rods in a perfectly ordered system can move as fast as in an empty system:

$$v_{1,\mathrm{pol}}(\tilde{\rho}) = v_0 \left(1 - \frac{\tilde{\rho}}{\tilde{\rho}^*}(1 - p(\alpha))\right) \tag{3.150}$$

For some combinations of $\tilde{\rho}$ and α, this expression can become negative in which case we just set the velocity to be 0. In the second ansatz, we assume the velocity to exponentially approach a finite velocity v_∞ at infinitely large densities:

$$v_{2,\mathrm{pol}}(\tilde{\rho}) = v_0 \exp\left(-\frac{\tilde{\rho}}{\tilde{\rho}^*}\right) + v_\infty p(\alpha) \left[1 - \exp\left(-\frac{\tilde{\rho}}{\tilde{\rho}^*}\right)\right] \tag{3.151}$$

The following calculations were performed for $v_\infty = \{0.1v_0, 0.5v_0, 0.9v_0\}$, but since $v_\infty = 0.1v_0$ yielded the best results, only those will be presented here.

Calculation of the ideal degree of order

At any specific density $\tilde{\rho}$, the free energy density in a system of polarly ordered rods is still a function of the degree of ordering α. The system will arrive at a degree of ordering for which the free energy density has a minimum with respect to α. We call this minimum $\alpha_{\min}$ and note that it is a function of $\tilde{\rho}$. Since we cannot derive $\alpha_{\min}(\tilde{\rho})$ analytically, we have to calculate it numerically. This is made more difficult by the fact that the excess term is an integral over the density and a function of α since the velocity is a function of α. This means that for calculating the free energy density at a certain $\tilde{\rho}$, we have to know $\alpha_{\min}(\tilde{\rho}')$ for all $\tilde{\rho}' < \tilde{\rho}$. So, we can only calculate $\alpha_{\min}(\tilde{\rho})$ – and thereby $\tilde{f}(\tilde{\rho}, \alpha_{\min})$ – iteratively starting at $\tilde{\rho} = 0$ and incrementally increasing $\tilde{\rho}$ while in each step using the previous results. For a more detailed description, see App. E.
After calculating the ideal degree of order, we automatically have $\tilde{f}_{\mathrm{pol}}(\tilde{\rho})$ for the polar phase.

Variant: Universal calculation of ideal degree of order

As described above, the excess term forces us to calculate $\alpha_{\min}(\tilde{\rho})$ iteratively because it depends not only on the degree of order at the actual density $\tilde{\rho}$ but on the degree of order for all densities $\tilde{\rho}' \leq \tilde{\rho}$. We can eliminate this problem by calculating $\alpha_{\min}(\tilde{\rho})$ using only the first three terms of the free energy – assuming that the excess term does not have much of an influence on the result. The justification for this is that the excess term is an integral over the particle velocity v which in our ansatzes only depends on α via the order parameter $p(\alpha)$. This function rapidly approaches 1 with increasing

α. Iterative calculations showed that $\alpha_{\min}(\tilde{\rho}) = 0$ up to a certain density at which we first find a minimum at a finite α. This finite value was never lower than $\alpha = 20$ which is equivalent to an order parameter $p(\alpha) > 0.9$. With increasing density, $\alpha_{\min}$ would rapidly increase as well which would make $p(\alpha)$ quickly approach 1. Hence, for a wide range of densities, the $p(\alpha)$ and thereby the particle velocity would be almost constant. As a result, $\alpha_{\min}$ would be determined only by the other terms in the free energy density.
This approach allows us to calculate the ideal degree of order universally. Parameters like the propulsion speed and the critical density, as well as the form of $v(\tilde{\rho})$ only affect the excess term. Hence, using the altered free energy density

$$\begin{aligned}\tilde{f}' &= \tilde{f} - \int_0^{\tilde{\rho}} \frac{1}{2} \ln(1 + \frac{v(\tilde{s}, \psi_\alpha)^2 \tau_{\text{rot}}}{2D_t})\, d\tilde{s} \\ &= \tilde{\rho}\,(\ln(\tilde{\rho}) - 1) + \tilde{\rho} \int \psi_\alpha(\vartheta) \ln(2\pi\psi_\alpha(\vartheta))\, d\vartheta \\ &\quad + \tilde{\rho}^2 \iint \psi_\alpha(\vartheta)\psi_\alpha(\vartheta') \sin(\vartheta - \vartheta')\, d\vartheta\, d\vartheta' \,,\end{aligned} \tag{3.152}$$

we only have to apply the method described above to find $\alpha_{\min}(\tilde{\rho})$ once. After this, we have $\tilde{f}'(\tilde{\rho})$ and $\alpha_{\min}(\tilde{\rho})$. For getting $\tilde{f}_{\text{pol}}(\tilde{\rho})$ for a specific velocity $v(\tilde{\rho})$ and certain parameters v_0 and $\tilde{\rho}^*$, we just need to evaluate the excess term at all densities $\tilde{\rho}$ and add it to the corresponding value for $\tilde{f}'(\tilde{\rho})$. This method saves a lot of computation time since we do not have to perform the iterative minimisation routine for each set of parameters. As will be described below, comparisons of the iterative method and the universal calculation show that the resulting $\alpha_{\min}$ are almost identical which confirms that the error we make by using the computationally more efficient universal calculation is negligible.

Free energy density in the isotropic phase

Some terms of the free energy density in the isotropic phase can be calculated analytically. Since there is no ordering, we have $\alpha = 0$ and the first two integrals in the free energy become

$$\int \psi_0(\vartheta) \ln(4\pi\psi_0(\vartheta))\, d\Omega = \int \frac{1}{2\pi} \ln(2\pi \frac{1}{2\pi})\, d\vartheta = 0 \tag{3.153}$$

$$\iint \psi_0(\vartheta)\psi_0(\Omega') \sin\gamma\, d\vartheta\, d\vartheta' = \iint \frac{1}{4\pi^2} \sin(\vartheta - \vartheta')\, d\vartheta\, d\vartheta' = \frac{2}{\pi} \tag{3.154}$$

reducing the free energy density to

$$\tilde{f}_{\text{iso}}(\tilde{\rho}) = \tilde{\rho}\,(\ln(\tilde{\rho}) - 1) + \frac{2}{\pi}\tilde{\rho}^2 + \int_0^{\tilde{\rho}} \frac{1}{2} \ln(1 + \frac{v_{\text{iso}}(\tilde{s}, \psi_\alpha)^2 \tau_{\text{rot}}}{2D_t})\, d\tilde{s} \tag{3.155}$$

This expression still has to be evaluated numerically due to the excess term.

Common tangent construction

For the common tangent construction, we use the numerically calculated values $\tilde{f}_{\text{pol}}(\tilde{\rho})$ and $\tilde{f}_{\text{iso}}(\tilde{\rho})$ and derive a polynomial fit for each of them. We do this because we can then easily calculate the first derivative which we need for finding the common tangent

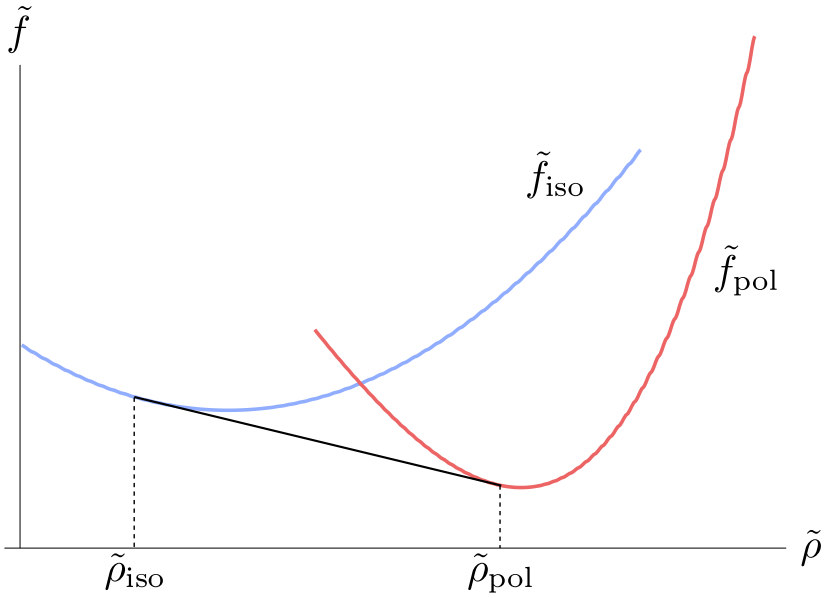

Figure 3.25: Exemplary plot of the common tangent construction for two free energy densities in the isotropic phase $\tilde{f}_{\mathrm{iso}}$ and in the polar phase $\tilde{f}_{\mathrm{pol}}$. The resulting coexisting densities are $\tilde{\rho}_{\mathrm{iso}}$ and $\tilde{\rho}_{\mathrm{pol}}$.

of the two functions.
Generally, a common tangent of two functions $f_1(x)$ and $f_2(x)$ is defined to be the line through two points $(x_1, f_1(x_1))$ and $(x_2, f_2(x_2))$ with the additional condition that the line's slope m is equal to the first derivatives of f_1 at x_1 and f_2 at x_2 respectively:

$$m = \left.\frac{df_1}{dx}\right|_{x=x_1} = \left.\frac{df_2}{dx}\right|_{x=x_2} . \tag{3.156}$$

This can be expressed by the two conditions

$$I. \qquad \left.\frac{df_1}{dx}\right|_{x=x_1} = \left.\frac{df_2}{dx}\right|_{x=x_2} \tag{3.157}$$

$$II. \qquad f_2(x_2) = f_1(x_1) + (x_2 - x_1) \left.\frac{df_1}{dx}\right|_{x=x_1} \tag{3.158}$$

Applying this to our problem, we need to find the densities $\tilde{\rho}_{\mathrm{iso}}$ and $\tilde{\rho}_{\mathrm{pol}}$ for which

$$I. \qquad \left.\frac{d\tilde{f}_{\mathrm{iso}}}{d\tilde{\rho}}\right|_{\tilde{\rho}=\tilde{\rho}_{\mathrm{iso}}} = \left.\frac{d\tilde{f}_{\mathrm{pol}}}{d\tilde{\rho}}\right|_{\tilde{\rho}=\tilde{\rho}_{\mathrm{pol}}} \tag{3.159}$$

$$II. \qquad \tilde{f}_{\mathrm{pol}}(\tilde{\rho}_{\mathrm{pol}}) = \tilde{f}_{\mathrm{iso}}(\tilde{\rho}_{\mathrm{iso}}) + (\tilde{\rho}_{\mathrm{pol}} - \tilde{\rho}_{\mathrm{iso}}) \left.\frac{d\tilde{f}_{\mathrm{iso}}}{d\tilde{\rho}}\right|_{\tilde{\rho}=\tilde{\rho}_{\mathrm{iso}}} \tag{3.160}$$

We solve this system of equations numerically using Mathematica. The resulting densities $\tilde{\rho}_{\mathrm{iso}}$ and $\tilde{\rho}_{\mathrm{pol}}$ are the densities of the coexisting phases. For an illustration, see Fig. 3.25.

Results for linear velocity

Calculating the coexisting densities for the linearly declining velocities $v_{1,\mathrm{iso}}(\tilde{\rho})$ and $v_{1,\mathrm{pol}}(\tilde{\rho})$, we see that the critical density $\tilde{\rho}^*$ significantly influences the results we get for

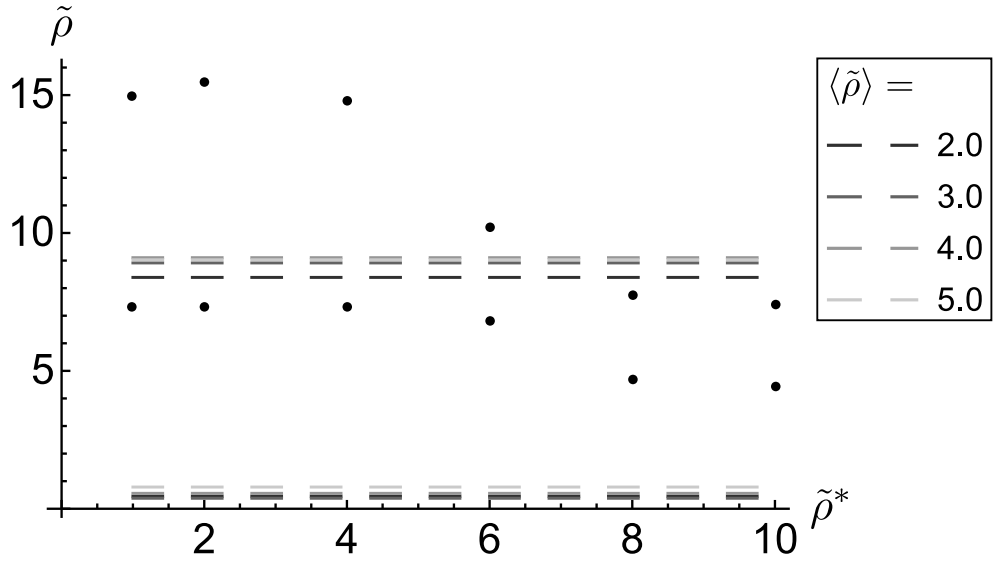

Figure 3.26: Phase separation at $Pe = 100$ as a function of the critical density $\tilde{\rho}^*$ (black dots) compared to values measured in simulations at different average densities (dashed lines). There is no value for $\tilde{\rho}^*$ at which both theoretical values are in agreement with the simulation results implying that the model with the linearly declining velocity is not valid for describing the phase separation.

$\tilde{\rho}_{\text{iso}}$ and $\tilde{\rho}_{\text{pol}}$. However, the results do not completely agree with the simulation results. Fig. 3.26 shows the values we get at a Péclet number $Pe = 100$ using the method described above in comparison to the simulation results. The ideal degree of order was calculated using the iterative method. The critical density was varied in the interval $\tilde{\rho}^* \in [1, 10]$, and for each value of $\tilde{\rho}^*$, two data points are plotted in the diagram. The lower one marks $\tilde{\rho}_{\text{iso}}$ and the upper one $\tilde{\rho}_{\text{pol}}$. The dashed lines represent the coexisting densities measured in simulated systems of average densities $\langle\tilde{\rho}\rangle \in [2, 5]$. We notice that if we choose $\tilde{\rho}^* \in [6.0, 8.0]$, $\tilde{\rho}_{\text{pol}}$ will agree with the high density we measured in simulations. However, for all critical densities, the calculation yields values for $\tilde{\rho}_{\text{iso}}$ that are far greater than the corresponding values in simulations. Hence, the above model using a linearly declining velocity can at best predict the density of the polar phase.

Results for universal calculation with linear velocity

As described above, we can efficiently explore a wide range of parameters by universally calculating the ideal degree of order at a certain density. However, we have to make sure that neglecting the excess term is a valid approximation. We find that $\alpha_{\min}(\tilde{\rho})$ is almost identical for all critical densities in the calculation described in Section 3.6.2. We again get almost identical values for $\alpha_{\min}(\tilde{\rho})$ when calculating the ideal degree of order using $\tilde{f}'$ – the free energy density without the excess term. Apparently, the excess term is negligible when it comes to calculating the ideal degree of order.
Using the ideal degree of order we obtain from the universal calculation, we can study the influence of the critical density and the propulsion speed on the phase separation. Specifically, this means calculating the excess term as a function of $\tilde{\rho}$ at different parameters and adding this to $\tilde{f}'(\tilde{\rho})$. Also, the free energy density of the isotropic phase is calculated at the different parameters. With the free energy densities, we can find the

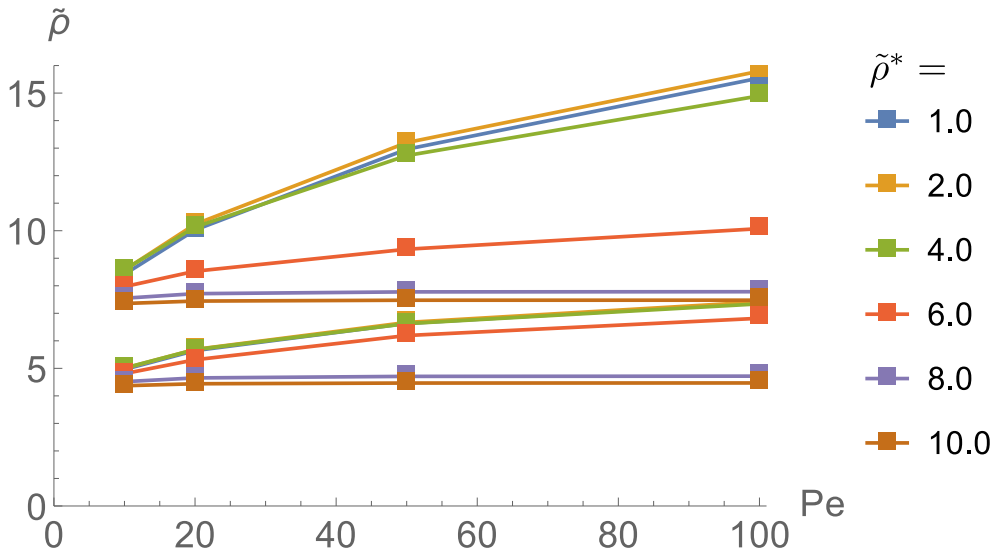

Figure 3.27: Phase separation as a function of the Péclet number for several critical densities $\tilde{\rho}^*$ when particle velocity declines linearly with density. Curves of the same color belong to the same $\tilde{\rho}^*$ with the upper one representing the density of the polar phase and the lower one representing the density of he isotropic phase.

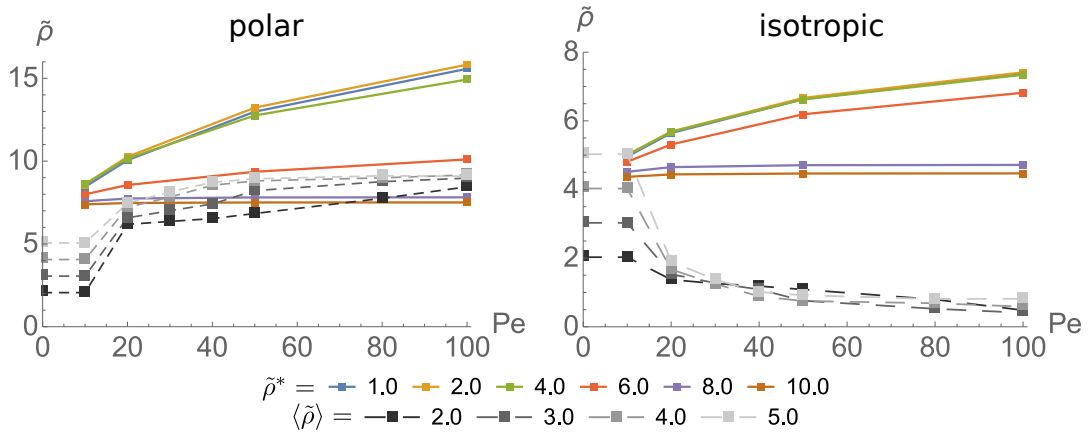

Figure 3.28: Comparison of the calculated densities as a function of Péclet number to simulation results. Left: polar phase, right: isotropic phase. Solid, coloured curves represent calculation results at different critical densities $\tilde{\rho}^*$ with linearly declining particle velocity. Dashed, grey curves represent simulation results at different average densities. At Péclet numbers $Pe \geq 20$ and average densities $\langle\tilde{\rho}\rangle \geq 3.0$, the model can predict the densities in the polar phase. However, the predicted densities in the isotropic phase are significantly greater than the measured densities for all parameters.

phase separations corresponding to the different parameters. The results are shown in Fig. 3.27 plotting $\tilde{\rho}_{\mathrm{iso}}$ (lower curves) and $\tilde{\rho}_{\mathrm{pol}}$ (upper curves) as functions of the Péclet number for several critical densities $\tilde{\rho}^* \in [1, 10]$. Different colours indicate different critical densities.
Again, we want to compare the theoretical results to the simulation data. For the non-universal calculation at a Péclet number $Pe = 100$, we found our model to only predict the density in the polar phase correctly. To check if this is the case at all Péclet numbers and critical densities, we plot the densities of the polar phase and of the isotropic phase as a function of the Péclet number at different $\tilde{\rho}^*$. In Fig. 3.28, we see that for critical densities $\tilde{\rho}^* \in [6.0, 8.0]$, the predicted density of the polar phase is similar to the simulation results at certain parameters, i.e., Péclet numbers $Pe \geq 20$ and average densities $\langle\tilde{\rho}\rangle \geq 3.0$. While this is a limited validity, it covers most of the parameter range explored in simulations. Unfortunately, the predictions for the density of the isotropic phase do not agree with the simulation data, see also Fig. 3.28. Independent of the parameters used, the densities we obtain from the calculation are significantly greater than the measured densities in the isotropic phase. Therefore, we have to conclude that this model is only suitable for describing the polar phase.

Results for universal calculation with exponential velocity

For a linearly declining velocity, we have already found the excess term to not affect the ideal degree of order. It is reasonable to assume the same to be true for an exponentially declining velocity. In fact, checking this at the arbitrarily chosen parameters $Pe = 20$, $\tilde{\rho}^* = 2.0$ yields the same result for $\alpha_{\mathrm{min}}(\tilde{\rho})$ as in the universal calculation without the excess term. So, we can again calculate the excess term as a function of $\tilde{\rho}$ at different parameters, add this to $\tilde{f}'(\tilde{\rho})$ to get the free energy density of the polar phase, calculate the free energy density in the isotropic phase at the same parameters, and finally find the corresponding phase separation. The results – $\tilde{\rho}_{\mathrm{iso}}$ (lower curves) and $\tilde{\rho}_{\mathrm{pol}}$ (upper curves) as functions of the Péclet number for several critical densities $\tilde{\rho}^* \in [1, 10]$ – are shown in Fig. 3.29. Different colours indicate different critical densities.
Compared to the results with linear velocity, we notice some differences. For the isotropic phase, we find lower densities which are almost identical regardless of the chosen parameters – with the only exception being $\tilde{\rho}^* = 1.0$. For the polar phase, the densities also depend only weakly on critial density and Péclet number – again $\tilde{\rho}^* = 1.0$ being the exception. Despite these differences, the agreement with the simulation results is similar. The densities predicted for the polar phase agree with the simulation results on the same range of parameters than the results for linearly declining velocities but for a wider range of critical densities $\tilde{\rho}^* \in [2.0, 6.0]$. For the isotropic phase, the model still yields densities that are too great, see Fig. 3.30. Therefore, the model assuming an exponentially declining velocity is also only valid for the polar phase.

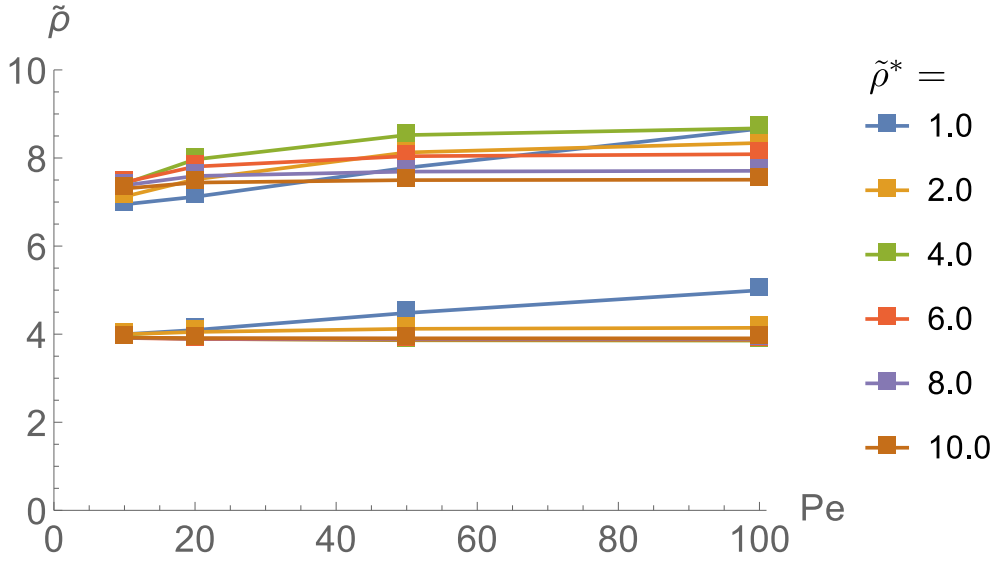

Figure 3.29: Phase separation as a function of the Péclet number for several critical densities $\tilde{\rho}^*$ when particle velocity declines exponentially with density. Curves of the same color belong to the same $\tilde{\rho}^*$ with the upper one representing the density of the polar phase and the lower one representing the density of the isotropic phase.

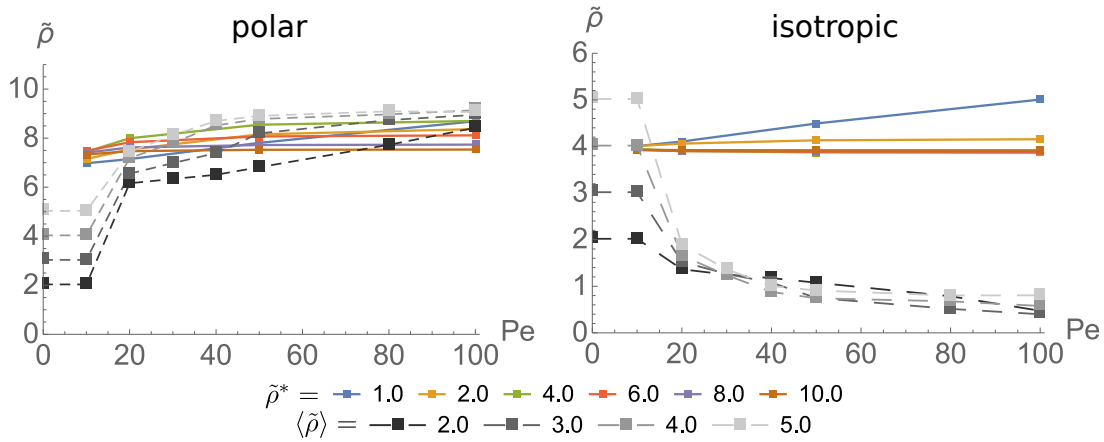

Figure 3.30: Comparison of the calculated densities as a function of Péclet number to simulation results. Left: polar phase, right: isotropic phase. Solid, coloured curves represent calculation results at different critical densities $\tilde{\rho}^*$ with exponentially declining particle velocity. Dashed, grey curves represent simulation results at different average densities. The predicted densities in the polar phase are similar to the measured densities for a wide range of parameters, but the model predicts densities in the isotropic phase that are too large for all parameters.

3.6.3 Model with Persistence Length

As mentioned before, the third term in (3.146) is the second virial coefficient which accounts for the rods' excluded volume interaction. As explained in Section 3.1.4, this term favours alignment as a reduced excluded volume yields greater positional entropy. It was shown by Kraikivski et al. that self-propulsion enhances nematic order in that the isotropic-nematic transition in two-dimensional systems occurs at lower densities when the particles are actively driven [179]. They were able to map the active systems onto passive systems by introducing an effective length

$$L_{\text{eff}} = \sqrt{L(L + l_p)}\ , \tag{3.161}$$

with l_p being the persistence length. Since we are studying similar systems, this effect should also be relevant here.
To take into account the effective elongation of rods due to propulsion, we replace the rod length L in the prefactor of the excluded volume term in (3.146) by the effective length as given by Kraikivski et al. [179] which results in the prefactor

$$\rho L^2 \to \rho L(L + l_p) =: \rho L_p^2 \tag{3.162}$$

Again, we want to express the free energy in terms of a dimensionless density – this time choosing $\tilde{\rho}_p = \rho L_p^2$. In this case, we get for the free energy density:

$$\begin{aligned}\tilde{f}_p = \frac{\beta f L_p^2}{V} &= \tilde{\rho}_p\left(\ln(\tilde{\rho}_p) - 1\right) + \tilde{\rho}_p \int \psi_\alpha(\vartheta)\ln(2\pi\psi_\alpha(\vartheta))\, d\vartheta \\ &\quad + \tilde{\rho}_p^2 \iint \psi_\alpha(\vartheta)\psi_\alpha(\vartheta')\sin(\vartheta - \vartheta')\, d\vartheta\, d\vartheta' \\ &\quad + \int_0^{\tilde{\rho}_p} \frac{1}{2}\ln(1 + \frac{v(\tilde{s}_p, \psi_\alpha)^2\tau_{\text{rot}}}{2D_t})\, d\tilde{s}_p + \tilde{\rho}\ln\frac{\Lambda^2}{L_p^2}\end{aligned} \tag{3.163}$$

As explained earlier, the last term can be ignored for the common tangent calculation.

Results for universal calculation with linear velocity

We can assume that the ideal degree of order is unaffected by the excess term as was the case in the basic model. So, we use a modified free energy density again for calculating $\alpha_{\min}(\tilde{\rho})$:

$$\begin{aligned}\tilde{f}_p' &= \tilde{f}_p - \int_0^{\tilde{\rho}_p} \frac{1}{2}\ln(1 + \frac{v(\tilde{s}_p, \psi_\alpha)^2\tau_{\text{rot}}}{2D_t})\, d\tilde{s}_p \\ &= \tilde{\rho}_p\left(\ln(\tilde{\rho}_p) - 1\right) + \tilde{\rho}_p \int \psi_\alpha(\vartheta)\ln(2\pi\psi_\alpha(\vartheta))\, d\vartheta \\ &\quad + \tilde{\rho}_p^2 \iint \psi_\alpha(\vartheta)\psi_\alpha(\vartheta')\sin(\vartheta - \vartheta')\, d\vartheta\, d\vartheta'\end{aligned} \tag{3.164}$$

The following steps are equivalent to the ones described for the basic model. We find the minimum value $\tilde{f}_p'(\tilde{\rho}_p)$ of the above term with respect to α for a certain density $\tilde{\rho}_p$. Then, we vary the propulsion speed and the critical density, calculate the excess term, and add this to $\tilde{f}_p'(\tilde{\rho}_p)$ in order to get the total free energy density. This – together

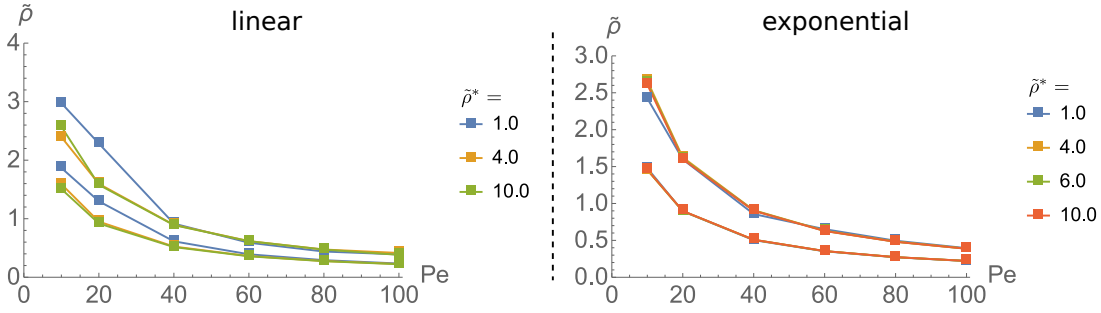

Figure 3.31: Phase separation as a function of the Péclet number for several critical densities $\tilde{\rho}^*$ when considering effectively elongated particles. Left: linearly declining velocity, right: exponentially declining velocity. Curves of the same colour belong to the same $\tilde{\rho}^*$ with the upper one representing the density of the polar phase and the lower one representing the density of the isotropic phase.

with the free energy density in the isotropic phase – is used for calculating the common tangent.

First, we assume a linearly declining velocity of the rods. Checking the result for $\alpha_{\min}(\tilde{\rho}_p)$ we obtain from the universal calculation, we notice that neglecting the excess term is in fact justified. This was done by iteratively calculating $\alpha_{\min}(\tilde{\rho}_p)$ using the full free energy density at arbitrarily chosen parameters $Pe = 100$, $\tilde{\rho}^* = 1.0$. This calculation yields the same ideal degree of order as the universal calculation.

The coexisting densities we find still include the persistence length. For comparison with the results from the basic model and the simulation data, we convert these back to $\tilde{\rho} = \tilde{\rho}_p \frac{L^2}{L_p^2}$. The resulting values at different propulsion speeds and critical densities are plotted in Fig. 3.31. Varying the critical density in the interval $\tilde{\rho}^* \in [1, 10]$ has only little influence on the coexisting densities in this model.

We already notice that the density of the polar phase declines with increasing Péclet number which contradicts what we find in simulations. A direct comparison shows major deviations of the calculated results from simulation data – see Fig. 3.32. For the isotropic phase, the densities predicted by this ansatz are in good agreement with the simulation data. This is especially true for a critical density $\tilde{\rho}^* = 1.0$ and Péclet numbers $Pe \geq 20$. The predicted values are generally lower than the measured densities with slightly better agreement at higher Péclet numbers, but as already pointed out in Section 3.5.2, the explanation for this deviation could be that the parameter $\tilde{\rho}_{\text{sp}}$ was chosen incorrectly or that the simulated systems were too small. Hence, we can conclude that this approach gives a good prediction for the density of the isotropic phase.

Results for universal calculation with exponential velocity

Finally, we want to investigate if we can get a better prediction of the phase separation when taking into account effective elongation due to propulsion while assuming an exponentially declining velocity as introduced in (3.148) and (3.151). First, we check again if the ideal degree of order we get from using the modified free energy density defined in (3.164) is the same as if we would minimise the full free energy density. This

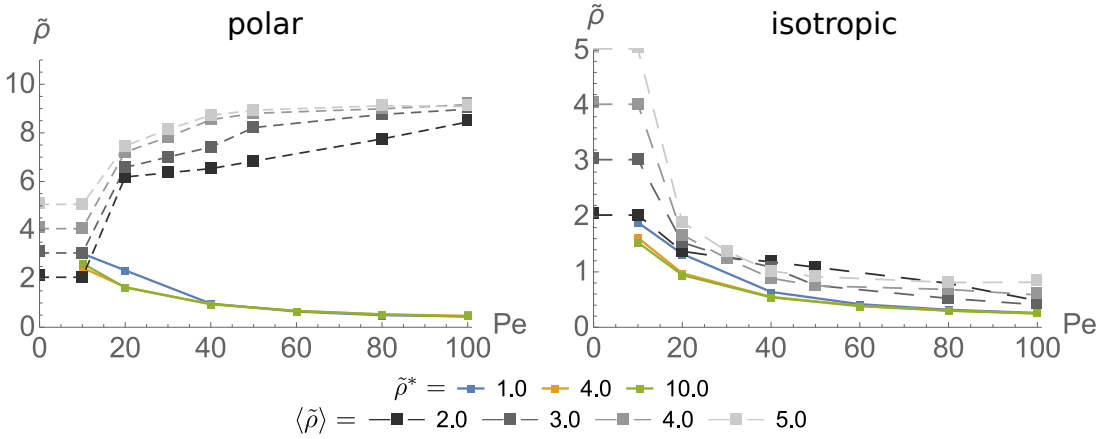

Figure 3.32: Comparison of the calculated densities as a function of Péclet number when considering effectively elongated particles to simulation results. Left: polar phase, right: isotropic phase. Solid, coloured curves represent calculation results at different critical densities $\tilde{\rho}^*$ with linearly declining particle velocity. Dashed, grey curves represent simulation results at different average densities. Regardless of the chosen parameters, the predicted densities in the polar phase are significantly smaller than the measured densities. In the isotropic phase, the predicted densities are in good agreement with the simulation results – especially for $\tilde{\rho}^* = 1.0$ and Péclet numbers $Pe \geq 20$.

turns out to be true with the arbitrarily chosen parameters $Pe = 60$, $\tilde{\rho}^* = 4.0$. The maximum deviation we find for $\alpha_{\min}(\tilde{\rho}_p)$ is smaller than 8%, and the deviations we find for the coexisting densities are in the range of 1%. This indicates that neglecting the excess term when calculating $\alpha_{\min}(\tilde{\rho}_p)$ is justified.
The coexisting densities we obtain from this calculation are again converted to $\tilde{\rho} = \tilde{\rho}_p \frac{L^2}{L_p^2}$ and plotted in Fig. 3.31. We see that the results do not differ greatly from the ones with linear velocity – $\tilde{\rho}_{\text{pol}}$ declines with increasing Péclet number and the critical density has almost no effect. Due to this similarity to the results from calculation with linear velocity, the comparison to simulation data leads to the same conclusions: this variant of the model is also only valid for the isotropic phase.

3.6.4 Summary

We tried calculating the phase separation in a system of self-propelled rods using a modified Onsager theory based on a model presented by Cates and Tailleur [178] for spherical particles. The model uses a simplified density functional theory and expresses the free energy density as a function of density and degree of order. The particles' motility was taken into account by including an excess term. Several different ansatzes were tested in order to consider possibly relevant features of the system such as an effective elongation of the rods, slowing down of particles at high densities, and high degrees of order counteracting this effect.
None of these ansatzes was successful in predicting the phase separation comprehensively, but they yielded good agreement with the simulation results for one of the phases. The basic model omitting effective elongation of the rods gave a good approximation for the density of the polar phase for most of the parameter range explored in simulations, but the density it predicted for the isotropic phase was significantly greater than the

simulation results. The model considering effectively elongated particles yielded densities for the isotropic phase which agreed with simulation data, but the density of the polar phase exhibited an incorrect dependence on propulsion speed and no agreement with simulation data.
Therefore, we have to conclude that the phase separation can only be partially described by the presented model. This could have several reasons. First of all, the applied free energy density was derived for dilute suspensions and is not valid at high densities – this deviation could be great enough to lead to false results for the coexisting densities. Also, as pointed out in Section 3.1.4, considering only terms up to second order in the virial expansion when deriving the free energy density is not a good approximation in two dimensions. Additionally, the model does not take into account the rods' finite thickness and the – weak but still existent – attractive potential between them. It is also possible that the effective elongation we assumed was too simplistic. We used the persistence length of a single particle in a vacuum as additional length, but in dense systems, the persistence length of a particle will be smaller due to rotation-inducing interactions with other particles. Finally, it may simply be impossible to map a complex dynamical system like this onto an effective equilibrium system.
Interestingly, the two presented approaches are each valid for one of the phases which suggests an opportunity for further research: a combination of the two could give a more comprehensive description of the phase separation.

3.7 Conclusion and discussion

This chapter presented the author's work on the collective dynamics of self-propelled rodlike particles. In Section 3.2, various methods of studying active matter were introduced as well as a variety of discoveries these methods led to. Special emphasis was given to collective phenomena most relevant to this work – see Section 3.2.4. These included particle aggregation in confined geometries, the formation of asters, and collective motion. Many of these phenomena can be described as phase-separated configurations consisting of an ordered high-density phase and an unordered low-density phase. A current problem in these systems is predicting the densities of the coexisting phases. Analytical models developed for doing this in systems of spherical particles were described in Section 3.2.5. The main focus of this work was adapting these models to systems of rodlike particles. The secondary aim was to reproduce rotating structures that were observed in experiments but not in simulations of straight-moving particles without explicit alignment interactions so far.

The simulations performed for studying systems of self-propelled rodlike particles were described in Section 3.3. Particles were modelled as spherocylinders with hard-core interactions and an additional Lennard-Jones potential. They were simulated in confined environments of various shapes as well as without confinement. Particles' trajectories were calculated using the established framework of Brownian dynamics simulations in which the particles' dynamics result from a combination of self-propulsion and thermal diffusion. Simulations were performed using a variety of average densities and propulsion speeds. Systems were investigated by measuring inter alia their degree of nematic ordering, average particle speed, centre of mass, and density distributions.

In Section 3.4, the simulation results were presented. In confined geometries, self-propelled particles would accumulate near the edges of the simulation cell. This effect was not observed for passive particles, so we can conclude that particle accumulation is caused by self-propulsion. Systems without confinement exhibited particle accumulation as well. For particle motilities $Pe \geq 20$, static asters or collectively moving structures such as polar clusters and enclosed lanes could be observed. The probability of finding the different patterns depended on the systems' average density and the particles' propulsion speed. The observed patterns met the criteria for phase-separated systems with an ordered high-density phase and an unordered low-density phase. Summarising them, a phase diagram indicating the coexisting densities in the phase-separated systems as a function of particle motility was generated. Phase separation was found to become more pronounced with increased particle motility.

Despite the variety of observed collectively moving patterns, rotating structures could not be found in the studied parameter space. Besides not occurring spontaneously, swirling configurations were demonstrated to not be stable even when enforced at the start of simulations. A comparison with circular patterns observed in experiments [124–126] indicated that these could not be reproduced as the simulated systems were too small.

In the last two sections, analytical models for phase separation in systems of spherical particles were adapted to rodlike particles in order to predict the coexisting densities. In Section 3.5, a force equilibrium approach was used to describe the coexistence of a perfectly ordered high-density phase and an isotropic low-density phase. The density in the isotropic phase was derived assuming a dynamic equilibrium between a gas phase and a cluster of particles as presented by Abkenar et al. [147]. This model

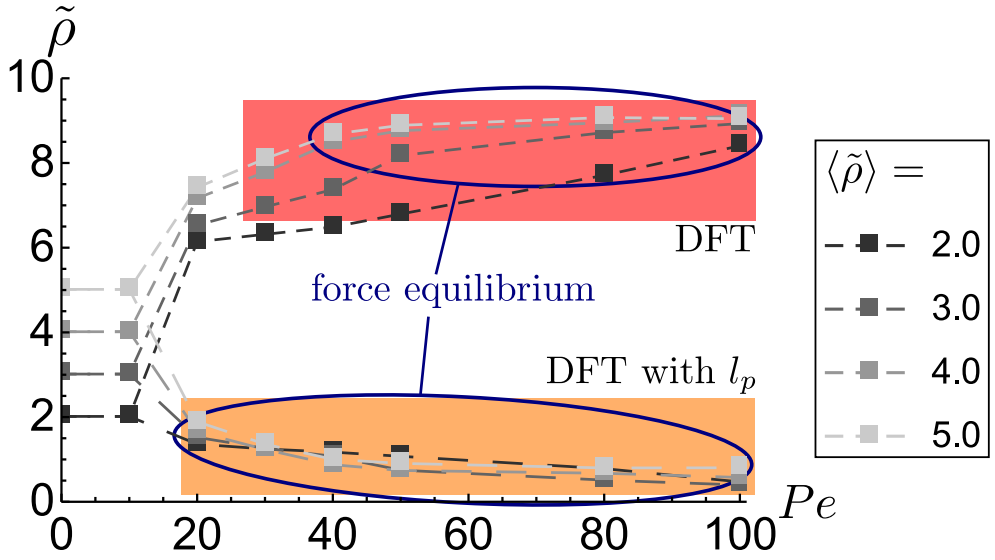

Figure 3.33: Illustration of the agreement of the different analytical models with the simulation results (dashed, grey lines). The force equilibrium model – indicated by the blue ellipses – predicts the density in the isotropic phase fairly well for $Pe \geq 20$ while also yielding good agreement in the high-density phase for large enough average densities and $Pe \geq 40$. The basic density functional theory approach (red rectangle) yields good results for the high-density phase only. Taking into account the particles' effective elongation by their persistence length l_p, this model describes only the low-density phase well (yellow rectangle).

predicts densities that are generally lower than the simulation results but are still in fairly good agreement. Possible explanations for the deviations are the choice of the parameter $\tilde{\rho}_{\mathrm{sp}}$, the system size, and approximations made by the model. The density in the ordered phase was then calculated from an equilibrium condition for the forces the two phases would exert on the interface between them. This approach yielded good agreement with the simulation results for particle motilities $Pe \geq 40$ and large enough average densities. Even though the predicted densities were too large at smaller Péclet numbers, the model is quite accurate in a large range of parameters – especially when considering that it not only describes the high-density phase but also the isotropic phase. For an illustration of the agreement, see Fig. 3.33. One likely explanation for the occurring deviations is the perfect order and stability assumed for the high-density phase. Configurations observed in simulations would not exhibit same degree of order and stability as the model. Also, the simulation data was calculated by averaging over different types of configurations such as asters, collectively moving clusters, and enclosed lanes. Due to their fundamental differences, they cannot be expected to be described by the same model.

In Section 3.6, a density functional theory was used to derive the coexisting densities following a similar approach for spherical particles presented by Cates and Tailleur [178]. The system's free energy was expressed as a function of the local density ρ and minimised with regards to the orientational order parameter α. Since the free energy contained an excess term depending on the particles' speed $v(\rho)$,but the precise form of $v(\rho)$ was unknown, two different ansatzes were tested – a linear and an exponential

dependence. This model made good predictions for the density in the ordered phase, but the density in the isotropic phase would be significantly larger than the simulation results. In order to take into account the particles' increased excluded volume due to their motility, the model was modified by introducing an effective elongation of the particles. In this case, the model could reproduce the density in the isotropic phase for certain parameters but would yield an incorrect density in the ordered phase. This agreement for different phases is also illustrated in Fig. 3.33. We have to conclude that the density functional theory presented here is only suitable for correctly predicting one of the coexisting densities. This is not ideal but could be a promising starting point for further research. The deviations could have several reasons. First, the free energy density derived in the underlying theory is only valid in dilute systems. Secondly, only terms up to second order in the virial expansion are considered which is not a good approximation in two dimensions – see Section 3.1.4. Thirdly, the particles' finite thickness is not taken into account by the model, and it is uncertain whether their effective elongation is correctly described by the simplistic ansatz used here. Finally, self-propelled rodlike particles constitute a non-equilibrium system. Mapping it onto an effective equilibrium system may not be possible as it is for spherical particles. This is the worst case scenario but still a possibility.

Chapter 4

Conclusion

In this thesis, two biophysical topics were investigated numerically and analytically.

4.1 Sheared semiflexible polymer networks

4.1.1 Summary

In Chapter 2, wrinkling in semiflexible polymer networks due to shear strain was studied. Linear elasticity theory for thin membranes was used to find predictions for the critical shear angle γ_c at which wrinkling sets in, the wrinkles' wavelength λ, and their amplitude A. The derived expressions were then applied to discrete networks. The resulting predictions were tested in numerical simulations using an athermal model for semiflexible polymer networks. The simulated networks were generated with a regular or random geometry in two dimensions, and displacements into the third dimension were enabled via positional perturbations of the networks' nodes.
The simulation results yielded good agreement with the theoretical predictions for γ_c and λ suggesting that these measurements can be used in experimental setups to determine the elasticity of sheet-like semiflexible polymer networks and comparable materials. At large strains, deviations from the theory were observed indicating nonlinear effects: Instead of increasing steadily with the shear strain, A would decrease above a maximum shear angle in regular networks. Also, the elastic energies in wrinkled and planar networks would become similar at large strains in contrast to maintaining a constant ratio as predicted by linear elasticity theory. The latter effect is likely to be caused by strain stiffening. Nonlinear elasticity in semiflexible polymer networks has been associated with a transition from a bending dominated regime at small strains to a stretching dominated regime at large strains. It is therefore relevant that the simulation results presented here indicate that wrinkling causes an immediate transition into the stretching dominated regime.

4.1.2 Outlook

As pointed out in Section 2.1.5, this work may be the first studying wrinkling in sheared semiflexible polymer networks. Hence, there are many open questions that could not be addressed yet. The following section aims to outline some viable options for further research.
The simulations described here implemented an athermal model of two-dimensional

networks. The crosslinks forming these were modelled as freely rotating and permanent. There are many ways in which this model could be modified. First, instead of using two-dimensional networks, it would be interesting to study three-dimensional networks with a finite thickness. These are computationally more expensive but would be a more realistic representation of semiflexible polymer networks we find in biological systems such as the cytoskeleton of eukaryotic cells. The elasticity of three-dimensional networks has been studied in simulations [57–59, 206–208], but none of those considered networks that are thin in one dimension. It is quite possible that in these networks, the results for two-dimensional networks regarding wrinkling should remain valid. An indication for this is that wrinkling patterns in experiments with other sheet-like materials have proven to be in good agreement with predictions from elasticity theory [65–67, 74, 76, 79, 85]. However, it has been argued that the mechanical response of three-dimensional networks is more likely to be dominated by nonaffine deformations than in two-dimensional networks [12] which could also affect wrinkling.
Another point to consider is that realistic networks are not necessarily composed of only individual fibers. Depending on the crosslinker density, composite networks of single and bundled filaments can be found as well as networks consisting of only bundles [24, 25]. These networks differ greatly from non-bundled networks regarding their elastic properties [34, 52, 209–213]. Hence, we can expect significant differences with regards to wrinkling as well. For example, the anisotropic structure in composite networks could yield anisotropic wrinkling patterns - an effect that has already been reported in experiments with metal and polyimide films [73, 80]. One simple numerical approach that has been used to generate and investigate composite networks is to use a mixture of rods with different bending rigidities [212, 214, 215].
Another option for making the simulated networks more realistic would be to move away from the purely athermal model and consider the polymers' thermal fluctuations. A viable method for doing this would be to generate the networks using undulated filaments as described by Onck et al. [43] and Huisman et al. [57].
Finally, there is a number of modifications one can make to the crosslinks. Some crosslinking proteins enforce a fixed angle between filaments, see Section 1.2.1. This could be implemented in simulations by an additional energy contribution for angular changes. The resulting networks would have a fundamentally different microstructure than the random networks simulated here which could also affect their elastic properties. Another important property of the crosslinking proteins in real polymer networks is their ability to unbind from the polymers which is a stochastic process that provides the networks with a stress release mechanism [24]. In experiments, unbinding of crosslinkers was shown to have a significant effect on the networks' elasticity [39, 52, 216, 217], so considering it in simulations would yield more realistic behaviour. Due to the stochastic nature of the unbinding mechanism, it would require simulating the systems' time-development though. This would make the simulations computationally expensive compared to the non-dynamic simulations presented here. In addition to stochastic unbinding, crosslinkers can also be forced to unbind by external forces [39, 218–220]. This mechanism is easier to consider in non-dynamic simulations as it does not include a time-dependence. An example for these kinds of simulations has been presented by Åström et al. [59].

4.2 Collective behaviour of active rods

4.2.1 Summary

In Chapter 3, the collective behaviour of active rodlike particles was studied in simulations. These systems are known to exhibit phase separation into an ordered high-density phase and an unordered low-density phase. The main focus of this chapter was finding an analytical model for predicting the coexisting densities by adapting similar models developed for spherical particles. The secondary aim was to reproduce experimentally observed rotating structures.
Simulations were performed using the established framework of Brownian dynamics. The particles were modelled as spherocylinders interacting via a Lennard-Jones potential and a hard-core interaction. Confined systems as well as systems without confinement were considered.
The simulated systems exhibited a variety of patterns including static asters and collectively moving structures such as clusters and enclosed lanes. These patterns met the criteria for phase-separated systems mentioned above which yielded a phase diagram indicating the coexisting densities. Phase separation would occur for particle motilities $Pe \geq 20$ and become more pronounced with increased Péclet number. Despite the variety of the observed patterns, rotating structures did not occur. When manually enforced at the start of simulations, these were not stable leading to the conclusion that the simulated systems were too small to allow the formation of circular structures.
The phase separation observed in the simulations was analysed using two different approaches adapted from analytical models developed for spherical particles. First, the coexisting densities of the two phases were derived from a force equilibrium at the interface between them. This approach could not describe the coexisting densities at small particle motilities – most likely because the model assumes a perfectly ordered and stable high-density phase which is not the case in the simulations. At high particle motilities and large enough average densities, the model was quite successful yielding fairly good agreement with the simulation results for both coexisting densities.
Secondly, the systems' free energy density was approximated using a density functional theory, and the coexisting densities were derived from a common tangent construction. The two variants of this model were able to reproduce one of the coexisting densities each but not both. Possible reasons for this shortcoming could be that some of the approximations made for deriving the free energy density are not valid. Also, this approach tries to map a non-equilibrium systems onto an effective equilibrium system which may not be possible for this problem.

4.2.2 Outlook

As summarised above, the simulations presented here were not able to reproduce rotating structures that were observed in experiments with active rodlike particles. Also, the analytical models developed in this work could only partly describe the phase separation in the simulated systems. The following section will present some options for adjusting the simulations and analytical models in order to obtain better results.
Circular patterns have been reported in experiments and simulations of active rodlike particles [109, 110, 124–126, 137, 155]. In comparison to those examples, the systems simulated here were too small to allow the formation of circular patterns. The obvious solution to this would be to simulate larger systems, but this would of course result in

increased computation time. Hence, increasing the system size would only be a viable option if the simulation algorithm could be made more efficient. Other crucial factors affecting the formation of circular patterns are the interactions between particles. Lushi et al. found in simulations of self-propelled rods confined in a circular geometry that the particles would form a single vortex but only when hydrodynamic interactions were considered [155]. The occurrence of swirling patterns due to hydrodynamic interactions has also been confirmed in analytical models by Yang and Marchetti [196]. The simulations presented here did not include hydrodynamics though. This could be an explanation why circular patterns were not observed. Besides hydrodynamic interactions, explicit aligning interactions between particles were found to enable the formation of such patterns. Yang et al. found in analytical investigations that the strength of an explicit aligning interaction had to be in a certain range in order to generate spiralling patterns [153]. In this work, interactions between particles were modelled as a Lennard-Jones potential with an additional hard-core potential. This interaction favours alignment of particles, but its strength was kept constant at a low value throughout different simulations. This could be another reason why circular patterns were not observed. We could test the influence these interactions have on the formation of circular patterns by implementing hydrodynamic interactions and modifying the strength of the implemented Lennard-Jones potential.
There are also a few possibilities to improve the analytical models for calculating the coexisting densities in phase separated systems. The main shortcomings of the force equilibrium model were its oversimplified modelling of the ordered phase and the fact that it was based on a specific configuration while trying to describe simulation data that was extracted by averaging over different types of configurations. One solution to the second aspect would be to find a way to identify the occurring patterns in real-time. This way, their density distributions could be evaluated separately which would yield more specific results. Then, individual force equilibrium models could be used to describe each of the configurations, and the coexisting densities could be predicted for each of them individually. This approach would eliminate averaging over different configurations as a source of error. The oversimplified modelling could be improved by assuming a high-density phase that is not perfectly ordered since this is not the case in simulations either. Also, the model presented here neglects thermal effects which are a significant factor in simulations. Taking into account thermal fluctuations in the high-density phase would yield additional internal forces that would increase the distance between particles and thereby reduce density.
The density functional theory presented here has two intrinsic deficiencies that are hard to resolve: only taking into account terms up to second order in the virial expansion is not a good approximation in two dimensions, and the free energy density derived with this approach is only valid in dilute systems. The second point has been addressed by Wensink and Trizac who modified the Onsager theory for elongated particles by combining the second-virial approach with a mean-field approximation that is valid at high densities [221]. The resulting theory is an interpolation between the low-density and the high-density regime, but the authors explicitly pointed out that it is not applicable to the Lennard-Jones potential considered here. Other shortcomings of the density functional theory presented here might be possible to eliminate. One of those is the particles' effective elongation due to their propulsion. We assumed the particles to be elongated by their persistence length in a vacuum which is a very simplistic model. This could be improved by taking into account interactions with other particles that might

reduce the particles' persistence length. The resulting elongation would likely depend on the local density. Another problem was that the precise form of the particles' speed as a function of local density and degree of order is unknown. The assumed dependencies were adapted from models for spherical particles but not derived analytically. Such an explicit derivation could yield a more accurate model for the particle speed and hence improve the theory's validity. In this context, it would also be useful if the simulations allowed measuring the particles' speed as a function of local density and degree of order because this would allow testing the analytical model. This problem is not trivial since it is hard to control the particles' density and ordering in simulations – see App. F.

Another possibility for further research was already pointed out in Section 3.6.4: the two variants of the model presented here yielded good results for one of the phases each, so it might be possible to get a more comprehensive description by combining the two.

However, it is also possible that other models are more suitable for describing systems of self-propelled rods than the density functional theory. In the last years, continuum models have been reported to successfully describe collective motion in such systems including the formation of collectively moving clusters [191, 195], lanes [153, 192], and even swirling patterns [153, 196]. Some of these models consider hydrodynamic effects which were shown to significantly affect the behaviour of active particles in general [155, 222] and flagellated bacteria specifically [223]. Since the density functional theory does not include hydrodynamics, those other approaches may be the better choice.

Finally, it should be noted that the investigation of three-dimensional systems is likely to become important in the near future since most biological systems are three-dimensional. Self-propelled spherical particles have already been studied in three-dimensional simulations and were found to exhibit phase separation and collectively moving patterns similar to their two-dimensional counterparts [224, 225]. This raises the question whether three-dimensional systems of self-propelled rodlike particles would also behave similarly to two-dimensional ones. At this point in time, the main difficulty with these kinds of systems is probably the requirement for very large systems [224] which makes the simulations computationally expensive.

Appendix A

The virial expansion

Since biological systems consist of large numbers of particles, it makes sense to study them using thermodynamics. Ideally, we would like to know the system's equation of state from which we can derive all thermodynamic quantities. However, we are dealing with systems of interacting particles, so the equation of state cannot be derived exactly as would be the case for a gas of non-interacting particles. However, it is possible to approximate the equation of state as a power series in the system's density ρ. This description is called the virial expansion and will be introduced here following the books "Statistische Physik" by Torsten Fließbach [226] and "Statistische Mechanik" by Franz Schwabl [227].

We consider a dilute gas of N identical particles with the Hamiltonian

$$H = \sum_{i=1}^{N} \frac{p_i^2}{2m} + \sum_{i=2}^{N} \sum_{j=1}^{i-1} v(\boldsymbol{r}_i, \boldsymbol{r}_j) \ , \tag{A.1}$$

where m is the particles' mass, $\boldsymbol{p}_i$ the momentum of particle i, and $v(\boldsymbol{r}_i, \boldsymbol{r}_j)$ is a potential describing the interaction between two particles at positions $\boldsymbol{r}_i$ and $\boldsymbol{r}_j$. The assumption that the system' particle density ρ is small is important because it allows us to neglect rarely occurring interactions of three or more particles. We also assume that we can treat the system classically which is usually true.
In the grand canonical ensemble, the natural variables are the temperature T, the volume V and the chemical potential μ. We start by expressing the grand canonical partition function Z_g in terms of the canonical partition function Z:

$$Z_g(T, V, \mu) = \sum_{N=0}^{\infty} Z(T, V, N) \exp(\beta \mu N) = \sum_{N=0}^{\infty} Z_N \exp(\beta \mu N) \ , \tag{A.2}$$

where $\beta = (k_B T)^{-1}$ and we have defined $Z_N = Z(T, V, N)$. From the ideal gas, we know that the fugacity $z = \exp(\beta\mu)$ is small when ρ is small. However, since the Z_N grow exponentially with N, we cannot neglect the terms of greater N in this series. For the grand canonical potential which is given as

$$J = -k_B T \ln Z_g = -k_B T \ln \left(1 + Z_1 z + Z_2 z^2 + \ldots\right) \ , \tag{A.3}$$

this is possible though as we can see when we calculate the Taylor series of the right-hand side with z as the variable of the expansion:

$$\ln\left(1 + Z_1 z + Z_2 z^2 + \ldots\right) = Z_1 z + \left(Z_2 - \frac{Z_1^2}{2}\right) z^2 + \ldots \ . \tag{A.4}$$

From this, we can calculate the average number of particles

$$N = -\frac{\partial J}{\partial \mu} = Z_1 z + 2 Z_2 z^2 + \ldots \ , \tag{A.5}$$

which we can rearrange to

$$z = \frac{N}{Z_1} - \frac{2\left(Z_2 - \frac{Z_1^2}{2}\right)}{Z_1} z^2 + \mathcal{O}(z^3) \ . \tag{A.6}$$

Entering this into the approximation for J yields

$$J = -k_B T \left[N - \left(Z_2 - \frac{Z_1^2}{2}\right)\left(\frac{N}{Z_1}\right)^2 + \ldots\right] \ . \tag{A.7}$$

With $J = -pV$ where p denotes the pressure, we arrive at the equation of state

$$p = k_B T \rho \left[1 - \left(Z_2 - \frac{Z_1^2}{2}\right)\frac{N}{Z_1^2} + \ldots\right] \ . \tag{A.8}$$

In order to express this in terms of the density, we calculate the canonical partition function Z_1 explicitly:

$$Z_1 = (2\pi\hbar)^{-3} \int_V d^3 r \int d^3 p \exp\left(-\frac{p^2}{2 m k_B T}\right) = V \Lambda^{-3} \ , \tag{A.9}$$

with $\Lambda = \sqrt{\frac{2\pi\hbar^2}{m k_B T}}$ being the thermal de Broglie wavelength. With this result, the equation of state becomes

$$p = k_B T \rho \left[1 - \frac{\Lambda^6}{V}\left(Z_2 - \frac{V^2}{2\Lambda^6}\right)\rho + \ldots\right] \ , \tag{A.10}$$

which we can identify as a power series in ρ. The generalised form of this is the virial expansion

$$p = k_B T \rho \left[1 + B_2(T)\rho + B_3(T)\rho^2 + \ldots\right] \ . \tag{A.11}$$

The B_n are the virial coefficients which are determined by the n-particle canonical partition function Z_n and therefore take into account n-particle interactions.
In our case, we want to consider pair interactions only, so we neglect terms of order ρ^3 and higher. Due to the calculations above, we already know how to determine the second virial coefficient:

$$B_2(T) = -\frac{V}{Z_1^2}\left(Z_2 - \frac{Z_1^2}{2}\right) \ . \tag{A.12}$$

We still need to calculate Z_2 which yields

$$\begin{aligned} Z_2 &= \frac{1}{2!}(2\pi\hbar)^{-6} \iint_V d^3r_1\, d^3r_2 \iint d^3p_1\, d^3p_2 \exp\left(-\frac{p_1^2+p_2^2}{2mk_BT} - \frac{v((\boldsymbol{r}_1,\boldsymbol{r}_2)}{k_BT}\right) \\ &= \frac{1}{2!}\Lambda^{-6} \iint_V d^3r_1\, d^3r_2 \exp\left(-\frac{v((\boldsymbol{r}_1,\boldsymbol{r}_2)}{k_BT}\right) \ . \end{aligned} \tag{A.13}$$

For a potential $v(\boldsymbol{r}_1,\boldsymbol{r}_2) = v(r)$ that is only a function of the distance $r = |\boldsymbol{r}_1 - \boldsymbol{r}_2|$, this can be written as

$$Z_2 = \frac{V}{2}\Lambda^{-6} \int_V d^3r \exp\left(-\frac{v(r)}{k_BT}\right) \ . \tag{A.14}$$

With this, we get

$$\begin{aligned} B_2(T) &= -\frac{1}{2}\left[\int_V d^3r \exp\left(-\frac{v(r)}{k_BT}\right) - V\right] \\ &= -\frac{1}{2}\int_V d^3r \left[\exp\left(-\frac{v(r)}{k_BT}\right) - 1\right] \ . \end{aligned} \tag{A.15}$$

For a usual gas, the term in the integral only gives a contribution for distances way smaller than the system size, so we get the same result when integrating over the whole position space. This has the advantage that we are left with only the radial integration:

$$B_2(T) = -2\pi \int dr\, r^2 \left[\exp\left(-\frac{v(r)}{k_BT}\right) - 1\right] \ . \tag{A.16}$$

This expression allows us to apply the virial expansion to any gas as long as we know the exact form of the pair potential $v(r)$. Interactions of more than two particles are neglected in this description.

Appendix B

Calculation of hard-core distance

In areas of high particle density, the distances between particles can become very small. Due to the repulsive Lennard-Jones interaction, this would lead to large forces acting on the particles causing them to move very far. However, since the density is high, it is very unlikely that a particle can actually move far without collisions. Such a collision would interrupt the move and hence prevent the force from coming into effect completely. So, large forces are a problem in simulation because they decrease the algorithm's efficiency.
We want to find an expression for the minimum distance d_{hc} we allow between particles as a function of the length of the resulting move l_m. For simplicity, we consider two perfectly aligned rodlike particles at a distance r. The repulsive force then acts exactly perpendicular to the rods' main axes and does not generate a torque. Therefore, the resulting move of the entire rod is equivalent to the move of each segment, so we can just calculate the force on a single segment. We neglect interactions with all but the nearest segment – at distance r – which leads to the resulting force

$$F_{LJ}(r) = 48\frac{\epsilon}{r}\left(\frac{d}{r}\right)^{12} - 24\frac{\epsilon}{r}\left(\frac{d}{r}\right)^{6} \ . \tag{B.1}$$

At small distances, the repulsive term is dominant, so we also neglect the attractive term:

$$F_{LJ}(r) \approx 48\frac{\epsilon}{r}\left(\frac{d}{r}\right)^{12} \ . \tag{B.2}$$

Since this force acts perpendicularly to the rod's orientation, the resulting velocity is

$$v_{LJ}(r) = \frac{1}{\gamma_\perp} F_{LJ}(r) \ . \tag{B.3}$$

In a time-step Δt, the segment will then move a distance l_m which we can express as a multiple of d:

$$l_m = nd = v_{LJ}(r)\Delta t \ . \tag{B.4}$$

Finally, we solve the above equation for r which yields an expression for d_{hc} as a function of n – the factor defining the maximum length of a move resulting from the Lennard-Jones interaction – at given parameters:

$$d_{\mathrm{hc}}(n) = \left[\frac{48\epsilon d^{11}\Delta t}{n\gamma_\perp}\right]^{\frac{1}{13}} \ . \tag{B.5}$$

Appendix C

Density Distributions

C.1 Determining grid cell size

As described in Section 3.3.7, density distributions in the simulated systems are measured using a grid of square-shaped cells with dimensions $l_\rho \times l_\rho$. Since we want to be able to distinguish phase separation from isotropic configurations, we have to choose the cell size carefully. Using cells that are too large could lead to averaging over areas with different densities. An extreme example of this would be using only one cell as large as the simulation cell itself. In this case, the measured density would always be the average density of the system – regardless of whether or not areas of different densities exist. On the other hand, cells that are too small would cover areas that do not contain multiple particles. Hence, these cells would measure densities on the level of single particles instead of phases which could yield distributions that falsely indicate phase separation. The relevant length scale in this case should be the mean distance between particles in the isotropic phase. Below this length scale, only one particle contributes to the measured density making it mainly dependent on the cell size. The reason is that the length of the particle in the cell is proportional to l_ρ while the area of the cell is proportional to l_ρ^2, so the density in the cell is proportional to l_ρ^{-1}. When l_ρ is greater than the average distance between particles though, the number of particles in the cell scales with l_ρ making the total length in the cell proportional to l_ρ^2. Hence, the measured density in the cell should be independent of its size in this case.
For finding the ideal cell size, we measured the density distributions in systems with isotropic density and with phase separation and varied the cell size. The aim was to find a cell size at which both configurations would be identified correctly. In an isotropic system, the particles are evenly distributed yielding a uniform density thoughout the whole system. Hence, we expect the density distribution to be peaked around the system's average density $\langle\tilde{\rho}\rangle$. In a system of two perfectly separated phases, we have one area of low density and one of high density. In this case, the density distribution should consist of only two peaks – one at a density smaller than $\langle\tilde{\rho}\rangle$ and one at a density greater than $\langle\tilde{\rho}\rangle$.
As outlined above, we can expect the average distance of particles in the isotropic phase to be an important length scale. This distance is inversely proportional to the average density, so we will from now on specify the cell size in terms of use the dimensionless parameter $\tilde{l}_\rho = l_\rho L^{-1}\langle\tilde{\rho}\rangle$.

As isotropic systems, we used initial configurations of systems at average densities

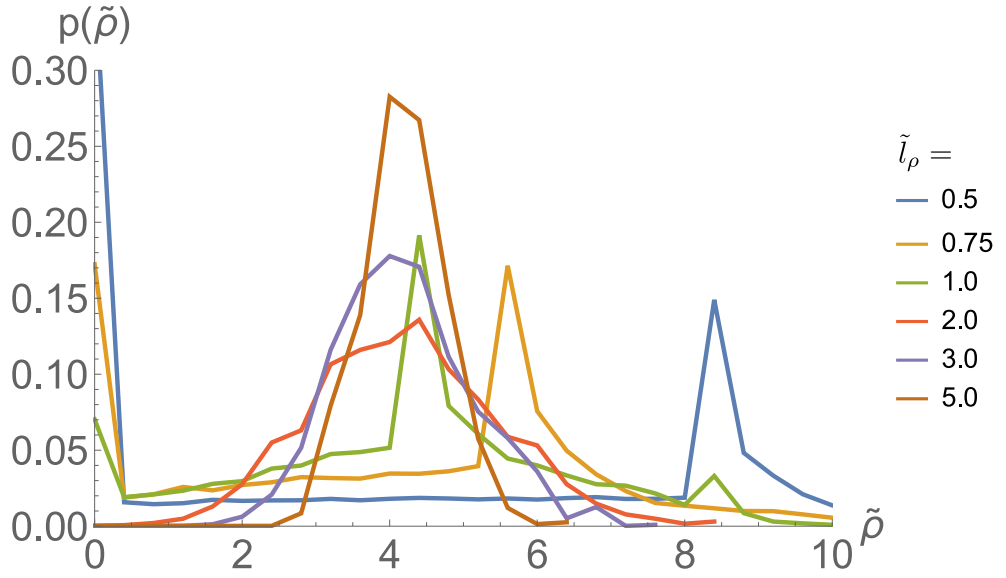

Figure C.1: Comparison of different cell sizes $\tilde{l}_\rho$ for measuring the density distribution of an isotropic system with average density $\langle\tilde{\rho}\rangle = 4.0$. For $\tilde{l}_\rho \leq 0.75$, the distribution does not consist of just one peak at the average density which we would expect in an isotropic system. In fact, even for $\tilde{l}_\rho = 1.0$, the peak is shifted to a slightly greater density than $\langle\tilde{\rho}\rangle$ and we notice a local maximum at $\tilde{\rho} = 0$.

$\langle\tilde{\rho}\rangle \in \{2.0, 3.0, 4.0, 5.0\}$ with a total number of particles in the range of $N \approx 2000$. Since these were generated by depositing particles into the simulation cell at random positions and orientations, we can safely expect the particle positions to be distributed evenly. We varied the cell size in the range $\tilde{l}_\rho \in [0.5, 5.0]$ and measured the density distribution at each cell size.

We found that for $\tilde{l}_\rho \leq 0.75$, the distributions would have two maxima – one at $\tilde{\rho} = 0$ and another one at a density greater than the average density in the system – see Fig. C.1 for an example at $\langle\tilde{\rho}\rangle = 4.0$. Since the systems were isotropic, we could conclude that the cells were too small and the indicated phase separation was an effect of the cell size. Deviations also occured for $\tilde{l}_\rho = 1.0$. The resulting distributions would have peaks at slightly larger densities than $\langle\tilde{\rho}\rangle$ and a second small maximum at $\tilde{\rho} = 0$. Since the deviations from the expected distribution were small, we did not rule out this cell size yet and concluded that cell sizes of at least $\tilde{l}_\rho \geq 1.0$ were necessary to correctly identify an isotropic system by its density distribution.

For measuring density distributions in systems with phase separation, we used snapshots from simulations in which the particles were clearly divided into one bulk phase of high density and another phase of very low density. Again, we used several average densities $\langle\tilde{\rho}\rangle \in \{2.0, 3.0, 4.0, 5.0\}$ but with a total number of particles in the range of $N \approx 200$. This time, we only used cell sizes meeting the condition that they would give a correct distribution for isotropic systems: $\tilde{l}_\rho \in [1.0, 5.0]$.

For $\langle\tilde{\rho}\rangle = 2.0$ and cell sizes $\tilde{l}_\rho \geq 3.0$, the distributions would exhibit multiple peaks over a wide range of densities. Distributions for $\tilde{l}_\rho \in [1.0, 2.0]$ would have two maximums as expected in a system with two separate phases of different density. This was also the case for larger average densities – see the example plot for a system of $\langle\tilde{\rho}\rangle = 4.0$

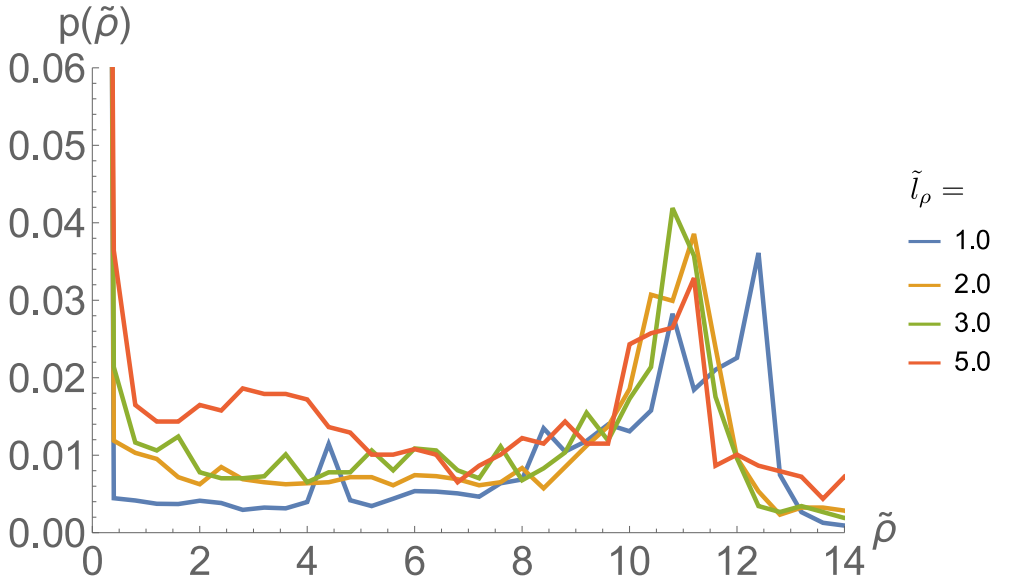

Figure C.2: Comparison of different cell sizes $\tilde{l}_\rho$ for measuring the density distribution of a system exhibiting phase separation with average density $\langle\tilde{\rho}\rangle = 4.0$ and particle motility $Pe = 100$. For all $\tilde{l}_\rho$, the distribution has two maximums – one at $\tilde{\rho} = 0$ and one at $\tilde{\rho} \approx 11$. This meets our expectation for systems with two separate phases of different density. However, for $\tilde{l}_\rho = 1.0$, we find an additional local maximum near $\langle\tilde{\rho}\rangle$.

and $Pe = 100$. in Fig. C.2. The correct form of the density distributions would make the according cell sizes viable options for correctly identifying phase separation. However, the density distributions for $\tilde{l}_\rho = 1.0$ would in some cases exhibit a small local maximum near the system's average density. For $\tilde{l}_\rho = 2.0$, this effect was not observed. As mentioned before, small deviations from the expected density distribution were also found in isotropic systems for $\tilde{l}_\rho = 1.0$ but not for $\tilde{l}_\rho = 2.0$. Therefore, $\tilde{l}_\rho = 2.0$ was used for further measurements of the density distribution.

C.2 Influence of the splitting density

As described in Section 3.3.7, we used $\tilde{\rho}_{\text{crit}} = 3\pi/2$ as the splitting density $\tilde{\rho}_{\text{sp}}$ when calculating the coexisting densities in a system with phase separation. We chose this value because it is the geometrical limit up to which a two-dimensional system of infinitely thin rods can remain isotropic – see Section 3.1.4. However, this value is not distinguished, and it would also be possible to split the density distributions at a different values $\tilde{\rho}_{\text{sp}}$. Different splitting densities would yield different results for the coexisting densities as illustrated in Fig. C.3 for a system with average density $\langle\tilde{\rho}\rangle = 5.0$ at different particle motilities. We see both coexisting densities increasing with $\tilde{\rho}_{\text{sp}}$. This is not surprising since the simulated systems would not exhibit perfect phase separation, i.e., their density distributions would consist of two smoothed out peaks. Hence, depending on which phase the densities in the intermediate range would be assigned to, the coexisting densities would vary. Since we would average over all densities attributed to each phase, including higher densities in the low-density phase would increase its average density. Coincidently, the same densities would be excluded from the high-density

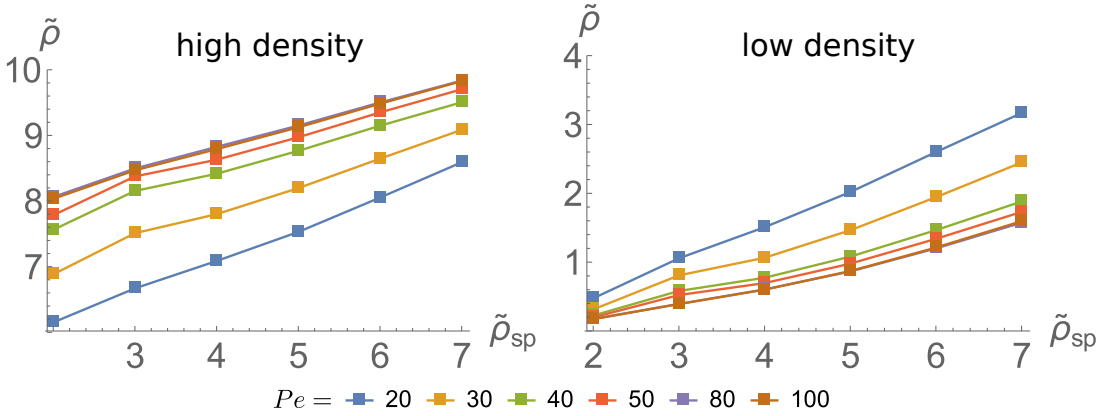

Figure C.3: High density (left) and low density (right) in a phase-separated system with average density $\langle\tilde{\rho}\rangle = 5.0$ at different particle motilities as a function of the splitting density $\tilde{\rho}_{sp}$. The obtained results vary significantly with the value of splitting density in the examined range.

phase increasing this average density as well.

In order to quantify the effect the splitting density $\tilde{\rho}_{sp}$ has on the coexisting densities, we calculated the phases' average densities with respect to different values $\tilde{\rho}_{sp}$. These values would be different for each particle motility. Next, we compared the average value to the corresponding minimum and maximum density. We found that these values could deviate from the average value by up to 102% in the low-density phase. In the high-density phase, the greatest deviation was 30%. Hence, we have to acknowledge that the coexisting densities we measured were quite sensitive to the choice of $\tilde{\rho}_{sp}$. As mentioned before, we would not necessarily have to use $\tilde{\rho}_{sp} = \tilde{\rho}_{crit}$. This should be considered when evaluating the simulation results as these would only be accurate within the above mentioned margins of error.

Appendix D

Consistence of common tangent when adding a linear term

The common tangent of two functions $f_1(x)$, $f_2(x)$ is defined by two points $(x_1, f_1(x_1))$ and $(x_2, f_2(x_2))$ with x_1, x_2 meeting the following conditions:

$$I. \qquad \left.\frac{df_1}{dx}\right|_{x=x_1} = \left.\frac{df_2}{dx}\right|_{x=x_2} \tag{D.1}$$

$$II. \qquad f_2(x_2) = f_1(x_1) + (x_2 - x_1) \left.\frac{df_1}{dx}\right|_{x=x_1} \tag{D.2}$$

Now, we add a linear term αx with $\alpha = \text{const.}$ to both functions and call the resulting functions $\tilde{f}_1$ and $\tilde{f}_2$:

$$\tilde{f}_1 = f_1 + \alpha x \tag{D.3}$$

$$\tilde{f}_2 = f_2 + \alpha x \tag{D.4}$$

We want to demonstrate that x_1 and x_2 also meet the two conditions presented above for $\tilde{f}_1$ and $\tilde{f}_2$:

$$I. \qquad \left.\frac{d\tilde{f}_1}{dx}\right|_{x=x_1} \stackrel{?}{=} \left.\frac{d\tilde{f}_2}{dx}\right|_{x=x_2} \tag{D.5}$$

$$II. \qquad \tilde{f}_2(x_2) \stackrel{?}{=} \tilde{f}_1(x_1) + (x_2 - x_1) \left.\frac{d\tilde{f}_1}{dx}\right|_{x=x_1} \tag{D.6}$$

The solution is straight-forward:

$$I. \qquad \left.\frac{d\tilde{f}_1}{dx}\right|_{x=x_1} = \left.\frac{df_1}{dx}\right|_{x=x_1} + \alpha = \left.\frac{df_2}{dx}\right|_{x=x_2} + \alpha = \left.\frac{d\tilde{f}_2}{dx}\right|_{x=x_2} \tag{D.7}$$

$$\begin{aligned} II. \qquad & \tilde{f}_1(x_1) + (x_2 - x_1) \left.\frac{d\tilde{f}_1}{dx}\right|_{x=x_1} \\ & = f_1(x_1) + \alpha x_1 + (x_2 - x_1) \left.\frac{df_1}{dx}\right|_{x=x_1} + \alpha(x_2 - x_1) \\ & = f_2(x_2) + \alpha x_1 + \alpha(x_2 - x_1) = f_2(x_2) + \alpha x_2 \\ & = \tilde{f}_2(x_2) \end{aligned} \tag{D.8}$$

So, adding the same linear term to two functions f_1 and f_2 does not alter the x-values of the points defining their common tangent.

Appendix E

Iterative Calculation of the degree of ordering as a function of density

When calculating the free energy

$$\begin{aligned}\tilde{F} = \frac{\beta F L^2}{V} = \tilde{\rho}\,(\ln(\tilde{\rho}) - 1) + \tilde{\rho} \int \psi_\alpha(\vartheta) \ln(2\pi\psi_\alpha(\vartheta))\, d\vartheta \\ + \tilde{\rho}^2 \iint \psi_\alpha(\vartheta)\psi_\alpha(\vartheta') \sin(\vartheta - \vartheta')\, d\vartheta\, d\vartheta' \\ + \int_0^{\tilde{\rho}} \frac{1}{2} \ln(1 + \frac{v(\tilde{s})^2 \tau_r}{2D_t})\, d\tilde{s}\end{aligned} \tag{E.1}$$

at a certain density $\tilde{\rho}$, we have to find the minimum of $\tilde{F}$ with respect to α. However, the velocity is also a function of α. In the excess term, we have to integrate the logarithm of the velocity over all densities $\tilde{s} \leq \tilde{\rho}$. Therefore, we need to know the degree of ordering that minimises $\tilde{F}$ for each density below $\tilde{\rho}$.
So, we have to perform the calculation iteratively starting at $\tilde{\rho} = 0$ and incrementally increasing $\tilde{\rho}$.
In each step i of the iteration, we numerically calculate $\tilde{F}$ as a function of α at the fixed density $\tilde{\rho}_i$. Then, we identify the value $\alpha > 0$ for which $\tilde{F}$ has a minimum and call this α_i. For the evaluation of the integral in the excessive term, we calculate a fitting function $\alpha(\tilde{\rho})$ using the pairs of values $\{(\tilde{\rho}_0, \alpha_0), \ldots, (\tilde{\rho}_{i-1}, \alpha_{i-1})\}$. For densities in the interval $[\tilde{\rho}_{i-1}, \tilde{\rho}_i]$, we interpolate linearly between α_{i-1} and the value of α for which we are calculating the free energy.
As mentioned above, we start at $\tilde{\rho}_0 = 0$ which gives $\tilde{F} = 0$ independent of α, so we set $\alpha_0 = 0$ as well. We also set $\alpha_i = 0$ every time we cannot find a minimum in $\tilde{F}$. When we do find a minimum though, we have automatically calculated $\tilde{F}(\tilde{\rho}_i)$. In the end, this gives us pairs of values $\left\{\left(\tilde{\rho}_i, \tilde{F}(\tilde{\rho}_i)\right)\right\}$ we need for the common tangent construction.

Appendix F

Measuring particle speed

In Section 3.6, an analytical model for calculating the coexisting densities in a phase-separated system of self-propelled rods was presented. One important element of this approach was approximating the system's free energy density using a density functional theory. In order to take into account the particles' motility, an excess term was considered in the free energy density. This term turned out to be a source of uncertainty though since it depends on the particles' speed as a function of density $v(\rho)$ of which the precise form is unknown. Different ansatzes were tested throughout the analysis, but none of these was based on experimental or numerical results.
In order to improve the analytical model, we tried measuring the particles' speed in simulations. We used a slightly different environment in the simulations than the ones described in Section 3.3.1: particles were confined in channels with fixed boundaries in one dimension and periodic boundary conditions in the other dimension. Also, during system the generation process, the rods' orientations were restricted to an angular range centered around an axis parallel to the confinement. The latter aspect was implemented to generate systems with a specific degree of ordering, and the confinement in one dimension was supposed to stabilise this ordered configuration during simulation. Simulations were performed at various densities and degrees of order with the intention to measure the particles' speed as a function of these two parameters. However, the systems evolved differently than expected. Instead of maintaining their initial degree of order, the particles would aggregate near the channel walls. The resulting configurations therefore had inhomogeneous density distributions and degrees of order deviating from their initial ones. As a result, it was not possible to perform controlled, systematic measurements of the particles' speed as a function of density and degree of order. In order to obtain these data, a different simulation setup would have to be designed in which density and degree of order could be more rigorously controlled.

Bibliography

[1] Wikipedia. *Frankenstein in popular culture — Wikipedia, The Free Encyclopedia.* [Online; accessed 6-September-2016]. 2016.

[2] Peter Weingart, Claudia Muhl and Petra Pansegrau. 'Of Power Maniacs and Unethical Geniuses: Science and Scientists in Fiction Film'. In: *Public Understanding of Science* 12.3 (2003), pp. 279–287.

[3] Roslynn Haynes. 'From Alchemy to Artificial Intelligence: Stereotypes of the Scientist in Western Literature'. In: *Public Understanding of Science* 12.3 (2003), pp. 243–253.

[4] N Bostrom. 'In defense of posthuman dignity'. In: *Bioethics* 19.3 (2005). Transvision 2003 Conference, Yale Univ, New Haven, CT, 2003, 202–214.

[5] RT Kell, G Bell and A Quinney. 'Musculoskeletal fitness, health outcomes and quality of life'. In: *Sports Medicine* 31.12 (2001), 863–873.

[6] L Hood et al. 'Systems biology and new technologies enable predictive and preventative medicine'. In: *Science* 306.5696 (2004), 640–643.

[7] Kristina Riehemann et al. 'Nanomedicine–Challenge and Perspectives'. In: *Angewandte Chemie International Edition* 48.5 (2009), pp. 872–897.

[8] K. K. Jain. 'Synthetic Biology and Personalized Medicine'. In: *Medical Principles and Practice* 22.3 (2013), 209–219.

[9] Hans Frauenfelder, Peter G. Wolynes and Robert H. Austin. 'Biological Physics'. In: *Rev. Mod. Phys.* 71 (1999), S419–S430.

[10] Erich Sackmann. 'Biological Physics–Origin and Perspectives'. In: *ChemPhysChem* 3.3 (2002), pp. 237–242.

[11] Olaf S. Andersen. 'Introduction to Biophysics Week: What is Biophysics?' In: *Biophysical Journal* 110.5 (2016), E01–E03.

[12] C. P. Broedersz and F. C. MacKintosh. 'Modeling semiflexible polymer networks'. In: *Rev. Mod. Phys.* 86 (2014), pp. 995–1036.

[13] R. C. Picu. 'Mechanics of random fiber networks-a review'. In: *Soft Matter* 7 (2011), pp. 6768–6785.

[14] M. C. Marchetti et al. 'Hydrodynamics of soft active matter'. In: *Rev. Mod. Phys.* 85 (2013), pp. 1143–1189.

[15] Sriram Ramaswamy. 'The Mechanics and Statistics of Active Matter'. In: *Annual Review of Condensed Matter Physics* 1.1 (2010), pp. 323–345.

[16] Stephen J. Ebbens and Jonathan R. Howse. 'In pursuit of propulsion at the nanoscale'. In: *Soft Matter* 6 (2010), pp. 726–738.

[17] Michael F Hagan and Aparna Baskaran. 'Emergent self-organization in active materials'. In: *Current Opinion in Cell Biology* 38 (2016), pp. 74–80.

[18] J. Elgeti, R. G. Winkler and G. Gompper. 'Physics of microswimmers–single particle motion and collective behavior: a review'. In: *Reports on Progress in Physics* 78.5, 056601 (2015), p. 056601.

[19] Romanczuk, P. et al. 'Active Brownian Particles'. In: *Eur. Phys. J. Special Topics* 202 (2012), pp. 1–162.

[20] Bruce Alberts et al. *Molecular Biology of the Cell: Reference edition*. Molecular Biology of the Cell: Reference Edition 1. Garland Science, 2008.

[21] F. Jülicher et al. 'Active behavior of the Cytoskeleton'. In: *Physics Reports* 449.1-3 (2007), pp. 3–28.

[22] Thomas D. Pollard and John A. Cooper. 'Actin, a Central Player in Cell Shape and Movement'. In: *Science* 326.5957 (2009), pp. 1208–1212.

[23] Qi Wen and Paul A. Janmey. 'Polymer physics of the cytoskeleton'. In: *Current Opinion in Solid State and Materials Science* 15.5 (2011), pp. 177–182.

[24] Oliver Lieleg, Mireille M. A. E. Claessens and Andreas R. Bausch. 'Structure and dynamics of cross-linked actin networks'. In: *Soft Matter* 6 (2010), pp. 218–225.

[25] Daniel A. Fletcher and R. Dyche Mullins. 'Cell mechanics and the cytoskeleton.' In: *Nature* 463.7280 (2010), pp. 485–492.

[26] Sampriti Mukherjee, Paul Babitzke and Daniel B. Kearns. 'FliW and FliS Function Independently To Control Cytoplasmic Flagellin Levels in Bacillus subtilis'. In: *Journal of Bacteriology* 195.2 (2013), pp. 297–306.

[27] Christopher Dombrowski et al. 'Self-Concentration and Large-Scale Coherence in Bacterial Dynamics'. In: *Phys. Rev. Lett.* 93 (2004), p. 098103.

[28] H. P. Zhang et al. 'Collective motion and density fluctuations in bacterial colonies'. In: *Proceedings of the National Academy of Sciences* 107.31 (2010), pp. 13626–13630.

[29] T. Ishikawa et al. 'Energy Transport in a Concentrated Suspension of Bacteria'. In: *Phys. Rev. Lett.* 107 (2011), p. 028102.

[30] M E Cates. 'Diffusive transport without detailed balance in motile bacteria: does microbiology need statistical physics?' In: *Reports on Progress in Physics* 75.4 (2012), p. 042601.

[31] Daniel B Kearns. 'A field guide to bacterial swarming motility'. In: *Nature Reviews Microbiology* 8.9 (2010), pp. 634–644.

[32] M. L. Gardel et al. 'Prestressed F-actin networks cross-linked by hinged filamins replicate mechanical properties of cells'. In: *Proceedings of the National Academy of Sciences of the United States of America* 103.6 (2006), pp. 1762–1767.

[33] M. L. Gardel et al. 'Scaling of F-Actin Network Rheology to Probe Single Filament Elasticity and Dynamics'. In: *Phys. Rev. Lett.* 93 (2004), p. 188102.

[34] M. L. Gardel et al. 'Elastic Behavior of Cross-Linked and Bundled Actin Networks'. In: *Science* 304.5675 (2004), pp. 1301–1305.

[35] Norman Y. Yao et al. 'Nonlinear Viscoelasticity of Actin Transiently Cross-linked with Mutant α-Actinin-4'. In: *Journal of Molecular Biology* 411.5 (2011), pp. 1062–1071.

[36] Yi-Chia Lin et al. 'Origins of Elasticity in Intermediate Filament Networks'. In: *Phys. Rev. Lett.* 104 (2010), p. 058101.

[37] Yi-Chia Lin et al. 'Divalent Cations Crosslink Vimentin Intermediate Filament Tail Domains to Regulate Network Mechanics'. In: *Journal of Molecular Biology* 399.4 (2010), pp. 637–644.

[38] Paul H. J. Kouwer et al. 'Responsive biomimetic networks from polyisocyanopeptide hydrogels'. In: *Nature* 493.7434 (2013), pp. 651–655.

[39] R. Tharmann, M. M. A. E. Claessens and A. R. Bausch. 'Viscoelasticity of Isotropically Cross-Linked Actin Networks'. In: *Phys. Rev. Lett.* 98 (2007), p. 088103.

[40] David A. Head, Alex J. Levine and F. C. MacKintosh. 'Deformation of Cross-Linked Semiflexible Polymer Networks'. In: *Phys. Rev. Lett.* 91 (2003), p. 108102.

[41] D. A. Head, A. J. Levine and F. C. MacKintosh. 'Distinct regimes of elastic response and deformation modes of cross-linked cytoskeletal and semiflexible polymer networks'. In: *Phys. Rev. E* 68 (2003), p. 061907.

[42] Jan Wilhelm and Erwin Frey. 'Elasticity of Stiff Polymer Networks'. In: *Phys. Rev. Lett.* 91 (2003), p. 108103.

[43] P. R. Onck et al. 'Alternative Explanation of Stiffening in Cross-Linked Semiflexible Networks'. In: *Phys. Rev. Lett.* 95 (2005), p. 178102.

[44] A. J. Licup, A. Sharma and F. C. MacKintosh. 'Elastic regimes of subisostatic athermal fiber networks'. In: *Phys. Rev. E* 93 (2016), p. 012407.

[45] Claus Heussinger and Erwin Frey. 'Floppy Modes and Nonaffine Deformations in Random Fiber Networks'. In: *Phys. Rev. Lett.* 97 (2006), p. 105501.

[46] Claus Heussinger, Boris Schaefer and Erwin Frey. 'Nonaffine rubber elasticity for stiff polymer networks'. In: *Phys. Rev. E* 76 (2007), p. 031906.

[47] Paul A. Janmey et al. 'Negative normal stress in semiflexible biopolymer gels'. In: *Nature Materials* 6.1 (2007), pp. 48–51.

[48] Hyeran Kang et al. 'Nonlinear Elasticity of Stiff Filament Networks: Strain Stiffening, Negative Normal Stress, and Filament Alignment in Fibrin Gels'. In: *J. Phys. Chem. B* 113.12 (2009), pp. 3799–3805.

[49] K. E. Kasza et al. 'Nonlinear elasticity of stiff biopolymers connected by flexible linkers'. In: *Phys. Rev. E* 79 (2009), p. 041928.

[50] K.E. Kasza et al. 'Actin Filament Length Tunes Elasticity of Flexibly Cross-Linked Actin Networks'. In: *Biophysical Journal* 99.4 (2010), pp. 1091–1100.

[51] Hyungsuk Lee et al. 'Passive and active microrheology for cross-linked F-actin networks in vitro'. In: *Acta Biomaterialia* 6.4 (2010), pp. 1207–1218.

[52] O. Lieleg et al. 'Mechanics of Bundled Semiflexible Polymer Networks'. In: *Phys. Rev. Lett.* 99 (2007), p. 088102.

[53] Yiider Tseng et al. 'The Bimodal Role of Filamin in Controlling the Architecture and Mechanics of F-actin Networks'. In: *Journal of Biological Chemistry* 279.3 (2004), pp. 1819–1826.

[54] Jingyuan Xu, Yiider Tseng and Denis Wirtz. 'Strain Hardening of Actin Filament Networks: REGULATION BY THE DYNAMIC CROSS-LINKING PROTEIN α-ACTININ'. In: *Journal of Biological Chemistry* 275.46 (2000), pp. 35886–35892.

[55] Ovijit Chaudhuri, Sapun H. Parekh and Daniel A. Fletcher. 'Reversible stress softening of actin networks'. In: *Nature* 445.7125 (2007), pp. 295–298.

[56] Enrico Conti and Fred C. MacKintosh. 'Cross-Linked Networks of Stiff Filaments Exhibit Negative Normal Stress'. In: *Phys. Rev. Lett.* 102 (2009), p. 088102.

[57] E. M. Huisman et al. 'Three-Dimensional Cross-Linked F-Actin Networks: Relation between Network Architecture and Mechanical Behavior'. In: *Phys. Rev. Lett.* 99 (2007), p. 208103.

[58] E. M. Huisman, C. Storm and G. T. Barkema. 'Monte Carlo study of multiply crosslinked semiflexible polymer networks'. In: *Phys. Rev. E* 78 (2008), p. 051801.

[59] Jan A. Åström et al. 'Strain hardening, avalanches, and strain softening in dense cross-linked actin networks'. In: *Phys. Rev. E* 77 (2008), p. 051913.

[60] Cornelis Storm et al. 'Nonlinear elasticity in biological gels'. In: *Nature* 435.7039 (2005), pp. 191–194.

[61] T. van Dillen, P.R. Onck and E. Van der Giessen. 'Models for stiffening in cross-linked biopolymer networks: A comparative study'. In: *Journal of the Mechanics and Physics of Solids* 56.6 (2008), pp. 2240–2264.

[62] C. P. Broedersz, C. Storm and F. C. MacKintosh. 'Nonlinear Elasticity of Composite Networks of Stiff Biopolymers with Flexible Linkers'. In: *Phys. Rev. Lett.* 101 (2008), p. 118103.

[63] Hyungsuk Lee et al. 'Molecular origin of strain softening in cross-linked F-actin networks'. In: *Phys. Rev. E* 82 (2010), p. 011919.

[64] B. A. DiDonna and T. C. Lubensky. 'Nonaffine correlations in random elastic media'. In: *Phys. Rev. E* 72 (2005), p. 066619.

[65] E Cerda, K Ravi-Chandar and L Mahadevan. 'Thin films - Wrinkling of an elastic sheet under tension'. In: *Nature* 419.6907 (2002), 579–580.

[66] E. Cerda and L. Mahadevan. 'Geometry and Physics of Wrinkling'. In: *Phys. Rev. Lett.* 90 (2003), p. 074302.

[67] E. Cerda. 'Mechanics of scars'. In: *Journal of Biomechanics* 38.8 (2005), pp. 1598–1603.

[68] Andrew B. Croll and Alfred J. Crosby. 'Pattern Driven Stress Localization in Thin Diblock Copolymer Films'. In: *Macromolecules* 45.9 (2012), 4001–4006.

[69] Yuri Ebata and Alfred J. Crosby. 'Wrinkling membranes with compliant boundaries'. In: *Soft Matter* 10 (2014), pp. 1963–1968.

[70] Yuri Ebata, Andrew B. Croll and Alfred J. Crosby. 'Wrinkling and strain localizations in polymer thin films'. In: *Soft Matter* 8 (2012), pp. 9086–9091.

[71] E. K. Hobbie et al. 'Wrinkling and Strain Softening in Single-Wall Carbon Nanotube Membranes'. In: *Phys. Rev. Lett.* 104.12 (2010).

[72] Jiangshui Huang et al. ‘Capillary wrinkling of floating thin polymer films’. In: *Science* 317.5838 (2007), 650–653.

[73] Wilhelm T. S. Huck et al. ‘Ordering of Spontaneously Formed Buckles on Planar Surfaces’. In: *Langmuir* 16.7 (2000), pp. 3497–3501.

[74] Jérémy Hure, Benoît Roman and José Bico. ‘Stamping and Wrinkling of Elastic Plates’. In: *Phys. Rev. Lett.* 109 (2012), p. 054302.

[75] Vishal Nayyar, K. Ravi-Chandar and Rui Huang. ‘Stretch-induced stress patterns and wrinkles in hyperelastic thin sheets’. In: *International Journal of Solids and Structures* 48.25–26 (2011), pp. 3471–3483.

[76] Vishal Nayyar, K. Ravi-Chandar and Rui Huang. ‘Stretch-induced wrinkling of polyethylene thin sheets: Experiments and modeling’. In: *International Journal of Solids and Structures* 51.9 (2014), pp. 1847–1858.

[77] Matthew R. Semler et al. ‘Localization and length-scale doubling in disordered films on soft substrates’. In: *Phys. Rev. E* 88 (2013), p. 032409.

[78] Christopher M. Stafford et al. ‘A buckling-based metrology for measuring the elastic moduli of polymeric thin films’. In: *Nature Materials* 3.8 (2004), pp. 545–550.

[79] Y. Wesley Wong and Sergio Pellegrino. ‘Wrinkled membranes Part I: experiments’. In: *J. Mech. Mater. Struct.* 1.1 (2006), 3–25.

[80] Dong Yan, Kai Zhang and Gengkai Hu. ‘Wrinkling of structured thin films via contrasted materials’. In: *Soft Matter* 12 (2016), pp. 3937–3942.

[81] S. Cai et al. ‘Periodic patterns and energy states of buckled films on compliant substrates’. In: *Journal of the Mechanics and Physics of Solids* 59.5 (2011), pp. 1094–1114.

[82] Benny Davidovitch et al. ‘Prototypical model for tensional wrinkling in thin sheets’. In: *Proceedings of the National Academy of Sciences* 108.45 (2011), pp. 18227–18232.

[83] Z.Y. Huang, W. Hong and Z. Suo. ‘Nonlinear analyses of wrinkles in a film bonded to a compliant substrate’. In: *Journal of the Mechanics and Physics of Solids* 53.9 (2005), pp. 2101–2118.

[84] Bo Li et al. ‘Surface Wrinkling Patterns on a Core-Shell Soft Sphere’. In: *Phys. Rev. Lett.* 106 (2011), p. 234301.

[85] Y. Wesley Wong and Sergio Pellegrino. ‘Wrinkled membranes Part II: analytical models’. In: *J. Mech. Mater. Struct.* 1.1 (2006), 27–61.

[86] Pascal Müller and Jan Kierfeld. ‘Wrinkling of Random and Regular Semiflexible Polymer Networks’. In: *Phys. Rev. Lett.* 112 (2014), p. 094303.

[87] Pascal Müller. ‘Shear-induced wrinkling of semiflexible polymer-networks’. Diploma thesis. TU Dortmund, 2011.

[88] H. Balke. *Einführung in die Technische Mechanik: Festigkeitslehre*. Springer-Lehrbuch. Springer Berlin Heidelberg, 2014.

[89] L.D. Landau et al. *Theory of Elasticity*. Bd. 7. Elsevier Science, 2012.

[90] D.H. Boal. *Mechanics of the Cell*. Cambridge University Press, 2002.

[91] David S. Courson and Ronald S. Rock. 'Actin Cross-link Assembly and Disassembly Mechanics for α-Actinin and Fascin'. In: *Journal of Biological Chemistry* 285.34 (2010), pp. 26350–26357.

[92] J. Liu et al. 'Visualizing the Strain Field in Semiflexible Polymer Networks: Strain Fluctuations and Nonlinear Rheology of F-Actin Gels'. In: *Phys. Rev. Lett.* 98 (2007), p. 198304.

[93] William H Press et al. *Numerical Recipes: the art of scientific computing, Third Edition (C++)*. Cambridge University Press, 2007.

[94] S. Kaufmann et al. 'Talin anchors and nucleates actin filaments at lipid membranes A direct demonstration'. In: *FEBS Letters* 314.2 (1992), pp. 203–205.

[95] H Kojima, A Ishijima and T Yanagida. 'Direct measurement of stiffness of single actin filaments with and without tropomyosin by in vitro nanomanipulation'. In: *Proceedings of the National Academy of Sciences* 91.26 (1994), pp. 12962–12966.

[96] H.E. Huxley et al. 'X-ray diffraction measurements of the extensibility of actin and myosin filaments in contracting muscle'. In: *Biophysical Journal* 67.6 (1994), pp. 2411–2421.

[97] H Isambert et al. 'Flexibility of actin filaments derived from thermal fluctuations. Effect of bound nucleotide, phalloidin, and muscle regulatory proteins'. In: *Journal of Biological Chemistry* 270.19 (1995), pp. 11437–11444.

[98] E. Pasternak and A.V. Dyskin. 'Materials and structures with macroscopic negative Poisson's ratio'. In: *International Journal of Engineering Science* 52 (2012), pp. 103–114.

[99] Timothy J. Healey, Qingdu Li and Ron-Bin Cheng. 'Wrinkling Behavior of Highly Stretched Rectangular Elastic Films via Parametric Global Bifurcation'. In: *Journal of Nonlinear Science* 23.5 (2013), pp. 777–805.

[100] Sylke Rohrlach. *Striped Eel Catfish (Stinging Eel Catfish)-Plotosus lineatus*. online. 2013.

[101] Rasika M. Harshey. 'Bacterial Motility on a Surface: Many Ways to a Common Goal'. In: *Annual Review of Microbiology* 57.1 (2003), pp. 249–273.

[102] D.J.T Sumpter. 'The principles of collective animal behaviour'. In: *Philosophical Transactions of the Royal Society of London B: Biological Sciences* 361.1465 (2006), pp. 5–22.

[103] David J. T. Sumpter. *Collective Animal Behavior*. Berlin, Boston: Princeton University Press, 2010.

[104] Andrea Cavagna et al. 'Scale-free correlations in starling flocks'. In: *Proceedings of the National Academy of Sciences* 107.26 (2010), pp. 11865–11870.

[105] Tamás Vicsek and Anna Zafeiris. 'Collective motion'. In: *Physics Reports* 517.3–4 (2012). Collective motion, pp. 71–140.

[106] Fernando Peruani et al. 'Collective Motion and Nonequilibrium Cluster Formation in Colonies of Gliding Bacteria'. In: *Phys. Rev. Lett.* 108 (2012), p. 098102.

[107] Luis H. Cisneros et al. 'Fluid dynamics of self-propelled microorganisms, from individuals to concentrated populations'. In: *Experiments in Fluids* 43.5 (2007), pp. 737–753.

[108] Julien Deseigne, Olivier Dauchot and Hugues Chaté. 'Collective Motion of Vibrated Polar Disks'. In: *Phys. Rev. Lett.* 105 (2010), p. 098001.

[109] Igor S. Aranson, Dmitri Volfson and Lev S. Tsimring. 'Swirling motion in a system of vibrated elongated particles'. In: *Phys. Rev. E* 75 (2007), p. 051301.

[110] Arshad Kudrolli et al. 'Swarming and Swirling in Self-Propelled Polar Granular Rods'. In: *Phys. Rev. Lett.* 100 (2008), p. 058001.

[111] Vijay Narayan, Sriram Ramaswamy and Narayanan Menon. 'Long-Lived Giant Number Fluctuations in a Swarming Granular Nematic'. In: *Science* 317.5834 (2007), pp. 105–108.

[112] M. V. Sapozhnikov, I. S. Aranson and J. S. Olafsen. 'Coarsening of granular clusters: Two types of scaling behaviors'. In: *Phys. Rev. E* 67 (2003), p. 010302.

[113] Dmitri Volfson, Arshad Kudrolli and Lev S. Tsimring. 'Anisotropy-driven dynamics in vibrated granular rods'. In: *Phys. Rev. E* 70 (2004), p. 051312.

[114] J. S. Olafsen and J. S. Urbach. 'Clustering, Order, and Collapse in a Driven Granular Monolayer'. In: *Phys. Rev. Lett.* 81 (1998), pp. 4369–4372.

[115] Jérémie Palacci et al. 'Sedimentation and Effective Temperature of Active Colloidal Suspensions'. In: *Phys. Rev. Lett.* 105 (2010), p. 088304.

[116] Jeremie Palacci et al. 'Living Crystals of Light-Activated Colloidal Surfers'. In: *Science* 339.6122 (2013), pp. 936–940.

[117] Walter F. Paxton et al. 'Catalytic Nanomotors: Autonomous Movement of Striped Nanorods'. In: *J. Am. Chem. Soc.* 126.41 (2004), pp. 13424–13431.

[118] Gastón Miño et al. 'Enhanced Diffusion due to Active Swimmers at a Solid Surface'. In: *Phys. Rev. Lett.* 106 (2011), p. 048102.

[119] P. Dhar et al. 'Autonomously Moving Nanorods at a Viscous Interface'. In: *Nano Letters* 6.1 (2006). PMID: 16402789, pp. 66–72.

[120] Giovanni Volpe et al. 'Microswimmers in patterned environments'. In: *Soft Matter* 7 (2011), pp. 8810–8815.

[121] Ivo Buttinoni et al. 'Dynamical Clustering and Phase Separation in Suspensions of Self-Propelled Colloidal Particles'. English. In: *Phys. Rev. Lett.* 110.23 (2013).

[122] I. Theurkauff et al. 'Dynamic Clustering in Active Colloidal Suspensions with Chemical Signaling'. In: *Phys. Rev. Lett.* 108 (2012), p. 268303.

[123] Félix Ginot et al. 'Nonequilibrium Equation of State in Suspensions of Active Colloids'. In: *Phys. Rev. X* 5 (2015), p. 011004.

[124] Yutaka Sumino et al. 'Large-scale vortex lattice emerging from collectively moving microtubules'. English. In: *Nature* 483.7390 (2012), 448–452.

[125] Volker Schaller et al. 'Polar patterns of driven filaments.' In: *Nature* 467.7311 (2010), pp. 73–77.

[126] Volker Schaller et al. 'Frozen steady states in active systems'. English. In: *Proceedings of the National Academy of Sciences* 108.48 (2011), 19183–19188.

[127] Volker Schaller et al. 'Polar pattern formation: hydrodynamic coupling of driven filaments'. In: *Soft Matter* 7 (2011), pp. 3213–3218.

[128] Tariq Butt et al. 'Myosin Motors Drive Long Range Alignment of Actin Filaments'. In: *Journal of Biological Chemistry* 285.7 (2010), pp. 4964–4974.

[129] Yoshie Harada et al. 'Sliding movement of single actin filaments on one-headed myosin filaments'. In: *Nature* 326.6115 (1987), pp. 805–808.

[130] Eric Bertin, Michel Droz and Guillaume Grégoire. 'Boltzmann and hydrodynamic description for self-propelled particles'. In: *Phys. Rev. E* 74 (2006), p. 022101.

[131] Francesco Ginelli et al. 'Large-Scale Collective Properties of Self-Propelled Rods'. In: *Phys. Rev. Lett.* 104 (2010), p. 184502.

[132] C. A. Weber et al. 'Long-Range Ordering of Vibrated Polar Disks'. In: *Phys. Rev. Lett.* 110 (2013), p. 208001.

[133] F. D. C. Farrell et al. 'Pattern Formation in Self-Propelled Particles with Density-Dependent Motility'. In: *Phys. Rev. Lett.* 108 (2012), p. 248101.

[134] Yaouen Fily and M. Cristina Marchetti. 'Athermal Phase Separation of Self-Propelled Particles with No Alignment'. In: *Phys. Rev. Lett.* 108 (2012), p. 235702.

[135] Gabriel S. Redner, Michael F. Hagan and Aparna Baskaran. 'Structure and Dynamics of a Phase-Separating Active Colloidal Fluid'. In: *Phys. Rev. Lett.* 110 (2013), p. 055701.

[136] Julian Bialké, Hartmut Löwen and Thomas Speck. 'Microscopic theory for the phase separation of self-propelled repulsive disks'. In: *Europhysics Letters* 103.3 (2013), p. 30008.

[137] Adrien Lefauve and David Saintillan. 'Globally aligned states and hydrodynamic traffic jams in confined suspensions of active asymmetric particles'. In: *Phys. Rev. E* 89 (2014), p. 021002.

[138] Guillaume Grégoire and Hugues Chaté. 'Onset of Collective and Cohesive Motion'. In: *Phys. Rev. Lett.* 92 (2004), p. 025702.

[139] Frank Schweitzer and Lutz Schimansky-Geier. 'Clustering of "active" walkers in a two-component system'. In: *Physica A: Statistical Mechanics and its Applications* 206.3–4 (1994), pp. 359–379.

[140] F. J. Nédélec et al. 'Self-organization of microtubules and motors'. In: *Nature* 389.6648 (1997), pp. 305–308.

[141] H H Wensink and H Löwen. 'Emergent states in dense systems of active rods: from swarming to turbulence'. In: *Journal of Physics: Condensed Matter* 24.46 (2012), p. 464130.

[142] Yingzi Yang, Vincent Marceau and Gerhard Gompper. 'Swarm behavior of self-propelled rods and swimming flagella'. In: *Phys. Rev. E* 82 (2010), p. 031904.

[143] Henricus H. Wensink et al. 'Meso-scale turbulence in living fluids'. In: *Proceedings of the National Academy of Sciences* 109.36 (2012), pp. 14308–14313.

[144] Fernando Peruani, Andreas Deutsch and Markus Bär. 'Nonequilibrium clustering of self-propelled rods'. In: *Phys. Rev. E* 74 (2006), p. 030904.

[145] A. Kaiser, H. H. Wensink and H. Löwen. 'How to Capture Active Particles'. In: *Phys. Rev. Lett.* 108 (2012), p. 268307.

[146] H. H. Wensink and H. Löwen. 'Aggregation of self-propelled colloidal rods near confining walls'. In: *Phys. Rev. E* 78 (2008), p. 031409.

[147] Masoud Abkenar et al. 'Collective behavior of penetrable self-propelled rods in two dimensions'. In: *Phys. Rev. E* 88 (2013), p. 062314.

[148] Samuel R. McCandlish, Aparna Baskaran and Michael F. Hagan. 'Spontaneous segregation of self-propelled particles with different motilities'. In: *Soft Matter* 8 (2012), pp. 2527–2534.

[149] Christoph A Weber, Florian Thüroff and Erwin Frey. 'Role of particle conservation in self-propelled particle systems'. In: *New Journal of Physics* 15.4 (2013), p. 045014.

[150] Christoph A. Weber et al. 'Nucleation-induced transition to collective motion in active systems'. In: *Phys. Rev. E* 86 (2012), p. 030901.

[151] Thomas Surrey et al. 'Physical Properties Determining Self-Organization of Motors and Microtubules'. In: *Science* 292.5519 (2001), pp. 1167–1171.

[152] Jean-Baptiste Caussin et al. 'Emergent Spatial Structures in Flocking Models: A Dynamical System Insight'. In: *Phys. Rev. Lett.* 112 (2014), p. 148102.

[153] X. Yang, D. Marenduzzo and M. C. Marchetti. 'Spiral and never-settling patterns in active systems'. In: *Phys. Rev. E* 89 (2014), p. 012711.

[154] Antoine Bricard et al. 'Emergent vortices in populations of colloidal rollers'. In: *Nature Communications* 6 (2015).

[155] Enkeleida Lushi, Hugo Wioland and Raymond E Goldstein. 'Fluid flows created by swimming bacteria drive self-organization in confined suspensions'. In: *Proceedings of the National Academy of Sciences of the United States of America* 111.27 (2014), pp. 9733–9738.

[156] S. Ramaswamy, R. Aditi Simha and J. Toner. 'Active nematics on a substrate: Giant number fluctuations and long-time tails'. In: *Europhysics Letters* 62.2 (2003), p. 196.

[157] J. Tailleur and M. E. Cates. 'Statistical Mechanics of Interacting Run-and-Tumble Bacteria'. In: *Phys. Rev. Lett.* 100 (2008), p. 218103.

[158] M. E. Cates and J. Tailleur. 'When are active Brownian particles and run-and-tumble particles equivalent? Consequences for motility-induced phase separation'. In: *Europhysics Letters* 101.2 (2013), p. 20010.

[159] Yaouen Fily, Silke Henkes and M. Cristina Marchetti. 'Freezing and phase separation of self-propelled disks'. In: *Soft Matter* 10 (2014), pp. 2132–2140.

[160] Sebastian Weitz, Andreas Deutsch and Fernando Peruani. 'Self-propelled rods exhibit a phase-separated state characterized by the presence of active stresses and the ejection of polar clusters'. In: *Phys. Rev. E* 92 (2015), p. 012322.

[161] Aparna Baskaran and M Cristina Marchetti. 'Nonequilibrium statistical mechanics of self-propelled hard rods'. In: *Journal of Statistical Mechanics: Theory and Experiment* 2010.04 (2010), P04019.

[162] Andrey Sokolov et al. 'Concentration Dependence of the Collective Dynamics of Swimming Bacteria'. In: *Phys. Rev. Lett.* 98 (2007), p. 158102.

[163] Rudolf Gross and Achim Marx. *Festkörperphysik*. Berlin, Boston: De Gruyter Oldenbourg, 2014.

[164] Siegfried Hunklinger. *Festkörperphysik*. Berlin, Boston: De Gruyter Oldenbourg, 2014.

[165] Kellar Autumn et al. 'Evidence for van der Waals adhesion in gecko setae'. In: *Proceedings of the National Academy of Sciences* 99.19 (2002), pp. 12252–12256.

[166] Gerhard Kahl and Hartmut Löwen. 'Classical density functional theory: an ideal tool to study heterogeneous crystal nucleation'. In: *Journal of Physics: Condensed Matter* 21.46 (2009), p. 464101.

[167] Matthew G. Knepley et al. 'An efficient algorithm for classical density functional theory in three dimensions: Ionic solutions'. In: *The Journal of Chemical Physics* 132.12, 124101 (2010).

[168] Robert Evans. 'Nature of the liquid-vapor interface and other topics in the statistical-mechanics of nonuniform, classical fluids'. In: *Advances in Physics* 28.2 (1979), 143–200.

[169] J.L. Barrat and J.P. Hansen. *Basic Concepts for Simple and Complex Liquids*. Cambridge University Press, 2003.

[170] Jonathan V. Selinger. *Introduction to the Theory of Soft Matter*. Soft and Biological Matter. Springer International Publishing, 2016.

[171] G J Vroege and H N W Lekkerkerker. 'Phase transitions in lyotropic colloidal and polymer liquid crystals'. In: *Reports on Progress in Physics* 55.8 (1992), p. 1241.

[172] Lars Onsager. 'The Effects of Shape on the Interaction of Colloidal Particles'. In: *Annals of the New York Academy of Sciences* 51.4 (1949), pp. 627–659.

[173] Richard F. Kayser and Harold J. Raveché. 'Bifurcation in Onsager's model of the isotropic-nematic transition'. In: *Phys. Rev. A* 17 (1978), pp. 2067–2072.

[174] J M Kosterlitz and D J Thouless. 'Ordering, metastability and phase transitions in two-dimensional systems'. In: *Journal of Physics C: Solid State Physics* 6.7 (1973), p. 1181.

[175] D. Frenkel and R. Eppenga. 'Evidence for algebraic orientational order in a two-dimensional hard-core nematic'. In: *Phys. Rev. A* 31 (1985), pp. 1776–1787.

[176] M. Doi and S.F. Edwards. *The Theory of Polymer Dynamics*. International series of monographs on physics. Clarendon Press, 1988.

[177] D. S. Lemons and A. Gythiel. 'Paul Langevin's 1908 paper 'On the theory of Brownian motion'' '. In: *American Journal of Physics* 65.11 (1997), pp. 1079–1081.

[178] M. E. Cates and J. Tailleur. 'Motility-Induced Phase Separation'. In: *Annual Review of Condensed Matter Physics* 6 (2015), pp. 219–244.

[179] Pavel Kraikivski, Reinhard Lipowsky and Jan Kierfeld. 'Enhanced Ordering of Interacting Filaments by Molecular Motors'. In: *Phys. Rev. Lett.* 96 (2006), p. 258103.

[180] Solon, A.P., Cates, M.E. and Tailleur, J. 'Active brownian particles and run-and-tumble particles: A comparative study'. In: *Eur. Phys. J. Special Topics* 224.7 (2015), pp. 1231–1262.

[181] J. Tailleur and M. E. Cates. 'Sedimentation, trapping, and rectification of dilute bacteria'. In: *Europhysics Letters* 86.6 (2009), p. 60002.

[182] Mihaela Enculescu and Holger Stark. 'Active Colloidal Suspensions Exhibit Polar Order under Gravity'. In: *Phys. Rev. Lett.* 107 (2011), p. 058301.

[183] Joakim Stenhammar et al. 'Continuum Theory of Phase Separation Kinetics for Active Brownian Particles'. In: *Phys. Rev. Lett.* 111 (2013), p. 145702.

[184] Ronald D Vale, Thomas S Reese and Michael P Sheetz. 'Identification of a Novel Force-Generating Protein, Kinesin, Involved in Microtubule-Based Motility'. In: *Cell* 42.1 (1985), pp. 39–50.

[185] S J Kron and J A Spudich. 'Fluorescent actin filaments move on myosin fixed to a glass surface.' In: *Proceedings of the National Academy of Sciences of the United States of America* 83.17 (1986), pp. 6272–6276.

[186] Anne-Marie Lauzon et al. 'A Multi-Scale Approach to Airway Hyperresponsiveness: From Molecule to Organ'. In: *Frontiers in Physiology* 3 (2012), p. 191.

[187] M. Rex, H. H. Wensink and H. Löwen. 'Dynamical density functional theory for anisotropic colloidal particles'. In: *Phys. Rev. E* 76 (2007), p. 021403.

[188] Raphael Wittkowski and Hartmut Löwen. 'Dynamical density functional theory for colloidal particles with arbitrary shape'. In: *Molecular Physics* 109.23-24 (2011), pp. 2935–2943.

[189] Aparna Baskaran and M. Cristina Marchetti. 'Hydrodynamics of self-propelled hard rods'. In: *Phys. Rev. E* 77 (2008), p. 011920.

[190] Aparna Baskaran and M. Cristina Marchetti. 'Enhanced Diffusion and Ordering of Self-Propelled Rods'. In: *Phys. Rev. Lett.* 101 (2008), p. 268101.

[191] A. Baskaran and M. C. Marchetti. 'Self-regulation in self-propelled nematic fluids'. In: *The European Physical Journal E* 35.9 (2012), pp. 1–8.

[192] Elias Putzig and Aparna Baskaran. 'Phase separation and emergent structures in an active nematic fluid'. In: *Phys. Rev. E* 90 (2014), p. 042304.

[193] A. Kaiser et al. 'Capturing self-propelled particles in a moving microwedge'. In: *Phys. Rev. E* 88 (2013), p. 022311.

[194] Yaouen Fily, Aparna Baskaran and Michael F. Hagan. 'Dynamics of self-propelled particles under strong confinement'. In: *Soft Matter* 10 (2014), pp. 5609–5617.

[195] Cameron W Harvey et al. 'Continuum modeling of myxobacteria clustering'. In: *New Journal of Physics* 15.3 (2013), p. 035029.

[196] Xingbo Yang and M. Cristina Marchetti. 'Hydrodynamics of Turning Flocks'. In: *Phys. Rev. Lett.* 115 (2015), p. 258101.

[197] A G Thompson et al. 'Lattice models of nonequilibrium bacterial dynamics'. In: *Journal of Statistical Mechanics: Theory and Experiment* 2011.02 (2011), P02029.

[198] J. V. Sengers and J. T. R. Watson. 'Improved International Formulations for the Viscosity and Thermal Conductivity of Water Substance'. In: *Journal of Physical and Chemical Reference Data* 15.4 (1986), pp. 1291–1314.

[199] Greg M. Barbara and James G. Mitchell. 'Bacterial tracking of motile algae'. In: *FEMS Microbiology Ecology* 44.1 (2003), pp. 79–87.

[200] Avraham Be'er et al. 'Periodic Reversals in Paenibacillus dendritiformis Swarming'. In: *Journal of Bacteriology* 195.12 (2013), 2709–2717.

[201] Jens Efsen Johansen et al. 'Variability in motility characteristics among marine bacteria'. In: *Aquat Microb Ecol* 28.3 (2002), pp. 229–237.

[202] Matthias Theves et al. 'A Bacterial Swimmer with Two Alternating Speeds of Propagation'. In: *Biophysical Journal* 105.8 (2013), pp. 1915–1924.

[203] Yilin Wu et al. 'Periodic reversal of direction allows Myxobacteria to swarm'. In: *Proceedings of the National Academy of Sciences* 106.4 (2009), pp. 1222–1227.

[204] L Cisneros et al. 'Reversal of bacterial locomotion at an obstacle'. In: *Phys. Rev. E* 73.3, 1 (2006).

[205] PS Grassia, EJ Hinch and LC Nitsche. 'Computer simulations of Brownian motion of complex systems'. In: *Journal of Fluid Mechanics* 282 (1995), pp. 373–403.

[206] Chase P. Broedersz et al. 'Criticality and isostaticity in fibre networks.' In: *Nature Physics* 7.12 (2011), pp. 983–988.

[207] Gavin A. Buxton and Nigel Clarke. '"Bending to Stretching" Transition in Disordered Networks'. In: *Phys. Rev. Lett.* 98 (2007), p. 238103.

[208] E. M. Huisman and T. C. Lubensky. 'Internal Stresses, Normal Modes, and Nonaffinity in Three-Dimensional Biopolymer Networks'. In: *Phys. Rev. Lett.* 106 (2011), p. 088301.

[209] B. Wagner et al. 'Cytoskeletal polymer networks: The molecular structure of cross-linkers determines macroscopic properties'. In: *Proceedings of the National Academy of Sciences* 103.38 (2006), pp. 13974–13978.

[210] Claus Heussinger, Mark Bathe and Erwin Frey. 'Statistical mechanics of semiflexible bundles of wormlike polymer chains'. In: *Phys. Rev. Lett.* 99.4 (2007).

[211] KM Schmoller, O Lieleg and AR Bausch. 'Structural and Viscoelastic Properties of Actin/Filamin Networks: Cross-Linked versus Bundled Networks'. In: *Biophysical Journal* 97.1 (2009), pp. 83–89.

[212] E. M. Huisman et al. 'Semiflexible Filamentous Composites'. In: *Phys. Rev. Lett.* 105 (2010), p. 118101.

[213] Izabela K. Piechocka et al. 'Multi-scale strain-stiffening of semiflexible bundle networks'. In: *Soft Matter* 12 (2016), pp. 2145–2156.

[214] Mo Bai et al. 'The mechanics and affine-nonaffine transition in polydisperse semiflexible networks'. In: *Soft Matter* 7 (2011), pp. 907–914.

[215] A. S. Shahsavari and R. C. Picu. 'Exceptional stiffening in composite fiber networks'. In: *Phys. Rev. E* 92 (2015), p. 012401.

[216] O. Lieleg et al. 'Transient Binding and Dissipation in Cross-Linked Actin Networks'. In: *Phys. Rev. Lett.* 101 (2008), p. 108101.

[217] Sabine M. Volkmer Ward et al. 'Dynamic Viscoelasticity of Actin Cross-Linked with Wild-Type and Disease-Causing Mutant alpha-Actinin-4'. In: *Biophysical Journal* 95.10 (2008), 4915–4923.

[218] Hidetake Miyata, Ryohei Yasuda and Kazuhiko Kinosita. 'Strength and lifetime of the bond between actin and skeletal muscle α-actinin studied with an optical trapping technique'. In: *Biochimica et Biophysica Acta (BBA) - General Subjects* 1290.1 (1996), pp. 83–88.

[219] Bin Guo and William H Guilford. 'Mechanics of actomyosin bonds in different nucleotide states are tuned to muscle contraction'. In: *Proceedings of the National Academy of Sciences of the United States of America* 103.26 (2006), pp. 9844–9849.

[220] Jorge M Ferrer et al. 'Measuring molecular rupture forces between single actin filaments and actin-binding proteins'. In: *Proceedings of the National Academy of Sciences of the United States of America* 105.27 (2008), pp. 9221–9226.

[221] H. H. Wensink and E. Trizac. 'Generalized Onsager theory for strongly anisometric patchy colloids'. In: *The Journal of Chemical Physics* 140.2, 024901 (2014).

[222] Andrey Sokolov and Igor S. Aranson. 'Rapid expulsion of microswimmers by a vortical flow'. In: *Nature Communications* 7 (2016).

[223] M. Tournus et al. 'Flexibility of bacterial flagella in external shear results in complex swimming trajectories'. In: *Journal of The Royal Society Interface* 12.102 (2015).

[224] Joakim Stenhammar et al. 'Phase behaviour of active Brownian particles: the role of dimensionality'. In: *Soft Matter* 10 (2014), pp. 1489–1499.

[225] Adam Wysocki, Roland G. Winkler and Gerhard Gompper. 'Cooperative motion of active Brownian spheres in three-dimensional dense suspensions'. In: *Europhysics Letters* 105.4 (2014), p. 48004.

[226] Torsten Fließbach. *Statistische Physik*. Spektrum Akademischer Verlag, 2010.

[227] Franz Schwabl. *Statistische Mechanik*. Springer Berlin Heidelberg, 2006.

Acknowledgements

First of all, I would like to thank Jan Kierfeld for giving me the opportunity to work on my PhD under his supervision, for his guidance, and many helpful discussions.
I also want to thank Tanniemola Liverpool for his supervision during my research visit in Bristol.
I acknowledge financial support from the German Academic Exchange Service (DAAD) during my stay in Bristol.
Last but not least, I want to thank Lukas Langer, Matthias Kampmann, and Steffen Varwig for helpful comments on this manuscript.